Controlled switching of fluorescent organic nanoparticles through energy transfer for bioimaging applications

Kateryna Trofymchuk

UNIVERSITÉ DE STRASBOURG

ÉCOLE DOCTORALE DES SCIENCES DE LAVIE ET DE DA SANTE

Laboratoire de Biophotonique et Pharmacologie – UMR 7213

THÈSE présentée par :

Kateryna TROFYMCHUK

soutenue le : **16 Décembre 2016**

pour obtenir le grade de : **Docteur de l'université de Strasbourg**

Discipline/ Spécialité : physique-nanophysique

Controlled switching of fluorescent organic nanoparticles through energy transfer for bioimaging applications

THÈSE dirigée par :

M. KLYMCHENKO Andrey Docteur, Université de Strasbourg

RAPPORTEURS :

M. JULLIEN Ludovic Professeur, ENS de Paris

M. METIVIER Rémi Docteur, ENS de Cachan

AUTRES MEMBRES DU JURY :

M. LEONARD Jérémie Docteur, Université de Strasbourg

Acknowledgments

First of all, I would like to express my sincere gratitude to my supervisor Dr. Andrey KLYMCHENKO for the continuous support of my Ph.D. study, for his patience, motivation, immense knowledge, for being not only my Boss but also a Friend. His guidance helped me during all the time of research and writing of my thesis. I could not have imagined having a better advisor and mentor for my Ph.D. study.

My sincere thanks also goes to Prof. Yves MELY for accepting me as a Master student to the Lab four years ago.

I would like also to thank my committee members for their willingness to participate in the examining of my Ph.D. thesis: Prof. Ludovic JULLIEN from ENS de Paris, Dr. METIVIER Rémi from ENS de Cachan and Dr. Jérémie LEONARD from Strasbourg University.

I am deeply thankful to Dr. Guy DUPORTAIL for his continuous care and help, to Dr. Andreas REISCH, without whose precious support it would not be possible to conduct this research, to Dr. Mayeul COLLOT for creation of an amazingly pleasant atmosphere in the Lab of chemistry, to Dr. Youri ARNTZ for his advices, to Dr. Frédéric PRZYBILLA, Dr. Pascal DIDIER, Dr. Nicolas HUMBERT, Dr. Ludovic RICHERT for their help in any situation. I have many thanks to Ingrid BARTHEL and Marlyse WERNERT for their availability and help.

I'm grateful to my mother and brother for their enormous support and encouragements.

Many thanks to my fellow labmates Iryna, Lesia, Bogdan, Ievgen¸ Oleksandr, Taras, Rajhans, Liliana, Redouane, Oleksii, Doriane and others for the stimulating discussions, for the sleepless nights we were working together before deadlines, and for all the fun we have had in the last four years.

Last but not the least, I want to acknowledge Ecole doctorale des Science de la Vie et de la Sante for providing me the financial support.

Thank you very much!

Kateryna TROFYMCHUK

Contents

Acknowledgments *1*
Contents *3*
List of abbreviations *7*
Aim of the PhD thesis *9*
1. PART 1. Bibliographical overview *11*
1.1. Principle of fluorescence **11**
1.2. Characteristics of fluorescence **13**
1.2.1. Emission and excitation spectra 13
1.2.2. Fluorescence Lifetime 14
1.2.3. Quantum yield and fluorescence brightness 15
1.2.4. Fluorescence Anisotropy 16
1.3. Fluorescent probes **18**
1.3.1. Requirements for fluorescent probes 18
1.3.2. Organic dyes 19
1.3.3. Fluorescent proteins 21
1.3.4. Quantum dots 22
1.3.5. Upconversion nanoparticles 24
1.3.6. Carbon dots 25
1.3.7. Polymer dots 26
1.3.8. Dendrimers 26
1.3.9. Fluorescent organic dye nanoparticles 27
1.3.10. Dye-doped silica nanoparticles 28
1.3.11. Dye-loaded polymer NPs 29
1.4. Excitation energy transfer **32**
1.4.1. Dexter energy transfer 33
1.4.2. Förster Resonance Energy Transfer 34
1.4.3. EET in multi-fluorophore systems 39
1.4.3.a. Systems with low donor cooperativity 41
1.4.3.b.Systems with high donor cooperativity 50

1.4.4. EET in other systems 58

1.5. Technics for characterization of NPs 65

1.5.1. Dynamic Light Scattering 66

1.5.2. Fluorescence Correlation Spectroscopy 67

1.5.3. Total Internal Reflection Fluorescence microscopy 68

1.5.4. Transmission Electron Microscopy 69

1.5.5. Scanning Electron Microscopy 70

1.5.6. Atomic Force Microscopy 71

2. PART 2. Results and discussions 72

2.1. Development of dye-loaded polymer NPs 72

2.1.1. Article 1:"Tuning the color and photostability of perylene diimides inside polymer nanoparticles: towards biodegradable substitutes of quantum dots" 74

2.1.2. Tailoring fluorescence and blinking in dye loaded NPs by polymer matrix 89

2.2. Design of efficient FRET inside polymer NPs 103

2.2.1. Article 2: "Exploiting Fast Exciton Diffusion in Dye-Doped Polymer Nanoparticles to Engineer Efficient Photoswitching" 104

2.2.2. Article 3: "Giant light harvesting nano-antenna for single-molecule detection at ambient light" 119

2.3. FRET to the surface of polymer NPs: Organic nanoparticle antenna for amplified FRET-based biosensing 147

2.4. Conclusions and perspectives 155

3. PART 3. Materials and methods 158

3.1. Materials 158

3.2. Preparation of polymer NPs 160

3.3. NPs characterization 160

3.4. Single particle measurements 160

3.4.1. Fluorescence correlation spectroscopy (FCS) and data analysis 160

3.4.2. Single particle imaging 161

3.4.3. Detection of proteins at single molecule level 162

3.4.4. TEM imaging 162
3.4.5. Time-resolved fluorescence..... 163

3.5. Cellular studies..... 163

Résume de la thèse en français 165
References 174
List of publications..... 187
List of conferences..... 188

List of abbreviations

ACQ	aggregation-caused quenching
AFM	atomic force microscopy
AIE	aggregation-induced emission
BHQ	black hole quencher
BODIPY	boron-dipyrromethene
BPB	bromophenol blue
C-dots	carbon dots
cmc	critical micelle concentration
CNMBC	conjugated-nonconjugated multiblock copolymers
CR	cross relaxation
CSU	cooperative sensitization upconversion
CuAAC	copper catalyzed azide–alkyne cycloaddition
DCF	2',7'-dichlorofluorescein
DLS	dynamic light scattering
DNA	deoxyribonucleic acid
DOX	doxorubicin
EET	excitation energy transfer
ESA	excited-state absorption
ESIPT	excited-state intramolecular proton transfer
ETU	energy transfer upconversion
FCS	fluorescence correlation spectroscopy
FITC	fluorescein isothiocyanate
FLIM	fluorescence-lifetime imaging microscopy
FOD-NPs	fluorescent organic dye nanoparticles
FP	fluorescent protein
FRET	Förster resonance energy transfer
FWHM	full width at half maximum
GES	genetically encoded sensors
IC	internal conversion
ICT	intramolecular charge transfer
ISC	intersystem crossing
LOD	limit of detection
MANI	4-methamino-9-allyl-1,8-naphthalimide
MEH-PPV	poly[2-methoxy-5-(2-ethylhexyloxy)-1,4-phenylenevinylene]
NIR	near-infrared
NPs	nanoparticles
PA	photon avalanche
PAMAM	polyamidoamine
pcFRET	photochromic Förster resonance energy transfer

PCL	polycaprolactone
PCQ	proximity-caused quenching
P-dots	polymer dots
PEG	polyethylene glycol
PLGA	poly(d,l-lactic-co-glycolic acid)
PluS NPs	Pluronic silica nanoparticles
PMMA	polymethylmethacrylate
PMAMA	poly-(methyl methacrylate-co-methacrylic acid
PPO	polypropylene oxide
QDs	quantum dots
QY	quantum yield
RhB	rhodamine B
TCSPC	time-correlated single-photon counting
TEM	transmission electron microscopy
TEOS	tetraethoxysilane
TIRF	total internal reflection fluorescence
TMR	tetramethylrhodamine
TPLSM	two-photon laser scanning microscopy
UC	upconversion
UCNPs	upconversion nanoparticles
UV/Vis	ultraviolet-visible

Aim of the PhD thesis

The human organism is composed of number of various cells, which, in their turn, contain a huge amount of different biomolecules. Their concentration, modification and interaction are usually controlled with high spatial and temporal precision. Knowledge of these mechanisms, as well as a possibility to detect biomolecules even at extremely low concentrations, would allow to not only reveal some mysteries of life but would lead to the early diagnosis of several diseases, such as cancer. For this propose, fluorescence imaging is a very promising technique. It allows highly sensitive and non-invasive detection by relatively inexpensive instruments. Fluorescence signal may be modulated in response to the presence of target biomolecules by fluorescence resonance energy transfer (FRET).

Speed, resolution and sensitivity of today's fluorescence bioimaging can be significantly improved by fluorescent nanoparticles (NPs), which are many times brighter than organic dyes and fluorescent proteins. Dye-loaded polymer NPs are interesting alternatives to dominating in this field inorganic quantum dots (QDs) because of their potential biodegradability. Nevertheless, their preparation is difficult because of the problem of self-quenching of encapsulated dyes, and the photostability of organic dyes is usually lower than that of QDs. In addition, the size of NPs, normally around 15-60 nm, is much larger than FRET radius. That could be an obstacle for their successful application as an energy donor in FRET domain.

The aim of my PhD project to develop bright and photostable dye-loaded polymer NPs capable to undergo efficient FRET beyond the Förster radius and then to apply them for biomolecular sensing.

The first step for performing this project was design of NPs. The characteristics of polymer NPs are determined mainly by properties and organization of encapsulated dyes and by physical properties of hosted polymer. It is crucial to determine the particularity of dye structure that provides the most efficient encapsulation, the highest possible brightness and photostability. Another important point that should be considered during design of NPs is the absence of dyes leaching from NPs especially in a biological environment. To this end, studies of encapsulation behavior of perylene

and rhodamine B derivative dyes was performed in several biodegradable/biocompatible polymer matrices.

The second step consisted of determination of the most favorable conditions for energy transfer in order to obtain efficient FRET to single acceptors inside NPs. Two applications of this phenomenon were investigated, namely amplified photoswitching and antenna effect.

The third step was creation of a biosensor with a single molecule sensitivity based on highly efficient FRET to the surface of NPs.

PART 1. Bibliographical overview

1.1. Principle of fluorescence

Usually *fluorescence* is defined as a phenomenon of emission of a photon by matter after initial electronic excitation in light absorption process. It is a part of a more general phenomenon, that called *luminescence,* and includes the emission of substance excited in the course of chemical reactions (*chemiluminescence*), biochemical reactions (*bioluminescence*) or upon oxidation/reduction at electrode (*electrochemiluminescence*).

Light is an electromagnetic radiation consisting of fluctuations of electric and magnetic fields. The word “light” usually refers to a region of electromagnetic radiation, which is visible to the human eye (wavelength in the range 400-700 nm). For molecular media, like biological systems, the interaction with light is described by the dipole approximation, where the electronic polarization of a molecule is exposed to an electric field. But the wave representation of light does not correctly explain the processes of absorption or scattering. They could be described by assuming that the light behaves like particles called photons, exhibiting properties of both waves and particles (the wave–particle duality).[1] A photon of light of specific frequency v has a discrete fixed energy $E_{photon}=hv$, where h is a Planck’s constant, that is equal to $6.63*10^{-34}$ J*sec.

Matter is composed of atoms, ions or molecules that have defined energy levels usually associated with energy levels that electrons can hold. And at each of these electronic energy levels molecules can exist in a number of vibrational energy levels. If the energy of photons propagating in molecular media matches the difference of energy levels between ground and first (or second) excited state the *absorption process* can occur. After this several deactivation processes can take place. They are usually illustrated by the *Jablonski diagram* (Figure 1.1). [2]

The singlet ground, first and second electronic states are depicted by S_0, S_1 and S_2, respectively. The transitions between $S_0 \rightarrow S_1$ (or $S_0 \rightarrow S_n$) states depict the processes of a photon *absorption*. Transitions occur in about 10^{-15} s, a time too short for significant displacement of nuclei (the Franck-Condon principle). The quantitative measure of fluorophore absorption is called a *molar extinction coefficient* ε (measured

in $M^{-1}cm^{-1}$). Molecule is usually excited to higher vibrational levels, and then it rapidly relaxes to the lowest vibrational level of S_1. This process is called the *internal conversion* and occurs within 10^{-12} s. Thus *fluorescence* ($S_1 \rightarrow S_0$) emission occurs from a thermally equilibrated excited state to higher vibrational levels of the ground state (with subsequent thermal equilibration within 10^{-12} s). Being in the state S_1 molecules can make *intersystem crossing* ($S_1 \rightarrow T_1$) with a spin conversion. As transition $T_1 \rightarrow S_0$ is "forbidden" in quantum mechanics, it occurs within time 10^{-3} s and called *phosphorescence* (Figure 1.1).

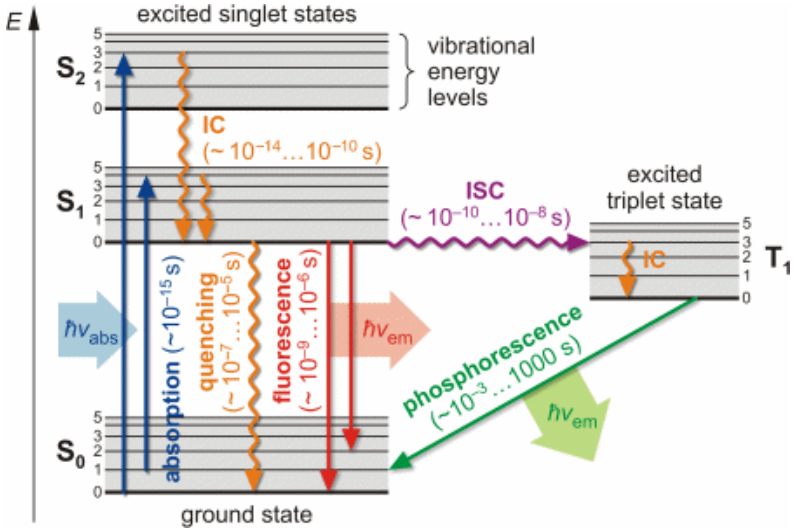

Figure 1.1. Jablonski energy diagram illustrating the transition between electronic states of a molecule for the quantum mechanical processes of fluorescence and phosphorescence. Waved lines mark non-radiative transitions. IC means internal conversion, ISC intersystem crossing. Adopted from http://home.uni-leipzig.de.

A fluorophore can be excited not only by absorbing a single photon but also by simultaneous absorption of two or more photons, the sum energy of which corresponds to the energy of $S_0 \rightarrow S_1$ transition. This phenomenon is called *multiphoton excitation*. In bioimaging, two-photon excitation is widely used, because only the focal point of the laser beam has enough power to generate this process, ensuring absence of background excitation. Moreover, near-infrared (NIR) lasers, used for two-photon excitation, match perfectly to so called optical window of living tissue (region from 650nm to 1350 nm), where the light has its maximal depth of penetration of tissue and allows deep tissue imaging. [3] Although in bioimaging two-photon excitation is more popular, the examples of using three-photon excitation are also known. [4, 5]

1.2. Characteristics of fluorescence

1.2.1. Emission and excitation spectra

Emission spectrum is the wavelength distribution of an emission measured at a single constant excitation wavelength. *Excitation spectrum* is the dependence of emission intensity, measured at a single emission wavelength, upon scanning the excitation wavelength.

Due to discrete nature of the electronic states, emission and excitation spectra generally follows several rules:

The Stokes shift: due to the rapid relaxation to the lowest vibrational level of S_1, the energy of emission is typically less than that of excitation. Furthermore, radiative transition takes place to higher vibrational levels of S_0, resulting in an additional loss of energy. In addition to these effects, fluorophores can display further Stokes shifts due to solvent effects, excited-state reactions, complex formation, and/or energy transfer.

Kasha-Vavilov rule: Emission spectra (and quantum yield) are generally independent of the excitation wavelength, because the excess of energy quickly dissipates from high electronic and vibration levels leaving a fluorophore in the lowest vibrational level of S_1.

Mirror image rule: For most of fluorophores absorption spectrum is a mirror image of emission spectrum. According to the Franck-Condon principle the nucleus does not move and as a result the vibrational levels of the S_1 resemble the ones of S_0 state.

Emission and excitation spectra could be measured empirically using a *spectrofluorometer*. The excitation light passes through a monochromator, which allows a wavelength of interest to be selected for use as the exciting light. The emission is collected at 90 degrees to the exciting light. The emission is also either passed through a filter or a monochromator before being detected by a photomultiplier tube (Figure 1.2).

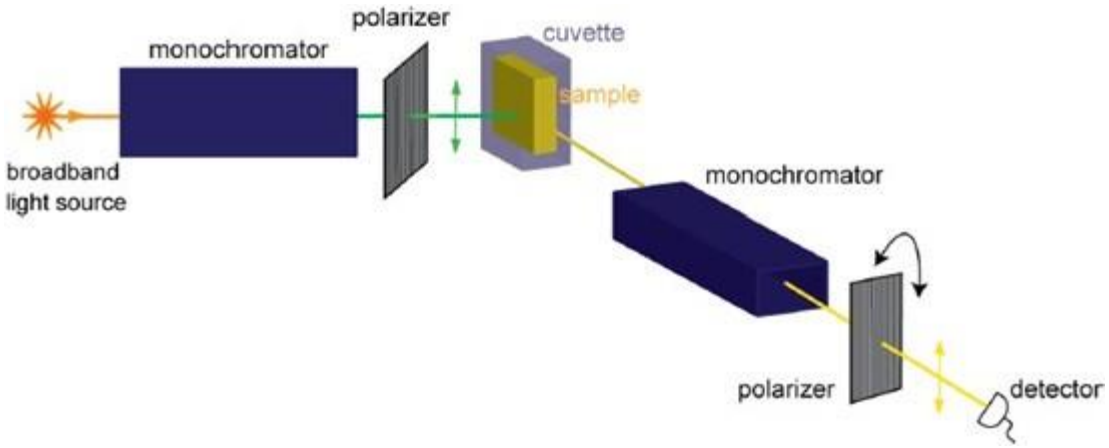

Figure 1.2. Schematic diagram of a spectrofluorometer. The light from source passes through the monochromator selecting the fixed wavelength and excites the sample. The fluorescence is collected at 90° and passes through another monochromator and collected by detector. For anisotropy measurements additional polarizer between the first monochromator and sample and between the second monochromator and detector could be added. Image adopted form semrock.com.

1.2.2. Fluorescence Lifetime

The average time that molecule stays in its excited state before emitting a photon is called *fluorescence lifetime* and depends on the sum of decay rates of all deactivation processes.

Absorption and emission processes are usually studied based on populations of molecules. In general, the behavior of an excited population of fluorophores is described by a rate equation:

$$\frac{d\,n^*(t)}{dt} = -kn^*(t) + f(t)$$

where n* is the number of excited elements at time t, f(t) is an arbitrary function of the time, describing the time course of the excitation and the rate k is the sum of the rates of all possible deactivation pathways: fluorescence, internal conversion and vibrational relaxation, intersystem crossing, energy transfer and other non-radiative pathways. The dimensions of k are s^{-1} (transitions per molecule per unit time).

If excitation is switched off at t = 0, the equation describes the decrease in excited molecules at all further times:

$$\frac{d\,n^*(t)}{dt} = -kn^*(t)$$

And after integration:

$$n^*(t) = n^*(0)\exp(-kt)$$

The lifetime $\boldsymbol{\tau}$ is equal to k^{-1}.

Two complementary techniques for fluorescence lifetime measurements exist: the time domain (time-correlated single-photon counting (TCSPC), gating method) and the frequency domain (phase modulation). In the time domain, a short pulse of light excites the sample and fluorescent signal is recorded. In the frequency domain, the fluorophore is excited with modulated source of light, and the emission has a phase-shifted similar waveform, and from this modulation lifetime can be determined (Figure 1.3). [2]

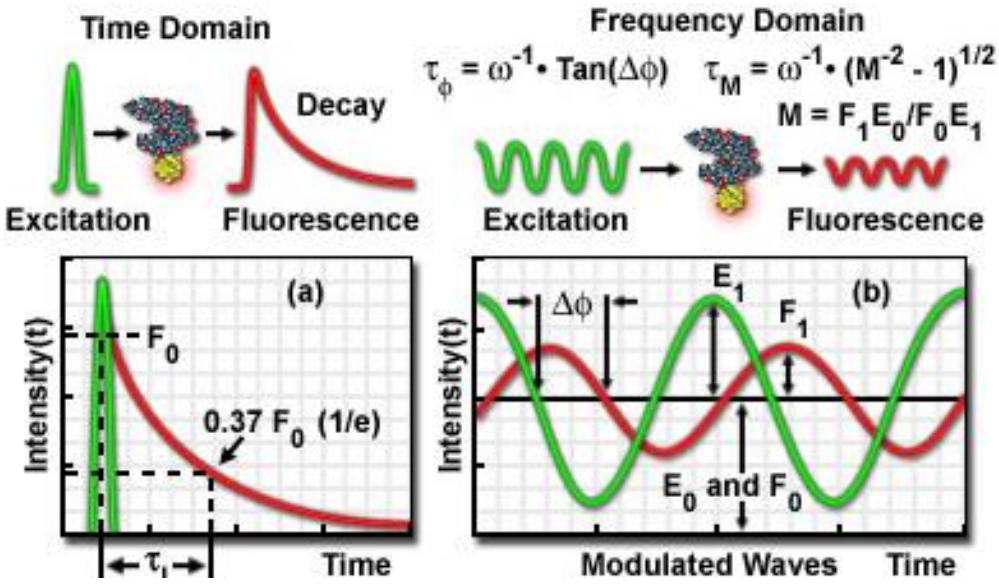

Figure 1.3. Principles of fluorescence lifetime measurements. In the time domain, fluorescent signal is recorded after a short excitation pulse. In the frequency domain, phase-modulation method is used. Image adopted from ref. [8]

Fluorescence-lifetime imaging microscopy (FLIM) is an imaging technique based on the measurement of differences in the exponential decay rate from a fluorescent sample. FLIM found numerous applications, because it is more robust than fluorescence intensity measurements, as it doesn't depend on the concentration of the fluorophores. [6]

1.2.3. Quantum yield and fluorescence brightness

Quantum yield (QY) is the ratio between the number of emitted photons and the number of absorbed photons. It is measured as the ratio of fluorescence emission to nonradiative losses:

$$QY = \frac{k_f}{k_f + k_{nr}} = \frac{k_f}{k} \approx \tau$$

where k_f is fluorescence emission rate, k_{nr} is the sum of rates of all non-emissive pathways. QY is proportional to fluorescence lifetime: addition of another non-radiative pathway increase k_{nr} and thus decrease $\boldsymbol{\tau}$ and QY.

QY of fluorescence could be determined absolutely or relatively. For absolute determinations a calibrated stand-alone integrating sphere setup is usually used.

For relative determination, the comparative method is applied, which involves the use of well characterized standard samples with known QY value. For this, emission and absorption spectra of the sample and the reference are measured at the same excitation wavelength, gain and slit bandwidths. And then the QY is calculated as:

$$QY = QY_{ref} \frac{\eta^2}{\eta_{ref}^2} \frac{I}{A} \frac{A_{ref}}{I_{ref}}$$

where QY_{ref} is the quantum yield of the reference compound, η is the refractive index of the solvent, I is the integrated fluorescence intensity and A is the absorbance at the excitation wavelength. The absorbance at the wavelength of excitation is optimally kept in between A = 0.02-0.05 in order to avoid inner filter effects and ensure linear response on the intensity. The quantum yield of fluorescence is always less than unity because of Stokes losses.

The *brightness* of the fluorophore is the product of the extinction coefficient and the fluorescence quantum yield:

$$B = QY * \varepsilon$$

1.2.4. Fluorescence Anisotropy

Fluorescence anisotropy is a phenomenon of depolarization of emitted light. Its measurements are based on principle of *photoselective excitation* of fluorophores by polarized light: the probability of excitation of a chromophore is maximal when the electric vector of light is parallel to molecular dipole (Figure 1.4).

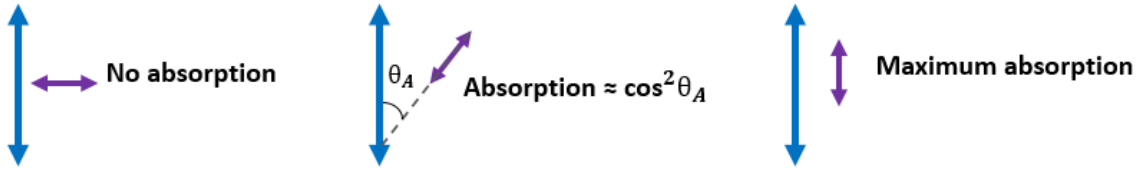

Figure 1.4. Principle of photoselective excitation. $\boldsymbol{\theta_A}$ is the angle between the electric vector of the indecent light (blue arrows) and the absorption transition moment of the molecule (purple arrows).

The emitted fluorescence is anisotropic, because the distribution of excited fluorophores is anisotropic, and any change in orientation of molecular dipole during the lifetime of the excited state will induce depolarization of fluorescence.[7] The main causes of fluorescence depolarization are internal and Brownian motion and excitation energy transfer (EET) to another molecule, chemically identical but with a different orientation (Figure 1.5).

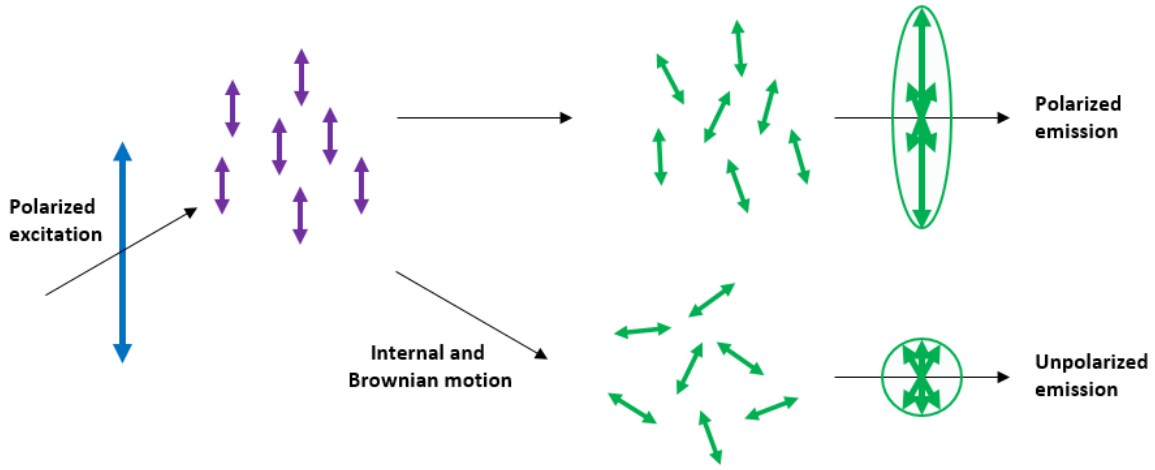

Figure 1.5. Fluorescence polarization and anisotropy. Polarized excitation is used to selectively excite dipole-aligned fluorophores.

To measure anisotropy the sample is excited with vertically polarized light, and the intensity of emission is measured through a polarizer (Figure 1.2). [2] When the emission polarizer is parallel to the polarized excitation, the intensity is called $I_{||}$. And when the polarizer is perpendicular (⊥) to the excitation the intensity is called $I_{\perp}$. Fluorescence anisotropy (r) and polarization (P) are defined as:

$$r = \frac{I_{||} - I_{\perp}}{I_{||} + 2I_{\perp}}$$

$$P = \frac{I_{||} - I_{\perp}}{I_{||} + I_{\perp}}$$

Measurements of anisotropy of fluorophores dispersed in polymer films are useful to estimate the EET. When the energy migrates within encapsulated fluorophores that are randomly distributed inside a polymer matrix, the fluorescence anisotropy should decrease due to the energy hopping between dyes. [8]

1.3. Fluorescent probes

As biological samples are poorly fluorescent, biosensing and bioimaging requires special fluorescent agents – fluorescent probes.

1.3.1. Requirements for fluorescent probes

To be successfully used in imaging or sensing fluorescent probes should meet some criteria [9, 10]:

- High quantum yield. It will not only increase fluorescence intensity, but suggests that alternative photochemical processes, such as bleaching or radical formation are less possible.
- High molar absorbance (extinction coefficient, ε). High ε of a fluorophore leads to a high *brightness* (product of QY and ε), and means that low intensity of excitation can be used. It could be useful for imaging of living tissue or imaging of very low quantity of fluorophores.[11]
- Optimal excitation wavelength. Practical consideration suggests that classical sources available for microscope should efficiently excite fluorophores. To avoid cell autofluorescence, the excitation wavelengths longer than 400-460 nm are preferable. For deeper penetration in tissue imaging, NIR sources of excitation around 650−1450 nm are optimal.[12]
- Optimal emission wavelength and large Stokes shift. Similarly to the excitation wavelength, the optimal emission wavelength for biological applications should be in red to NIR region. Stronger separation between absorption and emission bands reduces the light-scattering effects and allows more efficient collection of emitted light with broad-band filters or larger monochromator slits.

- Optimal fluorescence lifetime $\boldsymbol{\tau}$. Although longer lifetimes are easy to detect and to analyze, the lifetimes longer than 10^{-7} s (pyrene) are quenched by oxygen [13], that could be difficult to control. For some applications, such as flow cytometry short lifetime is more preferable in order to obtain response during the excitation-emission cycle. [14] For anisotropy measurements lifetime should fit timescale of molecular rotation. [1]
- High photostability. Fluorophores can undergo only limited number of cycles between ground and excited states. This is related to high reactivity of the excited state of the molecules. The interaction of the triplet state of a molecule and molecular oxygen is considered to be one of the main pathways of photobleaching. Regarding this, in many single molecule experiments oxygen scavenging systems are used for improving the dye stability[15], or even photostabilizing compounds such as 6-hydroxy-2,5,7,8-tetramethylchroman-2-caboxylic acid(Trolox), cyclooctatetraene (COT) or 4-nitrobenzyl alcohol (NBA) could be chemically attached to the molecules. [16]
- Solubility in the biological media and environmental stability. The stability of a fluorophore *in vivo* is another important consideration, probes should be insensitive to factors like pH or temperature if it is not wanted.

1.3.2. Organic dyes

Organic dyes are indispensable tools for fluorescent imaging and sensing. They are successfully used as biomolecular labels, environmental indicators and for cellular staining.[2, 17-19] The small size allows their incorporation into biological structures such as double-helical DNA (usually fluorescent nucleic acid base analogues [20]) and biomembranes [21, 22] with minimal perturbation.

They typically contain several combined aromatic rings and characterized by presence of delocalized π-electrons forming discrete energy states. Their emission wavelength covers all range from UV to NIR (Figure 1.6). The increase in the number of π-electrons usually shifts the fluorescence to longer wavelengths. [23] Based on the decades of works of chemists an enormous variation of structure, chemical reactivity and spectroscopic properties is available now. [18, 19]

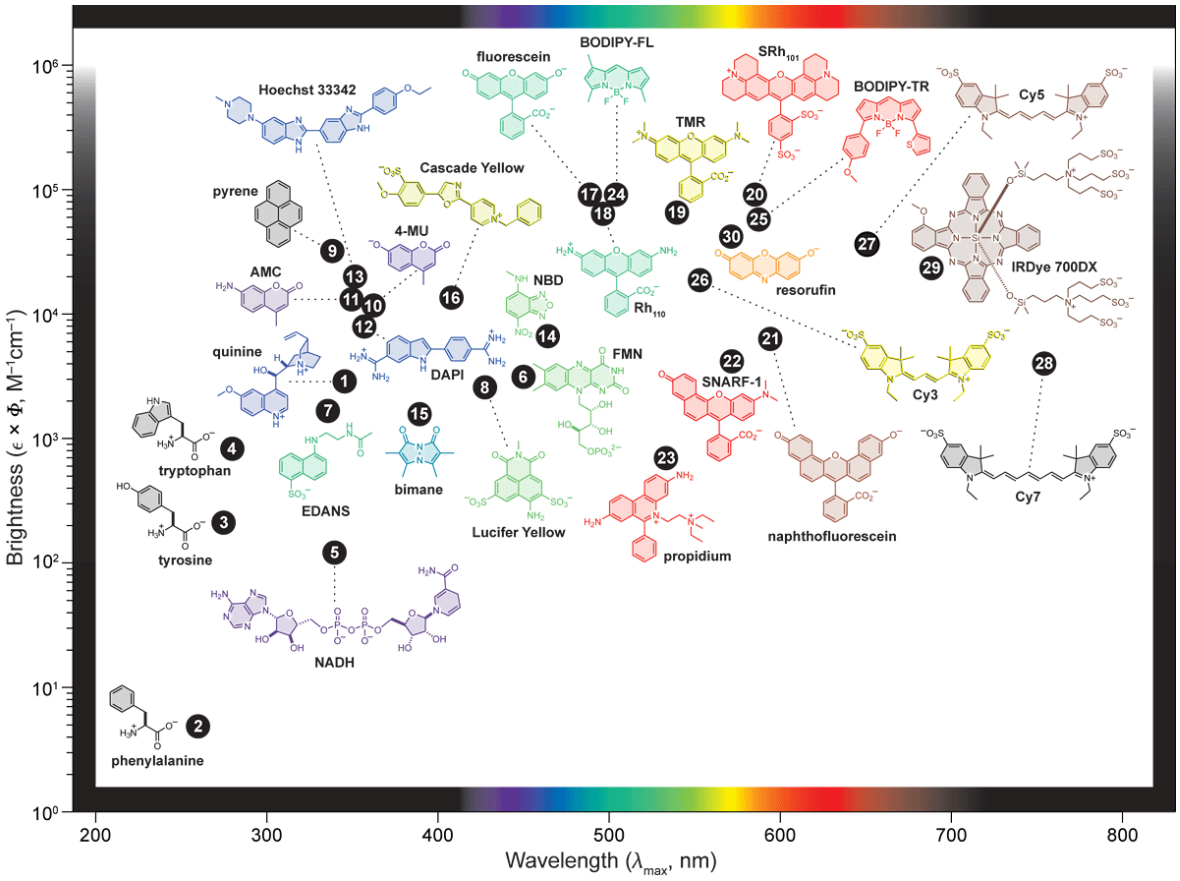

Figure 1.6. Fluorophore brightness versus the wavelength of maximum absorption (λ_{max}) for different classes of fluorophores. The colors of depicted structure illustrate their wavelengths of emission (λ_{em}). Adopted from ref. [19]

Fluorescent dyes could be classified into two categories: non-responsive (labels) and responsive (sensors/probes). Some prediction of their properties, based on the dyes structure, could be made: if the electronic density is delocalized symmetrically over the whole dye, the spectral sensitivity to the environment will be low, whereas the possibility of the polarization of its electronic structure suggests that this dye can be a reporter for sensing. [9]

Organic dyes family with rigid skeleton, such as *fluoresceins, rhodamines* and *cyanines,* have minimal vibrations-related energy losses, electronic density delocalized symmetrically over the whole structure, which provides high QY and low spectral sensitivity to the environment. That makes these dyes optimal for labeling.

Sensitivity to the polarity of the environment of the dye could be based on *intramolecular charge transfer* (ICT) that results in spectral shifts as a function of

polarity, or on *excited-state intramolecular proton transfer* (ESIPT) that provides the strong variation in the dual emission. [24-26]

Pyrene dyes are known to create stable excimers (complex between exited and non-exited fluorophores) that change dramatically fluorescence spectrum and lifetime. This property was used in fluorescence sensing of zinc and pyrophosphate ions [27] and “turn-on” sensing for iron ions in aqueous solution. [28] Based on organic dyes many types of molecular sensors were developed: the pH [29-31] ,temperature [32], oxygen [33], metal ions in living systems [34], etc.

1.3.3. Fluorescent proteins

Since 90^{s}, when the green fluorescent protein (GFP) was successfully cloned from the jellyfish *Aequorea Victoria [35]* and used as a gene expression reporter, FPs became widely used in biological research.[36] Its fluorophore is essentially an ‘organic dye’ located inside a barrel-like protein structure of molecular mass of 28 kDa (Figure 1.7).

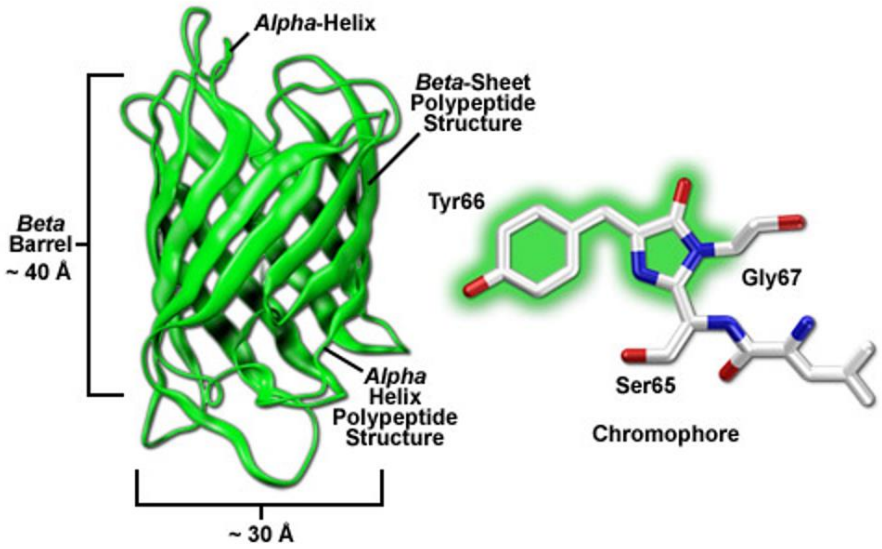

Figure 1.7. Architecture of Green Fluorescent Protein from *Aequorea Victoria* and chemical structure of its chromophore. Adopted from zeiss-campus.magnet.fsu.edu.

Mutant of GFP with improved optical properties enhanced GFP (EGFP) allows the practical use of GFPs in mammalian cells. It has an extinction coefficient of 55,000 $M^{-1}cm^{-1}$ and QY of 0.6. [37] Nowadays absorption and emission spectra of FPs cover almost the whole visible range (Figure 1.8). Some of FPs are able to switch between

various fluorescent and non-fluorescent states under the illumination with light, resulting in processes known as photoactivation, photoconversion or photoswitching. [38, 39] FPs could be synthesized inside the living cell as genetically engineered fusion products with other proteins. This allows locating different proteins inside the cell and visualizing the structures formed by them. Their fluorescence properties are similar to those of organic dyes, and some members of this family demonstrate increased photostability and high fluorescence quantum yield. [36]

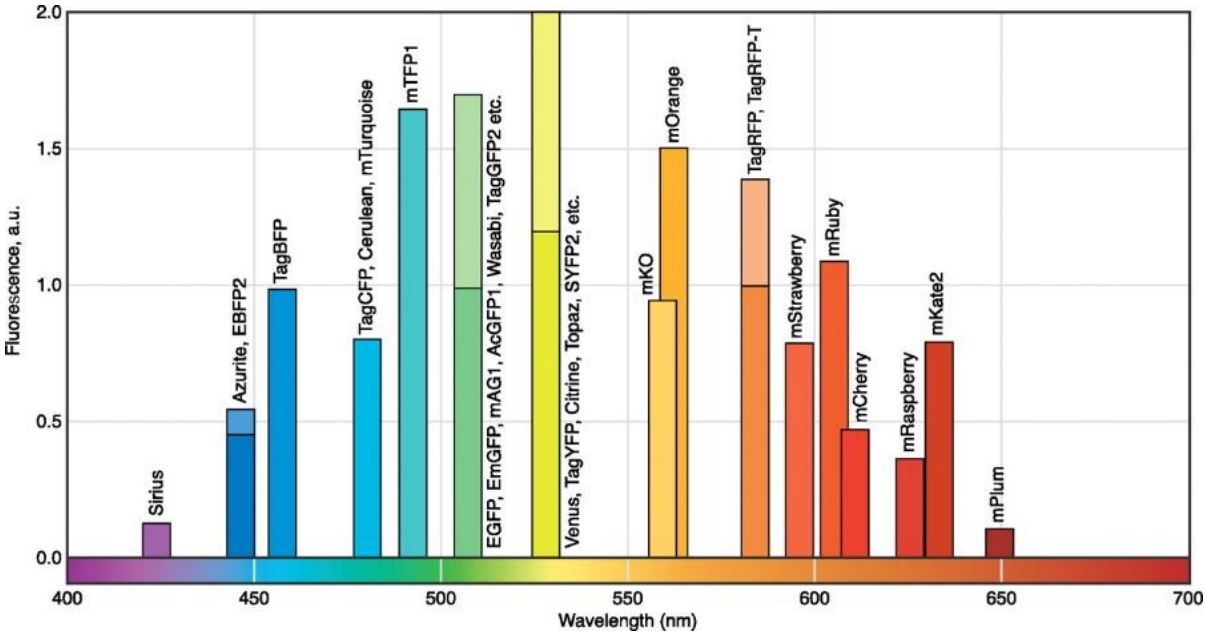

Figure 1.8. Spectral diversity of monomeric FPs. Columns present positions of emission λ_{max} and brightness normalized per EGFP brightness. Adopted from ref. [36]

1.3.4. Quantum dots

Quantum dots (QDs) are nanocrystals made of semiconductor materials from groups II-VI, III-V, or IV-VI of the periodic table (CdS, CdSe, CdTe, ZnS, PbS), with diameter in range of 2-10 nm. Although, together with biocompatible shell their size can reach up to 30 nm. QDs possess electronic properties that are intermediate between those of bulk semiconductors and discrete molecules. The size of QDs is smaller than Bohr radius (the average distance between the electron in conduction band and the hole it leaves in the valence band) the discrete quantization of energy level occurs (more similar to atoms than bulk materials). The absorption of light by QDs results in transition of an electron from the valence to conduction band and generation of electron-hole pairs. The recombination of these pairs results in release

of energy in form of emitted light. Decrease in size of QDs leads to increase in the difference in energies between the highest valence band and the lowest conduction band, and thus more energy is released after returning nanocrystal to ground state, resulting in a size-dependence of the color of the emitted light (Figure 1.9). [40]

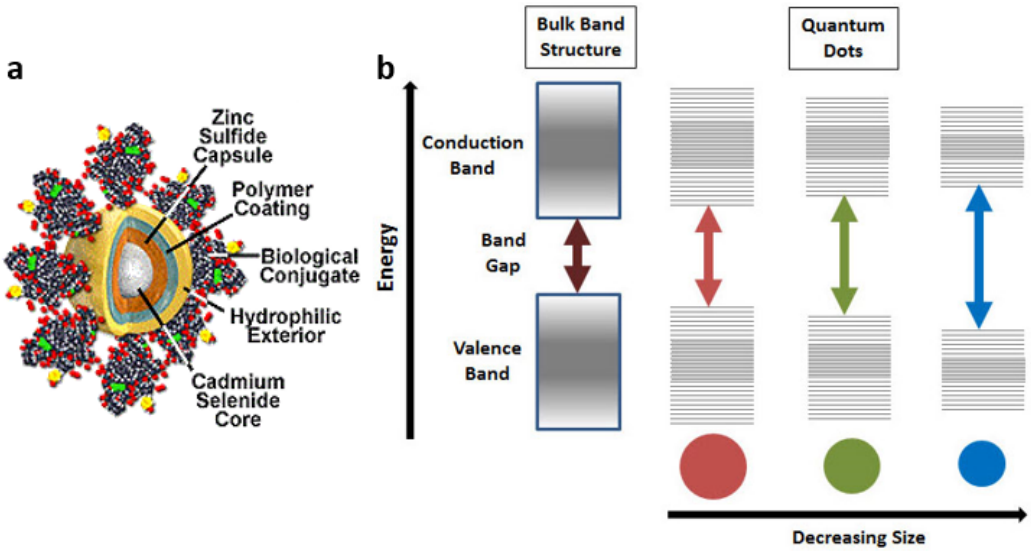

Figure 1.9. Schematic representation of QD and its energy levels. **a)** Schematic structure of QDs. Image adopted from www.olympusmicro.com. **b)** Splitting of energy levels in QDs due to the quantum confinement effect: semiconductor band gap increases with decrease in size of the nanocrystal. Image adopted from www.sigmaaldrich.com.

QDs have a range of properties that are desirable for biological imaging and sensing application [41]: large molar absorption coefficient (100,000−1000,000 $M^{-1}cm^{-1}$), high QY (0.3-1), a narrow emission profile (with full width at half maximum (FWHM) 20-30 nm), long fluorescence lifetimes (>10 ns) enables temporal imaging with significant improvement in signal-to-noise ratios in biological application (autofluorescence of biological media contributes to high background signal, but have shorter lifetimes) [42], and high resistance to photobleaching. But the blinking behavior of their emission [43] (rapid switching between emissive and non-emissive states) reduces their applicability in tracking applications. Due to the nature of the building materials QDs may be toxic. [44]

1.3.5. Upconversion nanoparticles

Lanthanide-doped upconversion NPs (UCNPs) are guest−host systems where trivalent lanthanide ions (Yb^{3+}, $Tm3^{+}$, and Er^{3+}) are dispersed as a guest in an appropriate dielectric host lattice ($NaYF_4$ or $NaGdF_4$) with a dimension of less than 100 nm . UCNPs convert NIR radiations into visible light via a nonlinear optical process in a broad range of wavelengths (Figure 1.10). The upconversion (UC) mechanisms can be categorized into five classes [45]:

1. Excited-state absorption (ESA) is a successive absorption of pump photons by a single ion 1 due to the ladder-like structure of a simple multilevel system).
2. Energy transfer upconversion (ETU). In this process, excited ion 1 transfers energy to the ground (G) state and excited state (E1) of ion 2.
3. Cooperative sensitization upconversion (CSU) is a process involving the interaction of three ions. After absorbing excitation photons, both ion 1 and ion 3 can interact with ion 2 simultaneously, cooperatively transfer the energy, and excite ion 2 to a higher state.
4. Cross relaxation (CR) is an energy transfer process, resulting from ion−ion interaction in which ion1 transfers part of its excited energy to ion 2
5. Photon avalanche (PA) is a process that produces UC above a certain threshold of excitation power. It is a looping process that involves processes of ESA for excitation light and an efficient CR that produces feedback.

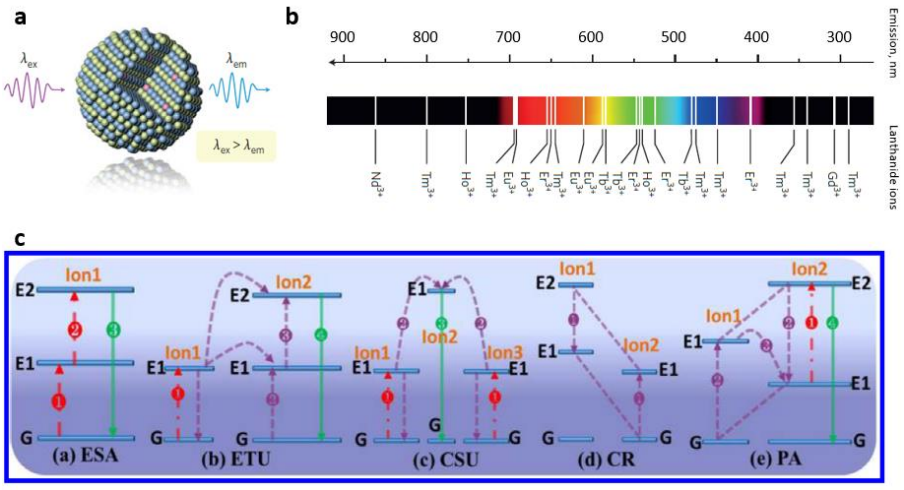

Figure 1.10. Schematic illustration of UCNP and illustration of its optical properties. **a)** Schematic illustration of UCNP composed of a crystalline "host" and embedded lanthanide dopant ions.

b) Typical Ln3+-based upconversion emission bands. Adopted from ref. [46] **c)** Principal UC processes for lanthanide-doped UCNPs: ESA, ETU, CSU, CR and PA. The red, violet and green lines represent photon excitation, energy transfer and emission processes, respectively. Adopted from ref. [45]

The fact that emission spectra is observed at shorter wavelength allows elimination of background signal, which together with the possibility of the excitation in the tissue transparent NIR window makes UPCNPs ideal for imaging. They have narrow and precisely located emission bands (which can enable referenced sensing and imaging), long life-time decays, very high chemical and photostability and the absence of blinking. [45, 46]

1.3.6. Carbon dots

Carbon dots (C-dots) are clusters of carbon atoms with diameter below 10 nm containing some fractions of oxygen and nitrogen. They could be prepared by many simple approaches: burning [47] or microwave heating [48] of organic matter (Figure 1.11). One-step synthesis allows placing the reactive amino groups on their surface, which strongly facilitates further functionalization. [49] Their emission color could be tuned by varying synthesis protocols, but both excitation and emission spectra are wide, which exclude multiplexing possibility. [50] They are biocompatible, have nanosecond lifetime and high two-photon absorption cross-section, QY in range 5-30% and good photostability, and found various application in imaging. [51]

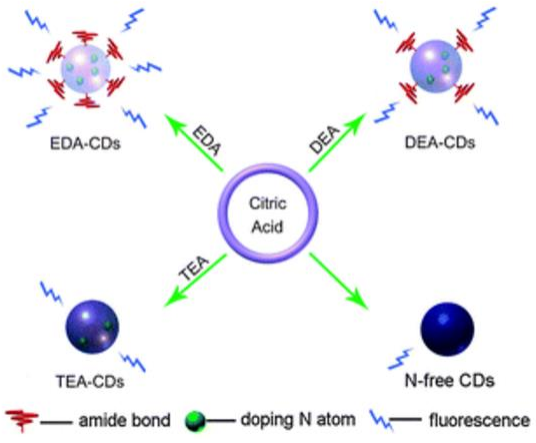

Figure 1.11. Schematic representation of synthesis of C-dots by microwave pyrolysis in the presence of various amines. Adopted from ref. [48]

1.3.7. Polymer dots

Polymer dots (P-dots) or conjugated polymer NPs (CPNs) are fluorescent NPs made from conjugated polymers (polymer molecules in which the π-electrons are delocalized over a significant part of chain) (Figure 1.12). Their size is in a range of 5 - 30 nm, they have broad absorption spectra with narrow emission profiles, high fluorescence QY (50-60%). They are prepared mainly by miniemulsion and reprecipitation methods. [52] Miniemulsion method consists of addition of dissolved polymers in water-immiscible organic solvent to an aqueous solution of appropriate surfactant with subsequent ultrasonication and solvent evaporation. In reprecipitation method, hydrophobic conjugated polymer is dissolved in a good solvent for the polymer and added into a miscible poor solvent (e.g., water), under stirring.

Changing the composition of P-dots results in tunable emission wavelength. The photophysical properties of conjugated polymers depend on the constituent elements and the particle size. [53] Generally, they exhibit very high extinction coefficient, moderate quantum yield and relatively short fluorescence lifetime. They are among the brightest fluorescent NPs developed to date.

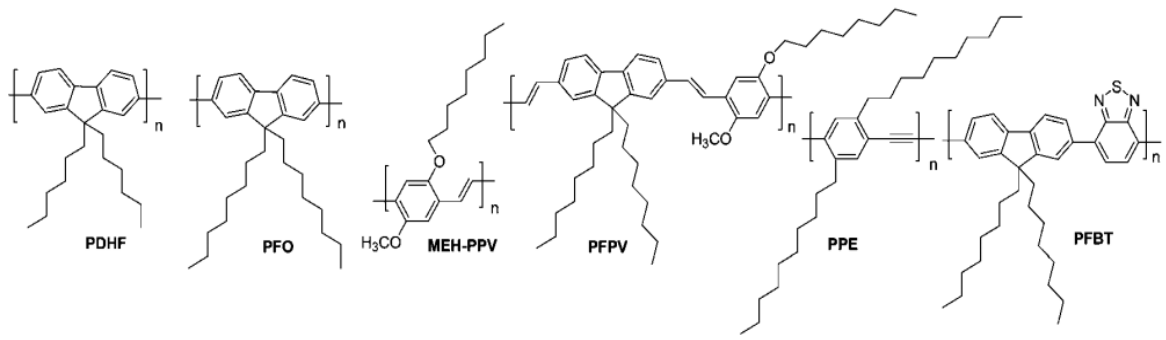

Figure 1.12. The structures of different conjugated polymers: poly(9,9-dihexylfluorene) (PDHF), poly(9,9-dioctylfluorene) (PFO), poly[2-methoxy-5-(2-ethylhexyloxy)-1,4-phenylenevinylene] (MEH-PPV), poly[2-methoxy-5-(2-ethylhexyloxy)-2,7-(9,9-dioctylfluorene)] (PFPV), poly(p-phenylene ethynylene) (PPE), poly(9,9-dioctylfluorene-2,7-diyl-co-benzothiadiazole) (PFBT).

1.3.8. Dendrimers

Dendrimers are repetitively branched molecules with size less than 2 nm, their fluorescence originates from fluorescent dyes grafted to extremities of the dendrimer. The dendritic architecture contains core, branches and end groups (Figure 1.13).

Synthesis of dendritic units is based on the principles of click chemistry. Solubility, chemical reactivity and glass transition temperature of dendrimers are controlled by nature of the terminal group. [54] The brightness of dendrimer is controlled by size, and the color by the terminal fluorophore. Their chemistry is well established. They have a large molar absorbance (up to 7000,000 $M^{-1}cm^{-1}$), QY ranges from very low up to 0.5. They were used for imaging and sensing, photodynamic therapy, drug delivery.[55, 56]

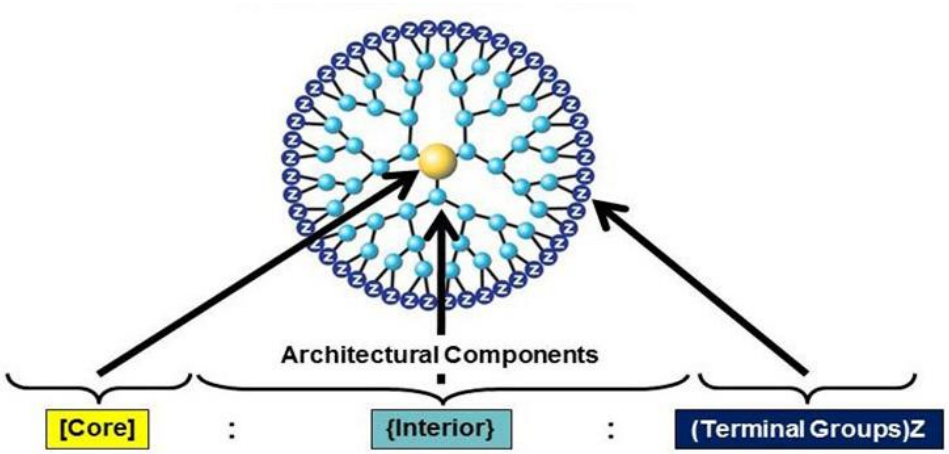

Figure 1.13. Architectural components of dendrimers. Adopted from ref. [54]

1.3.9. Fluorescent organic dye nanoparticles

Fluorescent organic dye nanoparticles (FOD-NPs) are nanostructured assemblies (aggregates) of specially designed organic dyes. [57] Several strategies for preparation of FOD-NPs exist (Figure 1.14):

A. Precipitation. Concentrated solution of hydrophobic dye in a solvent is added to water that results in rapid nucleation [58-60];
B. Ion-association of ionic dyes is a co-precipitation of ionic dyes in water in the presence of hydrophobic counter-ions [61-63];
C. Self-assembly of amphiphilic dyes. Specially designed organic amphiphilic molecules assemble in water solution into nanostructures with well-defined architecture [64, 65].

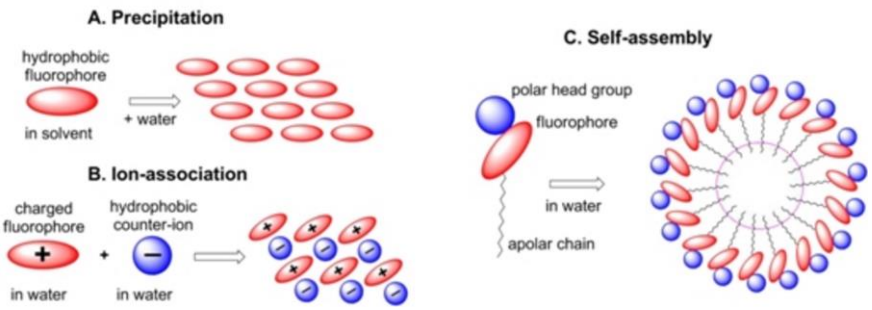

Figure 1.14. Precipitation, ion –association and self-assembly methods for preparation of FOD-NPs. Adopted from ref. [57]

Due to their nature they can be biodegradable and have various spectral properties and possibility of biofunctionalization. But the major challenge during preparation of FOD-NPs is to avoid fluorescence quenching due to electronic interactions of molecules in close proximity, so-called aggregation-caused quenching (ACQ). [66]

1.3.10. Dye-doped silica nanoparticles

Silica is a hydrophobic material, that is optically transparent and photophysically inert. [67] Silica nanoparticles (SiNPs) can be easily doped with various kinds of organic, metal–organic and metallic fluorophores, and their synthetic versatility allows preparation of multifunctional nanosystems (Figure 1.15). [68]. SiNPs also may be coated with fluorophores, but aggregation effects, accompanied by self-quenching, could be observed.

Several strategies for preparation of functionalized SiNPs were developed. Method, proposed by Stöber in the late 60s and modified by van Blaaderen, is based on condensing trialkoxysilane derivatives of fluorescent molecules with the monomeric tetraethoxysilane (TEOS) precursor during NPs growth, giving systems in which organic dyes are covalently linked to the silica matrix. Recently, other strategies for SiNPs have been developed, based on reverse microemulsions or on direct micelles as templates. [67] Emission wavelength, life-time decay, two-photon excitation properties are mostly defined by the embedded dyes. These are biocompatible particles with simple surface chemistry that are widely used in imaging and sensing. [69, 70]

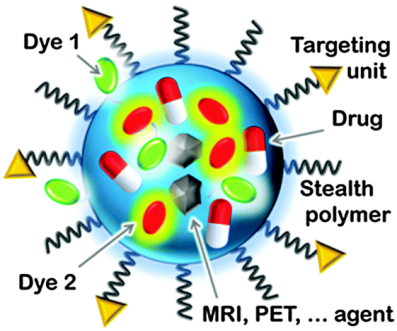

Figure 1.15. Schematic representation of a multifunctional SiNP. Adopted from ref. [68]

1.3.11. Dye-loaded polymer NPs

Polymer-based NPs have been already successfully applied in the field of drug-delivery, they have remarkable stability in biological media and well-controlled surface properties. Potentially, encapsulation of advanced non-toxic, bright and photostable fluorophores may give an ultimate tool for bioimaging and sensing application. The main principle for obtaining high brightness in dye-loaded polymer NPs is based on confining a large number of dyes in a small space, thus increasing particles' absorption coefficient. [71]

Various methods for preparation of NPs were proposed. [72] One way of preparing polymer NPs is direct polymerization of monomers (Figure 1.16). When polymerization starts with monomers of low water solubility dispersed with surfactant in an aqueous phase, it's called *conventional emulsion polymerization.* NPs of size 50-300 nm are obtained by this method. [73] In the case of *mini-emulsion polymerization* the size could be reduced by applying high-speed mechanic stirring or sonication and by addition of a water-soluble co-stabilizer. [74] In *micro-emulsion polymerization* a thermodynamically stable emulsion of monomer phase in aqueous phase is formed spontaneously and then polymerized. Through this technique, very small NPs (5-50 nm) could be obtained, but formation of empty micelles is also possible. [75]

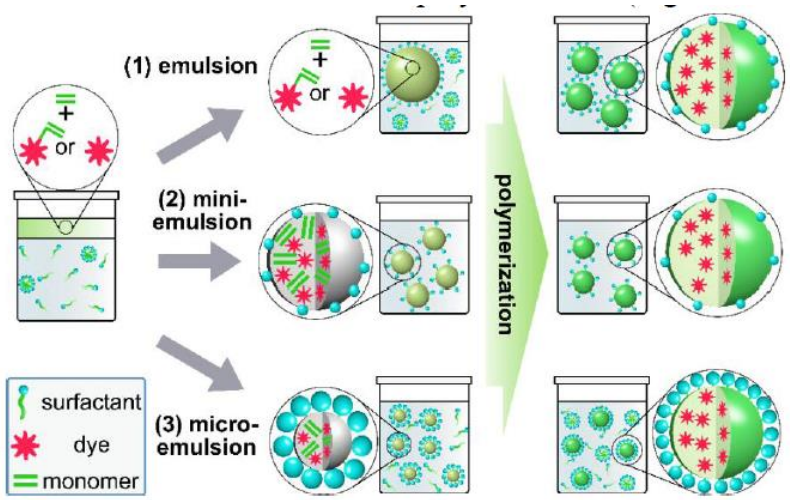

Figure 1.16. Preparation of dye-loaded polymer NPs though the polymerization strategies. Adopted from ref. [71]

Preparation of polymer NPs based on preformed polymers is also possible (Figure 1.17). In *emulsification solvent evaporation* the polymer dissolved in a water-immiscible solvent is dispersed in an aqueous phase with help of stabilizer under sonication or high-speed homogenization, which results in an emulsion of droplets of solvent with polymer inside. NPs of size 100-200 nm could be obtained. [76]

Certain amphiphilic polymers can *self-assemble* under thermodynamic conditions into NPs in form of micelles. [77] In this case solution of polymers in organic solvent is mixed with an aqueous phase, and when the concentration exceeds critical micelle concentration (CMC) the aggregation of the hydrophobic part of polymer takes place. This method allows to obtain NPs with size that range from <10 nm to 100 nm. The self-assembly is thermodynamically controlled process and micelles can undergo exchange. To avoid leaching the dyes are often covalently linked to the polymer.

Nanoprecipitation (or solvent displacement technique) is based on the addition of polymer, dissolved in a solvent, to aqueous phase. [78] It results in supersaturation of the polymer and formation of NPs. As it is a kinetically controlled process, the concentration of polymer, relative amount of organic and aqueous phase and mixing procedure influence the size. NPs from <10 nm up to hundreds nm could be obtained. The kinetically controlled formation makes easy confinement of dyes, but difference in solubility of polymer and organic dyes can lead to inhomogeneous distribution of dyes within NPs.

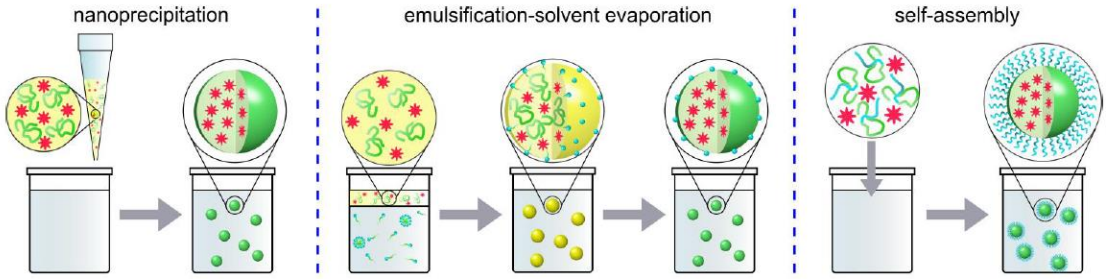

Figure 1.17. Techniques used for the preparation of dye loaded NPs from preformed polymers. Hydrophobic polymer segments are shown in green, hydrophilic ones in blue, organic solvent in yellow. Adopted from ref. [71]

Although the encapsulation of dye in rigid polymer matrix may serve as a shield from aggressive biological media, and dyes in solid environment exhibit much higher QY, high dye loading can lead to ACQ that decreases the QY. Several approaches were introduced that allow to strongly reduce ACQ in polymer NPs: aggregation induced emission (AIE) [79] as well as dye modification with bulky side groups [80] and bulky counterions. [81]

1.4. Excitation energy transfer

The process of excitation energy transfer (EET) occurs whenever the emission spectrum of a donor (D) fluorophore overlaps with the absorption spectrum of acceptor (A) molecule. Distinction should be made between *heterotransfer* and *homotransfer*, and between *radiative* and *nonradiative* transfer. [82]

Energy transfer from an excited molecule D*(donor) to another that is chemically different, A (acceptor) (D * + A→D+ A*) is called *heterotransfer*. If the donor and acceptor are identical, we have *homotransfe*r (D *+ D→D+D*). When the process can repeat itself so that the excitation migrates over several molecules, it is called *excitation transport* or *energy migration*.[7]

Radiative transfer is a two-step process: a photon emitted by a molecule D is absorbed by a molecule A (or D) (D* →D+ hv and then hv + A→A* or hv +D→D*). This transfer doesn't require interaction between the partners, but depends on their concentration and on spectral overlap. Radiative transfer results in decrease of donor fluorescence intensity in the region of spectral overlap. This distortion of the fluorescence spectrum is called *inner filter effect*.

Nonradiative transfer occurs without emission of (real) photons, although, as any electromagnetic interaction, it is still mediated by so-called virtual photons. It occurs at distances less than a wavelength, without previous emission of photons, and resulted from short- or long-range interactions between molecules.

Both of these EET have different effects on the fluorescence emission from the donor (Table 1).

Table 1.1. Effect of energy transfer on the fluorescence characteristics of the donor in the case of heterotransfer (D* + A → D + A*) and homotransfer (D* + D → D + D*)

Characteristics of the D emission	***Heterotransfer D*+A→D+A****		***Homotransfer D*+D→D+D****	
	Radiative transfer	**Non-radiative transfer**	**Radiative transfer**	**Non-radiative transfer**
Fluorescence spectrum	Modified in the region of spectral overlap	Unchanged	Modified in the region of spectral overlap	Unchanged
Steady-state fluorescence intensity	Decreased in the region of spectral overlap	Decreased by the same factor whatever λ_{em}	Decreased in the region of spectral overlap	Decreased by the same factor whatever λ_{em}
Fluorescence decay	Unchanged	Shortened	Slower	Unchanged
Steady-state emission anisotropy	Decreased	Strongly decreased	Decreased	Strongly decreased
Decay of emission anisotropy	Faster	Much faster	Faster	Much faster

Energy transfer can be a result of different interaction mechanisms: long-range dipole-dipole interactions (Förster's mechanism), short-range multipolar interactions, electron exchange (Dexter mechanism) and charge resonance interactions. For singlet-singlet EET all types of interactions are involved, whereas triplet-triplet energy transfer occurs only due to orbital overlap.

1.4.1. Dexter energy transfer

Dexter energy transfer or Dexter electron exchange is a fluorescence quenching mechanism in which an excited electron is transferred from D to A via a

non-radiative pathway. It can only occur at short distances (around 10 Å) because it requires a wave function overlap between D and A.

The rate constant for this process is given by:

$$k_T^{ex} = \frac{2\pi}{h} K J' \exp(\frac{-2r}{L})$$

where J' is the integral overlap:

$$J' = \int F_\lambda(\lambda)\varepsilon(\lambda)\lambda^4 d\lambda$$

where F_λ is the normalized emission spectrum of the excited donor, and ε is the absorption coefficient of the acceptor, L is the average Bohr radius, K is a constant related to orbital interaction. [82]

1.4.2. Förster Resonance Energy Transfer

Förster derived the following expression for the transfer rate constant:

$$k_T(r) = \frac{1}{\tau_D}(\frac{R_0}{r})^6$$

where r is the distance between the D and A and τ_D is the lifetime of the D in the absence of energy transfer, R_0 is the critical distance or the Förster radius, that is, the distance at which transfer and spontaneous decay of the excited donor are equally probable (Figure 1.18).

R_0, which is generally in the range of less than 10 nm, can be determined from spectroscopic data:

$$R_0^6 = \frac{9(\ln 10)k^2\Phi_D^0}{128\pi^5 N_A n^4} J$$

where k^2 is the orientation factor, Φ_D^0 is the fluorescence quantum yield of the donor in the absence of transfer, n is the refractive index of the medium, J is the spectral integral and can be written both in wavenumber and in wavelength scales:

$$J = \int F_\lambda(\lambda)\varepsilon(\lambda)\lambda^4 d\lambda$$

where F_λ is the normalized emission spectrum of the excited donor, and ε is the absorption coefficient of the acceptor.

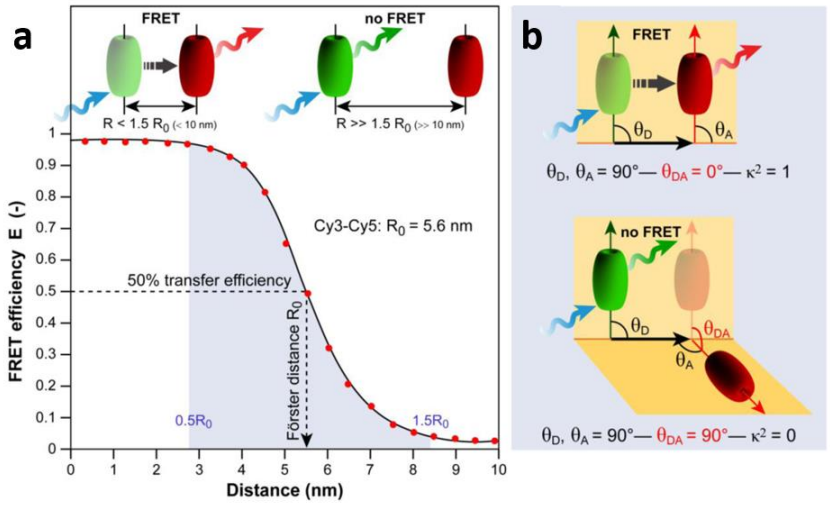

Figure 1.18. Schematic representation of FRET as a photophysical process. FRET efficiency depends on the distance **a)** and orientation **b)** of D (green ellipse) and A (red ellipse). Adopted from ref. [83]

The FRET efficiency of can be measured experimentally in a number of ways. [84, 85] The most popular ones:

1. Measurements based on D emission

$$E_{FRET} = 1 - \frac{I_D^A}{I_D}$$

where I_D and I_D^A are the D emission intensities in the absence and presence of A, respectively. The disadvantage of this method is that the concentration of D is rarely exactly the same throughout different samples. The concentration difference between the D+A sample and the D-only sample can be corrected:

$$E_{FRET} = 1 - \frac{A_D}{A_D^A}\frac{I_D^A}{I_D}$$

where A_D and A_D^A are the D absorbances at the excitation wavelength in the D-only and D+A samples, respectively.

2. Measurements based on D lifetime

$$E_{FRET} = 1 - \frac{\tau_D^A}{\tau_D}$$

where τ_D and τ_D^A are the decay times in absence and in presence of A, respectively.

Since lifetime is independent of concentration, this method is less prone to errors due to differences between samples. But when the donor has more than one lifetime, no simple, universal expression for the FRET efficiency exists.

3. Measurements based on A emission

If A is fluorescent molecule, the FRET efficiency can be determined by quantification of the A intensity.

$$E_{FRET} = \frac{I_A^D A_A^A - I_A^A A_A^D}{I_A^A A_D^D}$$

where I_A^D is the A intensity following D excitation, I_A^A is the A intensity following A excitation, $A_A^A$is the A absorbance at the A excitation wavelength, and A_A^D and A_D^D are the A and D absorbances, respectively, at the D excitation wavelength.

4. Measurements using D/A intensity ratio (ratiometric FRET)

If A is fluorescent, FRET could be characterized using the ratio between the D and A emission intensities. Since the ratio between the D and A intensities depends not only on the value of E_{FRET} but also on the QYs of the two dyes, ratiometric FRET is usually a relative method and should be used only for qualitative purposes or for monitoring relative changes in the FRET efficiency.

$$E_{FRET}^{rel} = \frac{I_A}{I_D + I_A}$$

where I_A and I_D are the total A and D fluorescence intensities, respectively, both following D excitation. If the D and A spectra overlap, the mixed D + A spectrum must be decomposed into isolated D and A component spectra.

FRET is widely used to estimate distances in biomolecules and supramolecular associations and assemblies. It can be used as a spectroscopic ruler in the range of 1–10 nm. [86, 87] The donor–acceptor distance can be determined via the value of the transfer efficiency defined as

$$E_{FRET} = \frac{1}{1 + (\frac{r}{R_0})^6}$$

FRET between two organic dyes or FPs remains the most used for many application. Small size and a huge choice of spectral properties make organic dyes widely used in FRET-based domain. They are considered to be “traditional” FRET materials (Figure 1.19). [88] The acceptor molecule does not necessarily have fluorescent properties, it could be a *dark quencher,* such as black hole quenchers (BHQs) [89] in visible spectrum or IR Dye QC-1 for visible and NIR dyes. [90] Their main advantage is the absence of background fluorescence from direct acceptor excitation or re-emission. Quenchers are often used in molecular beacons for DNA analysis. [91] The principal advantage of such configuration is a possibility to observe donor channel alone and do multicolor detection (multiplexing).

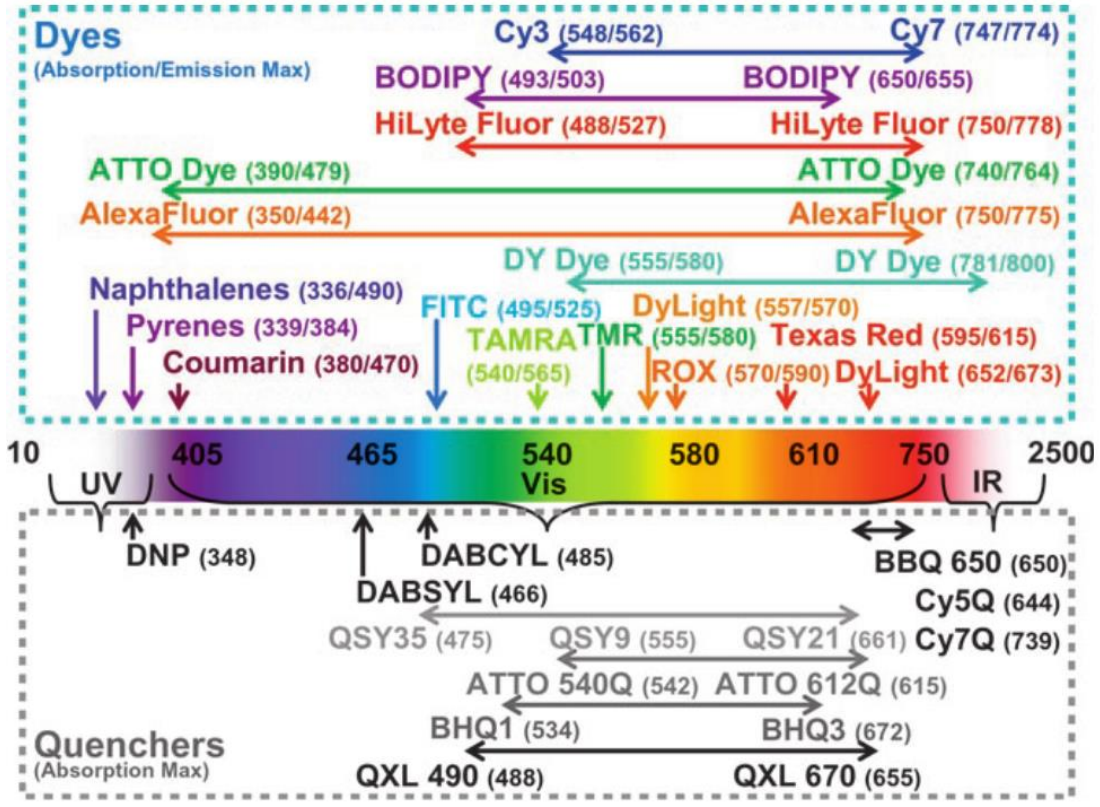

Figure 1.19. Examples of available fluorescent dye and quencher families used for FRET. λ_{abs} and λ_{em} are marked. Tetramethylrhodamine (TMR), carboxytetramethylrhodamine (TAMRA) and carboxy-X-rhodamine (ROX) are rhodamine-based dyes, FITC is a fluorescein isothiocyanate. Adopted from ref. [88]

Exploiting photochromic compounds (those that have property to change their absorbance reversibly as a response to illumination at appropriate wavelengths) as energy acceptors opens a new approach that is called photochromic FRET (pcFRET).

[92] Reversible transformation of such molecules can switch “on” and “off” FRET only by light. The best known photochromic compounds are spiropyran [93], cyanine [94] and diarylethenes [95].

FRET between two FPs is currently one of the most commonly used way to detect protein-protein interactions in living cells: two proteins of interest are fused to D and A FPs, and after the protein interaction they come in proximity that is sufficient for FRET detection. [36]

FPs are also highly used to create genetically encoded sensors (GES). To design the simplest GES, two FPs are fused via a peptide linker that can be specifically cleaved by a cellular protease of interest, such as caspase-1 or caspase-3. [96] The advantage of this approach is a high dynamic range, because after cleavage FRET signal completely disappears, but it is limited to only monitoring protease activity. An inverse approach is to fuse interacting domains with D and A proteins, or to fuse them to single active protein construct, whose conformational changes will bring them in close contact (Figure 1.20). The universality of design led to creation of variety of FRET-based sensors for monitoring changes in concentration of Ca^{2+}, glutamate, tryptophan, kinase activities and others. [36]

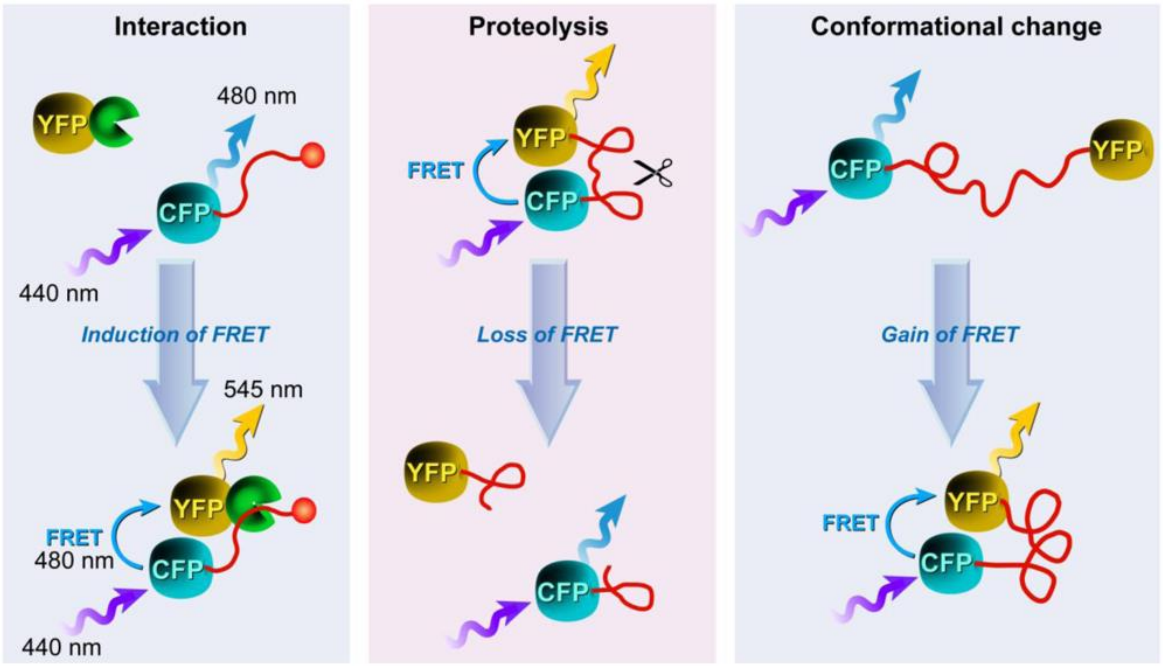

Figure 1.20. Main types of FP-based fluorescent sensors: protein-protein interaction, monitor protease activity and detection of protein conformational changes. Adopted from ref. [83]

1.4.3. EET in multi-fluorophore systems

System of multiple fluorophores at close proximity gives many advantages over systems of single fluorophores [97]: collective absorption and emission are higher, and new photophysical properties, different from the monomeric components, appear. [98] Interaction of fluorophores at the ground state and the excited state results in the formation of new complexes such as excited-state dimers (excimers) and exciplexes, that affect the absorption and emission spectra. In the ground state, the formation of J-aggregates and H-aggregates results in a change in the absorption spectra. J-aggregates induce a bathochromic shift (red shift) while H-aggregates induce a hypochromic shift (blue shift). [57] Some molecules, which are non-fluorescent in solution, can form strongly fluorescent aggregates. This phenomenon is called aggregation–induced emission. [99]

But the original mathematical description of FRET process was done for interaction of one D with one A. In case of interaction of multiple D and A the FRET theory becomes more complex. Multiple acceptors interacting with the same donor increase the probability of FRET and its efficiency. [100] Increase in the number of acceptors increases the probability of deexcitation pathway though FRET and increase the rate of transfer. If *n* identical acceptors interact with one donor, then the rate of transfer will be *n* times higher than the rate to one acceptor, so FRET efficiency could be determined as

$$E_{FRET} = \frac{nk_{FRET}}{nk_{FRET} + k_{other}} = \frac{\frac{nk_{FRET}}{k_{FRET} + k_{other}}}{\frac{k_{FRET} + k_{other} + (n-1)k_{FRET}}{k_{FRET} + k_{other}}} = \frac{nE_0}{1 + (n-1)E_0}$$

where E_0 is the FRET efficiency in case of one acceptor. To linearize the equation

$$A_0 = \frac{E_0}{1 - E_0}$$

$$A_n = \frac{E_n}{1 - E_n} = n\frac{E_0}{1 - E_0} = nA_0$$

So increase in the rate of transfer will result in a nonlinear increase in FRET efficiency with linear increase in E/(1-E)(Figure 1.21).

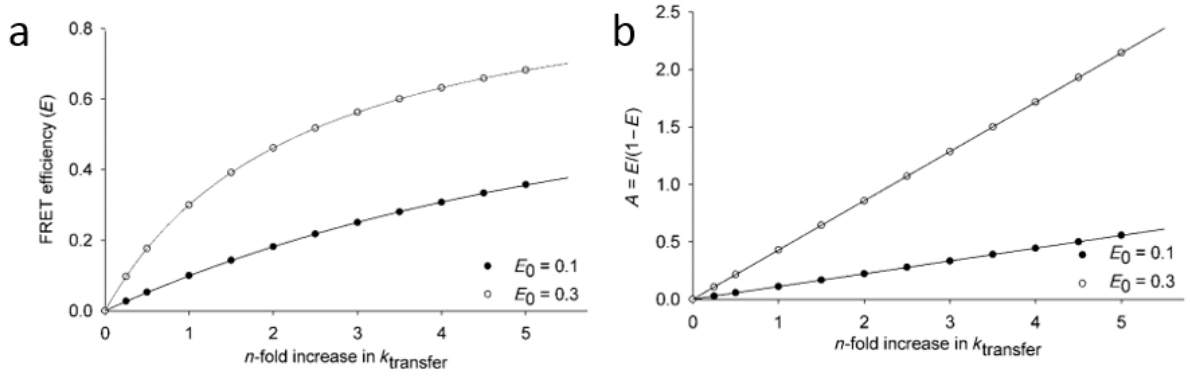

Figure 1.21. Effect of rate constant on FRET efficiency. **a)** FRET efficiency. **b)** The same data plotted as A = E/(1-E) as a function of rate constant. Adopted from ref. [100]

Based on results obtained in [100], by manipulating the fluorophore/protein ratio of fluorophore-conjugated antibody, R_0 of the system could be tuned by changing acceptor number. If $R_n$is the Forster radius for the system with n acceptors, then

$$E_n = \frac{nR_0^6}{nR_0^6 + r^6} = \frac{R_n^6}{R_n^6 + r^6}$$

where $R_n^6 = nR_0^6$. The benefit of this approach is a possibility to increase FRET sensitivity without choosing a new donor/acceptor pair. (Figure 1.22)

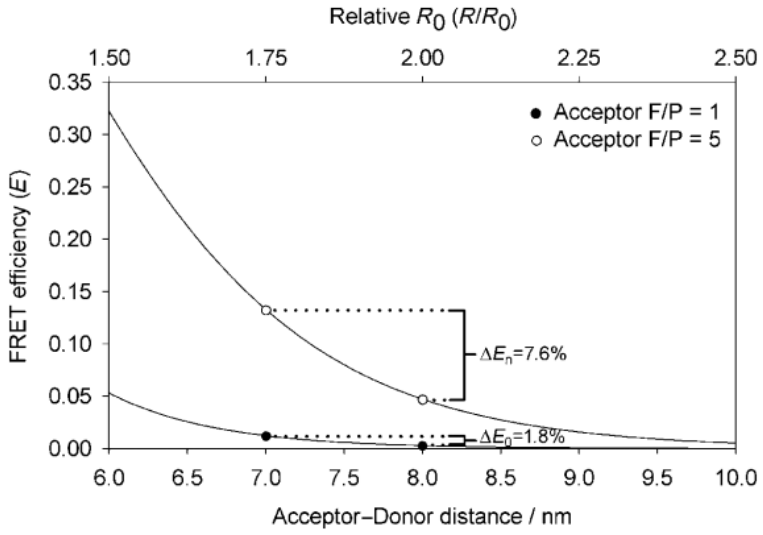

Figure 1.22. Simulated distance–FRET response curves. Theoretical curves show the FRET efficiency differences for intermolecular distances of 7 and 8 nm when measured with acceptor F/P=1 (ΔE_0) and acceptor F/P=5 (ΔE_n) with R_0 = 4 nm. Adopted from ref. [100]

If many FRET donors and acceptors are assembled in a small particle and appear within the critical distance, two distinct cases should be considered: energy

donors behave like individual fluorophores (systems without dye-dye communication or system with low cooperativity), or they are coupled by EET (homo-transfer) and demonstrate new collective effects (systems with high cooperativity). NPs of the same nature could demonstrate low or high donor dye cooperativity depending on preparation protocols. [81]

1.4.3.a. Systems with low donor cooperativity

In systems with low cooperativity high FRET efficiency could be achieved only by encapsulation or grafting on the surface of high number of acceptor molecules (usually D : A ratio is close to 1 : 1). Dye-loaded polymer NPs is an example of such systems.

The group of Law reported preparation of biocompatible polymeric NPs with encapsulated lipophilic NIR fluorophores from cyanine family, DiD and DiR (at ratio of1:1) as D and A respectively (Figure 1.23). [101] The FRET efficiency was found to be higher at higher dyes loading, although decrease of intensity and increase in NPs size were observed. NPs containing 2.1 wt % of dyes demonstrated 97% of FRET efficiency and resulted in large Stokes shift (>100nm) and were applied in animal imaging.

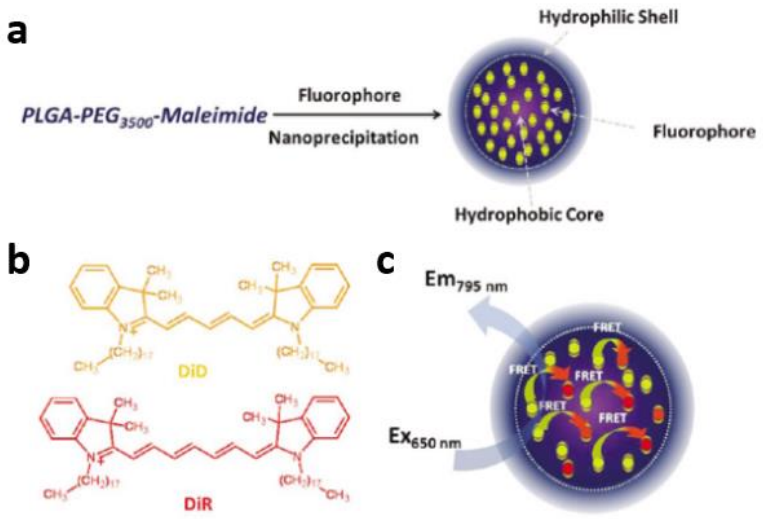

Figure 1.23. Design of FRET-NPs. **a)** Preparation of NPs by nanoprecipitation method. **b)** Chemical structures of DiD and DiR fluorophores. **c)** DiD with λ_{ex} at 644 nm and λ_{em} at 665 nm in methanol, and DiR with λ_{ex} at 750 nm and λ_{em} at 780 nm in methanol, were encapsulated inside FRET-NPs. The close proximity between the entrapped DiD and DiR fluorophores favored the FRET. Adopted from ref. [101]

The same group later developed polymer NPs with multiple FRET cascade mechanisms. [102] Four carbocyanine-based fluorophores DiO, DiI, DiD, and DiR were encapsulated into poly(d,l-lactic-co-glycolic acid)(PLGA) and polyethylene glycol (PEG) particles with size <100nm. NPs were able to emit at three different wavelength upon excitation at 485 nm due to FRET cascade between dyes located at close proximity in a confined volume of NPs (Figure 1.24 a) Particles with different ratio of dyes were functionalized with different ligands and applied for multiplex imaging *in vivo* (Figure 1.24 b).

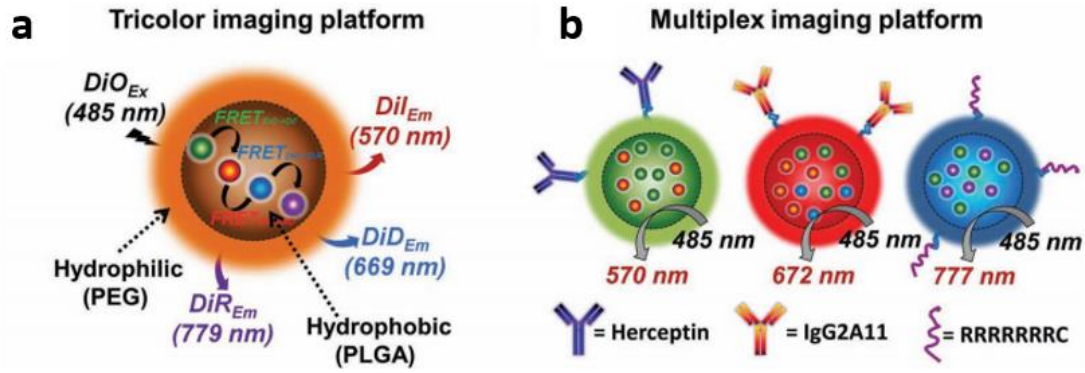

Figure 1.24. Schematic representation of polymer NPs with multiple FRET cascade mechanisms designed for **a)** multicolor and **b)** multiplex imaging. Adopted from ref. [102]

By using photochromic molecule as FRET acceptor Li et al. created photoswitchable NPs. [103] They were prepared by emulsion polymerization method and loaded with fluorescent perylene diimide dye and a photochromic spiropyran molecule. Perylene dye is characterized by strong green fluorescence (λ_{em} =535 nm, QY = 0.9) and has no spectral overlap with spiropyran absorption in its ring-closed (spiro) form. After UV-illumination the latter one undergoes transition into ring-opened (merocyanine) form with visible absorption band, overlapping the emission of perylene, so perylene emission could be quenched by FRET. Illumination with visible light brings the spiropyran back to closed-ring form, switching off FRET (Figure 1.25). Complete switching between two emission colors was achieved when number of A molecules was 100-200 times higher than number of D molecules.

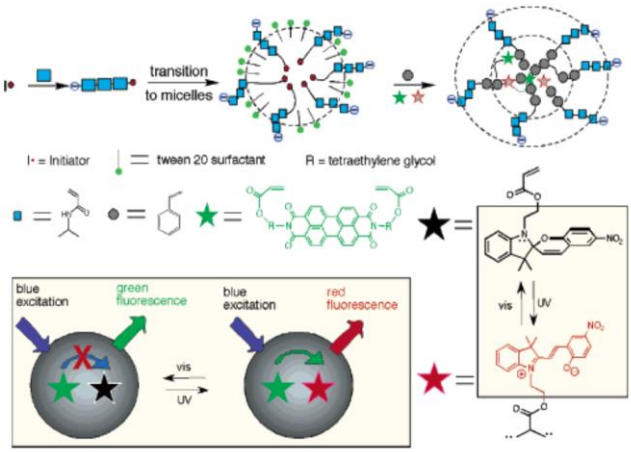

Figure 1.25. Schematic illustration of preparation of spiropyran-based dual-color photoswitchable NPs. Adopted from ref. [103]

Another example of FRET inside polymer polymethylmethacrylate (PMMA) NPs was shown by encapsulation of 9-nitrobenzoxadiazolyl (NBD) and 9-(diethylamino)benzo[a]phenoxazin-5-one (NR) by a one-step mini-emulsion polymerization by Yi et al. [104] By varying the doping ratio of two dyes, 60-nm NPs exhibiting multiplex colors of fluorescence under a single wavelength of excitation were obtained. FRET efficiency reached up to 75.2% in the case when one donor was surrounded by six acceptor molecules. Later, the same strategy was used to create 60-nm photoswitchable NPs by using photoswitchable acceptor, spiropyran derivative and fluorescent donor 9,10-diphenylanthracene (DPA). [105] By altering illumination 365 nm/525 nm the spiropyran changed its form from open-ring to closed, that was accompanied with changes in its absorption spectrum and thus modulated FRET efficiency more than two times. Application of 4-methamino-9-allyl-1,8-naphthalimide (MANI) as energy donor [74], allows to obtain FRET efficiency ~ 84.3% with photoswitching amplitude (I_{ON}/I_{OFF} ratio) more than 5-fold at A/D ratio 14.4, and using fluorescein-O,O-bis-propene (FBP) as energy donor gave FRET efficiency 98.5% in case when donor was surrounded with 49.6 effective acceptors inside ~ 170-nm NPs. [106] By combining FRET between two emissive dyes and FRET to photochromic molecule inside NPs, the nanoparticles exhibiting multiple colors under a single excitation wavelength were created (Figure 1.26).[107]

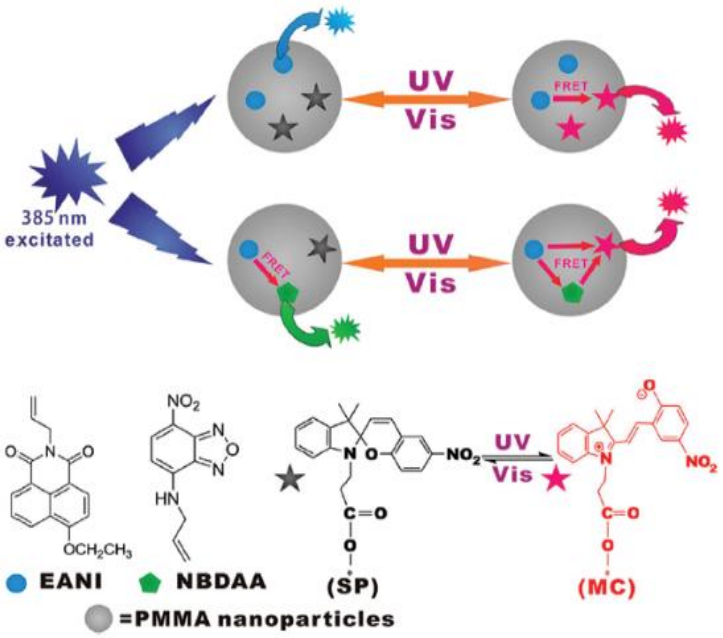

Figure 1.26. Schematic illustration of multicolor and photoswitchable fluorescent polymeric NPs covalently incorporating two (EANI and SPMA) or three fluorescent dyes (EANI, NBDAA, and SPMA) under excitation at 385 nm. Adopted from ref.[107]

Larpent and co-workers used dual-doped polystyrene NPs of 16 nm to detect Cu^{2+} in aqueous solution. [108] For this, NPs were loaded with ~25 D (9,10-diphenylanthracene,DPA) molecules and ~23 A molecules (pyrromethene 567, PM 567) that resulted in 80% of FRET efficiency, and their surface was functionalized with a copper selective ligand cyclam (~350 per NP). Detection was made by two sequential steps of energy transfer: from D to A molecules and then to the copper complexes on the surface that act as a quencher. (Figure 1.27). The same group later reported application of polystyrene–based NPs coated with FRET pair fluorophores that serve as a ratiometric sensor for pH. [109] Dansyl derivative (D) and pH-responsive fluorescein (A) were attached to the surface via copper-catalyzed azide–alkyne cycloaddition (CuAAC). FRET efficiency changed as a response to the changes in pH of the medium, and was maximal at pH >7 and estimated ~ 63%. It corresponded to a case when one fluorescein quenched about 2.5 dansyl dyes.

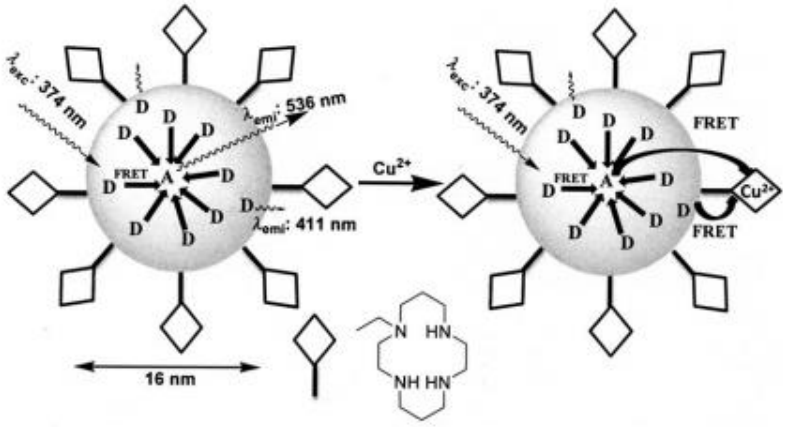

Figure 1.27. Schematic illustration of the FRET-based ratiometric measuring NPs: D are excited and the energy is transferred to the proximal A within the cyclam-coated dual-dye-doped NPs. In the absence of Cu^{2+}, EET leads to emission of the fluorescent A. In the presence of Cu^{2+}, the copper–cyclam complexes that form at the surface act as quenchers Q (or secondary acceptors), the sensitized emission of the primary acceptor A is efficiently attenuated through FRET to quencher Q, while the remaining emission of the primary donor D is less affected. Adopted from ref. [108]

Dual-step FRET-based quenching assay was proposed by Soukka et al. for screening of caspase-3 inhibitors. [110]. For this propose fluorescent europium(III)-chelate-doped donor NPs coated with streptavidin were labelled with Alexa Fluor 680 fluorescent acceptor and BlackBerry Quencher 650 and caspase-3-specific peptide substrate modified with a biotin moiety (Figure 1.28). In this case, FRET excites the A, whose intensity is controlled by the proximity of the quencher. In inhibitory conditions, the biotinylated substrate remains intact and acceptor emission is efficiently attenuated by the BlackBerry Quencher 650, but in non-inhibitory conditions, the enzyme cleaves the biotinylated substrate releasing the quencher, and switching on the acceptor emission. To obtain high signal-to-noise ratio biotinylated substrates should excess the NPs concentration 5-6 times. Further increase in A concentration led to its self-quenching.

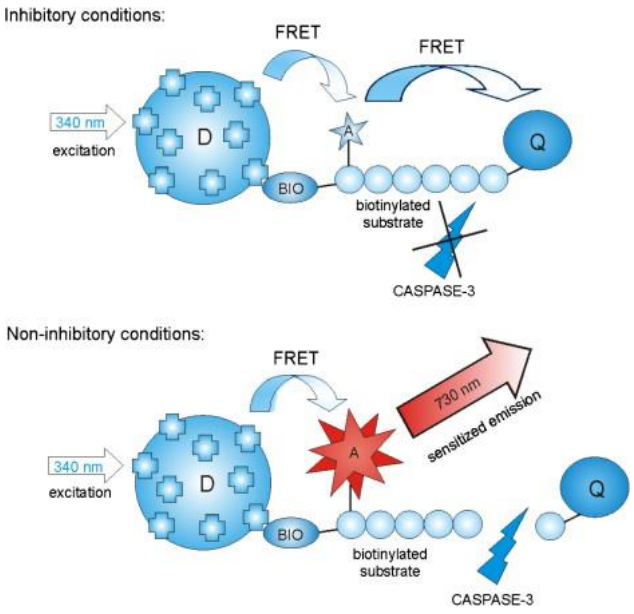

Figure 1.28. Principle of the dual-step FRET quenching assay. The streptavidin-coated europium(III)-chelate-doped nanoparticle donors (D) are excited, and the energy is transferred to the Alexa Fluor 680 acceptor (A). In inhibitory conditions (upper panel), the biotinylated substrate is intact and the A emission is efficiently attenuated by the BlackBerry Quencher 650 (Q). In non-inhibitory conditions (lower panel), the enzyme cleaves the biotinylated substrate releasing the Q leading to emission of the fluorescent A. Adopted from ref. [110]

Silica NPs could be another example of the system with low donor dye cooperativity. Thus, Longhinotti et al. reported preparation of 80-nm SiNPs containing 2',7'-dichlorofluorescein (DCF) (energy D) and Rhodamine B (energy A). [111] For calculated average distance between the DCF and RhB, equal to 3.6 nm, FRET efficiency was around 84% at ratio D : A = 0.5. The increase in this ratio up to 1.25 led to decrease in QY, suggesting that close proximity of the fluorophores might cause intermolecular self-quenching.

Multicolor FRET SiNPs by single excitation wavelength were realized by group of Tan by encapsulation of three organic dyes (FITC, R6G, and ROX). Variation of the dyes ratio and thus FRET efficiency allowed creating barcoding silica NPs for multiplexed signaling (Figure 1.29). [112] Later the same group reported application of multicolored FRET SiNPs for multiplexed bacteria monitoring. [113] NPs were prepared through a modified Strober synthesis method, encapsulating ~10000 dye molecules in a ~60 nm silica sphere. FAM-APTS, R6G-APTS, ROX-APTS at different ratio were used to obtain FRET.

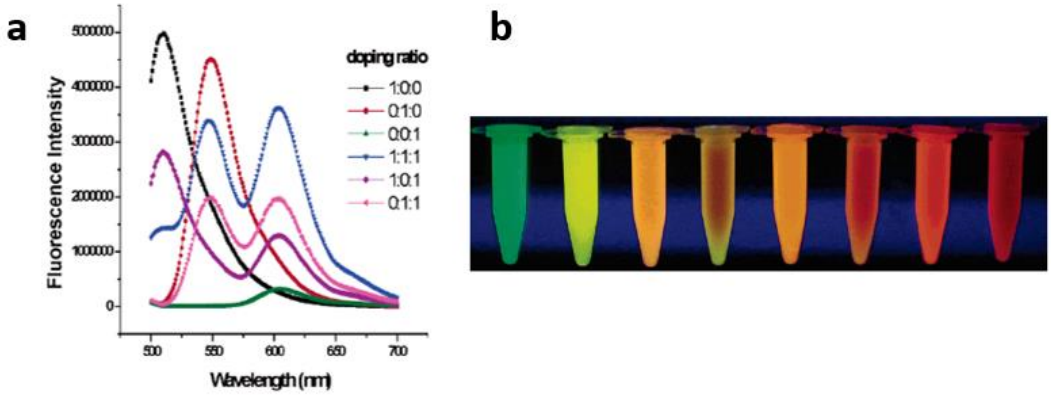

Figure 1.29. Multicolor FRET SiNPs. **a)** Fluorescence spectra of NP encapsulated with one, two, or three types of fluorophores. **b)** NP with different doping dye combinations under 300-nm UV illumination. Dye doping ratio (in order): 1:0:0, 0:1:0, 1:0:1, 4:1.5:3, 0.5:0.5:0.5, 2:2:2, 0:1:1, 0.5:0.5:4. Adopted from ref. [112]

Doping of SiNPs of 35-50 nm in diameter with oligothiophenes (TFs) with blue, green and orange emission resulted in creation of NPs with tunable emission from blue to white. [114] For this FRET between adjacent amounts of TFs was exploited. Its efficiency reached up 80-90% at ratio of components 1:1.

Multiple dye-doped NIR emitting SiNPs, suitable for optical imaging and multiparametric flow cytometry analyses, were developed by Secchiero and coworkers by encapsulation of alkoxysilane derivative of Cy5.5 in combination with IR813-alkoxysilane derivative of Cy7. [115] NPs were synthesized at two different Cy5.5 : Cy7 molecular ratios (2 : 1, 1 : 1). SiNPs displayed FRET efficiency of 38% and 70% respectively, and very similar overall quantum yields of 0.08 and 0.06.

Examples of photoswitchable SiNPs, created by encapsulation of photochromic acceptor molecules together with fluorescent dyes that serve as energy donor, are also known. [116, 117]

He et al. reported encapsulation of two highly water-soluble dyes, tris(2,2-bipyridyl)-dichlororuthenium(II) hexahydrate (RuBpy) and methylene blue (MB) as the model donor−acceptor pair into silica NPs around 40 nm in diameter (Figure 1.30). [118] FRET from RuBpy to MB resulted in a NIR fluorescence and large Stokes shift (>200 nm). The optimized NPs with the highest brightness with D : A ratio = 3:1 were used for imaging in animals.

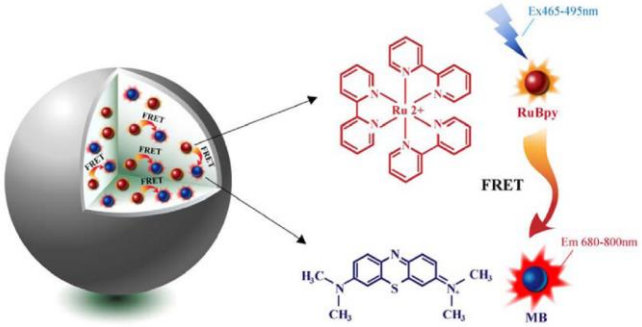

Figure 1.30. Schematic illustration SiNPs with FRET from RuBpy to MB and the chemical structures of RuBpy and MB. Adopted from ref. [118]

FRET-based system was built for ratiometric sensing of Hg^{2+} in water, with multilayered SiNPs as the scaffold, by Liu et al. [119] After formation of a ‘‘pure’’ silica core, a donor-containing layer was deposited on the core with subsequent deposition of a ‘‘spacer’’ layer, then NPs were coated with the probes. Detection of Hg^{2+} resulted in turning on FRET (Figure 1.31). The sample with a space layer of 4.3 nm, which is close to 1.5 R_0, shows FRET efficiency of 49%; that is much higher than the predicted by classical FRET approach. The authors suggest the reason for this may be the fact that one D may interact with multiple A and vice versa. Based on the same principles, core-shell SiNPs, loaded with fluorescent nitrobenzoxadiazolyl (FRET D) and spirolactam rhodamine (A), covalently linked to the surface were used to detect Hg^{2+}. [120]

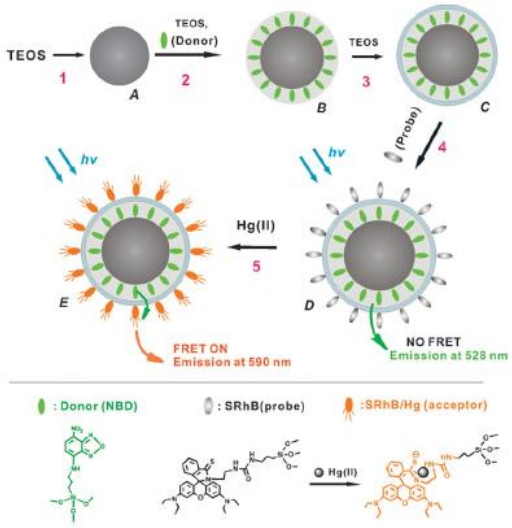

Figure 1.31. Schematic illustration for formation of a FRET-based ratiometric Hg2+ sensor with multilayered silica particles as the scaffold, and the proposed structural change of the probe. Adopted from ref. [119]

Using NPs as FRET D is challenging due to their relatively big size (diameter of NP is usually >>R_0). Several attempts were made in order to obtain FRET to NPs surface. The group of Wolfbeis reported the preparation of SiNPs for use in FRET-based affinity assays at the interface between particles and sample solution. [121] NPs were prepared by covalent attachment of fluorophores rhodamine B isothiocyanate (RITC), to the amino-modified surface of SiNPs with a typical diameter of 15 nm. They were used both as energy D and energy A to the fluorescently labeled avidin. The (Avidin-Fluorescein)-to-(Biotin-SiNP-RhB) FRET system exhibited good efficiency with up to 6.8-fold increase of A intensity. The FRET from (Biotin-SiNP-RhB) to (Avidin-merocyanine UR-800) was also efficient, with up to 7.3-fold increase of A intensity (Figure 1.32). This efficient FRET in this case is based on the relatively short distance for FRET, when both D and A are grafted to the the surface of SiNPs.

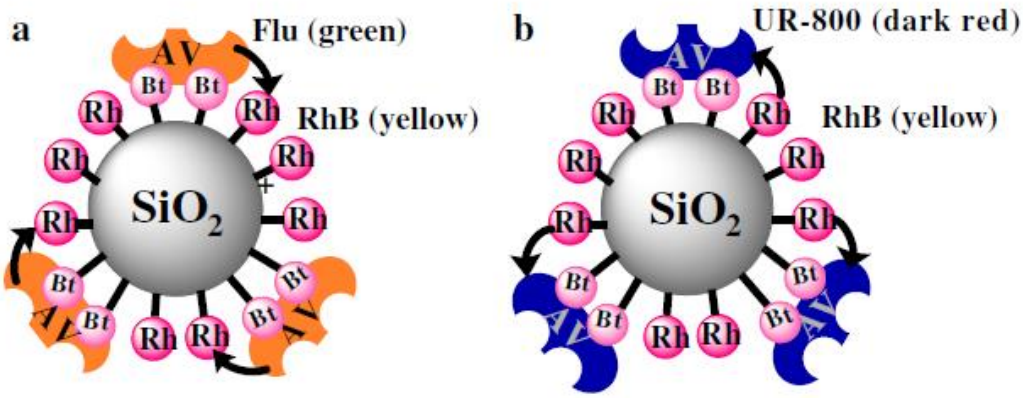

Figure 1.32. Schematic representation of the FRET model systems. **a)** FRET from fluorescein-labeled avidin to RITC-labeled biotinylated SiNPs. **b)** FRET from RITC-labeled biotinylated SiNPs labeled avidin. Adopted from ref. [121]

Another example of the FRET at the surface of SiNPs was reported by Babu et al. [122] These NPs were used as a biosensor for thrombin. Here, surface of $[Ru(dpsphen)3]^{4-}$ ion-doped SiNPs with a size ~ 70 nm was functionalized with thrombin-binding aptamer labeled with DABCYL. Binding of thrombin resulted in the conformational change of the aptamer, forming G-quadruplex that brings DABCYL in close proximity to NPs, resulting in FRET (Figure 1.33). The surface of NPs was covered with ~120 molecules of aptamer, allowing to obtain limit of detection (LOD) of 4 nM.

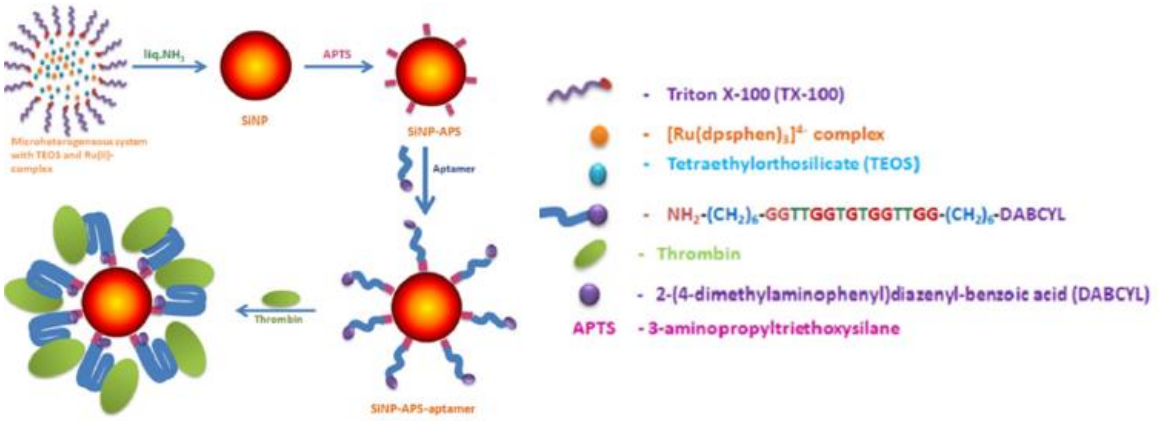

Figure 1.33. Schematic representation of the detection system for thrombin using [Ru (dpsphen)3]$^{4-}$ ion-doped SiNPs-aptamer conjugate. Adopted from ref. [122]

1.4.3.b.Systems with high donor cooperativity

The most common example of multi-fluorophore system with high cooperativity is the light-harvesting complexes of photosynthetic centers of bacteria [123] and plants [124], in which the first steps of photosynthesis occur. In such systems, fluorophores are surrounded by proteins that keep them at place via non-covalent interactions. The high resolution X-ray crystal structure of the photosynthetic unit (PSU) reveals a central reaction center (RC) that is surrounded by light harvesting (LH) complexes (Figure 1.34 a). The LH1 complex is composed of a ring-shaped assembly of chlorophyll and carotenoid moieties embedded in a protein matrix that immediately surrounds the RC. Similar ring-shaped assemblies make up the LH2. The role of these chlorophyll-containing assemblies is that of an antenna, absorbing photons that strike the relatively large surface area that they cover. Remarkably, the energy of any photon that strikes any of the several hundred chlorophylls within the extensive LH system is transferred to the RC with unit efficiency (Figure 1.34 b). [123]

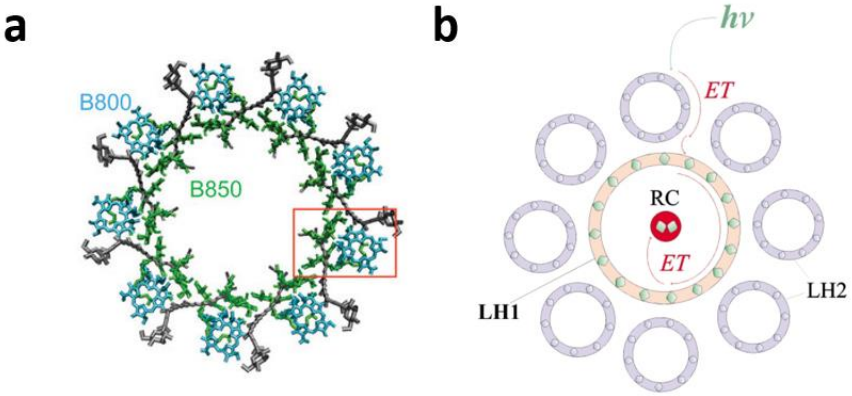

Figure 1.34. EET inside a light-harvesting complex. a) Structural model of the chromophores in the LH2 complex of *Rhodopseudomonas acidophila* (Purple bacteria). Adopted from ref. [125] b) Schematic representation of bacterial light-harvesting complexes (LH1 and LH2), showing the different protein-embedded light-absorbing porphyrins arranged in circles around the reaction center (RC). The path of energy transfer (ET) is indicated by arrows. Adopted from ref. [126]

The EET efficiency and "antenna" effect are two parameters generally used for description of light-harvesting efficiency. The EET quantifies the changes in the donor intensity in the presence of different concentrations of acceptors, and antenna describes changes in acceptor emission with changes in donor concentration. [90]. Several ways to determine antenna efficiency exist: measure the ratio of acceptor emission intensity upon excitation of donor $I_{AF\lambda(D)}$ and direct excitation of acceptor $I_{AF\lambda(A)}$

$$antenna\ effect = \frac{I_{AF\lambda(D)}}{I_{AF\lambda(A)}}$$

It could be expressed as the ratio of the maximal excitation intensity of the donor to that of the acceptor as well. [127] Knowing the number and extinction coefficient of donor and acceptor molecules, and FRET efficiency, antenna effect could be estimated [63]:

$$antenna\ effect = \frac{n_D \varepsilon_D E_{FRET}}{n_A \varepsilon_A}$$

Special organization of fluorophores and their spectroscopic properties plays crucial role for creation of the systems with efficient EET. Studying systems where donor and acceptor are covalently linked, provided most of fundamental advances in this field.

The structure of dendrimer molecule is similar to the architecture of natural light-harvesting complexes, where the reaction center is surrounded by antenna molecules, and the positioning of fluorophore could be achieved with high precision, locating them in the core, focal point, and periphery or at each branching point. [126]. EET in dendrimers can occur by Förster [128] and by Dexter [129] mechanisms. The pioneering work of light-harvesting dendrimers was reported in the early 1990s by Balzani et al. [129] For this, Ru(II) and Os(II) polypyridine complexes were used as building blocks. The first unidirectional FRET in a dendritic framework was achieved from phenylacetylene monomers to a single molecule of perylene located in the core by Xu and coworkers. [128]. In addition to the light-harvesting dendrimers with donor and acceptor connected by covalent bonds or coordination, EET can also take place in self-assembled dendritic structures, in which components (usually the energy acceptor) are incorporated into the systems by noncovalent interactions. [130] Nevertheless, occurrence of self-quenching and excimer formation increases in higher generation of dendrimers, decreasing EET efficiency.

Another example of artificial light-harvesting complexes are multiporphyrin arrays. [131] They are duplicating the structure and functions of LH antenna complexes. Creation of closed ring architecture is possible by covalent bonding, that gives precise control of spatial molecules arrangement [132] or by supramolecular self-assembly [133]. The main disadvantage of multiporphyrin arrays is the narrow absorption windows due to limited range of porphyrinoid macrocycles.

Different biomaterials, such as proteins and DNA, could be used as the scaffold for integration of multiple fluorophores with controlled distribution and rigid organization of fluorophores at close proximity for optimal EET without energy loss by contact quenching. [90, 134].

Recently Medintz and coworkers reported DNA-based molecular photonic wire (MPW) which exploited homo-FRET (Figure 1.35). [135] The created system with 5 dye-containing homo-FRET repeat sections can be extended up to 6 repeat dyes/5 steps with only a ≈55% energy transfer efficiency decrease. Using homo FRET allows to create MPW with over 30 nm in length, while previously reported MPW with seven dyes exploiting only hetero-FRET gave a maximum transfer distance of 20.5 nm.[136]

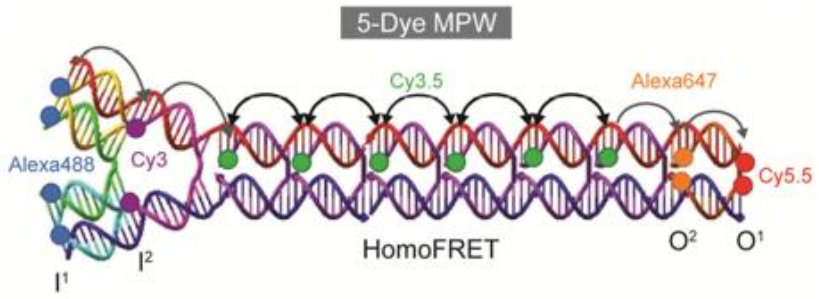

Figure 1.35. Schematic of the MPWs. The colored circles represent the dyes, while each DNA strand is presented by a different color. Arrows represent possible energy transfer steps and their directionality. b) 5-dye MPW. Dye positions are indicated below the MPW and apply to both systems. I = Input and O = Output. Adopted from ref. [135]

An example of protein-based light-harvesting platform, built from self-assembling chromophore-labeled monomers of the tobacco mosaic virus coat protein (TMVP) was reported by Miller et al. [137] Characterization of the system, using fluorescence spectroscopy, indicated that EET could be achieved from large numbers of donor chromophores to a single acceptor. The antenna effect, calculated as a ratio of A intensity under the excitation of D and direct excitation reached 11.2. Three-chromophore systems gave broad spectrum light collection with over 90% overall efficiency. Author suggested that for systems with large numbers of D, energy can be transferred to A chromophores through direct FRET or via multiple D-to-D transfers that reflected in increase in antenna effect with increase in D : A ratio. (Figure 1.36)

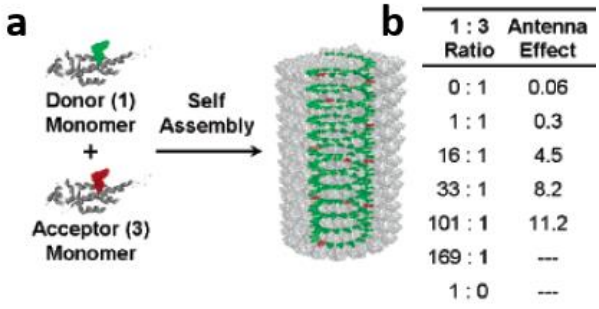

Figure 1.36. Self-assembly of light-harvesting structures. **a)** Mixtures of TMVP monomers labelled with donor 1 (Oregon green 488) and acceptor 3 (Alexa Fluor 594) were assembled into rods. **b)** Tabulated antenna effect for these systems. Adopted from ref. [137]

A high local density in confined volume, such as NPs, activates efficient EET within identical dyes (“homo-FRET”). But it could lead as well to formation of excimers and aggregates that will not only decrease the general brightness of the system, but will serve as a “trap” for migrating energy.

Pluronic SiNPs (PluSNPs) reported by group of Prodi [138] is an excellent example of the system with high fluorophore cooperativity. They are prepared with a simple one-pot direct micelles-assisted procedure using Pluronic F127 (polyethyleneglycol–polypropylene oxide–polyethyleneglycol (PEG–PPO–PEG) amphiphilic structure) as a surfactant. PluS NPs have a silica core of about 10 nm and an overall hydrodynamic diameter of about 25 nm with good monodispersity. Embedding dyes with small Stokes shift, such as rhodamines, BODIPYs or cyanines at high concentration in such low volume, leads to excitation energy migration. Multiple FRET events inside NPs create distribution of excitation energy in a high fraction of encapsulated dyes within the lifetime of the excited state. So, the excitation energy can move to a donor dye that are close enough to an acceptor dye. This makes excitation energy unavailable for further homo-FRET steps, and the last donor dye acts as the funnel that bridges homo-FRET with FRET to acceptor dyes, with a net increase in the overall efficiency of this latter process.

The importance of collective behavior to obtain efficient FRET was shown on the example of PluSNPs doped with rhodamine B and hosted single cyanine dyes on the surface. Simulation considering that each rhodamine dye independently transfers energy to a cyanine gives much lower FRET efficiency than experimental data (Figure 1.37). [139]

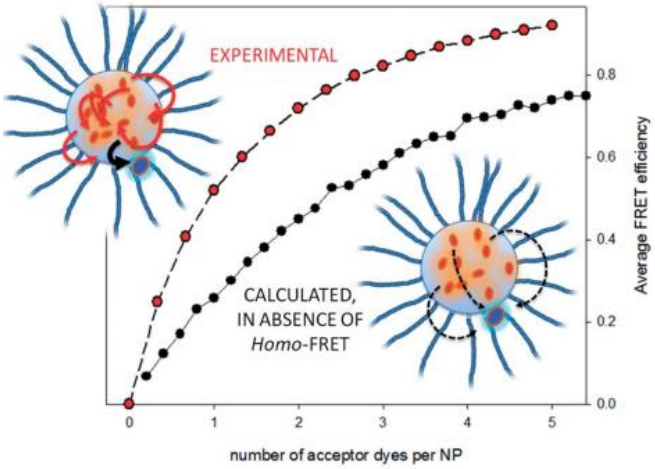

Figure 1.37. Experimental FRET efficiency (red dots, obtained by steady state emission quenching measurements) versus simulated average FRET efficiency (black dots). No homo-FRET between D is considered in the simulations. Each point represents the average FRET efficiency for a set of 1000 NPs containing 10 D on average embedded in a 5.5 nm radius core of PlusNPs, and an increasing number of acceptor dyes hosted in a very thin shell (0.2 nm). Forster distance considered to be R_0 = 5.0 nm. Adopted from ref. [138]

PluS NPs, loaded with coumarin dyes, hosting in the shell BODIPY -based sensor in stoichiometric ratio NP/ dye = 1: 1 were used to detect Cu^+. Creation of complexes with Cu^+ ions increased the molar extinction coefficient of the sensor, and consequent addition of Cu^+ ions to coumarin-doped PluS NPs, hosting sensors in the shell, resulted in increase of the efficiency of energy transfer from a large number of donor coumarin dyes (antenna effect) to a single acceptor sensor, thus affording a sensing response, which was at the same time amplified and ratiometric (Figure 1.38). [140].

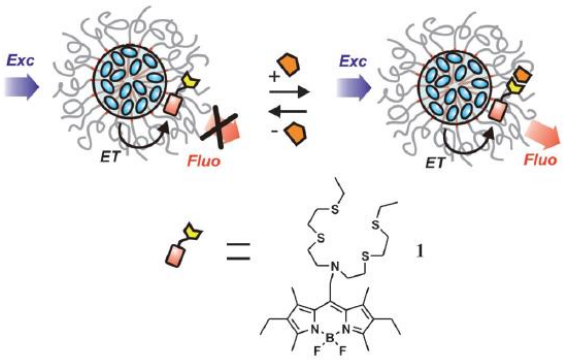

Figure 1.38. Schematic representation of the Cu^+ sensing mechanism by PluSNPs. Adopted from ref. [140]

As small amount of A dyes could catch energy from a large amount of donor dyes, they are strong competitors for excitation energy with poorly emitting states of D. Exploiting cooperativity of coumarin molecules fast and efficient FRET to A was obtained, that resulted in 3-fold increase of QY at high D dyes loading (Figure 1.39). [141]

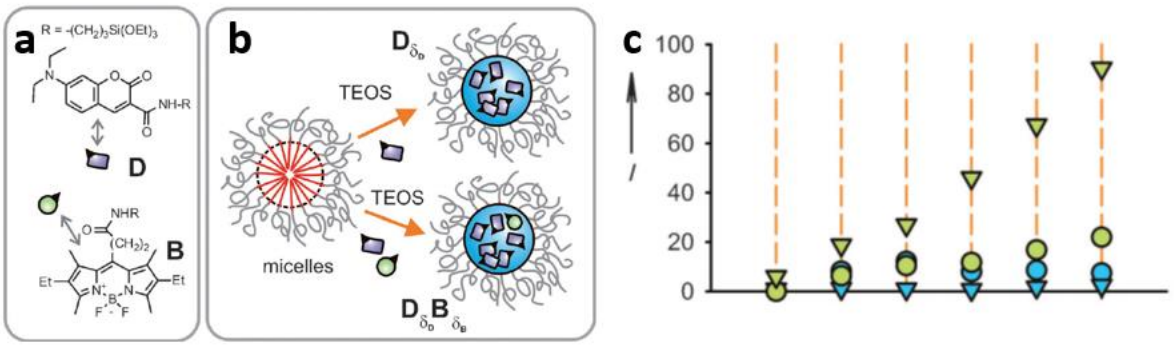

Figure 1.39. Exploiting of the cooperativity of the dye inside SiNPs for increasing of QY. **a)** Chemical structure of D and A molecules. **b)** Simplified representation of the synthesis of the NPs. **c)** The total NPs intensity. Adopted from ref. [141]

FOD-NPs prepared by ion-association method contain a large number of fluorescent dyes within very low interfluorophore distance that make them appropriate for EET. Thus, organic nanoparticles of 45 nm in diameter, consisting of 3,3'-diethylthiacyanine (TC) and ethidium (ETD) dyes, synthesized by ion-association between the cationic dye mixture (10% ETD doping) and tetrakis(4-fluorophenyl)borate (TFPB) anion, demonstrated efficient FRET (~70%) that was accompanied with an antenna effect of ~150. [142]

Another example of cooperative behavior in counterion-assembled NPs was shown by our team by creation of 10-20 nm NPs composed of lipophilic Rhodamine and perfluorinated tetraphenylborate. These NPs, containing >300 dyes with high QY (up to 60%), have extremely good FRET efficiency (~80%) at ratio D/A = 200/1 and antenna effect that reach 200 at D/A = 1000/1 (Figure 1.40). [63]

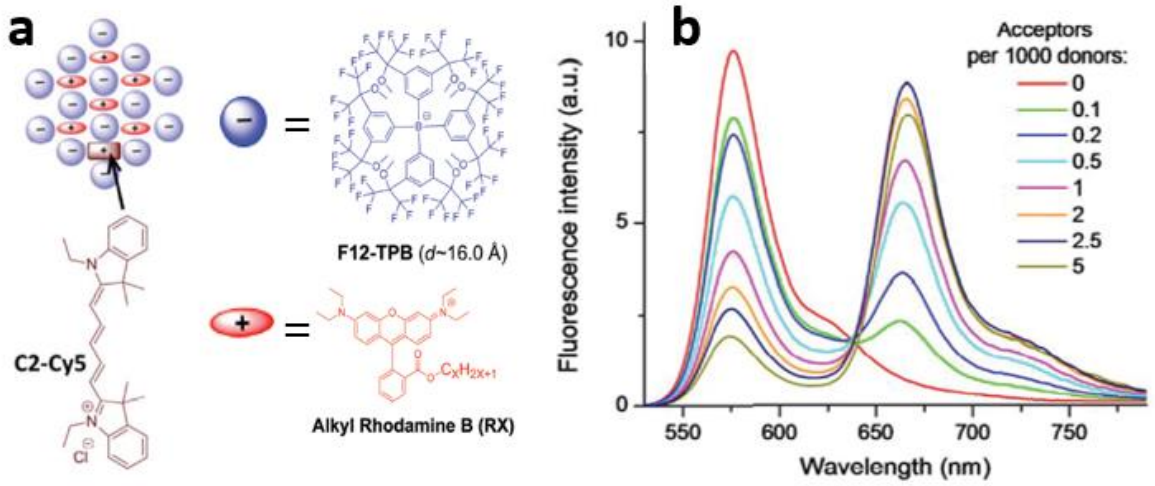

Figure 1.40. FRET from counterion-assembled NPs. **a)** Chemical structure of the C2-Cy5 acceptor, the rhodamine B derivatives, tetraphenylborate counterion and its encapsulation into counterion-assembled NPs. **b)** Fluorescence spectra NPs containing different amounts of A. Adopted from ref. [63]

Recently Su et al. reported using cooperative behavior for creation of giant amplification of fluorescence photoswitching inside 25-nm organic NPs based on a diarylethene (DAE) benzothiadiazole (BTD) dyad PF. The high contrast (10 000:1) due to a very efficient FRET is a result of the collective quenching of more than 400 molecules per switching event (Figure 1.41). [60]

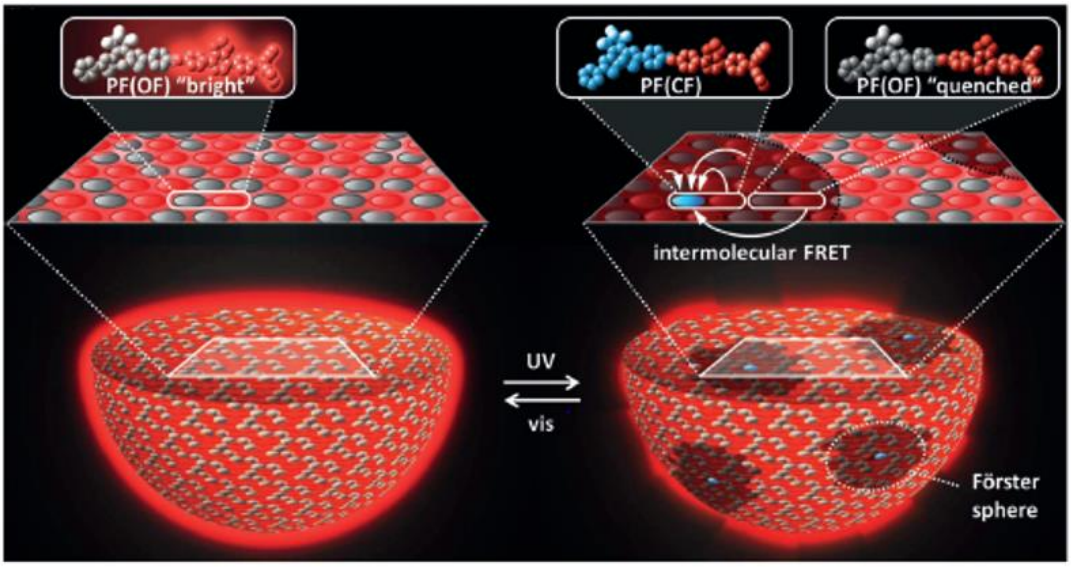

Figure 1.41. Illustration of the FRET-induced "giant amplification of fluorescence photoswitching" in NPs. After promotion of few molecules to the non-fluorescent state by UV irradiation, a large number of PF are quenched) by long-range intermolecular FRET process within each Förster sphere. Adopted from ref. [60]

Using polymer matrix for creation of NPs also allows to obtain cooperative behavior of dyes at certain conditions. Patra and coworkers reported encapsulation of multiple organic molecules in polymer NPs for artificial light harvesting. [143] Self-assembled oligothiophenes (quaterthiophene; QTH) poly(methylmethacrylate) (PMMA) polymer nanoparticles (NPs) prepared by precipitation method act as energy donor to doped Nile red (NR) dye. The antenna effect was calculated to be 3.2.

Example of extremely cooperative behavior of dyes was recently presented by our team by introducing a new concept of fluorescent polymer NPs, doped with ionic liquid-like salts of a cationic dye (octadecyl rhodamine B) with a bulky hydrophobic counterion (fluorinated tetraphenylborate), that serves as spacer minimizing dye aggregation and self-quenching. The obtained 40-nm poly(D,L-lactide-co-glycolide) NPs containing up to 500 dyes exhibit photo-induced reversible on/off fluorescence switching due to ultrafast excitation energy transfer (Figure 1.42). [81]

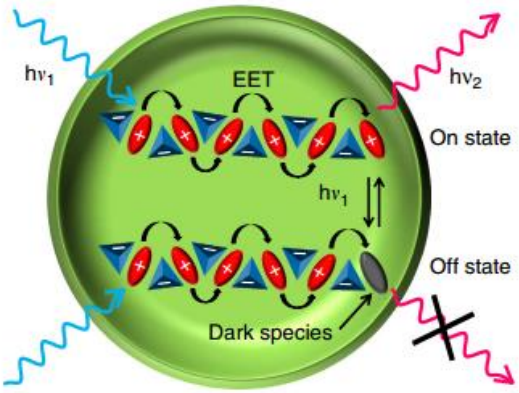

Figure 1.42. Proposed model of the counterion-assembled dyes inside NPs. Short-range ordering of rhodamine dyes (red) by the F5-TPB counterion (blue) inside the polymer matrix prevents dye aggregation and leads to the short inter fluorophore distance. Dark species (grey), generated by light, turn off the whole ensemble of dyes coupled by EET leading to on/off switching. Adopted from ref. [81]

1.4.4. EET in other systems

FRET involving a QD acting as a donor, attached to multiple acceptors, is becoming a common tool for sensing, biolabeling and energy transfer applications. QDs have two unique advantages over organic fluorophores for FRET: their donor emission could be size-tuned to improve spectral overlap with a particular acceptor dye, and having several acceptor dyes interact with a single QD-donor substantially improved FRET efficiency. [144, 145] Increase of A number from one to five for QD of 3 nm radius will give increase in FRET efficiency from 22% to 58% for dye located on the labelled protein at 70 Å from the core. Förster distance (R_0) for this QD donor–dye acceptor pair is equal to 56 Å. (Figure 1.43)

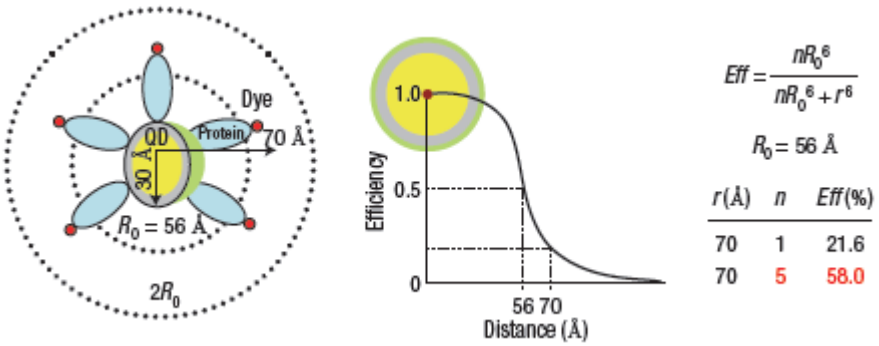

Figure 1.43. Demonstration of improved FRET efficiency derived from arraying multiple acceptor dyes around a single QD donor acting as a protein scaffold. Adopted from ref. [145]

FRET between CdSe/CdS core/shell NPs with different geometries and dimensionalities, and Atto 590 dye molecules, acting as multiple acceptors covalently linked to the NP surface, was examined by Halivni and coworkers [146]. Changes in the NP geometry, and consequently in the distributions of acceptors, lead to different FRET behaviors (Figure 1.44).

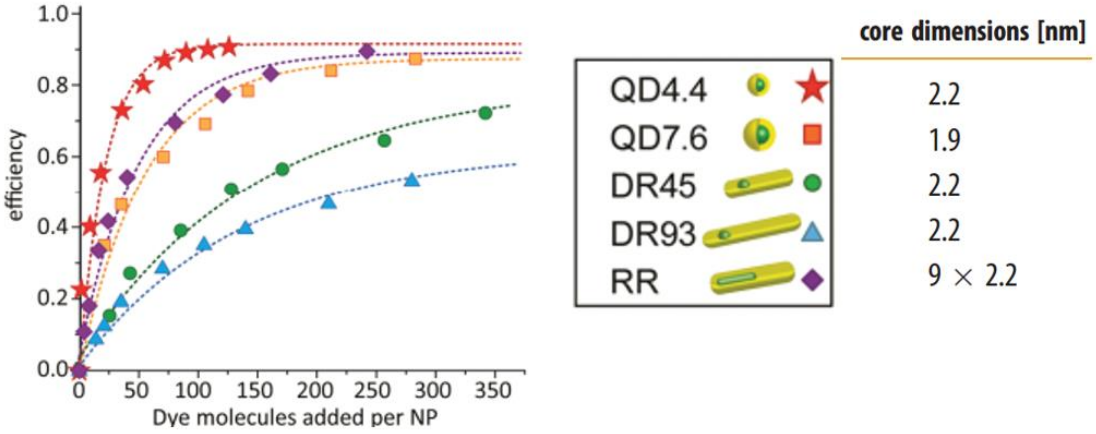

Figure 1.44. FRET efficiency as a function of dye molecules added per NP. Adopted from. [146]

Diaz et al. reported development of photoswitchable water-soluble QDs. [147] For this, ~7 nm in diameter commercial hydrophobic CdSe/ZnS QDs were covalently covered with amphiphilic polymers with photochromic diheteroarylethenes, which undergo thermally stable photoconversion between two forms with different spectral properties (Figure 1.45). As a result, the modulation was 35-40%, with fatigue resistance over at least 16 cycles of photoconversion.

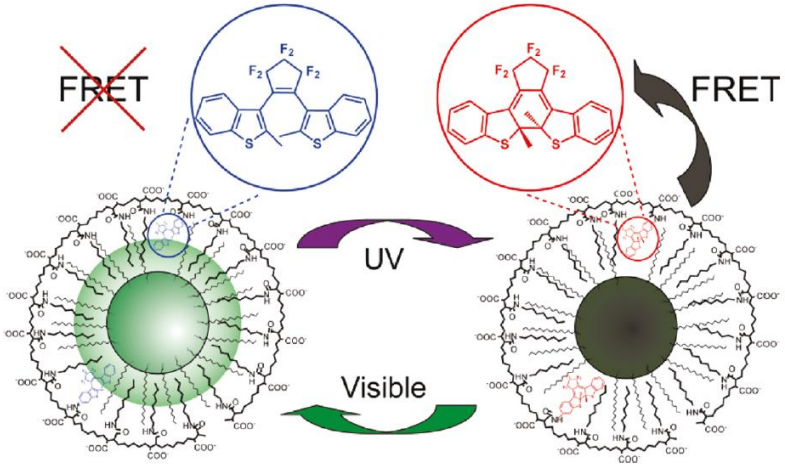

Figure 1.45. Photoswitching QDs coated with an amphiphilic photochromic polymer. Adopted from ref. [147]

Taking the advantage of the large surface area of QDs, that offers an opportunity for molecular adsorption or surface modification with multiple acceptors simultaneously, Zhang et al. reported FRET-based targeted DNA detection. [148] Streptavidin-coated CdSe/ZnS QD was used as a D, and organic fluorescent dye Cy5 as an A. The capture probes were conjugated with biotin, and the reporter probes with Cy5. After co-hybridization of target DNA with capture probes and reporter probes the strong affinity interaction between biotin and streptavidin would bring the Cy5 labeled sandwich hybrids and QDs into close proximity, leading to FRET (Figure 1.46). By monitoring the fluorescence signal, this QD-based FRET biosensor showed extraordinary performance with a limit of detection (LOD) of 4.8 fM.

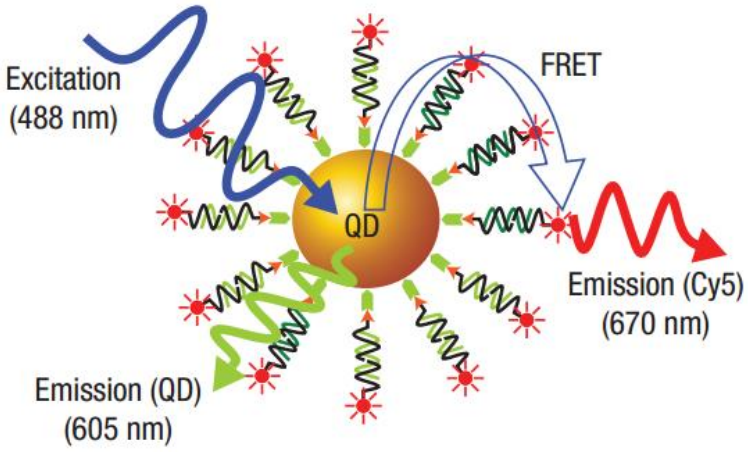

Figure 1.46. Schematic representation of DNA nanosensor assembly based on FRET QD and Cy5.Adoptd from ref. [148].

Petryayeva and Algar demonstrated a multiplexed QD-based FRET assay to detect the activity of three different proteases (trypsin, chymotrypsin, and enterokinase) using a smartphone camera [149]. Three QD-peptide conjugates with different emission colors were labeled with respective organic dye for FRET. Enzymatic cleavage of the peptides cause the release of the acceptor dyes and increasing in QD emission intensities. It was detected via the RGB channel by smartphone camera (Figure 1.47). The assay performance, obtained with smartphone imaging, gave the same quantitative results as measured with a sophisticated fluorescence plate reader.

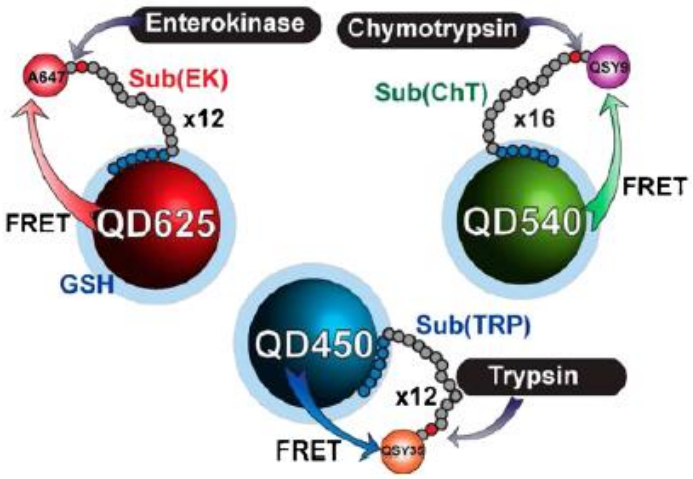

Figure 1.47. Schematic representation of a homogeneous multiplexed FRET assay to monitor the activity of trypsin (TRP), chymotrypsin (ChT), and enterokinase (EK) using three different QD donors (blue mitting QD450, green-emitting QD540, and red-emitting QD625) in combination with three different organic dye acceptors (QSY35, QSY9, and A647), respectively. Adopted from ref. [149]

But QD-based FRET has certain limitation: QDs require surface coating that decreases FRET efficiency.

UCNPs are generally used as donors in FRET assays, which typically rely on coupling with a downconverting acceptor molecule. The fluorophore should be chosen for the spectral overlap between the emission spectra of the UCNPs and the excitation spectra of the downconverting fluorophores. Under NIR excitation, UCNPs' emission is in the visible light range, which is necessary for excitation of conventional fluorophores. The NIR excitation range makes UCNPs good donor candidates, since NIR excitation light is far away from the excitation spectra of most acceptor molecules. [150] UCNP-organic dye based FRET assays have been developed for various biological applications. [150]

Zhang et al. designed a sandwich-type nucleotide biosensor based on energy transfer from UCNPs to TAMRA. [151] UCNPs were conjugated to the reporter and fluorophores to capture probes. The co-hybridization among target DNA, UCNPs-oligo and fluorophore-oligo FRET pair at close proximity leads to the emission of fluorophores (Figure 1.48). By monitoring the emission of fluorophores, the target DNA could be detected sensitively and specifically with a detection limit of 1.3 nM.

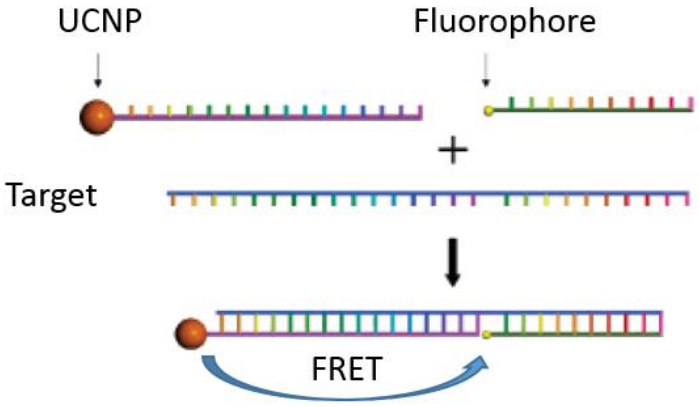

Figure 1.48. The schematic of the nucleotide sensor design based on FRET from UCNPs. Adopted from ref. [151]

Recently Cheng et.al reported multicolor *in vivo* imaging of UCNPs. [152] For this, fluorescent dye or quenchers were attached to the surface of PEGylated UCNPs. The formed complex demonstrate tuned emission due to luminescence resonance energy transfer (LRET) from NPs to organic dyes under NIR excitation and can be well-separated in multicolor imaging (Figure 1.49).

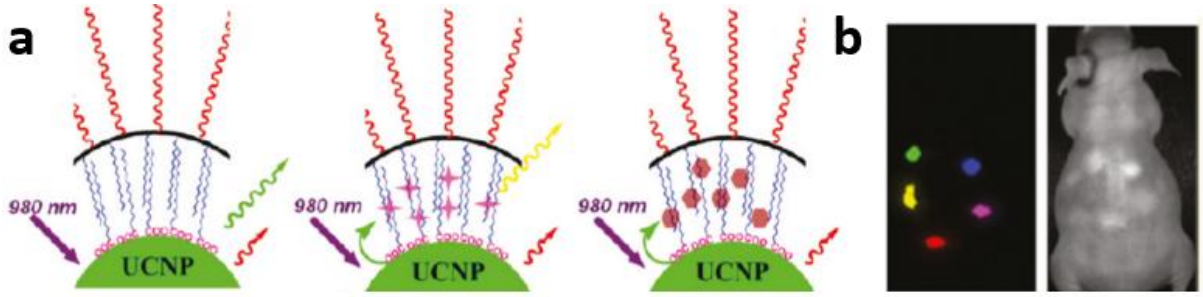

Figure 1.49. UCNP-based LRET system. **a)** A scheme of the UCNP-LRET system; the hydrophobic layer between the inorganic nanoparticle surface and the external PEG coating allows adsorption of organic dye molecules on UCNPs; **b)** *In vivo* multicolor UCL images of a nude mouse subcutaneously injected with five colors of UCNPs solutions. Merge-UCL (left) and white light (right). Adopted from ref. [152]

FRET has been successfully applied in P-dots to enhance the quantum efficiency, to tune the emission color and to create biosensing devices. [52, 153] Thus, energy transfer from conjugated-nonconjugated multiblock copolymers (CNMBC) to poly[2-methoxy-5-(2-ethylhexyloxy)-1,4-phenylenevinylene] (MEHPPV) leads to enhanced emission of the latter almost 500 times for some ratios. [154]

FRET in blend of conjugated polymers was demonstrated in NPs, consisting of a derivative of the blue-emitting conjugated polymer, polyfluorene-doped with green-, yellow-, and red-emitting conjugated polymers, prepared by a precipitation method. Fluorescence quenching analysis of the host polymer as a function of the dopant concentration indicated that one energy acceptor molecule can effectively quench 90% of the fluorescence of a nanoparticle consisting of 100−200 host conjugated polymer molecules. [155]

FRET from P-dots to doped fluorescent dyes is also possible. In the first example of this phenomenon, reported by Grigalevicius and co-workers, the blue fluorescence of the dye-coated polyfluorene nanoparticles was slightly quenched after dye deposition, that was accompanied with an appearance of a new emission band of the surface-bound dye (Rhodamine 6G or Rhodamine TM).[156]

Later, McNeill and co-workers prepared polyfluorene-based NPs, doped with various dyes by reprecipitation method. [157] The results indicated efficient EET from host (donor) polyfluorene to dopant (acceptor) dye molecules (Figure 1.50). Photobleaching experiments indicated that the photostability of the P-dots could be improved by doping them with energy acceptors.

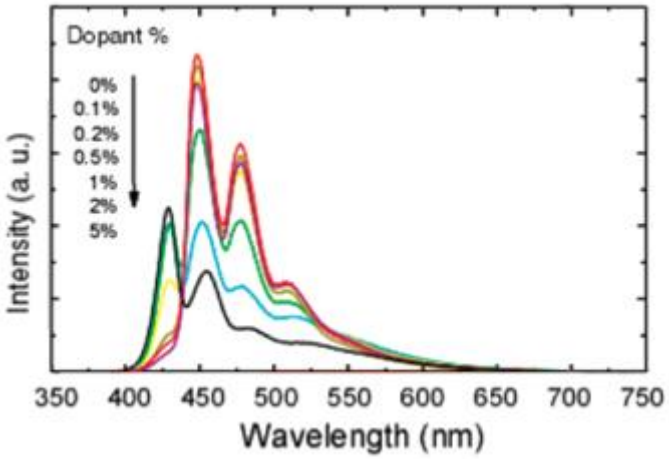

Figure 1.50. Concentration dependent fluorescence spectra of polyfluorene based NPs doped with perylene with increasing concentration. Adopted from ref. [158]

Harbron et al. demonstrated reversible photoswitching of fluorescence in MEH-PPV CPNs, doped with photochromic spirooxazine dye. [159] Upon alternating UV irradiation and dark recovery, more than 90% quenching of the MEH-PPV fluorescence was achieved which corresponds to a photoswitching ratio larger than

10. The photoswitching was reversibly cycled numerous times, with no detectable fatigue effect.

Exploiting FRET from conjugated polymer to doped molecule, the group of McNeil created biological oxygen sensor.[160] For this, EET from polyfluorene NPs to phosphorescent oxygen-sensitive platinum(II) octaethylporphine (PtOEP) was used (Figure 1.51). The bright phosphorescence fade within a few seconds after exposure to air/ indicating the oxygen permeability.

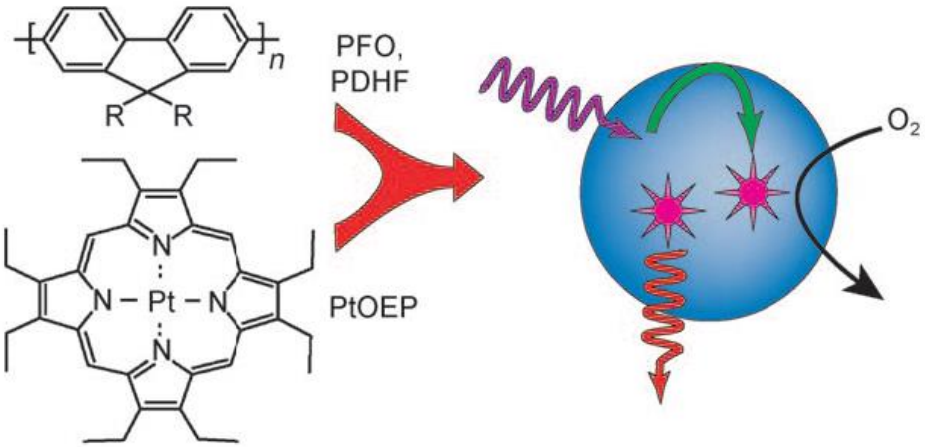

Figure 1.51. Schematic illustration of the formation of P- dots for oxygen sensing. Adopted from ref. [160]

1.5. Technics for characterization of NPs

Various techniques characterization of NPs exist. But there is no method that could be selected as “the best”. For determination of characteristics of each particular sample, all sample restrictions, the required information, time and the cost of the analysis should be considered (Table 1.2).

Table 1.2. Comparison of commonly used techniques for NPs characterization.

Technique	Measures	Sample	Sensitivity	Notes
DLS	average size and size distribution	dilute suspension	1nm -10μm	Determine only hydrodynamic size of NPs[a]
FCS	average size and size distribution, concentration and brightness[b]	dilute suspension of fluorescent sample	down to 1nm	Two –photon excitation or pinhole system required
TIRF	brightness[b] and brightness distribution, photostability, fluorescence behavior	Fluorescent, immobilized on a glass surface	No direct access to size	Visible “size” reflects both real size and brightness
TEM	size and characterization	< 1μg has to be prepared as a thin film and be stable under an electron beam and a high vacuum	down to 1nm	Sample preparation can be time consuming, phase-contrast results could be difficult to interpret,
SEM	size and characterization	conductive or sputter-coated easier to prepare than TEM sample	down to 1nm	Sample preparation can be time consuming
AFM	size and characterization	must be adhered to a surface, be rigid and dispersed	1nm - 8μm	slow scan time, which can lead to thermal drift of the sample

[a] size of a hypothetical hard sphere that has the same transitional diffusion coefficient as the particle and depends not only on the “core”, but also on surface structure and ionic strength of medium.

[b] reference sample required.

1.5.1. Dynamic Light Scattering

Dynamic Light Scattering (DLS) is a commonly used technique for determination of size and size distribution of particles, usually in the sub-micron region. It is based on measuring Brownian motion of NPs in suspension. *Brownian motion* is a random displacement of particle, caused by its bombardment by the solvents molecules. For larger particles movements is slower. DLS relates velocity of Brownian motion, known as translational diffusion coefficient, to the size of NPs according to the Stokes−Einstein equation.

$$d(H) = \frac{kT}{3\pi\eta D}$$

Where

$d(H)$) = hydrodynamic diameter

D = translation diffusion coefficient

k = Boltzmann's constant (physical constant relating energy at the individual particle level with temperature, equal to 1.38×10^{-23} J/K)

T = absolute temperature

η = viscosity

Brownian motion could be measured by analyzing the rate of scattered light fluctuation. Usually, photon auto-correlation function is used for this. The idea is to measure the degree of similarity between two signals, or one signal with itself at varying the time intervals.

The autocorrelation function usually decays starting from zero delay time, and faster dynamics due to smaller particles lead to faster decorrelation of scattered intensity trace (Figure 1.52).

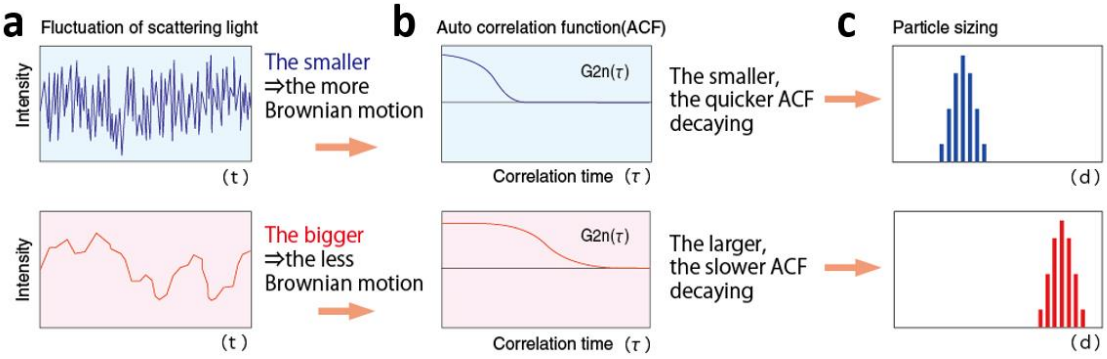

Figure 1.52. Examples of the dynamic light scattering measurements: **a)** autocorrelation curve **b)** and size distribution **c)** of small (upper panel) and big NPs (lower panel). Image adopted from otsukael.com.

Size could be obtained from correlation function either by fitting a single exponent to obtain mean size (z-average diameter) and an estimate of the width of the distribution(polydispersity index) or multi exponential fit to obtain the distribution of particle size(intensity size distribution). [161] Using Mie theory it is possible to obtain volume distribution that gives more realistic view.

The size, determined by DLS, is the size of a hypothetical hard sphere that has the same transitional diffusion coefficient as the particle and depends not only on the "core", but also on the surface structure and ionic strength of medium. [162]

1.5.2. Fluorescence Correlation Spectroscopy

Fluorescence Correlation Spectroscopy (FCS) is a correlation analysis of fluctuation of fluorescence intensity in sub-femtolitre volume. This fluctuation depends on the number of fluorophores and concentration of NPs that allow to determine these parameters. In a typical FCS measurement, fluorescence intensity is recorded for a small number of molecules in the detection volume over a time range from about 1 microsecond to 1 second. The time-dependent fluorescence intensity $F(\tau)$ is then analysed in terms of its temporal autocorrelation function$G(\tau)$, which compares the fluorescence intensity at time t with the intensity at$(t+\tau)$, where τ is a variable interval, averaged over all data points in the time series:

$$G(\tau) = \frac{\langle \delta F(\tau) * \delta F(t+\tau) \rangle}{\langle \delta F(\tau) \rangle^2}$$

The autocorrelation function contains information about equilibrium concentrations, reaction kinetics and diffusion rates of molecules in the sample. The

initial amplitude of the autocorrelation function is inversely proportional to the number of molecules in the detection volume. The autocorrelation function decays from its initial value with a time-dependence that is determined by molecular diffusion rates (Figure 1.53).

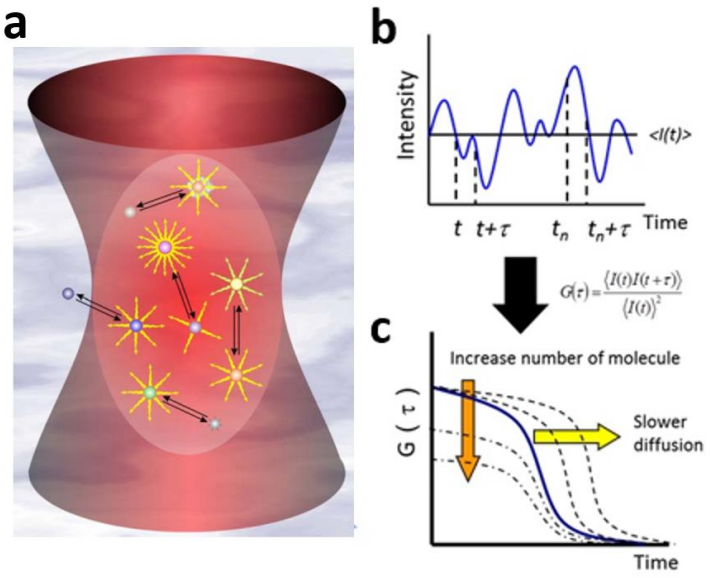

Figure 1.53. Schematic diagram of FCS. **a)** Schematic of observation area of FCS (confocal volume). **b)** Obtained fluctuation of fluorescence intensity. c) Autocorrelation functions. Adopted from ref. [163]

FCS can function properly only if the observation volumes is small enough and sample is diluted,so that only few molecules could be simultaneously detected. For this purpose, pinhole system or two-photon excitation are applied. [164]

1.5.3. Total Internal Reflection Fluorescence microscopy

The Total Internal Reflection microscopy (TIRF) relies on the excitation by *evanescent waves* that exist when the light is totally internally reflected at the interface between two media having dissimilar refractive indices. As a result only fluorophores in a thin zone of 100 nm from a solid surface of refractive index higher than the media of sample would be excited (Figure 1.54). This allows to obtain a high-quality image with very low background fluorescence and no out-of-focus fluorescence.[1]

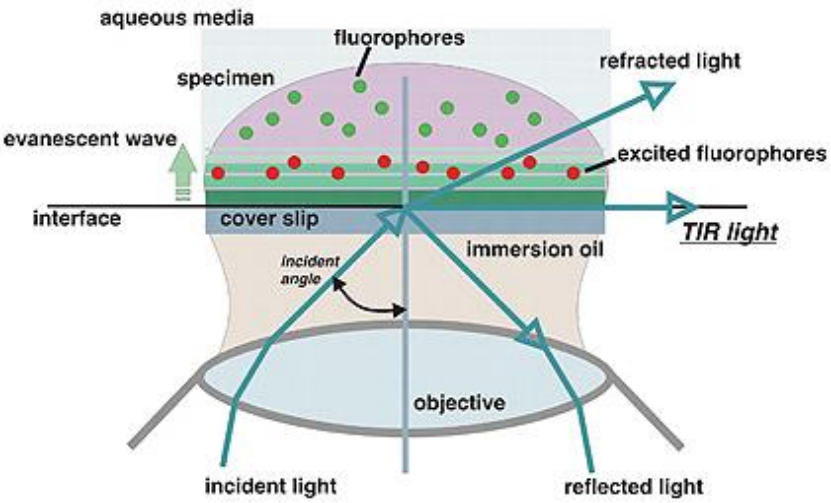

Figure 1.54. Schematic representation of TIRF. Adopted from ncl.ac.uk

1.5.4. Transmission Electron Microscopy

Transmission Electron Microscopy (TEM) operates the same basic principles as the optical microscopy, but exploits electrons that allow to obtain resolution up to 1 nm). An electron gun at the top of the microscope emits electrons through the vacuum in the column of the microscope, after they are focused by electromagnetic lenses into a very thin beam. This beam passes through the sample and, depending on the density of the material, some of electrons are scattered and disappear from the beam. At the bottom of the microscope the unscattered electrons hit a fluorescent screen and form a phase contrast image of the sample (Figure 1.55). [165]

Quality of the NPs imaging is strongly dependent on the contrast of the sample to the background. For this purpose, NPs should be dried on a copper grid, covered with thin layer of carbon. Materials with electron density higher than amorphous carbon could be easily imaged (silver, gold, copper, aluminium etc.), for other material additional staining should be applied. The analysis of the size is straightforward. Some complication could occur if NPs aggregate on the surface. The results are usually presented as the average and standard deviation of the sample.

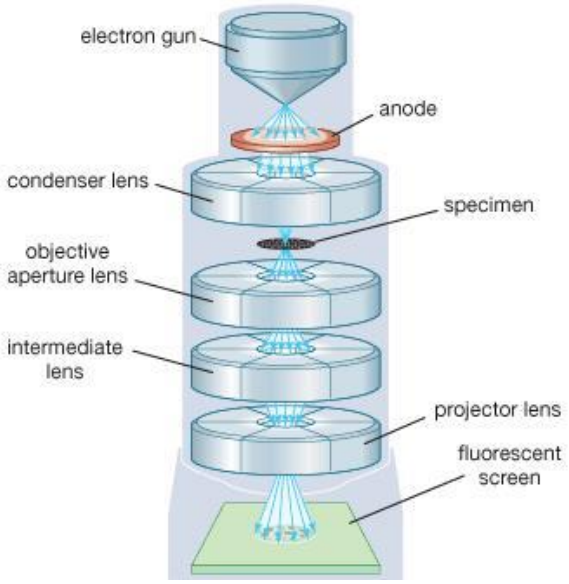

Figure 1.55. Main components of transmission electron microscopy. Adopted from britannica.com.

1.5.5. Scanning Electron Microscopy

Scanning Electron Microscopy (SEM) uses electron beam as TEM, but the beam scans over the surface and backscattered electrons are used for imaging (Figure 1.56). A variety of detectors are used to detect different types of scattered electrons, including secondary and backscattered electrons, as well as x-rays.[165] SEM produces black and white, three-dimensional images. The sample should be conductive.

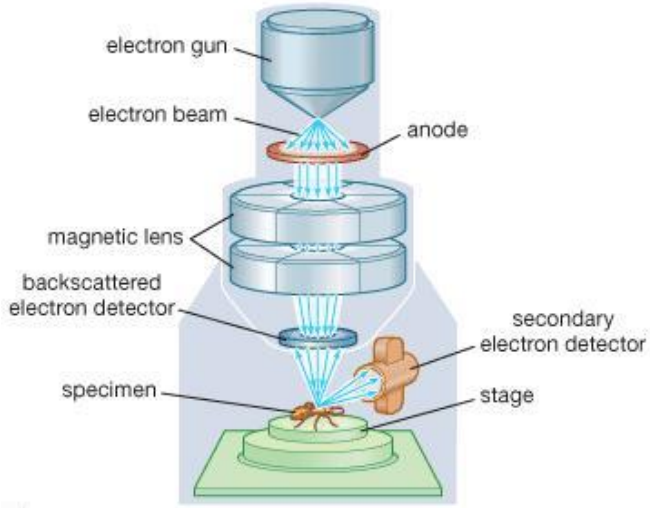

Figure 1.56. Principle of SEM. Adopted from britannica.com

1.5.6. Atomic Force Microscopy

Atomic Force Microscopy (AFM) is a form of Scanning Probe Microscopy that uses a mechanical probe to feel the surface of a sample (Figure 1.57). A cantilever with a probe is moved over the sample's surface and the forces between the probe tip and the sample are measured based on the deflection of the cantilever. [165] A rigid sample should be adhered to a surface, and the roughness of the surface must be less than the size of NPs.

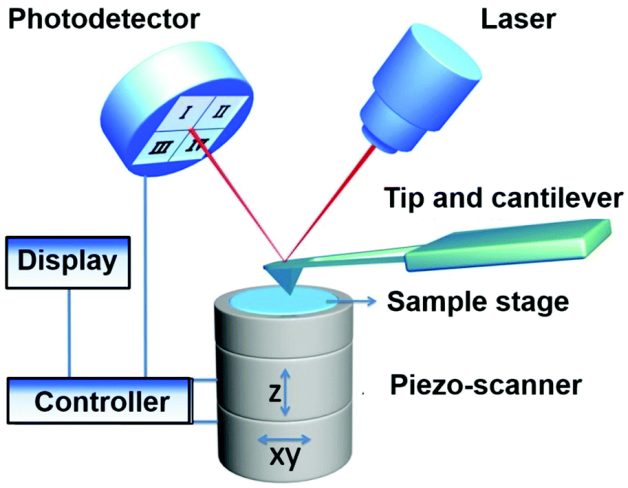

Figure 1.57. Schematic diagram of atomic force microscopy. Adopted from ref. [166]

PART 2. Results and discussions

2.1. Development of dye-loaded polymer NPs

Unique properties of fluorescent NPs, such as bright fluorescence and high biocompatibility, can drastically improve speed and resolution of fluorescence-based bioimaging techniques. High surface to volume ratio of NPs can provide multivalent scaffolds for functionalization that allow multiplexing. [102, 113] The field of fluorescent NPs is currently dominated by inorganic NPs, especially QDs, dye-doped silica NPs and upconverting NPs [167, 168] However, they lack flexibility in terms of tuning emitter properties and surface chemistry. Non-biodegradability and potential toxicity due to the nature of building materials limit their application *in vivo*. [44] Polymer-based NPs were widely used in drug delivery due to their complete biodegradability. But creation of highly dye-loaded polymeric NPs is problematic due to that fact that at high concentration dyes prone to create non-fluorescent aggregates that decrease QY. [101]

Fluorescent NPs should present some properties that are different from those of single dyes. The size of NPs is significantly larger, which can be a weak point for certain applications that require minimal perturbation of a biological process, but can be a strong point for *in vivo* imaging [101, 169] Brightness of NPs can be 100-fold higher than that of single molecules, which is advantageous for numerous imaging applications. Although encapsulation should improve dye photostability due to the shielding effect of the rigid polymer matrix, but aggregation may create photochemical processes that can decrease drastically dye stability. The color of NPs is directly defined by the color of encapsulated dyes, though in some cases dye aggregation can generate NPs with different absorption and emission maxima. Dyes, confined inside a polymer matrix at high concentrations, may produce cooperative phenomena, such as particle blinking/switching. [170]

Some properties of fluorescent polymer NPs, such as size, monodispersity and dye loading efficiency, can be modulated by choosing and modification of the preparation method. The fluorescent characteristics of polymer NPs (QY, brightness,

photostability, color and size) are determined mainly by the properties and organization of encapsulated dyes and properties of hosted polymer matrix.

My PhD project was focused on NPs prepared by nanoprecipitation (or solvent displacement) technique from acetonitrile or dioxane solution to phosphate buffer (Figure 1.17). This is very fast and simple method, but it requires sufficient level of hydrophobicity of the dye to be physically entrapped into forming polymer NPs.

To develop NPs with superior fluorescent properties, we determined the particularity of dye structure that provides the most efficient encapsulation, the highest possible brightness and photostability on the example of perylene diimide dyes. To control spatial organization of dyes inside NPs (thus creation of favorable conditions for EET), we studied the influence of the polymer matrix that are used to assemble dye-loaded NPs.

2.1.1. Article 1:"Tuning the color and photostability of perylene diimides inside polymer nanoparticles: towards biodegradable substitutes of quantum dots"

To address the problem of brightness and photostability of fluorescent polymer NPs, encapsulation of two bulky perylene diimide (PDI) derivatives into polymer poly (lactic-co-glycolic acid) PLGA NPs was studied (Figure 2.1). PDI dyes are considered as one of the most photostable dyes to date. [171] QY of PDI-1 in solution was reported to be close to unity [172] due to suppression of aggregation by addition of bulky peripheral groups. Lumogen Red (LR) has additional bulky group (aromatic rings) in the bay regions and characterized by QY = 0.96 and high resistance to aggregation. [8]

PLGA is a biodegradable and biocompatible copolymer, approved by of Food and Drug Administration (FDA). The mechanism of PLGA degradation is hydrolysis of the ester linkage in aqueous solution. The products of degradation are lactic and glycolic acids, that are naturally present in the body. The time required for degradation depends on monomers ratio. For higher amount of glycolic acid lower time for degradation is needed. [173]

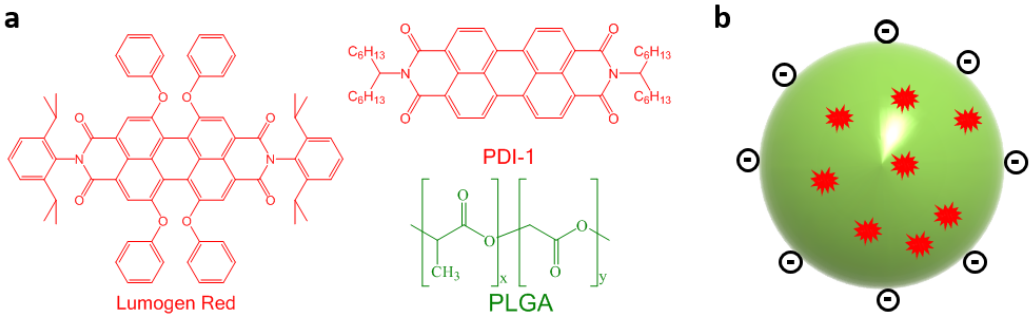

Figure 2.1. Chemical structure of PDI-1 and LR dyes, polymer PLGA **(a)** and schematic presentation of dye-doped PLGA nanoparticles **(b).**

As a result of co-precipitation of PLGA and dyes, monodisperse ~40-nm NPs were formed independently of the dye concentrations (from 0.02 wt% to 5 wt% with respect to the mass of the polymer) for both fluorophores. Addition of dye alone (without polymer) from organic solvent to the same aqueous buffer resulted in creation of 150-210 nm NPs. This difference in sizes evidenced the successful encapsulation of the dyes.

Remarkably, the spectroscopic properties of these two dyes demonstrated strong difference in aggregation behavior. Encapsulation of PDI-1 resulted in strong aggregation even at low dye loading (>0.02 wt%), which was accompanied by modulation of its emission color from green to red and a drop in its fluorescence QY. In contrast, Lumogen Red showed nearly no aggregation inside polymer NPs and preserved high fluorescence QY (Figure 2.2).

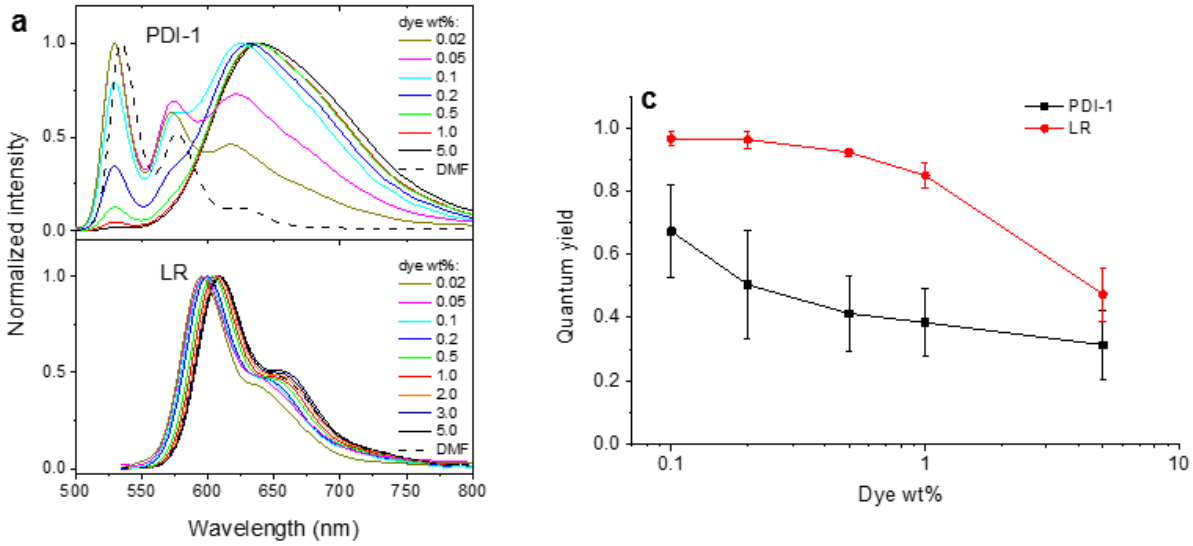

Figure 2.2. Difference of aggregation behavior of PDI-1 and LR in PLGA NPs. **a)** Normalized emission spectra and **b)** QY for different loading.

Single particle measurements on wide-field microscope in TIRF mode demonstrated difference in photostability between NPs loaded with these two dyes. PDI-1 at the lowest loading (non-aggregated form) had good photostability, but increase in loading to 1 wt% led to fast drop in photostability even at low laser power. This result was surprising, taking to account remarkable photostability of PDI in a solution. By contrast, LR showed remarkable photostability event at 5 wt% loading and at high laser power (Figure 2.3).

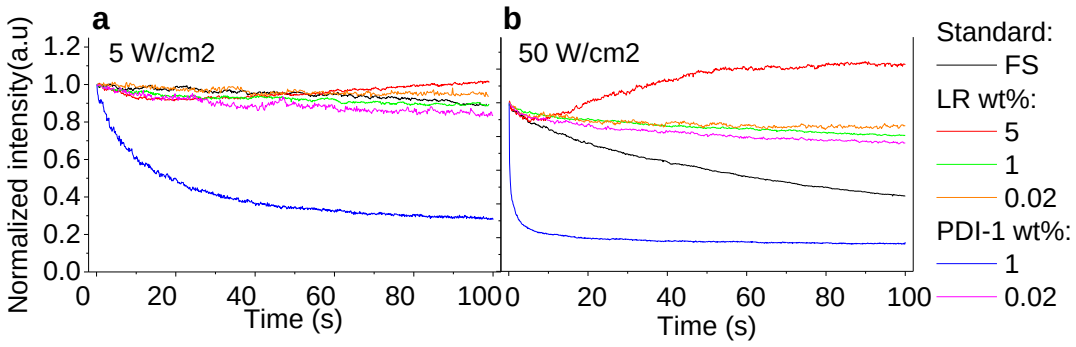

Figure 2.3. Photostability of NPs loaded with different amount of dyes. NPs are immobilized on glass surface and are continuously irradiated by a laser 532 nm at 5 **a)** and 50 **b)** W/cm^2. As a reference, FluoroSpheres (FS, Invitrogen, FluoSpheres® Carboxylate-Modified Microspheres, 0.04 µm, red-orange fluorescent (565/580), 5% solids, azide free) were used.

According to the measurements with a 532 nm excitation laser, our 40 nm PLGA NPs loaded with 1 wt% Lumogen Red were >10-fold brighter than quantum dots (QDs-585 streptavidine conjugate, Life Technologies).

The stability of NPs in presence of 10% serum was confirmed by FCS. These NPs were incubated with HeLa cells and then further imaged by confocal fluorescence microscopy. They entered spontaneously into cells by endocytosis showing no sign of cytotoxicity (confirmed by MTT-test).

The present work demonstrated the importance of introducing of bulky side groups into structure of encapsulated dyes to prevent their aggregation. The surprising result was very poor photostability of PDI-1 dye in an aggregated form. At the same time, excellent photostability and brightness of NPs loaded with LR make them biodegradable substitutes of quantum dots, which could find a variety of applications in biological imaging.

The results were published in the article: Trofymchuk, K.; Reisch, A.; Shulov, I.; Mely, Y.; Klymchenko, A. S., “Tuning the color and photostability of perylene diimides inside polymer nanoparticles: towards biodegradable substitutes of quantum dots” Nanoscale 2014, 6 (21), 12934-12942.

The full description of the work can be found in the article enclosed below.

Nanoscale

PAPER

View Article Online
View Journal | View Issue

CrossMark click for updates

Cite this: *Nanoscale*, 2014, **6**, 12934

Tuning the color and photostability of perylene diimides inside polymer nanoparticles: towards biodegradable substitutes of quantum dots†

Kateryna Trofymchuk, Andreas Reisch, Ievgen Shulov, Yves Mély and Andrey S. Klymchenko*

Fluorescent organic nanoparticles (NPs) are attractive alternatives to quantum dots due to their potential biodegradability. However, preparation of fluorescent organic NPs is challenging due to the problem of self-quenching of the encapsulated dyes. Moreover, the photostability of organic dyes is much lower than that of quantum dots. To address both problems, we studied encapsulation into biodegradable polymer PLGA NPs of perylene diimide (PDI) derivatives, which are among the most photostable dyes reported to date. Two PDIs were tested, one bearing bulky hydrophobic groups at the imides, while the other was substituted in both imide and bay regions (Lumogen Red). Encapsulation of the former resulted in aggregation, which was accompanied by the emission color change from green to red, some decrease in the fluorescence quantum yield and a significant drop in the photostability, unexpected for PDI dyes. In contrast, Lumogen Red showed nearly no aggregation inside polymer NPs and maintained high quantum yield and photostability. According to wide-field fluorescence microscopy with a 532 nm excitation laser, our 40 nm PLGA NPs loaded with 1 wt% Lumogen Red were >10-fold brighter than quantum dots (QD-585). These NPs were stable in biological media, including serum, and entered spontaneously into HeLa cells by endocytosis showing no sign of cytotoxicity. Due to excellent photostability, these nanoparticles could be considered as biodegradable substitutes of quantum dots in bioimaging.

Received 3rd July 2014,
Accepted 22nd August 2014

DOI: 10.1039/c4nr03718a

www.rsc.org/nanoscale

Introduction

The research on fluorescent nanoparticles (NPs) is growing exponentially as they are platforms for the fabrication of ultrabright multifunctional devices for imaging, diagnostics and therapy.[1] The most established examples of fluorescent NPs are quantum dots[2,3] and dye-doped silica NPs,[4,5] which are of inorganic nature. Despite their unique photophysical properties, they lack biodegradability and flexibility for the encapsulation of molecules. Therefore, the search for organic analogues of quantum dots is particularly active.[6–11] Biodegradable polymers are probably the most promising materials for fluorescent organic NPs. Notably, NPs based on the biodegradable polymer poly(D,L-lactide-*co*-glycolide) (PLGA) are known for many years as drug carriers,[12–14] but the first examples of highly fluorescent dye-doped PLGA nanoparticles appeared only recently.[15–18]

The key challenge in the design of fluorescent organic NPs is to confine the fluorophores inside NPs at extreme concentrations (10^3–10^6 times higher than those used in solutions), at which they tend to self-quench due to formation of non-fluorescent aggregates. These aggregates originate from the poorly controlled assembly of the dyes inside the NP matrix. Indeed, as all organic dyes are basically flat aromatic structures, they tend to self-assemble into π-stacked aggregates with forbidden fluorescence (so-called H-aggregates).[19–21]

In the case of charged dyes, such as rhodamine B or cyanines, the problem was solved by introducing a bulky hydrophobic counter-ion serving as a spacer between the encapsulated dyes.[10,17,22] On the other hand, neutral dyes require multiple bulky groups,[23,24] or modifications favoring emission in the solid state.[7,9,25,26] Important examples of neutral dyes are perylene diimides (PDIs), because they found a variety of applications in molecular electronics,[27,28] solar cells,[29] solar concentrators,[30] and as very bright and photostable fluorophores.[31–33] Their large and flat aromatic system shows a strong tendency for π-stacking, forming poorly

Laboratoire de Biophotonique et Pharmacologie, UMR 7213 CNRS, Université de Strasbourg, Faculté de Pharmacie, 74, Route du Rhin, 67401 ILLKIRCH Cedex, France. E-mail: andrey.klymchenko@unistra.fr; Tel: +33 368 85 42 55

†Electronic supplementary information (ESI) available: Additional data on absorption and single particle properties of PLGA NPs. See DOI: 10.1039/c4nr03718a

View Article Online

Nanoscale Paper

fluorescent H-type aggregates.[34–38] The self-assembly of PDIs was successfully controlled through molecular design that leads to fluorescent J-aggregates or emissive distorted H-aggregates.[36,39–41] As a general trend, aggregation of PDIs results in blue shifts and broadening of the absorption spectrum together with the appearance of new strongly red shifted emission bands.[36,38] This aggregation behavior is observed also after encapsulation into a polymer matrix. In representative studies, photonic materials obtained by co-polymerization of PDIs within a polymer matrix showed characteristic red-shifted excimer fluorescence.[42,43] Encapsulated into organic composite NPs, PDIs also showed excimer fluorescence at relatively high dye loading.[44] Attempts to prevent complete aggregation in solution and inside a polymer matrix have been made by introduction of very bulky groups at the imide nitrogen atom as well as in the bay region of PDI. Modification of PDIs only at the nitrogen region (example PDI-1, Fig. 1) does not completely prevent aggregation of PDI, unless extremely bulky dendrimeric structures are used.[30,34,36]

On the other hand, substitution at the bay region can provide core-twisted PDI aromatic systems with inhibited H-type aggregation and significantly decreased self-quenching.[35,45] For example, Lumogen Red (LR, Fig. 1) can be concentrated inside a PMMA polymer matrix at >50 mM concentrations without significant aggregation and self-quenching[46] and, therefore, is commonly used in solar concentrators.[47,48]

However, so far LR has never been applied for preparation of fluorescent polymer NPs. Moreover, the control of the aggregation behavior of PDI dyes encapsulated into the polymer NP matrix requires more systematic study, which could help obtaining NPs of superior brightness. Finally, there is limited information in the literature on how aggregation of PDIs affects their photostability, which is crucial for preparation of organic substitutes of QDs.

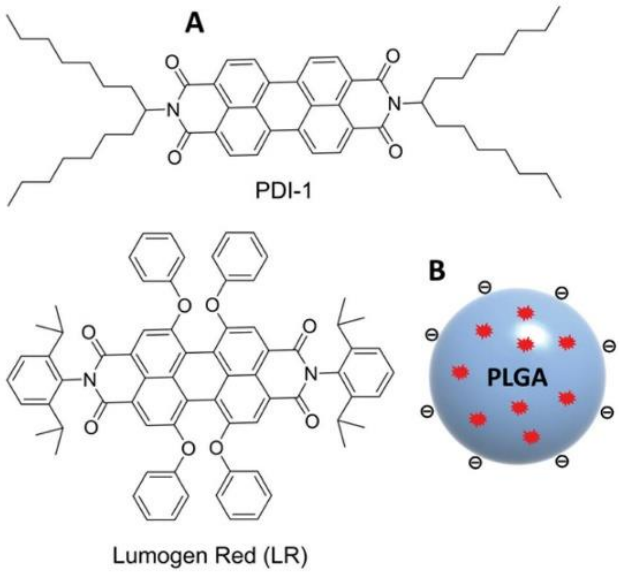

Fig. 1 Chemical structure of PDI-1 and LR dyes (A) and schematic presentation of dye-doped PLGA nanoparticles (B).

In the present work, we studied the encapsulation of two PDI dyes inside NPs composed of the biodegradable polymer PLGA. We found that inside polymer NPs, PDI-1 bearing bulky groups only at the imide nitrogens exhibited strong aggregation behavior, accompanied by characteristic modulation of the emission color from green to red and a considerable decrease in the fluorescence quantum yield. Remarkably, aggregation of PDI-1 was accompanied by a dramatic drop of its photostability, which is very rarely observed for PDI dyes. By contrast, LR bearing bulky groups at both imide nitrogens and bay regions showed negligible aggregation, high quantum yields and excellent photostability even at high dye loading. Cellular studies of these NPs showed the low toxicity and strong potential for bioimaging applications. The obtained LR-doped NPs could be considered as biodegradable substitutes of QD with superior brightness and excellent photostability.

Materials and methods

Materials

Poly(D,L-lactide-*co*-glycolide) (PLGA, lactide 50 mol%, glycolide 50 mol%, M_n 24 000; PDI 1.7) was purchased from Sigma-Aldrich and used as received. Sodium phosphate monobasic (>99.0%, Sigma-Aldrich) and sodium phosphate dibasic dihydrate (>99.0%, Sigma-Aldrich) were used to prepare 20 mM phosphate buffer solutions at pH 7.4. MilliQ-water (Millipore) was used in all experiments. *N*,*N*′-Bis-(2,6-diisopropylphenyl)-1,6,7,12-tetraphenoxy-3,4,9,10-perylenebis(dicarboximide) (Lumogen Red) was purchased from ORGANICA® Feinchemie GmbH Wolfen. *N*,*N*′-Bis(1-heptyloctyl)-3,4,9,10-perylenebis-(dicarboximide) (PDI-1) was synthesized from 1-heptyloctylamine (Sigma-Aldrich) and perylene-3,4,9,10-tetracarboxylic dianhydride (Sigma-Aldrich) as was described previously.[49,50]

Preparation of fluorescent NPs

PLGA was dissolved at 2 mg mL^{-1} in acetonitrile containing different amounts of dye (from 0 to 5 wt% relative to the PLGA). These solutions were added quickly and under stirring (shaking) using a micropipette to a 10-fold volume excess of 20 mM phosphate buffer at pH 7.4. The particle solution was then quickly diluted five-fold with the same buffer.

Characterization of NPs

Dynamic light scattering measurements were performed on a Zetasizer Nano series DTS 1060 (Malvern Instruments S.A.). It uses a laser source at 633 nm, which excludes any light excitation of our dye-doped NPs. Absorption and emission spectra were recorded on a Cary 400 scan UV-visible spectrophotometer (Varian) and a FluoroMax-4 spectrofluorometer (Horiba Jobin Yvon) equipped with a thermostated cell compartment, respectively. For standard recording of fluorescence spectra, the excitation wavelength was set to 485 and 530 nm for PDI-1 and LR, respectively. The fluorescence spectra were corrected for detector response and lamp fluctuations.

Fluorescence quantum yields were calculated using rhodamine B in methanol (QY = 0.69) with an absorbance of 0.01 at 530 nm according to ref. 51.

Fluorescence microscopy

For single particle fluorescence measurements, the NPs were immobilized on glass surfaces on which a polyethyleneimine (PEI) layer was initially adsorbed. The solutions of NPs were diluted to a particle concentration of about 6 pM with buffer. 400 μL of these solutions per cm^2 were then brought in contact with the PEI covered glass for 15 min, followed by extensive rinsing with milliQ-water. The surfaces were left in milliQ-water during the microscopy measurements. Quantum dots (QDot-585 streptavidin conjugate, Life Technologies) and FluoSpheres® red-orange (diameter 0.04 μm, carboxylate modified, Invitrogen) at 6 pM concentration were immobilized and imaged in the same way as PLGA NPs.

Single particle measurements were performed in the TIRF (Total Internal Reflection Fluorescence) mode on a home-made wide-field setup based on an Olympus IX-71 microscope with an oil immersion objective (NA = 1.49, 100×). A DPPS (Cobolt) continuous wave (CW) laser emitting at 532 nm was used for excitation. The laser intensity was changed between 5 and 50 W cm^{-2} using a polarizer and a half-wave plate (532 nm). The fluorescence signal was recorded with an EMCCD (ImagEM Hamamatsu).

Fluorescence correlation spectroscopy (FCS) and data analysis

FCS measurements were performed on a two-photon platform including an Olympus IX70 inverted microscope, as described previously.[23] Two-photon excitation at 780 nm (5 mW laser output power) was provided using a mode-locked Tsunami Ti:sapphire laser pumped using a Millenia V solid state laser (Spectra Physics). The measurements were carried out in an eight-well Lab-Tek II coverglass system, using 300 μL volume per well. The focal spot was set about 20 μm above the coverslip. The normalized autocorrelation function, $G(\tau)$, was calculated online using an ALV-5000E correlator (ALV, Germany) from the fluorescence fluctuations, $\delta F(t)$, by $G(\tau) = \langle \delta F(t) \delta F(t+\tau) \rangle / \langle F(t) \rangle^2$ where $\langle F(t) \rangle$ is the mean fluorescence signal and τ is the lag time. Assuming that NPs diffuse freely in a Gaussian excitation volume, the correlation function, $G(\tau)$, calculated from the fluorescence fluctuations was fitted according to Thompson:[52]

$$G(\tau) = \frac{1}{N}\left(1+\frac{\tau}{\tau_d}\right)^{-1}\left(1+\frac{1}{S^2}\frac{\tau}{\tau_d}\right)^{-1/2}$$

where τ_d is the diffusion time, N is the mean number of fluorescent species within the two-photon excitation volume, and S is the ratio between the axial and lateral radii of the excitation volume. The excitation volume is about 0.34 fL and S is about 3 to 4. The typical data recording time was 5 min, using freshly prepared PLGA NPs without further dilution. The measurements were done with respect to a reference 5(6)-carboxytetramethylrhodamine (TMR from Sigma-Aldrich) in water. The hydrodynamic diameter, d, of NPs was calculated as $d_{NPs} = \tau_{d(NPs)}/\tau_{d(TMR)} \times d_{TMR}$, where d_{TMR} is the hydrodynamic diameter of TMR (1.0 nm). The concentration of NPs was calculated from the number of species by $C_{NPs} = N_{NPs}/N_{TMR} \times C_{TMR}$, using a TMR concentration of 50 nM.

Cellular studies

HeLa cells (ATCC® CCL-2) were grown in Dulbecco's modified Eagle's medium (DMEM, Gibco-Invitrogen), supplemented with 10% fetal bovine serum (FBS, Lonza) and 1% antibiotic solution (penicillin–streptomycin, Gibco-Invitrogen) at 37 °C in a humidified atmosphere containing 5% CO_2. Cells were seeded onto a chambered coverglass (IBiDi) at a density of 5×10^4 cells per well 24 h before the microscopy measurement. For imaging, the culture medium was removed and the attached cells were washed with Opti-MEM (Gibco-Invitrogen). Then, a freshly prepared solution of NPs loaded with 1 wt% LR (at 20-fold dilution of the original formulation corresponding to ~0.15 nM of NPs) in Opti-MEM was added to the cells and incubated for different time periods. Cell membrane staining with wheat germ agglutinin-Alexa488 (Life Technologies) was done for 10 min at rt before the measurements. Confocal fluorescence images of the cells were taken on a Leica TSC SPE confocal microscope.

For cytotoxicity studies, HeLa cells were seeded in 96-well plates at a concentration of 10^4 cells per well in 100 μL of the DMEM growth medium and then incubated overnight at 37 °C in a humidified atmosphere containing 5% CO_2. Next, the PLGA NPs loaded with 1 wt% of PDI-1 or LR were added, by substituting the culture medium with the fresh one containing variable concentrations of NPs. After incubation for 24 h, the medium was removed and the adherent cell monolayers were washed with PBS. Then, the wells were filled with cell culture medium containing MTT, incubated for 4 h at 37 °C, and the formazan crystals formed were dissolved by adding 100 μL of a 10% sodium dodecylsulfate (SDS), 0.01 M hydrochloric acid solution. The absorbance was then measured at 570 nm with a microplate reader. Experiments were carried out in triplicate, and expressed as the percentage of viable cells compared to the control group.

Results and discussion

Nanoparticle preparation

PLGA nanoparticles were prepared using nano-precipitation of an acetonitrile or dioxane solution of the polymer in aqueous buffer, as we described previously.[17] Small particles of ~40 nm are formed, as a result of the use of diluted solutions of the polymer and control of pH, which ensures negative surface charge of the particles.[17] The dyes in the present study are highly hydrophobic and insoluble in water, so they should precipitate together with the PLGA polymer. When added from the stock solution in an organic solvent to aqueous buffer, the dyes alone aggregate and give, according to dynamic light scattering (DLS), relatively large particles of 150–210 nm (Table 1). To encapsulate the dyes inside the NPs, they were mixed with

Table 1 Hydrodynamic diameter and polydispersity of PLGA NPs encapsulating PDI-1 and LR measured by DLS[a]

Dye	PDI-1		LR	
Dye content (wt%)	Diameter (nm)	PDI	Diameter (nm)	PDI
0	47	0.27	43	0.20
0.02	46	0.24	42	0.30
0.05	46	0.29	42	0.21
0.1	40	0.24	42	0.19
0.2	43	0.08	45	0.23
0.5	48	0.30	42	0.12
1	47	0.30	41	0.13
2	—	—	42	0.09
3	—	—	48	0.12
5	43	0.32	38	0.17
1, w/o PLGA[b]	210	0.30	180	0.30
5, w/o PLGA[b]	150	0.20	160	0.16

[a] PDI is the polydispersity index. Statistics by volume was used in the analysis. [b] Samples prepared in the same way, but without PLGA. The error of size from 3 measurements was ±3 nm for all NPs except for samples without (w/o) PLGA (error ±15 nm).

the polymer in an organic solvent at the desired concentration before nano-precipitation. In this case, the particle size was found to be around 40 nm independently of the dye content, which was varied from 0.02 up to 5 wt% with respect to the polymer (Table 1). The slightly larger particle size observed with PDI-1 nanoparticles is related to the use of 10% dioxane in acetonitrile to ensure good solubility of PDI-1. These data suggest that being precipitated with PLGA, the dyes are encapsulated inside the polymer NPs and do not form separate large dye aggregates. Moreover, the absence of variation of the particle size with the dye content further shows that the dyes being encapsulated inside PLGA NPs do not significantly modify their interfacial properties.

Spectroscopic properties

Then, the optical properties of the obtained NPs were studied as a function of dye loading. For both dyes, an increase in the dye loading resulted in an almost linear increase in the absorbance (Fig. S1†). However, the absorbance of PDI-1 NPs at 530 nm (position of the absorption maximum in organic solvents) was systematically below the expected value, which could be related to the changes in the absorption spectral shapes. At very low dye loading, the spectrum is close to that observed in dimethylformamide (DMF). At higher loading, the observed bands broaden and the relative intensity of the shorter-wavelength maximum (~490 nm) strongly increases, so that it becomes dominant (Fig. 2A). Similar variations were previously described for other PDIs substituted at the imide nitrogens, suggesting that PDI-1 aggregates inside the polymer matrix at higher dye loading.[36,40] In contrast, the LR absorption spectra show minimal variations up to 5 wt% dye loading, where only a slight increase of the shorter wavelength band was observed (Fig. 2B) and, overall, the spectra were similar to that in DMF.

Fluorescence spectra of PDI-1 loaded NPs also show dramatic variations on dye loading. At the lowest dye loading, the

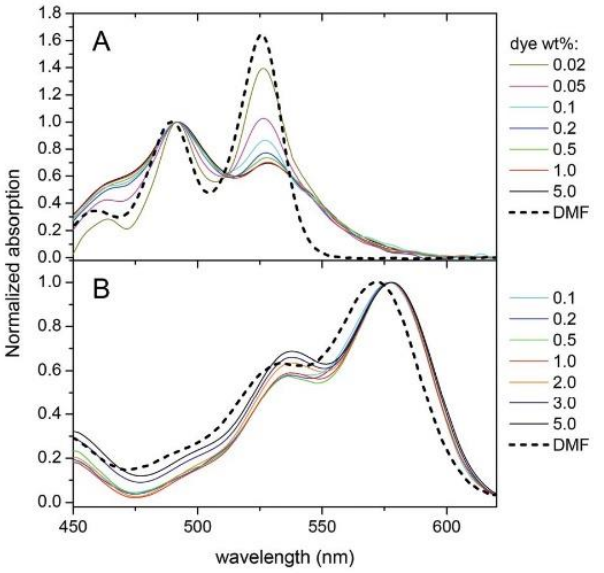

Fig. 2 Normalized absorption spectra of nanoparticles loaded with PDI-1 (A) and LR (B) at different weight concentrations with respect to PLGA. For comparison, the spectra of dyes in DMF are added.

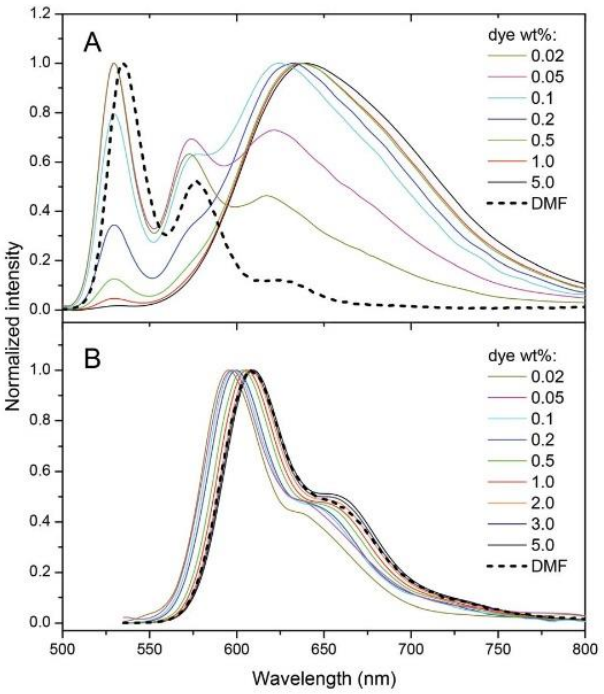

Fig. 3 Emission spectra of nanoparticles loaded with different PDI-1 (A) and Lumogen Red (B) weight concentrations. Excitation wavelengths were 485 nm and 530 nm, respectively.

fluorescence spectrum of encapsulated PDI-1 is similar to that in DMF (Fig. 3). Increasing dye loading leads to the appearance of a broad and strongly red-shifted band around 650 nm (Fig. 3A), similar to that reported for aggregates of other PDI dyes[36,40,53] and naphthalene diimides[54] substituted at the imide nitrogens. This suggests that the spectral variation of

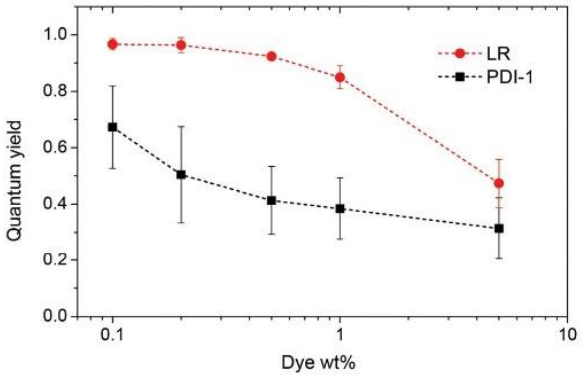

Fig. 4 Quantum yield of nanoparticles loaded with different weight concentrations of the dyes. Rhodamine B in methanol was taken as a reference.

PDI-1 is related to its aggregation inside the polymer matrix. Thus, variation of dye loading allows generating NPs with the emission color varying from green to red, which has not been shown so far for polymer NPs doped with PDI dyes. Their fluorescence quantum yield decreases gradually with increasing dye content (Fig. 4). However, even at high dye loading, the quantum yield remains relatively high, so that the new red-shifted band of the aggregates is appreciably emissive. As the aggregation of PDI-1 leads to fluorescent structures with blue-shifted absorption, this dye probably forms distorted H-aggregates, as suggested for assemblies of other PDI dyes.[36,40]

In the case of LR NPs, the emission spectrum varies to a much lower extent, as only a small red shift of its single emission band is observed (Fig. 3B). Moreover, its fluorescence quantum yield is higher than that of PDI-1 NPs, especially at high dye loading (Fig. 4). These data show that the additional bulky groups at the bay region inhibit drastically the aggregation of the LR dye inside the polymer matrix, leading to particles with more efficient fluorescence.

Single particle properties

Next, we monitored our NPs by fluorescence microscopy to access their single particle properties. To this end, we deposited at low density the NPs on a glass surface coated with PEI. This coating changes the glass surface charge from negative to positive, favoring the adsorption of PLGA NPs, which present negative surface charge.[17] In wide-field microscopy, the deposited NPs appear as bright spots (Fig. 5). At low dye loading (0.02 wt%), NPs loaded with LR and PDI-1 show brightness comparable to QDs (Fig. 5 and 6), LR NPs being the brightest. At 1 wt% dye loading, the brightness of LR NPs grows nearly 10-fold, while for PDI-1 it increases only 3.5-fold. Thus, due to aggregation of PDI-1 inside PLGA, ultrabright NPs could not be obtained. In the case of LR, that is not prone to aggregation, the obtained NPs are 14-fold brighter than QDs. Surprisingly, NPs loaded with LR at 5 wt% show only slightly higher brightness than those loaded at 1 wt%. According to the quantum yield measurements the former are supposed to be at least 2-fold brighter; however, it should be noted that the excitation power used in microscopy measurements is much higher compared to the spectroscopy measurements of the quantum yield. Therefore, we compared NPs at 1 and 5 wt% of dye at different illumination powers and found that the difference in brightness was significant (up to 2-fold) at much lower power, but was negligible at the highest laser powers (Fig. S2†). It could be speculated that high laser powers can simultaneously excite several fluorophores in a NP, which could lead to exciton–exciton annihilation[55] and thus decrease the overall intensity.

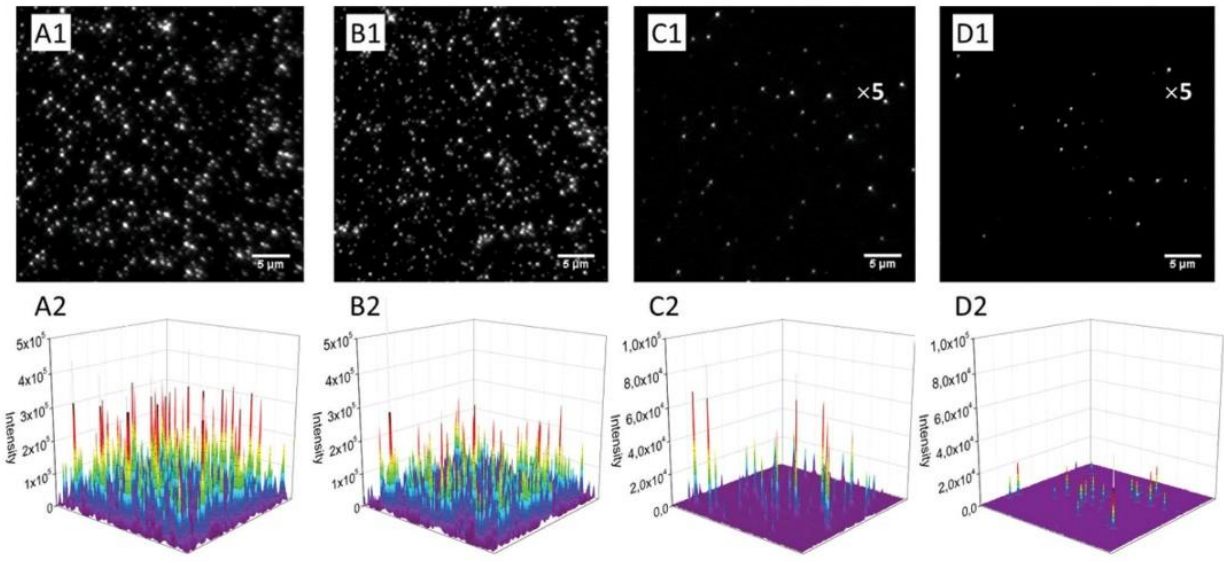

Fig. 5 Wide-field fluorescence microscopy images and the corresponding 3D profiles of fluorescent nanoparticles, encapsulating 5 (A1 and A2), 1 (B1 and B2) and 0.02 (C1 and C2) wt% of LR, on the glass surface in comparison with QD-585 (D1 and D2) under the same instrumental conditions. For a better visibility, the scale of intensity was amplified 5-fold for C1, C2, D1 and D2 panels. Illumination power was 5 W cm^{-2} at 532 nm.

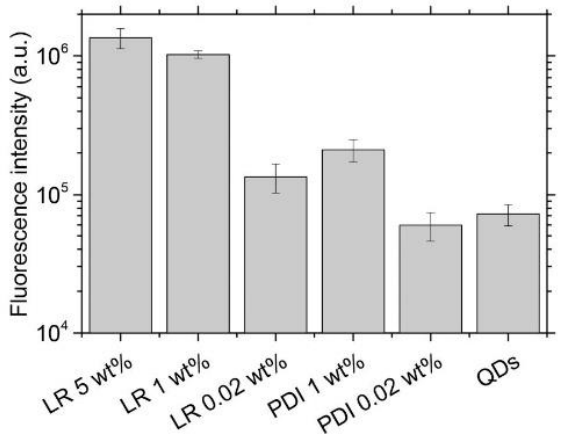

Fig. 6 Average fluorescence brightness of single dye-doped PLGA nanoparticles on the glass surface in comparison with QD-585. Illumination power was 5 W cm^{-2} at 532 nm.

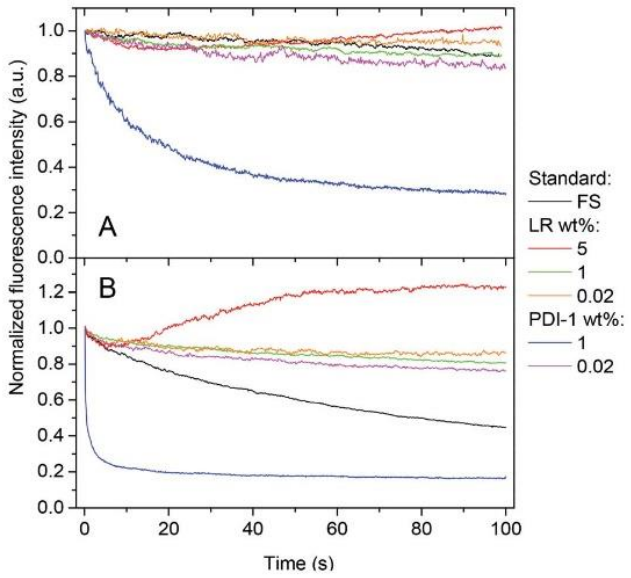

Fig. 7 Photostability of NPs loaded with different amounts of dyes. NPs are immobilized on the glass surface and are continuously irradiated with a 532 nm laser at 5 (A) and 50 (B) W cm^{-2}. As a reference, FluoroSpheres (FS, Invitrogen, FluoSpheres® carboxylate-modified microspheres, 0.04 μm, red-orange fluorescence, 565/580 nm) were used.

Using continuous video imaging, we studied the photostability of our NPs under relatively strong illumination power, namely 5 and 50 W cm^{-2}. At 50 W cm^{-2}, NPs at low content of either PDI-1 or LR show impressive photostability, which is even higher than that of FluoSpheres®, known for their high photostability (Fig. 7B). This excellent photostability of NPs is due to the unique properties of the PDI derivatives, which are among the most photostable dyes described to date.[36] NPs loaded with 1 wt% of LR also shows very high photostability, similar to 0.02 wt% dye loading. In sharp contrast, PDI-1 at 1 wt% loading is poorly photostable, as the half-life of fluorescence intensity recorded from the NPs was around 0.5 s for 50 W cm^{-2} illumination power.

The surprisingly low photostability of 1 wt% PDI-1 NPs was confirmed at lower excitation power, though intensity decay was considerably slower (Fig. 7A). As PDI-1 at 1 wt% is in the form of aggregates inside PLGA NPs, this aggregated state is likely responsible for the observed poor photostability. To the best of our knowledge, this is one of the first reports where the link between photostability and aggregation of PDI derivatives is shown. One recent report also suggested limited photostability for the red emitting aggregates of an imide-substituted PDI inside yeast cells.[38] It should be noted that at the highest dye loading of LR (5 wt%), an enhancement of the fluorescence is observed with time, especially at higher illumination power (Fig. 7). We expect that at 5 wt%, LR presents some fraction of poorly fluorescent aggregates, which may partially quench other encapsulated dyes. As these aggregates are probably less photo-stable than individual molecules, the strong illumination may selectively photobleach the aggregates, which should decrease self-quenching of the NPs and thus explain the observed fluorescence enhancement.

Fluorescence correlation spectroscopy (FCS)[56] is a powerful method to analyze fluorescent NPs, as it allows obtaining simultaneously information on the size, brightness and concentration of NPs *in situ*.[23,57] Using FCS with two-photon excitation, we analyzed our NPs with respect to the standard dye 5(6)-carboxytetramethylrhodamine (TMR). Unfortunately, only LR showed an appreciable two-photon absorption cross-section in the studied excitation range (see Fig. S3†), which allowed FCS measurements only for LR NPs. The brightness of the particles was found to increase gradually with the dye loading, reaching saturation at 1 wt% (Table 2). Indeed, from 0.02 till 1.0 wt% LR loading, the brightness per particle grows 24-fold, which correlates well with the single particle analysis by microscopy. However, in this two-photon measurement, LR-loaded NPs are less bright than QDs because the latter are well-known for their exceptionally high two-photon absorption cross-section.[58] Moreover, their size estimated from the correlation time remains around 35 nm, independent of the dye loading. This is in agreement with the DLS data (Table 1), suggesting that the only fluorescent species in solution are PLGA particles encapsulating LR. Therefore, formation of large aggregates from non-encapsulated LR molecules can be excluded, otherwise a population of fluorescent species of much larger size (~150 nm) would be observed.

The number of NPs per focal volume also remains relatively constant, which allows calculating the particle concentration. Then, knowing the molar concentration of LR in suspensions, the number of dyes per particle can be estimated (Table 2). This number grows with the dye loading and correlates well with the increasing brightness per particle. While at 0.02 wt% loading, the values of single and two-photon absorption coefficients of NPs are comparable to that of TMR, 40-fold larger values are observed at 1 wt%, which is of key importance for microscopy applications. It should be noted that at shorter excitation wavelengths (720–760 nm) the two-photon absorption cross-section of LR in methanol is >5-fold larger than that

Table 2 Two-photon excitation FCS of NPs loaded with different concentrations of the LR dye and comparison with TMR and LR in solution[a]

Sample	τ_d (ms)	Size (nm)	Number	Conc. (nM)	Dyes per NP	ε (M^{-1} cm^{-1})	Brightness/TMR	$\sigma^2\eta^2$ (GM)
TMR/water	0.053	1.0	28	50	—	1.0×10^5	1	134[b]
LR/MeOH	0.049	1.4	67	120	—	5.0×10^4	0.73	100
0.02 wt%	1.88	35.7	2.1	3.8	2	1.0×10^5	1.63	218
0.05 wt%	1.91	36.3	2.0	3.6	5	2.6×10^5	3.74	501
0.1 wt%	2.01	38.1	1.9	3.4	11	5.6×10^5	7.55	1011
0.2 wt%	1.97	37.4	1.9	3.3	22	1.1×10^6	12.1	1620
0.5 wt%	1.89	35.9	2.2	3.8	49	2.5×10^6	28.2	3770
1.0 wt%	1.82	34.5	2.5	4.5	82	4.2×10^6	39.2	5250
1.0 wt%/Serum, 20 min	2.98	56.5	2.6	4.6	81	4.1×10^6	38.1	5110
1.0 wt%/Serum, 2 h	3.02	57.2	2.6	4.6	81	4.1×10^6	30.6	4100
5.0 wt%	1.73	32.8	3.7	6.5	285	1.5×10^7	34.6	4640
QD-585[c]/water	1.3	24.3	5.7	10	—	3.1×10^5	122	16 300

[a] τ_d is the diffusion (correlation) time; size – the estimated hydrodynamic diameter of NPs; number – the number of NPs per focal volume; Conc. – the estimated molar concentration of NPs; ε – the molar extinction coefficient of dyes and NPs; brightness/TMR – two-photon brightness of single NPs divided by that of TMR in water; $\sigma^2\eta^2$ – the two-photon action cross-section. [b] Data from elsewhere.[59] [c] Extinction coefficient data at 532 nm are given by the manufacturer (Life Technologies). Incubation with 10% serum was done at rt. Two-photon excitation at 830 nm, 10 mW was used.

at 830 nm (Fig. S3†), which suggests that at this wavelength region our LR-doped NPs will be even more efficient.

As we showed recently, FCS allows also monitoring the leakage (or leaching) of dyes from NPs into biological media, such as serum.[23] Indeed, the leaching of the dye from NPs drastically decreases their brightness and increases the number of fluorescent species in solution. Here, using FCS, we evaluated the leakage of LR from the NPs into serum, which is a good acceptor medium for hydrophobic molecules. It can be seen that addition of 10 wt% serum changes neither the number of NPs nor their brightness even after 2 h incubation at room temperature (Table 2). This indicates that the NPs are stable in serum and no dye leaching into the medium is observed.

Cellular studies

The NPs that showed the most promising fluorescence characteristics, *i.e.* those loaded with 1 wt% LR, were further studied in cell cultures. These NPs were incubated with HeLa cells and then further imaged by confocal fluorescence microscopy. After 1 h incubation, NPs can be observed both inside the cells (red dots in Fig. 8A) and on the cell surface (yellow dots in Fig. 8A). After longer incubation times, such as 2 and 6 h (Fig. 8B and C), much larger quantities of NPs accumulate inside the cells, notably in perinuclear regions. This behavior is typical for cell internalization by endocytosis, a typical pathway for PLGA NPs.[17,60] Being used at very low concentrations, *i.e.* 0.1 nM corresponding to 8 nM dye concentration, these NPs show high signal to noise ratio as a result of their high brightness. The low background signal also suggests the absence of dye leaching from the NPs into the cellular medium, in line with our FCS data in serum.

Finally, according to the MTT assay, PLGA nanoparticles loaded with PDI-1 and LR do not show any sign of cytotoxicity in a broad concentration range (Fig. 9). Even at concentrations >100-times larger than that used for imaging, the cell viability is the same as for non-treated cells. This is not surprising, as PLGA is a non-toxic polymer approved by FDA. Moreover, the

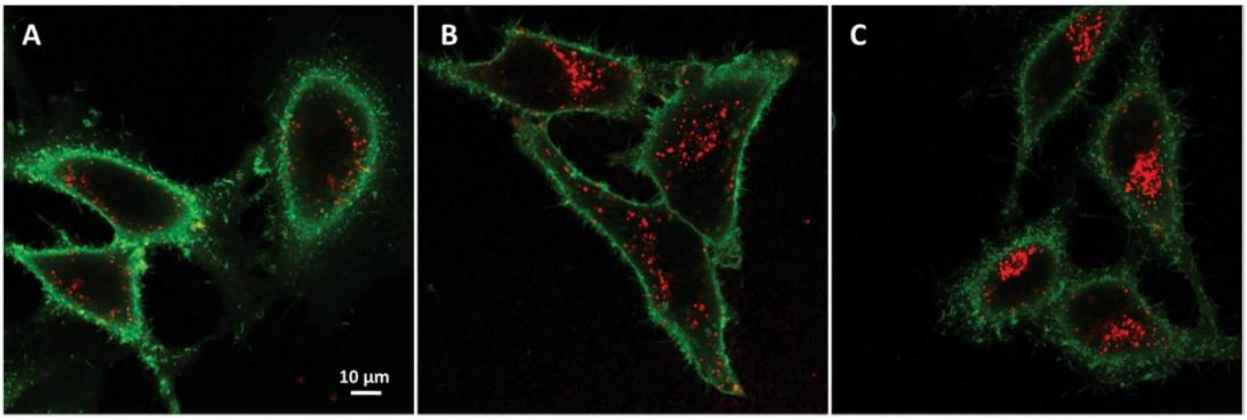

Fig. 8 Confocal fluorescence imaging of dye-doped NPs in HeLa cells. Micrographs of HeLa cells cultured for 1 (A), 2 (B) and 6 (C) h in the presence of 1 wt% LR NPs and for 10 min in the presence of wheat germ agglutinin-Alexa488 for labeling cell membranes.

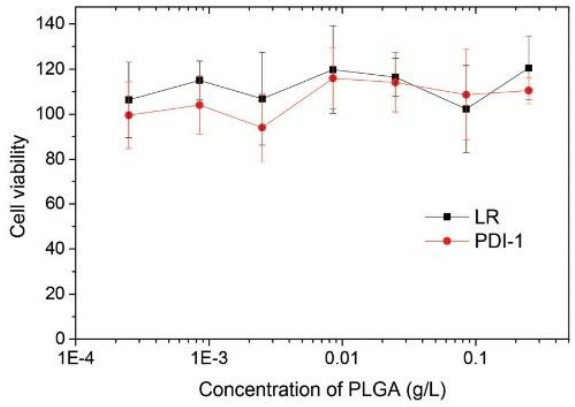

Fig. 9 Cytotoxicity of dye-doped NPs in HeLa cells. MTT viability studies of HeLa cells exposed for 24 h to different concentrations of PLGA NPs loaded with 1 wt% LR or PDI-1. The highest concentration of the 1 wt% NPs corresponds to 2 μM concentration of the dye, that is >100-fold larger than the highest concentration used for cellular imaging.

dyes used are perfectly encapsulated inside the PLGA and there are no reports in the literature on the cytotoxicity of PDI derivatives. Thus, our NPs appear well suited for cellular imaging.

Conclusions

In the present work, perylene diimide derivatives were encapsulated into PLGA NPs of 40 nm size. One PDI derivative bears bulky hydrophobic groups at the imide region, while the other is substituted with these groups in both imide and bay regions (Lumogen Red). Encapsulation of the former resulted in its strong aggregation even at low dye loading (>0.02 wt%), which was accompanied by modulation of its emission color from green to red and a decrease in its fluorescence quantum yield. Remarkably, aggregation of this dye induced a significant drop in its photostability, which is an unexpected phenomenon for perylene diimides. In contrast, Lumogen Red showed minimal aggregation inside polymer NPs together with high fluorescence quantum yield and photostability. The 40 nm PLGA NPs loaded with 1 wt% Lumogen Red were >10-fold brighter than quantum dots (QD-585). They were further shown to be stable in serum and live cells without signs of dye leaching and cytotoxicity. Due to their excellent brightness and photostability, the obtained NPs could be considered as new organic substitutes of quantum dots, which could find a number of applications in biological imaging.

Acknowledgements

We thank Pascal Didier and Frédéric Przybilla for help with single-particle measurements and Ludovic Richert for help with FCS measurements. Heinz Langhals is acknowledged for providing an analogue of PDI-1. This work was supported by CNRS, Université de Strasbourg and ANR JCJC (ANR-11-JS07-014-01).

Notes and references

1 M. E. Davis, Z. Chen and D. M. Shin, *Nat. Rev. Drug Discovery*, 2008, **7**, 771–782.
2 X. Michalet, F. F. Pinaud, L. A. Bentolila, J. M. Tsay, S. Doose, J. J. Li, G. Sundaresan, A. M. Wu, S. S. Gambhir and S. Weiss, *Science*, 2005, **307**, 538–544.
3 T. Trindade, P. O'Brien and N. L. Pickett, *Chem. Mater.*, 2001, **13**, 3843–3858.
4 S. Bonacchi, D. Genovese, R. Juris, M. Montalti, L. Prodi, E. Rampazzo and N. Zaccheroni, *Angew. Chem., Int. Ed.*, 2011, **50**, 4056–4066.
5 M. Montalti, L. Prodi, E. Rampazzo and N. Zaccheroni, *Chem. Soc. Rev.*, 2014, **43**, 4243–4268.
6 A. Kaeser and A. P. H. J. Schenning, *Adv. Mater.*, 2010, **22**, 2985–2997.
7 E. Genin, Z. Gao, J. A. Varela, J. Daniel, T. Bsaibess, I. Gosse, L. Groc, L. Cognet and M. Blanchard-Desce, *Adv. Mater.*, 2014, **26**, 2258–2261.
8 A. S. Klymchenko, *J. Nanosci. Lett.*, 2013, **3**, 21.
9 J. Geng, Z. Zhu, W. Qin, L. Ma, Y. Hu, G. G. Gurzadyan, B. Z. Tang and B. Liu, *Nanoscale*, 2014, **6**, 939–945.
10 D. K. Bwambok, B. El-Zahab, S. K. Challa, M. Li, L. Chandler, G. A. Baker and I. M. Warner, *ACS Nano*, 2009, **3**, 3854–3860.
11 C. Wu, B. Bull, C. Szymanski, K. Christensen and J. McNeill, *ACS Nano*, 2008, **2**, 2415–2423.
12 A. Kumari, S. K. Yadav and S. C. Yadav, *Colloids Surf., B*, 2010, **75**, 1–18.
13 F. Danhier, E. Ansorena, J. M. Silva, R. Coco, A. Le Breton and V. Préat, *J. Controlled Release*, 2012, **161**, 505–522.
14 R. A. Jain, *Biomaterials*, 2000, **21**, 2475–2490.
15 A. M. Breul, M. D. Hager and U. S. Schubert, *Chem. Soc. Rev.*, 2013, **42**, 5366–5407.
16 A. Wagh, S. Y. Qian and B. Law, *Bioconjugate Chem.*, 2012, **23**, 981–992.
17 A. Reisch, P. Didier, L. Richert, S. Oncul, Y. Arntz, Y. Mély and A. S. Klymchenko, *Nat. Commun.*, 2014, **5**, 4089.
18 A. Wagh, F. Jyoti, S. Mallik, S. Qian, E. Leclerc and B. Law, *Small*, 2013, **9**, 2129–2139.
19 M. Kasha, H. R. Rawls and M. A. El-Bayoumi, *Pure Appl. Chem.*, 1965, **11**, 371–392.
20 Y. N. Hong, J. W. Y. Lam and B. Z. Tang, *Chem. Soc. Rev.*, 2011, **40**, 5361–5388.
21 F. Wurthner, T. E. Kaiser and C. R. Saha-Moller, *Angew. Chem., Int. Ed.*, 2011, **50**, 3376–3410.
22 V. N. Kilin, H. Anton, N. Anton, E. Steed, J. Vermot, T. F. Vandamme, Y. Mely and A. S. Klymchenko, *Biomaterials*, 2014, **35**, 4950–4957.
23 A. S. Klymchenko, E. Roger, N. Anton, H. Anton, I. Shulov, J. Vermot, Y. Mely and T. F. Vandamme, *RSC Adv.*, 2012, **2**, 11876–11886.

24 Z. Chen, A. Lohr, C. R. Saha-Möller and F. Würthner, *Chem. Soc. Rev.*, 2009, **38**, 564–584.
25 B. K. An, S. K. Kwon, S. D. Jung and S. Y. Park, *J. Am. Chem. Soc.*, 2002, **124**, 14410–14415.
26 S. Fery-Forgues, *Nanoscale*, 2013, **5**, 8428–8442.
27 X. Zhan, A. Facchetti, S. Barlow, T. J. Marks, M. A. Ratner, M. R. Wasielewski and S. R. Marder, *Adv. Mater.*, 2011, **23**, 268–284.
28 R. C. Savage, E. Orgiu, J. M. Mativetsky, W. Pisula, T. Schnitzler, C. L. Eversloh, C. Li, K. Müllen and P. Samorì, *Nanoscale*, 2012, **4**, 2387–2393.
29 A. W. Hains, Z. Liang, M. A. Woodhouse and B. A. Gregg, *Chem. Rev.*, 2010, **110**, 6689–6735.
30 W. E. Benjamin, D. R. Veit, M. J. Perkins, E. Bain, K. Scharnhorst, S. McDowall, D. L. Patrick and J. D. Gilbertson, *Chem. Mater.*, 2014, **26**, 1291–1293.
31 F. Würthner, *Chem. Commun.*, 2004, 1564–1579.
32 C. Kohl, T. Weil, J. Qu and K. Müllen, *Chem. – Eur. J.*, 2004, **10**, 5297–5310.
33 A. Margineanu, J. Hofkens, M. Cotlet, S. Habuchi, A. Stefan, J. Qu, C. Kohl, K. Müllen, J. Vercammen, Y. Engelborghs, T. Gensch and F. C. De Schryver, *J. Phys. Chem. B*, 2004, **108**, 12242–12251.
34 H. Langhals, *Helv. Chim. Acta*, 2005, **88**, 1309–1343.
35 H. Langhals, R. Ismael and O. Yürük, *Tetrahedron*, 2000, **56**, 5435–5441.
36 D. Görl, X. Zhang and F. Würthner, *Angew. Chem., Int. Ed.*, 2012, **51**, 6328–6348.
37 T. Weil, T. Vosch, J. Hofkens, K. Peneva and K. Müllen, *Angew. Chem., Int. Ed.*, 2010, **49**, 9068–9093.
38 M. Montalti, G. Battistelli, A. Cantelli and D. Genovese, *Chem. Commun.*, 2014, **50**, 5326–5329.
39 T. E. Kaiser, H. Wang, V. Stepanenko and F. Würthner, *Angew. Chem., Int. Ed.*, 2007, **46**, 5541–5544.
40 X. Zhang, Z. Chen and F. Würthner, *J. Am. Chem. Soc.*, 2007, **129**, 4886–4887.
41 S. Yagai, T. Seki, T. Karatsu, A. Kitamura and F. Wurthner, *Angew. Chem., Int. Ed.*, 2008, **47**, 3367–3371.
42 M. Sommer, S. Hüttner, S. Wunder and M. Thelakkat, *Adv. Mater.*, 2008, **20**, 2523–2527.
43 M. Sommer, A. S. Lang and M. Thelakkat, *Angew. Chem., Int. Ed.*, 2008, **47**, 7901–7904.
44 H. Wang, H. Xie, Y. Liang, L. Feng, X. Cheng, H. Lu and S. Feng, *J. Phys. Chem. C*, 2013, **1**, 5367–5372.
45 Z. Chen, U. Baumeister, C. Tschierske and F. Würthner, *Chem. – Eur. J.*, 2007, **13**, 450–465.
46 K. A. Colby, J. J. Burdett, R. F. Frisbee, L. Zhu, R. J. Dillon and C. J. Bardeen, *J. Phys. Chem. A*, 2010, **114**, 3471–3482.
47 S. Y. Wang, D. A. Borca-Tasciuc and D. A. Kaminski, *J. Appl. Phys.*, 2011, **109**, 074910.
48 M. G. Hyldahl, S. T. Bailey and B. P. Wittmershaus, *Sol. Energy*, 2009, **83**, 566–573.
49 S. Demmig and H. Langhals, *Chem. Ber.*, 1988, **121**, 225–230.
50 H. Langhals, S. Demmig and T. Potrawa, *J. Prakt. Chem.*, 1991, **333**, 733–748.
51 R. A. Velapoldi and H. H. Tønnesen, *J. Fluoresc.*, 2004, **14**, 465–472.
52 N. L. Thompson, in *Topics in Fluorescence Spectroscopy Techniques*, ed. J. R. Lakowicz, Plenum Press, New York, 1991, vol. 1, p. 337.
53 X. Zhang, D. Görl, V. Stepanenko and F. Würthner, *Angew. Chem., Int. Ed.*, 2014, **53**, 1270–1274.
54 M. Kumar and S. J. George, *Nanoscale*, 2011, **3**, 2130–2133.
55 F. C. De Schryver, T. Vosch, M. Cotlet, M. Van Der Auweraer, K. Müllen and J. Hofkens, *Acc. Chem. Res.*, 2005, **38**, 514–522.
56 E. Haustein and P. Schwille, *Annu. Rev. Biophys. Biomol. Struct.*, 2007, **36**, 151–169.
57 S. Doose, J. M. Tsay, F. Pinaud and S. Weiss, *Anal. Chem.*, 2005, **77**, 2235–2242.
58 D. R. Larson, W. R. Zipfel, R. M. Williams, S. W. Clark, M. P. Bruchez, F. W. Wise and W. W. Webb, *Science*, 2003, **300**, 1434–1436.
59 J. Mütze, V. Iyer, J. J. MacKlin, J. Colonell, B. Karsh, Z. Petrášek, P. Schwille, L. L. Looger, L. D. Lavis and T. D. Harris, *Biophys. J.*, 2012, **102**, 934–944.
60 G. Sahay, D. Y. Alakhova and A. V. Kabanov, *J. Controlled Release*, 2010, **145**, 182–195.

Electronic Supplementary Material (ESI) for Nanoscale.

Supporting information

Tuning color and photostability of perylene diimides inside polymer nanoparticles: towards biodegradable substitutes of quantum dots

Kateryna Trofymchuk, Andreas Reisch, Ievgen Shulov, Yves Mély, and Andrey S. Klymchenko

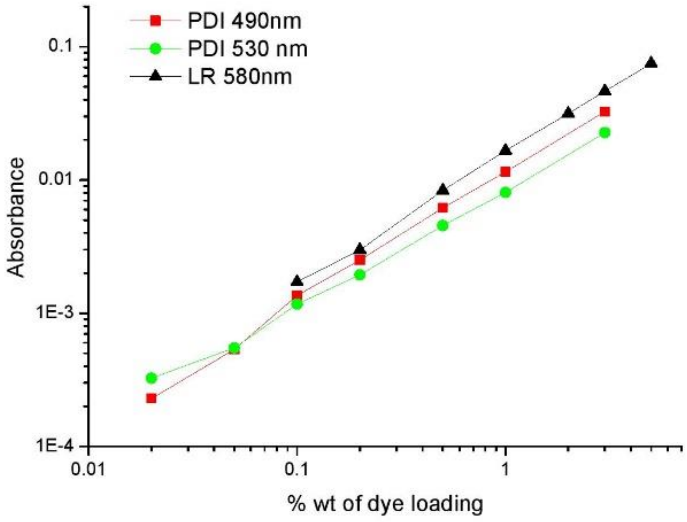

Figure S1. Absorbance at a given wavelength as a function of dye content in PLGA NPs.

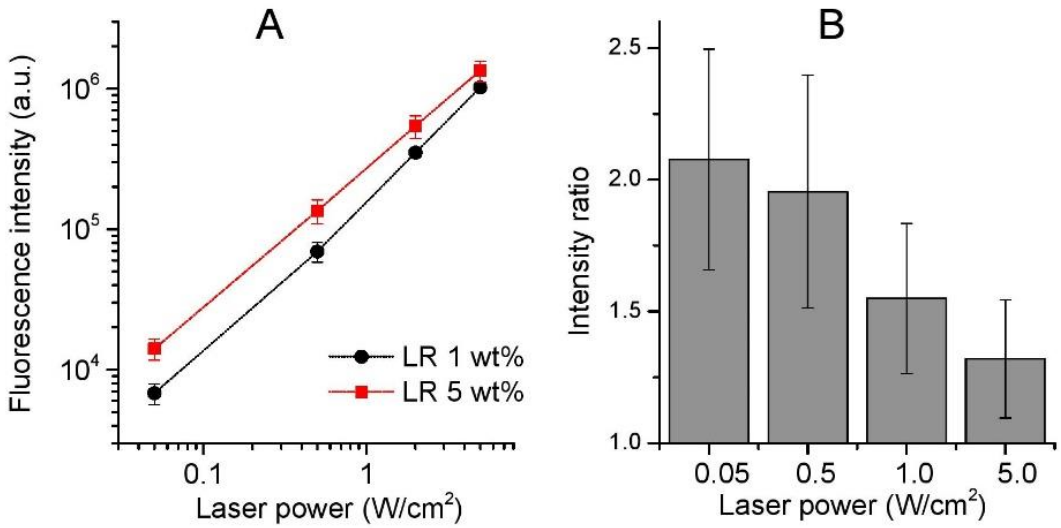

Figure S2. Fluorescence brightness dye-doped PLGA NPs loaded with 1 and 5 wt% LR and the intensity ratio of 5 to 1 wt% LR NPs at different illumination power.

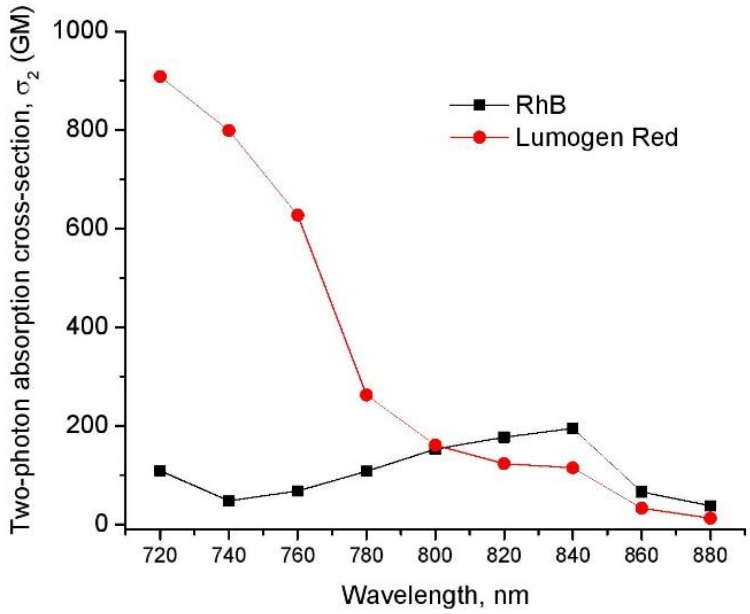

Figure S3. Two-photon absorption cross-section (GM, 10^{-50} cm^4 s photon^{-1}) of Lumogen Red (red circles) and reference dye Rhodamine B (black squares) in MeOH, as a function of the excitation wavelength. The experimental procedure and the data on rhodamine B are from ref. 1. The two-photon setup is described in the Materials and Methods section. The error is ±25%. The measurement assumes that the fluorescence quantum yield of Rhodamine B is 0.7 and for Lumogen Red is 1.0. The quadratic dependence of the intensity of dyes vs. two-photon excitation power was verified for optimal laser power conditions.

References

1. C. Xu and W. W. Webb, *J. Opt. Soc. Am. B*, 1996, **13**, 481–491.

2.1.2. Tailoring fluorescence and blinking in dye loaded NPs by polymer matrix

Spatial organization of fluorophore plays crucial role in governing excitation energy transfer (EET) processes. [90] Nature exemplifies this in the case of light harvesting complexes, capable of channeling light energy over tens of nanometers to the photosynthetic centers due to a finely controlled positioning of dyes. [124] The big achievement in the field of creation of artificial light-harvesting complexes was done by covalent linking of fluorophores in systems like dendrimers [174] or multiporphyrin complexes [175]. However, this requires long and precise synthesis, which ultimately limits the number of fluorophores that can be integrated in these systems.

Noncovalent interactions provide a much simpler (yet certainly much less precise) approach of controlling the organization of loading without time-consuming synthesis. Recently, our team reported creation of PLGA NPs loaded with salts of rhodamine B octadecylester (R18). Counterions were thought to act as spacers that prevent pi-pi stacking of the dyes, leading to aggregation and self-quenching. Encapsulation of 5 wt% salts R18 with F5-TPB (Figure 2.4) resulted in a strong decrease of self-quenching. At the same time, a collective on-off-switching of practically all the dyes in one particle led to an unprecedented whole NP blinking. This phenomenon was attributed to ultra-fast excitation energy migration between practically all the dyes in one particle. [170]

In present work, we investigated the influence of the polymer matrix, used to assemble dye-loaded NPs through nanoprecipitation, on their fluorescence properties, when the NPs were loaded with high amounts of dye salt, R18/F5-TPB, or a perylene diimide (PDI-1). PLGA, poly(methyl methacrylate-co-methacrylic acid) (noted PMMA here) and acid terminated polycaprolactone (PCL)) were chosen for this study due to their biodegradability/biocompatibility (Figure 2.4). In particular, we studied the collective behavior of the dyes within one NP and how these are linked to the organization of dyes. This approach is thus used to create ultrabright fluorescent nanoparticles with controlled dye organization and thus florescence properties, notably blinking.

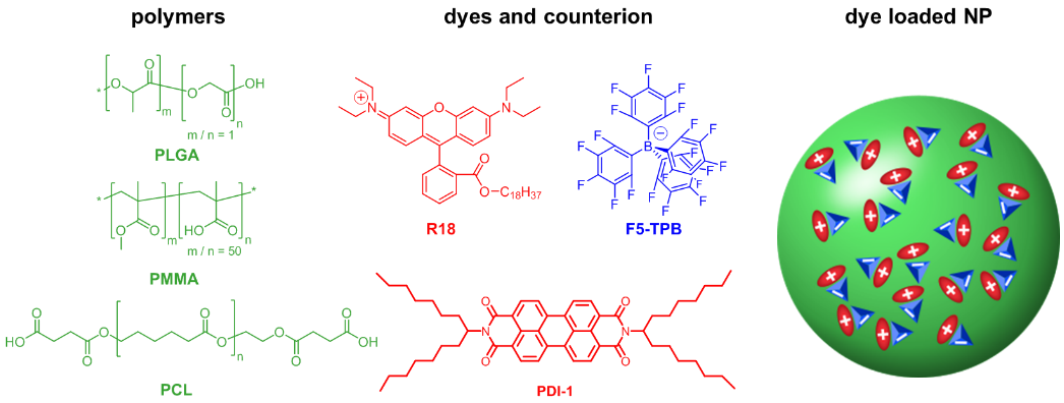

Figure 2.4. Structures of the polymers poly(lactic-co-glycolic acid) (PLGA), poly(methyl methacrylate-co-methacrylic acid) (noted PMMA here), and acid terminated polycaprolactone (PCL), of the dye rhodamine B octadecyl ester (R18) and its counterion tetrakis(pentafluorophenyl)borate (F5-TPB), and the dye PDI-1, used in this study, and schematic representation of a dye-loaded polymer nanoparticle.

Size and steady state fluorescence

Dye loaded NPs were obtained through nanoprecipitation of an acetonitrile solution of the polymer and the corresponding concentration of the dye salt R18/F5-TPB (expressed here as wt% relative to the polymer) in aqueous phosphate buffer. The sizes of the obtained NPs increased slightly for all three polymers with increasing dye loading (Figure 2.5 and Table 3) from around 26 nm for nonloaded NPs to about 33 nm for 30 wt% loading according to TEM. Interestingly, DLS data suggested a more pronounced difference between different polymers and depending on loading. Analysis of the TEM images suggests that this is due to the presence of a few bigger particles or aggregates (around 55 nm according to TEM), which have a pronounced effect on the size measured by DLS. Previous studies showed that encapsulation of the R18/F5-TPB dye-counterion pair was nearly quantitative in PLGA [81] and PMMA [176]. Therefore, we can estimate the mean number of dye molecules per NP (Table 2.1), which was on the order of 2200 to 2500 fluorophores per NP at the highest loadings.

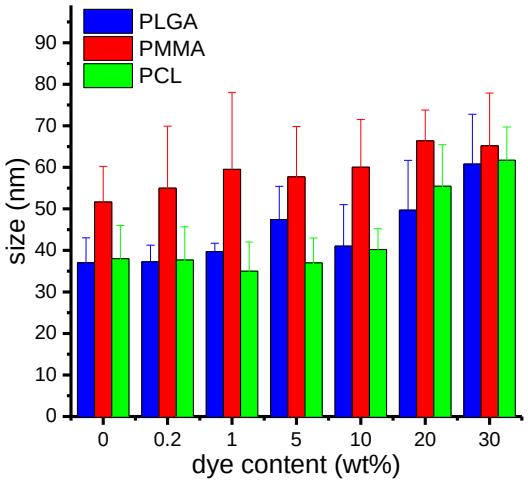

Figure 2.5. Size of NPs made from different matrix polymers as measured by DLS. Volume distribution averages are given, error bars correspond to standard error of mean over at least 3 independent measurements.

For these series of NPs we then measured the state absorption and fluorescence properties (Figure 2.6). In the case of PLGA NPs, increasing dye loading led to a blue shift of the absorption maximum, a broadening of the absorbance spectra, and an increase in the relative contribution of the short wavelength shoulder. There is notably a strong evolution of the spectrum when going from 0.2 to 1 wt% of dye loading. All these effects of dye loading were, though also observed, far less pronounced in the case of PMMA and especially PCL NPs, where the short wavelength shoulder became hardly more pronounced than for the dye in solution. The emission maxima showed a slight red shift with increasing dye loading, together with a reduction in the width of the spectra, most pronounced for PLGA.

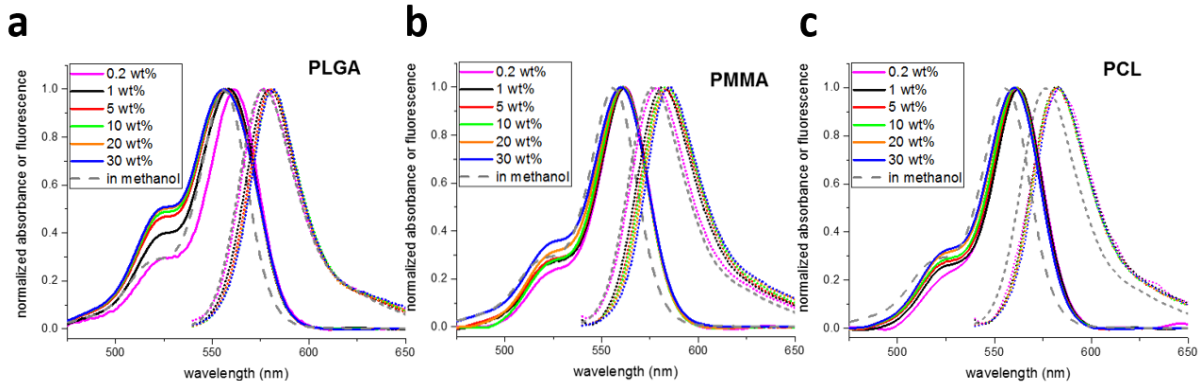

Figure 2.6. Normalized absorbance and emission spectra of a) PLGA, b) PMMA, and c) PCL NPs loaded with different amounts of R18/F5 and comparison to the spectra of R18/F5 in methanol. Emission spectra were recorded using an excitation at 530 nm.

In general, though the quantum yields (QYs) decreased with increasing dye loading they remained elevated even at high dye content (>20% in all cases for 20 wt%). For comparison, with inorganic counterion perchlorate, R18 showed QY value of 1% already at 5 wt% loading,[81] which demonstrates the efficiency of the use of the bulky fluorinated counterion F5 in decreasing aggregation caused quenching. For a given dye loading the QYs quantum yields increased in the following order PLGA < PCL < PMMA. Combining the measured QYs with the estimated number of fluorophores per NP and an extinction coefficient of 100,000 $M^{-1}cm^{-1}$ for the used rhodamine dye, the NP brightness could be calculated (Table 2.1).

Table 2.1. Mean size from TEM measurements, estimated number of dyes per NP, QY, and calculated particle brightness.

wt% dye	PLGA				PMMA				PCL		
	Size (nm)	N	QY	Brightness ($M^{-1}cm^{-1}$)	Size (nm)	N	QY	Brightness ($M^{-1}cm^{-1}$)	N	QY	Brightness ($M^{-1}cm^{-1}$)
0.2	27.6	10	0.75	7.7×10^5	25.8	8	1.02	8.5×10^5	8	1.02	8.4×10^5
1	30.0	62	0.55	3.6×10^6	29.8	61	0.87	5.6×10^6	51	0.79	4.3×10^6
5	32.5	392	0.41	1.7×10^7	33.8	444	0.72	3.4×10^7	331	0.65	2.3×10^7
10	34.1	906	0.35	3.4×10^7	34.4	933	0.67	6.7×10^7	777	0.57	4.7×10^7
20	34.7	1911	0.22	4.5×10^7	33.8	1771	0.41	7.7×10^7	1566	0.37	6.1×10^7
30	35.3	3020	0.10	3.3×10^7	33.2	2518	0.31	8.2×10^7	2368	0.34	8.6×10^7

The steady state brightness of these NPs thus increases continuously due to the increasing dye concentration and the high QYs even at high dye loadings. However, the decrease of the QYs levels off the increase above 20 wt% loading for PLGA. At the highest dye loadings studied here the values for PMMA and PCL NPs reached 0.8×10^8 $M^{-1}cm^{-1}$ corresponding to brightnesses 800 times higher than single fluorophores. Measuring photostability of these NPs in the fluorimeter revealed a strong difference in the behavior of NPs made from different polymers (Figure 2.7 b): for example for a 5 wt% loading PMMA NPs showed practically no decrease (<5%) in their fluorescence brightness over 1 h of illumination. PCL NPs showed a decrease in their fluorescence by about 25 % over 30 min, after that the fluorescence became stable. At this loading and illumination PLGA NPs, on the other hand, showed a strong decrease of the fluorescence by nearly 90 % over 1 h.

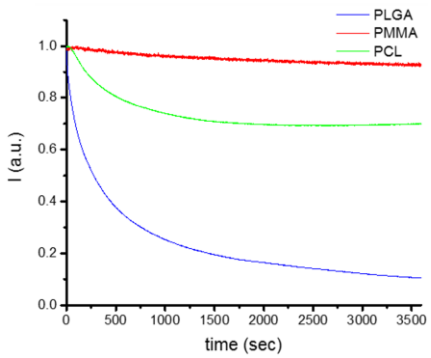

Figure 2.7. Photostability of NPs made from different polymers and loaded with 5 wt% of R18/F5-TPB.

Single particle fluorescence

The fluorescence of these three series of dye-loaded NPs was then studied on a single particle level. TIRF microscopy of particles adsorbed on a surface was used to access single particle brightness and fluorescence transients. At an excitation power of 0.5 W/cm^2 the single particle brightness increased initially strongly with dye loading for all three polymers, followed by a less strong increase at higher loadings (Figure 2.8 b). However, the detailed behavior differed again for the three polymers: PLGA NPs showed a relatively steep increase in brightness up to 1 wt%, and only a slight further increase by a factor of about 2. PMMA combined a strong initial increase up to 5 wt% with a further continuous increase, making PMMA NPs the brightest particles tested here. The brightness of PCL NPs increased less steeply with dye loading, but still relatively strongly up to 10 wt%. PCL NPs were thus less bright than PLGA NPs at low loading, but brighter at higher loadings. At a tenfold higher excitation power of 5 W/cm^2 the different NPs followed the same trends, but the brightness had a tendency to saturate at medium to high loadings. For example in the case of PMMA the brightness increased up to 10 wt% but then decreased upon further increase in the dye-loading. A better idea of the NP brightnesses can be obtained by comparing them to external standards: under the same measurement conditions the brightest PLGA, PMMA, and PCL NPs were, respectively, 2, nearly 5, and 3 times brighter than commercial FluoroSpheres of similar size (and 45, 90, and 75 brighter than corresponding QDs) (Figure 2.8 c).

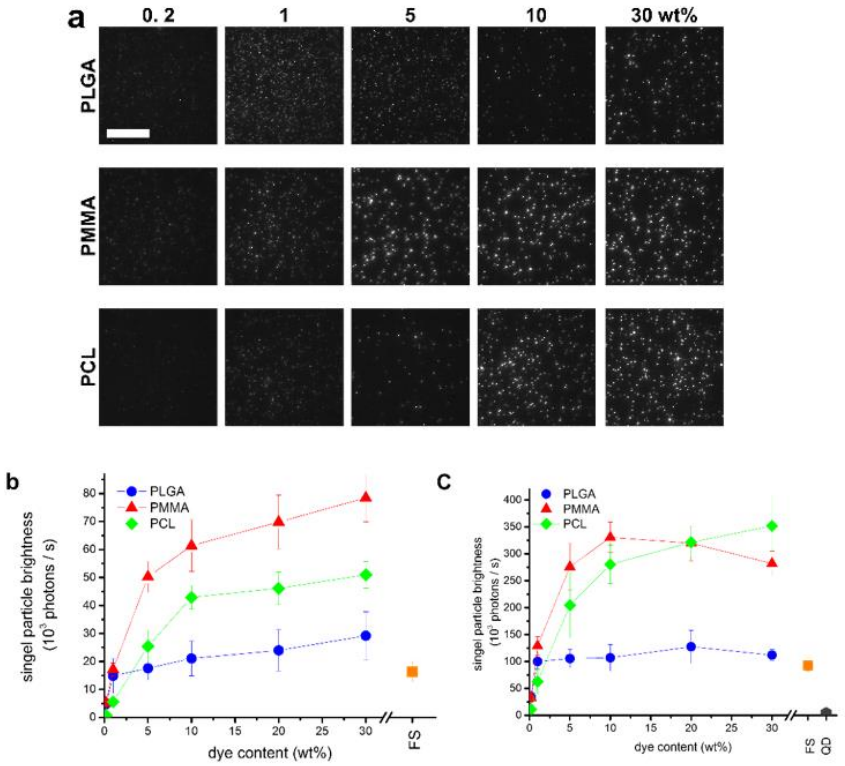

Figure 2.8. Single particle brightness of NPs made from different polymers and loaded with different amounts of R18/F5-TPB. **a)** Microscope images of NPs immobilized on a surface in TIRF mode using an illumination intensity of 0.5 W/cm^2. Scale bar corresponds to 20 µm. And brightness for at least 1000 particles as measured by TIRF microscopy using a 532 nm laser with an illumination intensity of **b)** 0.5 W/cm^2 and **c)** 5 W/cm^2

A still more remarkable difference between the NPs made from different polymers appeared when the fluorescence signal of single NPs was recorded as a function of time (Figure 2.9). At very low dye loading all three types of NPs showed a practically constant fluorescence. However, starting from 1 wt% of dye loading virtually all PLGA NPs showed a practically complete whole particle blinking, in line with our previous report. [170] With increasing dye loading the duration of on-state decreased, so that the on-to-off-time ratio decreased. At the very high dye loadings (starting from 20 wt%, but especially at 30 wt%) the blinking was not complete anymore, and the PLGA NPs remained partially on, with spikes of higher fluorescence intensity. For both PMMA and PCL NPs the behavior was very different: these NPs showed a constant fluorescence at 1 wt% dye loading, and no cases of particle blinking were observed. At 5 wt% loading these NPs did not show blinking either, though in many cases a stepwise modulation of the fluorescence intensity was observed. However, these

intensity modulations did not exceed 20 % of the fluorescence intensity. A further increase of the loading to 10 wt% led to an increase of the amplitude of the stepwise modulations and a decrease of their durations. In other words, a particle blinking appeared, but rather than showing a complete on-off-switching, the blinking was superimposed on a constant fluorescence signal from the particles. The blinking amplitude increased further with increasing loading for PMMA and PCL NPs and at 30 wt% dye loading especially many PMMA particles showed a practically complete on-off-blinking.

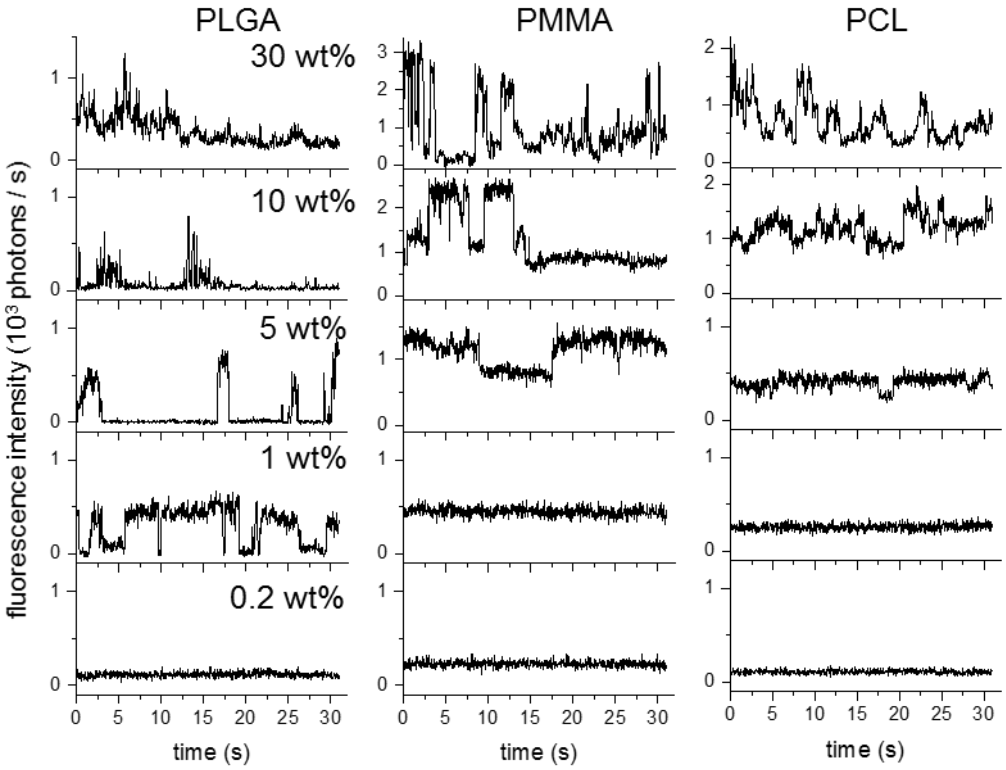

Figure 2.9. Single particle transients of NPs made from different polymers with different amounts of R18/F5-TPB. Given are representative transients as measured using TIRF microscopy using a 532 nm laser with an illumination intensity of 0.5 W/cm^2.

These differences in the particle behavior can also be seen from the projections of the instantaneous single particle brightness (Figure 2.10). In summary, while complete whole particle blinking appeared for PLGA NPs at 1 wt% of dye loading, and an increase in the loading mainly led to a decrease of the on-to-off time ratio of PLGA NPs, in the case of PMMA and PCL NPs the fluorescence was continuous at low to

medium dye loadings. For these NPs an increase in loading led then to an increase in blinking amplitude and a decrease in the on-to-off time ratio.

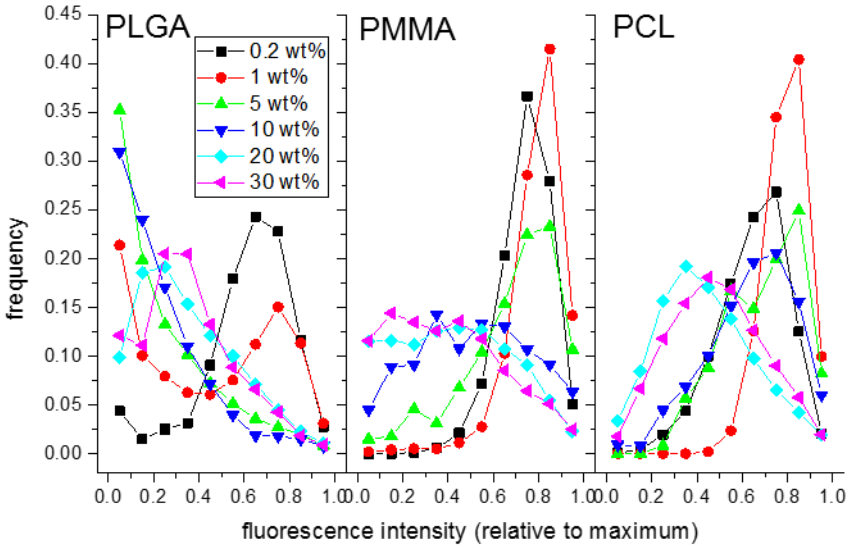

Figure 2.10. Histograms of the instantaneous fluorescence intensities (relative to the maximum intensity) of NPs with different dye loadings. Intensities were obtained from single particle transients recorded with TIRF microscopy using a 532 nm laser with an illumination intensity of 0.5 W/cm^2. About 500 NPs per condition were used.

Fluorescence anisotropy and Förster resonance energy transfer

To understand the observed differences further, we studied the fluorescence anisotropy of these NPs (Figure 2.11). The steady state anisotropy decreased much faster with dye-loading for PLGA NPs than for PMMA and PCL NPs, especially in the region up to 1 wt%. At this loading the anisotropy values were, respectively, 0.01, 0.04, and 0.06 for PLGA, PMMA, and PCL NPs. A further increase in the loading to 10 wt% resulted in anisotropies of 0.001 for PLGA and 0.003 for PMMA and PCL. Lifetime anisotropy measurements showed that at 1 wt% of dye loading PLGA NPs experienced a very fast initial anisotropy decrease with a decay time of less than 20 ps, which is below the resolution of the instrument, followed by a plateau corresponding to a residual anisotropy of 0.025. For PMMA and PCL NPs at the same dye loading, the decays are much slower and well described with stretched exponentials:

$$r(t) = r_0 \cdot \exp\left(-\left(\frac{t}{\tau}\right)^b\right) + r_\infty$$

having decay times τ of, respectively, 180 and 300 ps and a stretching exponent b of 0.5. In both cases the residual anisotropy r_∞ was about 0.025, but this plateau value was only reached after about 4 ns (versus 100 ps for the PLGA NPs). At a dye loading of 5 wt% the decays were very fast for all 3 types of NPs. Again the decay time for PLGA NPs was, with less than 20 ps, below the resolution of the instrument. The decay times of PMMA and PCL NPs at this loading were somewhat longer, and, assuming a stretched exponential, of the order of 20 ps, i.e. at the limit of the time resolution. Already after less than 100 ps for PLGA and 200 ps for the other two polymers plateaus were reached corresponding to a residual anisotropy close to zero in all three cases (about 0.001 ± 0.001).

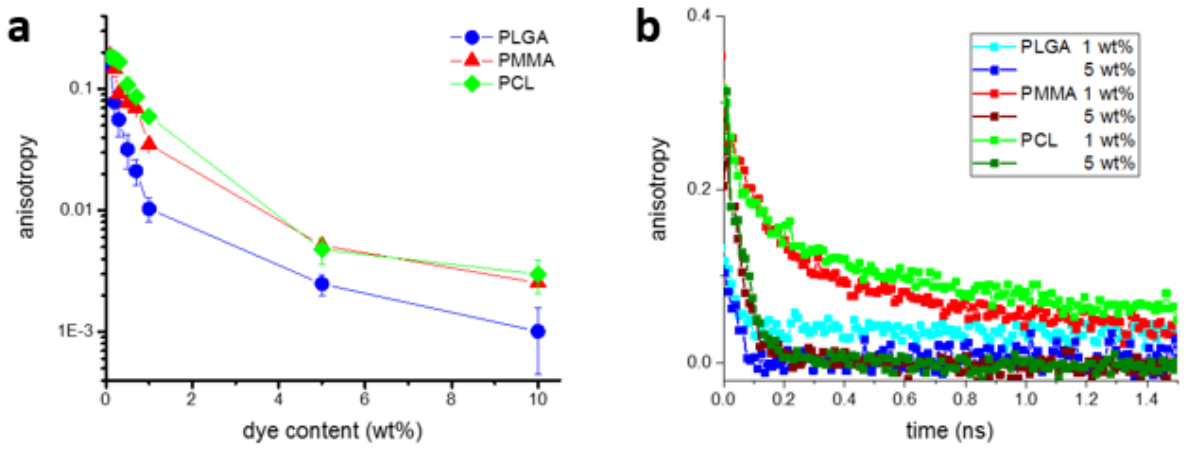

Figure 2.11. Fluorescence anisotropy of NPs. **a)** Steady state fluorescence anisotropy of nanoparticles made from different polymers and loaded with different amounts of R18/F5-TPB (λ_{ex} = 530 nm). Given values are averages over at least 3 measurements, error bars correspond to standard error of mean. **b)** Anisotropy decays of nanoparticles made from different polymers and loaded with 1 or 5 wt% of R18/F5-TPB.

In the cases of our dye-loaded NPs, the dyes are thought to be immobilized in the polymer matrix, and the rotational correlation times of objects of the size of our NPs are of the order of hundreds of ns. In consequence, the decrease in the fluorescence emission anisotropy in these systems is thought to be mainly due to the transfer of excitation energy between the fluorophores. Comparison of the different polymer NPs with respect to their steady state anisotropy thus suggests that this energy transfer is the most effective or/and fast in the case of PLGA particles. As the fluorophores are identical in the three systems, this could in turn be attributed to smaller inter-fluorophore distances in PLGA NPs compared to PMMA and PCL. The

lifetime anisotropy measurements, showed, indeed, that the anisotropy decay is much faster in PLGA NPs than in PMMA and PCL NPs loaded with 1 wt% of dye salt, which means that the energy transfer is faster in the former. The residual anisotropy obtained in these experiments can be used to estimate the mean number of fluorophores involved in energy transfer N according to

$$N = \frac{r_0}{r_\infty}$$

where r_0 is the fundamental anisotropy (0.37 for rhodamine) and r_∞ is the residual anisotropy. For all three types of NPs the residual anisotropy is of the order of 0.02, corresponding to several tens of fluorophores involved in energy transfer, which is close to the mean number of fluorophores per NP (see Table 2.1). An increase of the dye loading to 5 wt% results in an increase of the speed of the anisotropy decay for PMMA and PCL NPs, which can be attributed to an increase of the speed of energy transfer between the fluorophores. Though the decay time was still shorter for PLGA NPs than for PMMA and PCL NPs, the difference at higher dye loadings is not evident as the decay time is again below the resolution of the instrument. The residual anisotropies suggest that at 5 wt% hundreds of fluorophores are involved in energy transfer in all three cases.

Förster theory allows estimating the expected anisotropy decay times for a given concentration of randomly distributed fluorophores according to:

$$\tau_a = 0.0508 \frac{\tau_0}{R_0^6 C^2}$$

where τ_0 is the fluorescence lifetime in the absence of transfer (3.5 ns for R18/F5-TPB at 0.2 wt%), R_0 is the Förster radius for homo transfer (about 5.5 nm at 1 wt%), which can be calculated from the spectral data, and C is the concentration in molecules per nm^3. The theoretical values are thus 340 ps at 1 wt% and 15 ps at 5 wt%. Comparison of these theoretical values with the experimental decay times shows good agreement for PCL NPs (300 ps and ~20 ps at 1 and 5 wt%, respectively) and reasonable agreement for PMMA (180 ps and ~20 ps). However, in the case of PLGA the experimental decay time for 1 wt% is with less than 20 ps far below the theoretical estimation of 300 ps. The obtained decay time for this case would rather correspond to a fivefold higher fluorophore concentration, and suggests again smaller inter-fluorophore distances in the case of PLGA than what would be expected for a random distribution. In contrast the good agreement between theory and experiment suggests

a nearly random distribution of the fluorophores in the PCL NPs and an only slightly disturbed distribution in PMMA NPs at least up to 5 wt% loading.

NPs loaded with perylene diimide

We then wanted to know whether the described phenomenon of polymer directed organization of the load is unique for the studied dye/counterion system or is an inherent property of the polymer NPs studied. We hence used uncharged dye from the perylene diimide family, N,N′-Bis(1-heptyloctyl)-3,4,9,10-perylenebis-(dicarboximide) (PDI-1, Figure 2.4), known to undergo characteristic spectral shifts upon aggregation. Upon loading increasing amounts of PDI-1 into PLGA NPs an increasing deviations of the absorbance spectra relative to that of PDI-1 in dioxane were observed (Figure 2.12), as reported previously. [177] In particular, the height of the peak at 530 nm decreased relative to the shorter wavelength maximum at 490 nm. At the same time the fluorescence spectra showed the appearance of a broad, red-shifted band at about 650 nm that increased strongly with dye loading (Figure 2.12). Similar variations of absorbance and emission spectra have been reported for aggregates formed by other PDI and naphthalene diimides with similar structure, and were hence interpreted as signs of aggregation. When loading PDI-1 into PMMA based NPs these spectral variations were much less pronounced at the same dye loadings (Figure 2.12). In the case of PDI-1 loaded PCL NPs both the change in the relative intensities of the peaks in the absorbance spectra and the appearance of the emission band at 650 nm were virtually absent up to a dye loading of 1 wt%. At the same time the QYs of PDI-1 in these systems decreased much faster in the case of PLGA NPs than for PMMA and PCL NPs (Figure 2.12). Together these results indicate that the aggregation state of PDI-1 inside NPs depends on the matrix polymer, with strong aggregation taking place in PLGA even at very low loading, much less aggregation occurring in PMMA and practically no aggregation in PCL at the studied loadings. The observed aggregation behavior of PDI-1 as a function of polymer matrix is similar to that observed for the rhodamine ion pair R18/F5-TPB. This means in turn that the control of dye aggregation through the nature of the polymer is a more general phenomenon.

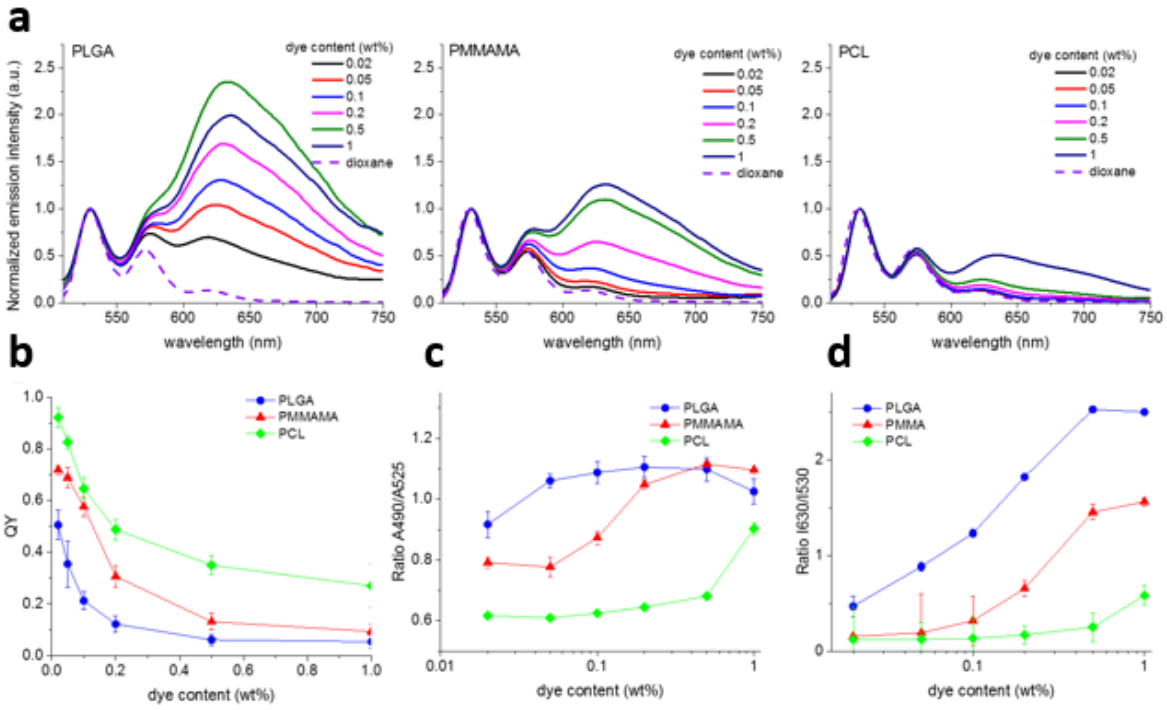

Figure 2.12. Absorption and emission properties of PDI-1-loaded NPs made from different polymers: **a)** Normalized fluorescence emission spectra of NPs of different polymers, containing different amounts of PDI-1 and comparison to PDI-1 in dioxane. (Normalization has been performed relative to the peak at 530 nm). **b)** QYs of NPs made from different polymers and loaded with different amounts of PDI-1. QYs were determined relative to Rh6G in ethanol as standard. Given values are averages over at least 3 measurements, error bars correspond to standard error of mean. **c)** Ratio of absorbance of these NPs at 490 nm and 525 nm. **d)** Ratio of fluorescence emission of these NPs at 630 nm and 530 nm

Polymers and precipitation

Formation of NPs through nanoprecipitation is a kinetically controlled process. We supposed, hence, that differences in the speed of NP formation by the three polymers could be at the origin of the observed differences in organization of the encapsulated compounds in the NPs. One important parameter in the kinetics of particle formation is the supersaturation of the polymer in acetonitrile-water mixture, forming after mixing of the two phases. Both nucleation and growth speed increase with increasing supersaturation. Assuming that the interdiffusion of the two phases does not depend on the nature of the polymer, this supersaturation should essentially depend on the solubility of the polymers in mixtures of acetonitrile and water. In order to evaluate these we performed turbidity studies of the polymers by adding increasing amounts of water to solutions of the polymers in acetonitrile (Figure 2.13).

Interestingly, turbidity for PCL appeared at the lowest water fraction, followed by PMMA, and finally PLGA. This indicates that, in such mixtures, the solubility of these polymers increases from PCL over PMMA to PLGA, in good agreement with increasing polarity of these polymers. It in turn suggests that during the fast mixing process supersaturation should be highest for PCL, leading to the highest particle formation speed.

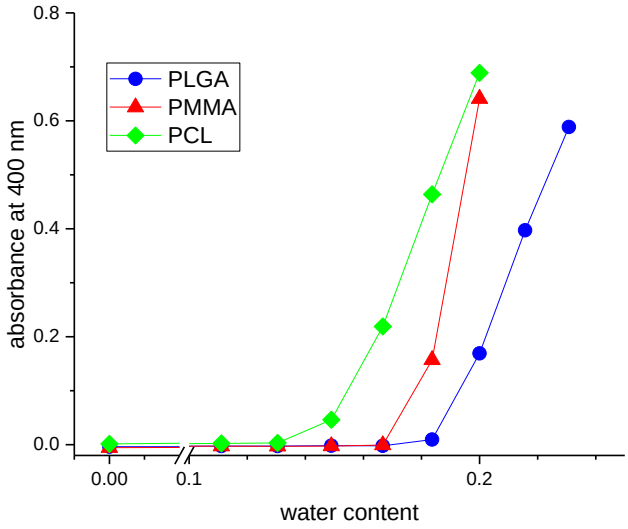

Figure 2.13. Turbidity measurement of different polymers in acetonitrile water mixtures. Given are the absorbance values measured at 400 nm for polymer solutions in acetonitrile with different water contents.

These differences could hence be at the origin of the differences of organization of the load inside the polymer NPs. In the case of fast particle formation the dye could simply be captured during the particle growth according to its distribution in solution, which would then lead to a homogeneous distribution of the load within the particle, as observed for PCL and PMMA. In the case of slower particle formation the load could have the time to embed into the forming nuclei at the very beginning of the particle growth. It could also form the nuclei itself or at least participate in their formation and thus initiate particle formation. Both scenarios could explain the formation of NPs having a core with very high concentration of the load and an outer part containing virtually no load. It remains, however very challenging to follow the formation of the particles directly. It is also possible that the organization takes place through migration of the load within the NPs. It would then depend on the mobility inside the polymer,

which is strongly influenced by the state of the polymer: PLGA and PMMA are both in there glassy state at the employed temperature, however, transition temperature of PLGA is about 60 °C, which is much lower than that of PMMA (about 100 °C). PCL, on the other hand, is a semicrystalline polymer with a melting temperature of about 60 °C.

Obtained results confirmed the polymer matrix-controlled dye organization and thus florescence properties. This enables preparation of ultrabright fluorescent NPs with tuned photostability and cooperative properties, notably blinking.

2.2. Design of efficient FRET inside polymer NPs

To obtain efficient FRET inside polymer NPs with size larger than Förster distance R_0, two strategies can be applied. First is loading of NPs with high quantity of both donor (D) and acceptor (A) molecules (usually ratio D to A ratio~1). [101, 104] Alternatively, NPs with high donor dye cooperativity (high EET) could be used, which should require much lower amount of acceptor (high D to A ratio).

As it was shown previously, PLGA-based NPs demonstrated favorable for EET organization of dyes (small inter-fluorophore distances) [81]. This suggested the possibility of efficient FRET inside NPs from multiple donors to single acceptors. We used EET inside polymer NPs loaded with huge amount of donor dyes (R18/F5-TPB) to create systems with efficient photoswitching through FRET and nano-antennas for the amplification of a single acceptor molecule emission.

2.2.1. Article 2: "Exploiting Fast Exciton Diffusion in Dye-Doped Polymer Nanoparticles to Engineer Efficient Photoswitching"

Possibility of tuning emission properties has numerous applications in the field of fluorescent bioimaging with superior resolution. [178] Photoswitchable NPs can be advantageous over molecular photochromic systems like dyads, which require multistep synthesis and have limited brightness and photostability.

We hypothesized that fast EET inside PLGA NPs [81] could be exploited to drive the photoswitching efficiency of dye-loaded polymer. To this end, we coencapsulated rhodamine B dye salt with four different bulky hydrophobic counterions as well as a photochromic acceptor of the diarylethene family into PLGA NPs (Figure 2.14).

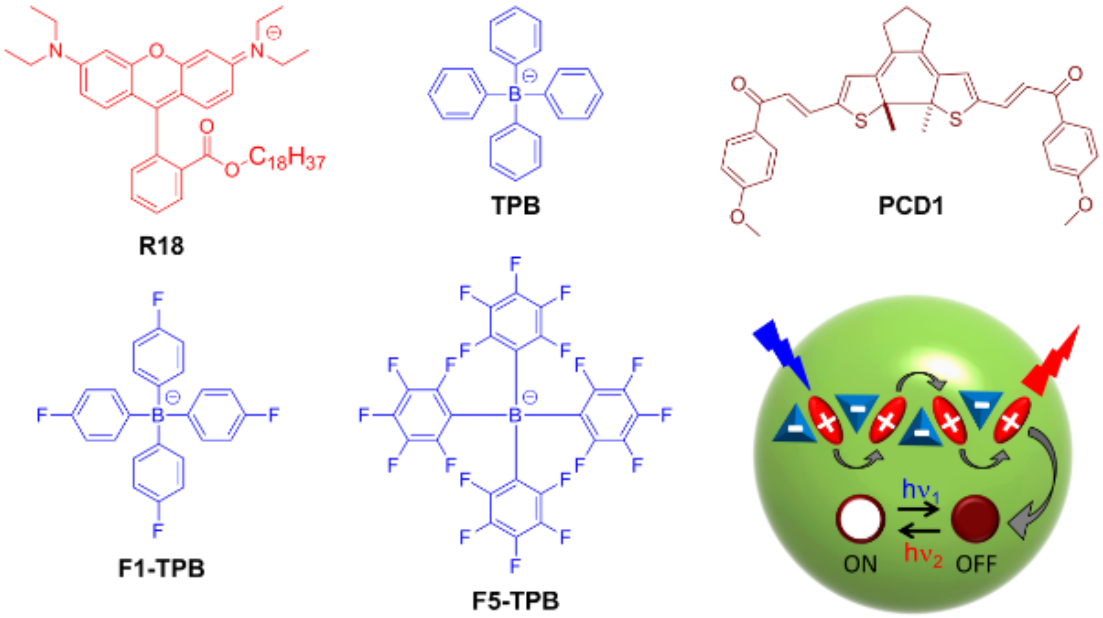

Figure 2.14. Chemical structure of the encapsulated fluorescent dye (R18) with different bulky counterions and the photochromic dye (PCD1), and schematic presentation of photoswitching concept in dye-doped NPs. Small grey arrows show the exciton diffusion, while the large grey arrow presents FRET to a photochromic dye (brown). Filled and open brown circles correspond to the closed and open forms of PCD1, respectively. Chemical structure of the closed form of PCD1 is shown only.

Among tested counterions, only perfluorinated tetraphenylborate enables high photoswitching efficiency (on/off ratio ~20), while for all other counterions, the switching efficiency was much lower (Figure 2.15 a).

To verify whether this effect of F5-TPB is linked with the exciton diffusion process (EET), we measured the steady-state fluorescence anisotropy of NPs with all

four counterions (Figure 2.15 b). When the energy migrates within encapsulated fluorophores that are randomly orientated inside the polymer matrix, the fluorescence anisotropy rapidly decreases after each step of energy hopping between dyes.[179] The perfect correlation between photoswitching efficiency of NPs and fluorescence anisotropy loss (i.e. EET efficiency) was observed (Figure 2.15).

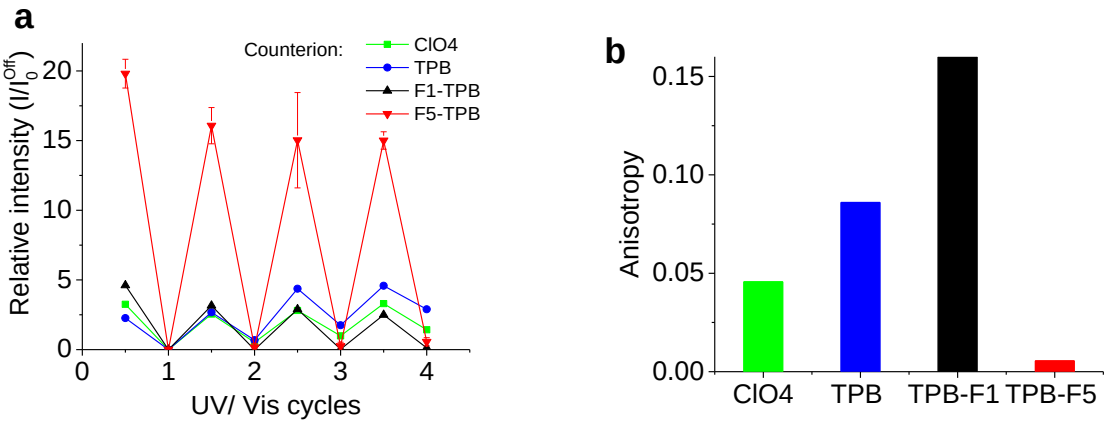

Figure 2.15. Correlation between photoswitching efficiency of NPs and fluorescence anisotropy of the encapsulated dyes .**a)** Variation of relative peak intensity under alternate irradiation of PLGA NPs loaded with 1 wt% of rhodamine R18 with different counterions and 0.3 wt% of photochromic dye PCD1.**b)** Fluorescence anisotropy of the encapsulated dyes NPs loaded with 1 wt% of rhodamine R18 with different counterions.

The performance of the new NPs was validated at the single particle level, where reversible photoswitching was demonstrated.

Our study shows that cooperative behavior of fluorophores inside NPs can ensure efficient FRET to the photochromic molecule producing highly efficient photoswitching. The proposed concept paves the way to new efficient photoswitchable nanomaterials.

The results were published in the article: Trofymchuk, K.; Prodi, L.; Reisch, A.; Mély, Y.; Altenhöner, K.; Mattay, J.; Klymchenko, A. S., “Exploiting Fast Exciton Diffusion in Dye-Doped Polymer Nanoparticles to Engineer Efficient Photoswitching”. The Journal of Physical Chemistry Letters 2015, 6 (12), 2259-2264.

The full description of the work can be found in the article enclosed below.

THE JOURNAL OF PHYSICAL CHEMISTRY Letters

Letter

pubs.acs.org/JPCL

Exploiting Fast Exciton Diffusion in Dye-Doped Polymer Nanoparticles to Engineer Efficient Photoswitching

Kateryna Trofymchuk,[†] Luca Prodi,[‡] Andreas Reisch,[†] Yves Mély,[†] Kai Altenhöner,[§] Jochen Mattay,[§] and Andrey S. Klymchenko*[,†]

[†]Laboratoire de Biophotonique et Pharmacologie, UMR 7213 CNRS, Université de Strasbourg, Faculté de Pharmacie, 74, Route du Rhin, 67401 Illkirch Cedex, France

[‡]Dipartimento di Chimica "Giacomo Ciamician", Università degli Studi di Bologna, via Selmi 2, 40126 Bologna, Italy

[§]Organic Chemistry I, Department of Chemistry, Bielefeld University, Universitätsstrasse 25, 33615 Bielefeld, Germany

Supporting Information

ABSTRACT: Photoswitching of bright fluorescent nanoparticles opens new possibilities for bioimaging with superior temporal and spatial resolution. However, efficient photoswitching of nanoparticles is hard to achieve using Förster resonance energy transfer (FRET) to a photochromic dye, because the particle size is usually larger than the Förster radius. Here, we propose to exploit the exciton diffusion within the FRET donor dyes to boost photoswitching efficiency in dye-doped polymer nanoparticles. To this end, we utilized bulky hydrophobic counterions that prevent self-quenching and favor communication of octadecyl rhodamine B dyes inside a polymer matrix of poly(D,L-lactide-*co*-glycolide). Among tested counterions, only perfluorinated tetraphenylborate that favors the exciton diffusion enables high photoswitching efficiency (on/off ratio ~20). The switching improves with donor dye loading and requires only 0.1−0.3 wt % of a diphenylethene photochromic dye. Our nanoparticles were validated both in solution and at the single-particle level. The proposed concept paves the way to new efficient photoswitchable nanomaterials.

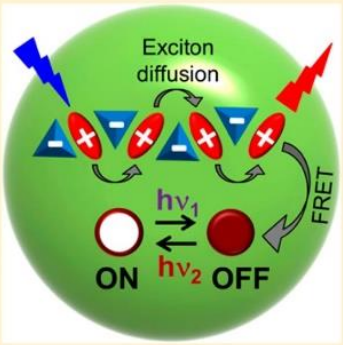

Photoswitchable fluorescence systems have gained growing attention because of numerous potential applications, particularly for fluorescence imaging with superior resolution.[1−4] Fluorescence switching requires coupling of the photoinduced chemical transformation with the fluorescence output.[5] This can be achieved with so-called photochromic dyes, where the light-induced chemical changes are associated with change of their optical properties.[6] Two approaches are used in this case. The first one exploits fluorescent photochromic dyes, which switch their fluorescence properties under light illumination.[7] Most common representatives are derivatives of spiropyran,[8] cyanine,[9,10] and some fluorescent proteins.[11,12] The second approach is to couple a fluorescent dye with a nonfluorescent photochromic dye, which operates as a FRET pair.[13] In this case, the photoisomerization of the photochromic dyes modulates the FRET efficiency and thus switches on/off the dye fluorescence.[14,15] This approach is more universal, as most of photochromic dyes are nonfluorescent, and their combination with fluorescent dyes enables access to any desired emission color associated with high fluorescence quantum yield. Photoswitchable FRET-based molecules work very well as the distance within a typical molecular dyad is much less than the Förster radius required for an efficient FRET. On the other hand, these systems present two limitations: (1) limited brightness of organic dyes and (2) multistep synthesis of the dyad, which makes these materials rather expensive. Both limitations could be overcome by the use of fluorescent nanoparticles (NPs). Indeed, they can be 10−100 times as bright as organic dyes, which opens new possibilities in fluorescence bioimaging. Second, using straightforward protocols, they can be readily prepared with an appropriate photochromic dye to achieve FRET-based photoswitching. However, as the fluorescent particles are usually >5 nm large, the distance between the particle donor and the photochromic acceptor can exceed the Förster distance and thus decrease the FRET efficiency.

The most developed fluorescent NPs are quantum dots,[16] dye-doped silica NPs,[17] and organic NPs.[18,19] In the past decade, significant efforts have been made to make these NPs photoswitchable.[20] To achieve efficient switching, quantum dots were covered with multiple photochromic acceptors within the particle organic shell.[21,22] However, it was found that the efficiency of switching despite optimized conditions remained modest (~2-fold). Examples in the literature on dye-doped silica NPs showed better switching efficiency, compared to QDs, because in this case the photochromic acceptor could be encapsulated directly inside the particle core together with the dye donors.[23−25] Within organic systems, photoresponsive polymer NPs have already shown very promising results.[26,27]

Received: April 13, 2015
Accepted: May 28, 2015
Published: May 28, 2015

DOI: 10.1021/acs.jpclett.5b00769
J. Phys. Chem. Lett. 2015, 6, 2259−2264

This is notably the case of conjugated polymer NPs, which also can encapsulate photochromic dyes directly inside the core.[28−31] In this case, the higher intensity variation (>10-fold) could be explained by fast energy transfer along the polymer conjugation, which ensures that the energy is efficiently transferred to long distances toward a single acceptor (i.e., photochromic dye).[32−34] This phenomenon is called exciton diffusion, and it is well-known in sensors,[32] light harvesting[35] and photovoltaic systems,[36] which rely on rapid communication within large ensemble of dyes to ensure efficient energy transfer.

Dye-doped polymer NPs are also very attractive organic fluorescent systems, as they can be built from biodegradable eco-friendly materials and present exceptional brightness.[37−40] However, only limited number of reports utilized FRET to obtain photoswitchable dye-doped polymer NPs.[41−44] One reason is that it is still a challenge to obtain dye-doped NPs with minimal self-quenching of the encapsulated dyes. Moreover, the problem of controlling FRET efficiency between the doped dyes and the photoswitch was rarely addressed.[43] In the present work, we hypothesized that exciton diffusion, which is the reason for superquenching in the conjugated polymers, could be exploited to drive the photoswitching efficiency of dye-doped polymer NPs. To this end, we selected our recently developed rhodamine doped NPs build from the biodegradable polymer poly(D,L-lactide-*co*-glycolide) (PLGA).[38] Using a hydrophobic perfluorinated counterion as an "insulator" between the cationic rhodamine dyes, we were able to prevent self-quenching at high dye loading. Unexpectedly, at high dye loading we observed for the first time a collective fluorescence blinking of 100−500 dyes encapsulated in one particle. This phenomenon was explained by the ultrafast exciton diffusion, so that a single dark species (triplet or radical state of the dye) could quench the whole particle.[38] Remarkably, other counterions at the same dye loading did not show this behavior, so that the perfluorinated counterion was responsible for assembling rhodamine dyes in a close proximity to ensure the energy migration. Therefore, this system appeared promising for developing photoswitching NPs.

In the present work, we exploit the phenomenon of the exciton diffusion to build dye-doped polymer nanoparticles with excellent photoswitching ability. To this end, we coencapsulated into PLGA NPs rhodamine B dye salt with perfluorinated counterion as well as a photochromic acceptor of the diarylethene family. To understand the role of the exciton diffusion, we prepared NPs with other counterions, which did not favor exciton diffusion of rhodamine dyes. It was found that with perfluorinated counterion light-driven variation of fluorescence intensity was up to 20-fold, while for all other counterions, the switching efficiency was much lower. Thus, for the first time, we showed a direct connection between the collectiveness of the encapsulated dyes inside polymer NPs and their capacity to photoswitch. The performance of the new NPs was validated at the single particle level, where reversible photoswitching was demonstrated.

Nanoparticles studied in this work were prepared by nanoprecipitation of PLGA from acetonitrile. As we have shown earlier, diluted solutions of a polymer once precipitated in water can form NPs of 40−50 nm that are stabilized by the negative charge of carboxylate groups.[38,45] To encapsulate a fluorophore and a photoswitch, they were simply added to the acetonitrile solution before the nanoprecipitation. As a fluorophore, we selected the octadecyl-rhodamine B (R18) bearing different counterions: inorganic perchlorate or tetraphenyl borates with different levels of fluorination (Scheme 1). As a photochromic dye, we selected the

Scheme 1. Chemical Structure of the Encapsulated Fluorescent Dye (R18) with Different Bulky Counterions and the Photochromic Dye (PCD1)[a]

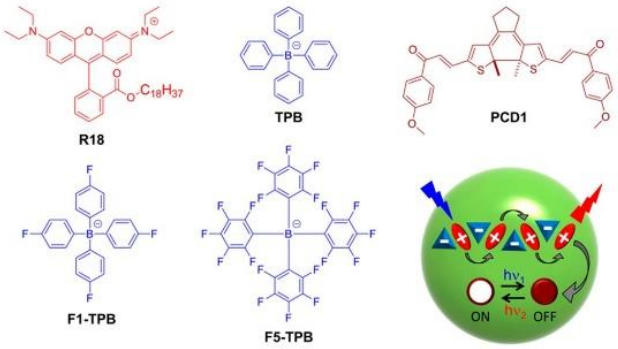

[a]Schematic presentation of photoswitching concept in dye-doped NPs. Small gray arrows show the exciton diffusion, while the large gray arrow presents FRET to a photochromic dye (brown). Filled and open brown circles correspond to the closed and open forms of PCD1, respectively. Chemical structure of the closed form of PCD1 is shown only.

diphenylethene derivative PCD1, which was described earlier.[46] It is hydrophobic and thus should be efficiently encapsulated into polymer NPs, as shown for other low polar switches.[44] PCD1 matches perfectly the optical properties of the donor dye R18, since its long-wavelength absorption band overlaps well with the emission of the donor (Figure 1A). Moreover, the photoswitch can be selectively illuminated with 405 and 645 nm lasers, necessary for switching, without direct excitation of the R18 dye, which is important to prevent bleaching of the fluorophore during the photoswitching cycles.

We first studied a small volume (200 μL) of the photochromic molecule PCD1 (0.02 mg/mL) in dioxane in a 1 mL quartz cuvette, which was needed to irradiate the whole sample by a laser or a lamp of a fluorometer. To optimize conditions for photoswitching, the sample was illuminated at 405 nm by the lamp of the fluorometer with a light flux of ~1 mW/cm^2 and by the defocused irradiation of a 645 nm laser with a light flux of ~200 mW/cm^2. Illumination at 405 nm resulted in the rapid growth of the absorbance at 630 nm, which reached saturation after ~2 min (Figure 1B). These changes indicated the formation of the closed (colored B) form of the photoswitch. In contrast, to switch the molecule back to the open (colorless A) form, an irradiation of the sample at 645 nm for at least 20 min with much higher power was required (Figure 1C). The observation of absorption peaks at 630 nm under alternate irradiation confirmed the reversibility of the photochromic isomerization without fatigue for at least 5 complete cycles (Figure 1D).

To investigate the photoisomerization conditions inside PLGA polymer NPs, we encapsulated 1 wt % of the photochromic dye with respect to the mass of polymer and performed the same cycles of irradiation. To obtain full photoisomerization inside PLGA, we increased the time of irradiation at 405 nm up to 10 min and at 645 nm up to 40 min (Figure S1).

DOI: 10.1021/acs.jpclett.5b00769
J. Phys. Chem. Lett. 2015, 6, 2259−2264

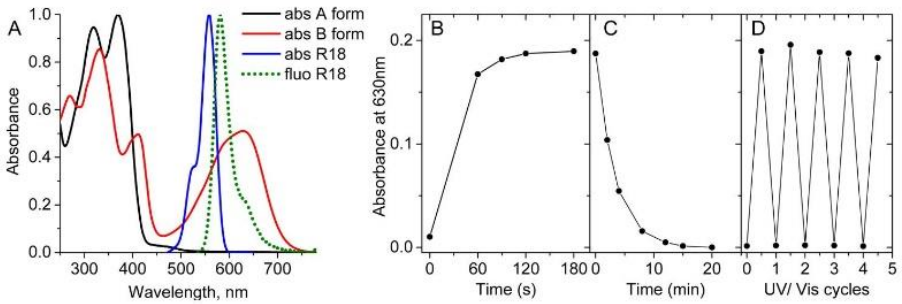

Figure 1. Spectroscopic properties of the R18 donor and the photochromic FRET acceptor PCD1, and photoswitching behavior of the latter in dioxane. (A) Absorption spectra of open A and closed B forms of PCD1 at 0.02 mg/mL in dioxane in comparison to the normalized absorption and fluorescence spectra of R18 with F5-TPB counterion in PLGA NPs (1 wt % loading). Time-dependent absorbance of PCD1 at 630 nm under illumination at 405 nm (B) and 645 nm (C). (D) Absorbance of PCD1 at 630 nm under alternate illumination at 405 nm (~1 mW/cm^2) for 3 min and at 645 nm (~200 mW/cm^2) for 20 min.

Next, the photochromic dye PCD1 was coencapsulated in PLGA NPs together with R18 dye salt containing four different counterions: perchlorate (ClO_4), TPB, F1-TPB, F5-TPB (Scheme 1). Dynamic light scattering (DLS) showed that the particle size remained in the range 42−47 nm (polydispersity index ~0.1) for most of formulations of R18 salts with or without PCD1 switch (Supporting Information Table S1). The only exception was NPs with R18/ClO_4 salt, which, in line with our earlier works, produced larger NPs.[38]

The emission of the obtained NPs was further studied under illumination cycles as it was established above in model conditions. We designated "off state" as the state of NPs where the photochromic dye in closed form behaves as an energy acceptor for rhodamine B, and "on state" as the opposite state without FRET. To characterize the system, we determined two parameters: the relative intensity = I/I_0^{off} and switching efficiency = I_{on}/I_{off}, where I is the peak fluorescence intensity at a given condition; I_0^{off} is the peak fluorescence intensity at the off state in the first illumination cycle; I_{on} and I_{off} are the peak fluorescence intensities of the on and off states, respectively, at a given illumination cycle. First, we verified for the most promising R18 salt with F5-TPB counterion the optimal concentration of the photochromic dye inside NPs. For 1 wt % loading of R18/F5-TPB dye, the switching efficiency grew up to 0.3 wt % of the photoswitch, while for 0.5 wt % the switching was already less efficient (Figure S2). The presence of 1 wt % of the fluorophore did not have any influence on the photoswitch fatigue (Figure S3), whereas the presence of 0.3 wt % of photoswitch did not influence the photostability of the fluorophore (Figure S4). Therefore, in all our further studies we used systematically 0.3 wt % of the photoswitch. We found that all NPs bearing one of the four different R18 salts were able to photoswitch their fluorescence, though the switching efficiency depended clearly on the nature of the counterion. Indeed, while for the perfluorinated counterion F5-TPB the switching efficiency was around 15, for all other counterions it was only 2−4 (Figure 2A).

The calculated Förster radius for a pair R18 and PCD1 was 2.1 and 4.9 nm for the open and closed forms of the switch, respectively. Assuming a homogeneous distribution of the PCD1 acceptors inside NPs, the volume taken by one acceptor was 240 nm^3, which gave an average distance between the acceptors of 7.7 nm. Theoretically, the closest average distance between R18 donor and PCD1 acceptors was 4.7 nm when R18 was located in the center of a tetrahedron formed by PCD1 (hexagonal arrangement of PCD1 separated by 7.7 nm). In this

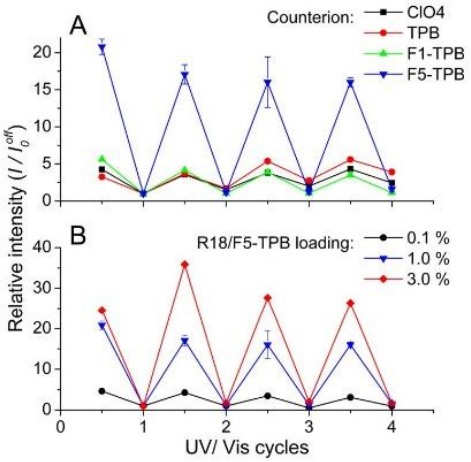

Figure 2. Switching properties of the dye-doped PLGA NPs as a function of counterion and dye loading in PLGA NPs. (A) Variation of relative peak intensity under alternate irradiation of PLGA NPs loaded with 1 wt % of rhodamine R18 with different counterions and 0.3 wt % of photochromic dye PCD1. (B) Variation of relative peak intensity under alternate irradiation of PLGA NPs loaded with 0.1−3 wt % of R18/F5-TPB and 0.3 wt % of PCD1. Excitation wavelength was 520 nm.

case, one R18 donor was surrounded by four acceptors, so that, using a FRET model for multiple (four) acceptors,[47] the estimated FRET efficiency was 3.1 and 84% for open and closed forms of PCD1, respectively. Thus, FRET can at least in part explain the switching behavior of our NPs. However, we should not exclude the electron transfer between R18 and the closed form of PCD1. Knowing the reduction and oxidation potentials of rhodamine B (−0.80 and 1.20 V, respectively)[48] and using the Rehm−Weller formalism,[49] the estimated reduction and oxidation potentials of this dye in the excited state were +1.38 and −0.98 V (vs SCE), respectively. For the switch, the redox data are available only for an analogue of PCD1 in the closed form with the oxidation and reduction potentials of +1.45 and −1.11 V (vs SCE), respectively.[50] The value of the oxidation potential of the model switch is close to the reduction potential of rhodamine B in the excited state, which (after neglecting small columbic effects) suggests that the electron transfer could take place from PCD1 to R18. In any case, the estimated FRET efficiency for the closed form is in line with the experimental data for all counterions, except F5-

DOI: 10.1021/acs.jpclett.5b00769
J. Phys. Chem. Lett. 2015, 6, 2259−2264

TPB (Figure 3A). For the latter, the FRET efficiency was much higher, so that the off state in these NPs was ~12-fold less

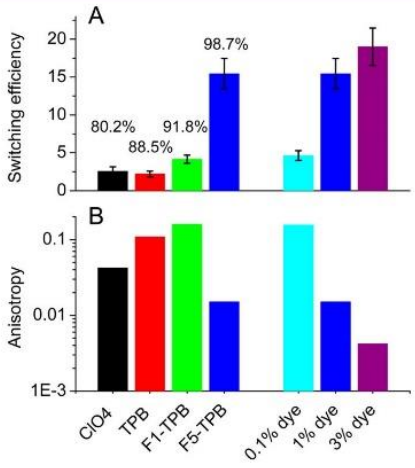

Figure 3. Correlation between photoswitching efficiency of NPs and fluorescence anisotropy of the encapsulated dyes. (A) Average switching efficiency (I_{on}/I_{off}) within four complete on/off cycles for dye-doped NPs containing 0.3 wt % of PCD1, with different counterions and at different R18/F5-TPB dye loading. The values given in this panel present the FRET efficiency (%) for the off state calculated from I_{off} and the intensity of NPs without PCD1. (B) Fluorescence anisotropy of the encapsulated dyes for the same NPs samples but without PCD1.

fluorescent than theoretically predicted. This is an indication that the counterion plays a particular role in the organization of R18 dyes. As we hypothesized earlier[38] F5-TPB could bring the donors close to each other, thus favoring exciton diffusion, which could boost the FRET efficiency.

To verify whether this effect of F5-TPB is linked with the exciton diffusion process, we measured the steady-state fluorescence anisotropy of NPs with all four counterions. When the energy migrates within encapsulated fluorophores that are randomly orientated inside the polymer matrix, the fluorescence anisotropy rapidly decreases after each step of the energy hopping between dyes.[51,52] As the fluorophores are confined within the rigid polymer matrix, the loss of fluorescence anisotropy in this system could be mainly attributed to the exciton diffusion process. In line with our earlier study,[38] NPs loaded with R18/F5-TPB salt presented much lower fluorescence anisotropy than all other salts, indicating that the most efficient exciton migration was achieved with this salt (Figure 3B). According to our previous time-resolved anisotropy data at 1 wt % R18/F5-TPB loading, corresponding to ~100 dyes per particle, at least 40 dyes were involved in the exciton diffusion.[38] These results correlated well the much higher efficiency of the photoswitching observed for R18/F5-TPB NPs (Figure 3A). The unique behavior of F5-TPB is probably related to its perfluorination, which may favor assembly of R18 dyes with short interfluorophore distances inside polymer matrix allowing fast exciton diffusion. The role of fluorines could be related to so-called fluorous effect (or superhydrophobicity)[53] as well as to their strong electronegativity that shifts the negative charge of F5-TPB to its periphery. To further check the importance of the exciton diffusion on the photoswitching efficiency, we varied the concentration of the fluorescent donor dyes (R18/F5-TPB), while keeping the photoswitch concentration constant. In the case of noncommunicating donors, the FRET efficiency, i.e., photoswitching efficiency, should be independent of the concentration of the donors.[54] However, we observed clearly that the photoswitching efficiency increased dramatically on increasing the donor dye concentration (Figures 2B and 3A). Moreover, this increase correlated perfectly with the decrease in the fluorescence anisotropy (Figure 3B), indicating faster rates of the exciton diffusion for higher dye loading. Indeed, at higher dye loading, the distance between the donor (R18) dyes should decrease, which should lead to faster energy hopping, as we showed earlier using time-resolved anisotropy and fluorescence blinking experiments.[38] The present data suggest that the energy transfer to the photoswitch can be drastically improved by exploiting the exciton diffusion within the donor dyes. To the best of our knowledge, it is the first time that a connection between the photoswitching efficiency and the exciton diffusion was established for dye-doped nanoparticles.

Finally, we evaluated the performance of our NPs at the single-particle level using wide-field fluorescence microscopy. To this end, we immobilized fluorescent NPs containing 1 wt % R18/F5-TPB and 0.3 wt % of PCD1 at the glass surface covered with the positively charged polymer PEI. Then, under the fluorescence microscope, we illuminated the observation region with alternating blue (405 nm) and red (645 nm) lasers

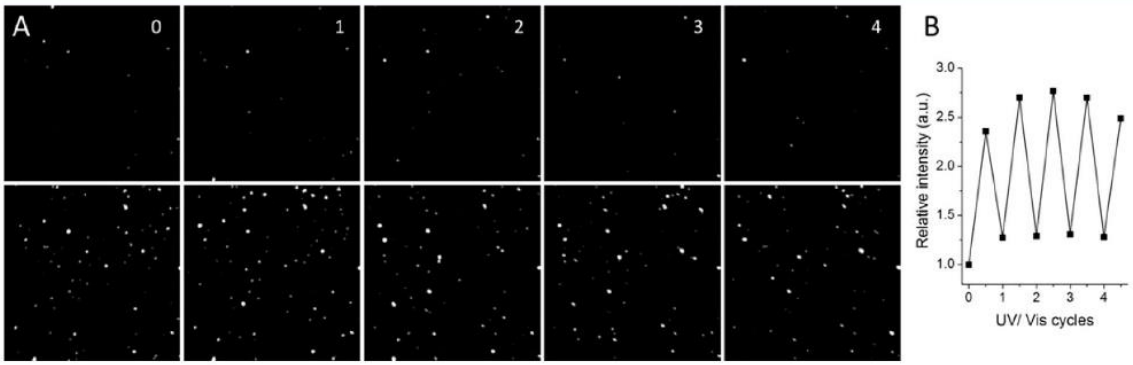

Figure 4. Single-particle observation of photoswitching of dye-doped NPs. (A) Wide field images of NPs containing 1 wt % R18/F5-TPB and 0.3 wt % of PCD1 after illumination at 405 (upper panels) and 645 nm (lower panels). (B) Average relative intensity (I/I_0^{off}) of NPs in the on and off state obtained from these images. The optimal conditions for photoswitching were 60 s illumination at 645 nm with laser power of 97 W/cm^2, and 5 s illumination at 405 nm with laser power of 8.7 W/cm^2. To record fluorescence images, the power of the laser at 532 was set to 0.2 W/cm^2.

DOI: 10.1021/acs.jpclett.5b00769
J. Phys. Chem. Lett. 2015, 6, 2259−2264

and recorded the fluorescence image after each illumination step. We found that after illumination at 645 nm, the particles appeared bright and were well seen on the images (Figure 4A). In contrast, after 405 nm illumination, most of the particles became dim, indicating that they underwent photoconversion into the off state. The average intensity variation showed a clear alternation of the particle intensity (Figure 4B). However, we should note that the value of the average intensity variation was lower than in solution. This is in line with other studies of NP switching showing that, at the single particle level, the switching appears less efficient.[55] There can be multiple factors, particularly related to the use of much higher illumination power under the microscope. The higher powers could bleach the encapsulated R18 dyes or the photoswitch and thus decrease the switching efficiency. Another reason is that at the single particle level, the signal-to-noise ratio is significantly lower than for NPs in solution, where a large population is simultaneously excited. Therefore, the absolute changes under the microscope could be decreased by the background noise. The other issue is the observed heterogeneity in the switching efficiency. While some particles showed switching efficiency reaching 30, for others it was below the average (Figure S5). This heterogeneity is related to inhomogeneity in the dye and photoswitch doping, particle size, etc. Therefore, an important challenge in the future will be to improve the homogeneity in the particle switching efficiency.

In the present work, we propose for the first time the utilization of exciton diffusion within encapsulated fluorophores to achieve efficient photoswitching. To this end, we applied our recently proposed concept of hydrophobic counterion for encapsulating a cationic dye (octadecyl rhodamine B) into NPs. This counterion serves as an insulator that prevents dye self-quenching but at the same time assembles the dyes in close proximity to ensure fast dye−dye communication inside a polymer matrix. We showed that only the perfluorinated tetraphenylborate counterion favoring the exciton diffusion enables high photoswitching efficiency (~20) of NPs in suspensions. For other counterions, where the interfluorophore communication was less pronounced, the photoswitching efficiency was much lower. Wide-field fluorescence microscopy studies confirmed the photoswitching of our NPs at the single-particle level. Our study shows that exciton diffusion within fluorophores inside NPs can ensure efficient FRET to the photoswitch producing highly efficient photoswitching. The proposed concept paves the way to new efficient photoswitchable nanomaterials.

■ ASSOCIATED CONTENT

Supporting Information

Detailed experimental section, and some additional optical spectroscopy and microscopy data. The Supporting Information is available free of charge on the ACS Publications website at DOI: 10.1021/acs.jpclett.5b00769.

■ AUTHOR INFORMATION

Corresponding Author

*E-mail: andrey.klymchenko@unistra.fr; Tel: +33 368 85 42 55.

Notes

The authors declare no competing financial interest.

■ ACKNOWLEDGMENTS

K.T. was supported by a fellowship from the Ministère de la Recherche. The work was supported by University of Strasburg (IdEX 2015, W15RAT68) and CNRS. J.M. gratefully acknowledges financial support by the Biophotonics Initiative of the German Ministry of Research and Education (BMBF).

■ REFERENCES

(1) Fernandez-Suarez, M.; Ting, A. Y. Fluorescent Probes for Super-Resolution Imaging in Living Cells. *Nat. Rev. Mol. Cell Biol.* **2008**, *9*, 929−943.

(2) Bates, M.; Huang, B.; Dempsey, G. T.; Zhuang, X. Multicolor Super-Resolution Imaging with Photo-Switchable Fluorescent Probes. *Science* **2007**, *317*, 1749−1753.

(3) Heilemann, M.; Dedecker, P.; Hofkens, J.; Sauer, M. Photoswitches: Key Molecules for Subdiffraction-Resolution Fluorescence Imaging and Molecular Quantification. *Laser Photon. Rev.* **2009**, *3*, 180−202.

(4) Tian, Z.; Li, A. D. Photoswitching-Enabled Novel Optical Imaging: Innovative Solutions for Real-World Challenges in Fluorescence Detections. *Acc. Chem. Res.* **2013**, *46*, 269−279.

(5) van de Linde, S.; Sauer, M. How to Switch a Fluorophore: From Undesired Blinking to Controlled Photoswitching. *Chem. Soc. Rev.* **2014**, *43*, 1076−1087.

(6) Irie, M. Diarylethenes for Memories and Switches. *Chem. Rev.* **2000**, *100*, 1685−1716.

(7) Pang, S. C.; Hyun, H.; Lee, S.; Jang, D.; Lee, M. J.; Kang, S. H.; H, A. K. Photoswitchable Fluorescent Diarylethene in a Turn-on Mode for Live Cell Imaging. *Chem. Commun.* **2012**, *48*, 3745−3747.

(8) Klajn, R. Spiropyran-Based Dynamic Materials. *Chem. Soc. Rev.* **2014**, *43*, 148−184.

(9) Heilemann, M.; Margeat, E.; Kasper, R.; Sauer, M.; Tinnefeld, P. Carbocyanine Dyes as Efficient Reversible Single-Molecule Optical Switch. *J. Am. Chem. Soc.* **2005**, *127*, 3801−3806.

(10) Bates, M.; Blosser, T. R.; Zhuang, X. W. Short-Range Spectroscopic Ruler Based on a Single-Molecule Optical Switch. *Phys. Rev. Lett.* **2005**, *94*, 108101.

(11) Habuchi, S.; Ando, R.; Dedecker, P.; Verheijen, W.; Mizuno, H.; Miyawaki, A.; Hofkens, J. Reversible Single-Molecule Photoswitching in the GFP-Like Fluorescent Protein Dronpa. *Proc. Natl. Acad. Sci. U.S.A.* **2005**, *102*, 9511−9516.

(12) Ando, R.; Mizuno, H.; Miyawaki, A. Regulated Fast Nucleocytoplasmic Shuttling Observed by Reversible Protein Highlighting. *Science* **2004**, *306*, 1370−1373.

(13) Sapsford, K. E.; Berti, L.; Medintz, I. L. Materials for Fluorescence Resonance Energy Transfer Analysis: Beyond Traditional Donor−Acceptor Combinations. *Angew. Chem., Int. Ed. Engl.* **2006**, *45*, 4562−4588.

(14) Raymo, F. M.; Tomasulo, M. Electron and Energy Transfer Modulation with Photochromic Switches. *Chem. Soc. Rev.* **2005**, *34*, 327−336.

(15) Ouhenia-Ouadahi, K.; Metivier, R.; Maisonneuve, S.; Jacquart, A.; Xie, J.; Leaustic, A.; Yu, P.; Nakatani, K. Fluorescence Photoswitching and Photoreversible Two-Way Energy Transfer in a Photochrome−Fluorophore Dyad. *Photochem. Photobiol. Sci.* **2012**, *11*, 1705−1714.

(16) Alivisatos, A. P. Semiconductor Clusters, Nanocrystals, and Quantum Dots. *Science* **1996**, *271*, 933−937.

(17) Bonacchi, S.; Genovese, D.; Juris, R.; Montalti, M.; Prodi, L.; Rampazzo, E.; Zaccheroni, N. Luminescent Silica Nanoparticles: Extending the Frontiers of Brightness. *Angew. Chem., Int. Ed. Engl.* **2011**, *50*, 4056−4066.

(18) Kaeser, A.; Schenning, A. P. H. J. Fluorescent Nanoparticles Based on Self-Assembled π-Conjugated Systems. *Adv. Mater.* **2010**, *22*, 2985−2997.

(19) Li, K.; Liu, B. Polymer-Encapsulated Organic Nanoparticles for Fluorescence and Photoacoustic Imaging. *Chem. Soc. Rev.* **2014**, *43*, 6570−6597.

DOI: 10.1021/acs.jpclett.5b00769
J. Phys. Chem. Lett. 2015, 6, 2259−2264

(20) Tian, Z.; Wu, W.; Li, A. D. Photoswitchable Fluorescent Nanoparticles: Preparation, Properties and Applications. *ChemPhysChem* **2009**, *10*, 2577−2591.
(21) Diaz, S. A.; Menendez, G. O.; Etchehon, M. H.; Giordano, L.; Jovin, T. M.; Jares-Erijman, E. A. Photoswitchable Water-Soluble Quantum Dots: pcFRET Based on Amphiphilic Photochromic Polymer Coating. *ACS Nano* **2011**, *5*, 2795−2805.
(22) Medintz, I. L.; Trammell, S. A.; Mattoussi, H.; Mauro, J. M. Reversible Modulation of Quantum Dot Photoluminescence Using a Protein-Bound Photochromic Fluorescence Resonance Energy Transfer Acceptor. *J. Am. Chem. Soc.* **2004**, *126*, 30−31.
(23) Genovese, D.; Montalti, M.; Prodi, L.; Rampazzo, E.; Zaccheroni, N.; Tosic, O.; Altenhoner, K.; May, F.; Mattay, J. Reversible Photoswitching of Dye-Doped Core-Shell Nanoparticles. *Chem. Commun.* **2011**, *47*, 10975−10977.
(24) May, F.; Peter, M.; Hutten, A.; Prodi, L.; Mattay, J. Synthesis and Characterization of Photoswitchable Fluorescent SiO_2 Nanoparticles. *Chemistry* **2012**, *18*, 814−821.
(25) Folling, J.; Polyakova, S.; Belov, V.; van Blaaderen, A.; Bossi, M. l.; Hell, S. W. Synthesis and Characterization of Photoswitchable Fluorescent Silica Nanoparticles. *Small* **2008**, *4*, 134−142.
(26) Swaminathan, S.; Garcia-Amoros, J.; Fraix, A.; Kandoth, N.; Sortino, S.; Raymo, F. M. Photoresponsive Polymer Nanocarriers with Multifunctional Cargo. *Chem. Soc. Rev.* **2014**, *43*, 4167−4178.
(27) Li, C.; Liu, S. Polymeric Assemblies and Nanoparticles with Stimuli-Responsive Fluorescence Emission Characteristics. *Chem. Commun.* **2012**, *48*, 3262−3278.
(28) Harbron, E. J. Fluorescence Intensity Modulation in Photochromic Conjugated Polymer Systems. *Isr. J. Chem.* **2013**, *53*, 256−266.
(29) Chan, Y. H.; Gallina, M. E.; Zhang, X.; Wu, I. C.; Jin, Y.; Sun, W.; Chiu, D. T. Reversible Photoswitching of Spiropyran-Conjugated Semiconducting Polymer Dots. *Anal. Chem.* **2012**, *84*, 9431−9438.
(30) Feng, G.; Ding, D.; Li, K.; Liu, J.; Liu, B. Reversible Photoswitching Conjugated Polymer Nanoparticles for Cell and Ex Vivo Tumor Imaging. *Nanoscale* **2014**, *6*, 4141−4147.
(31) Osakada, Y.; Hanson, L.; Cui, B. Diarylethene Doped Biocompatible Polymer Dots for Fluorescence Switching. *Chem. Commun.* **2012**, *48*, 3285−3287.
(32) Thomas Iii, S. W.; Joly, G. D.; Swager, T. M. Chemical Sensors Based on Amplifying Fluorescent Conjugated Polymers. *Chem. Rev.* **2007**, *107*, 1339−1386.
(33) Achyuthan, K. E.; Bergstedt, T. S.; Chen, L.; Jones, R. M.; Kumaraswamy, S.; Kushon, S. A.; Ley, K. D.; Lu, L.; McBranch, D.; Mukundan, H.; Rininsland, F.; Shi, X.; Xia, W.; Whitten, D. G. Fluorescence Superquenching of Conjugated Polyelectrolytes: Applications for Biosensing and Drug Discovery. *J. Mater. Chem.* **2005**, *15*, 2648−2656.
(34) Wang, X. L.; Groff, L. C.; McNeill, J. D. Multiple Energy Transfer Dynamics in Blended Conjugated Polymer Nanoparticles. *J. Phys. Chem. C* **2014**, *118*, 25731−25739.
(35) Bopp, M. A.; Sytnik, A.; Howard, T. D.; Cogdell, R. J.; Hochstrasser, R. M. The Dynamics of Structural Deformations of Immobilized Single Light-Harvesting Complexes. *Proc. Natl. Acad. Sci. U.S.A.* **1999**, *96*, 11271−11276.
(36) Menke, S. M.; Luhman, W. A.; Holmes, R. J. Tailored Exciton Diffusion in Organic Photovoltaic Cells for Enhanced Power Conversion Efficiency. *Nat. Mater.* **2013**, *12*, 152−157.
(37) Trofymchuk, K.; Reisch, A.; Shulov, I.; Mely, Y.; Klymchenko, A. S. Tuning the Color and Photostability of Perylene Diimides inside Polymer Nanoparticles: Towards Biodegradable Substitutes of Quantum Dots. *Nanoscale* **2014**, *6*, 12934−12942.
(38) Reisch, A.; Didier, P.; Richert, L.; Oncul, S.; Arntz, Y.; Mely, Y.; Klymchenko, A. S. Collective Fluorescence Switching of Counterion-Assembled Dyes in Polymer Nanoparticles. *Nat. Commun.* **2014**, *5*, 4089.
(39) Wagh, A.; Qian, S. Y.; Law, B. Development of Biocompatible Polymeric Nanoparticles for in Vivo NIR and FRET Imaging. *Bioconjugate Chem.* **2012**, *23*, 981−992.
(40) Wagh, A.; Jyoti, F.; Mallik, S.; Qian, S.; Leclerc, E.; Law, B. Polymeric Nanoparticles with Sequential and Multiple FRET Cascade Mechanisms for Multicolor and Multiplexed Imaging. *Small* **2013**, *9*, 2129−2139.
(41) Zhu, M. Q.; Zhu, L.; Han, J. J.; Wu, W.; Hurst, J. K.; Li, A. D. Spiropyran-Based Photochromic Polymer Nanoparticles with Optically Switchable Luminescence. *J. Am. Chem. Soc.* **2006**, *128*, 4303−4309.
(42) Chen, J.; Zhang, P.; Fang, G.; Weng, C.; Hu, J.; Yi, P.; Yu, X.; Li, X. One-Pot Synthesis of Amphiphilic Reversible Photoswitchable Fluorescent Nanoparticles and Their Fluorescence Modulation Properties. *Polym. Chem.* **2012**, *3*, 685−693.
(43) Chen, J.; Zeng, F.; Wu, S. Construction of Energy Transfer Systems within Nanosized Polymer Micelles and Their Fluorescence Modulation Properties. *ChemPhysChem* **2010**, *11*, 1036−1043.
(44) Yildiz, I.; Impellizzeri, S.; Deniz, E.; McCaughan, B.; Callan, J. F.; Raymo, F. M. Supramolecular Strategies to Construct Biocompatible and Photoswitchable Fluorescent Assemblies. *J. Am. Chem. Soc.* **2011**, *133*, 871−879.
(45) Reisch, A.; Runser, A.; Arntz, Y.; Mély, Y.; Klymchenko, A. S. Charge-Controlled Nanoprecipitation as a Modular Approach to Ultrasmall Polymer Nanocarriers: Making Bright and Stable Nanoparticles. *ACS Nano* **2015**, *9*, 5104−5116.
(46) Altenhoener, K.; Lamm, J.-H.; Mattay, J. Novel Dithienylethenes with Extended π-Systems: Synthesis by Aldol Condensation and Photochromic Properties. *Eur. J. Org. Chem.* **2010**, 6033−6037.
(47) Fabian, A. I.; Rente, T.; Szoellosi, J.; Matyus, L.; Jenei, A. Strength in Numbers: Effects of Acceptor Abundance on FRET Efficiency. *ChemPhysChem* **2010**, *11*, 3713−3721.
(48) Valenti, G.; Rampazzo, E.; Bonacchi, S.; Khajvand, T.; Juris, R.; Montalti, M.; Marcaccio, M.; Paolucci, F.; Prodi, L. A Versatile Strategy for Tuning the Color of Electrochemiluminescence Using Silica Nanoparticles. *Chem. Commun.* **2012**, *48*, 4187−4189.
(49) Rehm, D.; Weller, A. Kinetics of Fluorescence Quenching by Electron and H-Atom Transfer. *Isr. J. Chem.* **1970**, *8*, 259−271.
(50) Berberich, M.; Wuerthner, F. Tuning the Redox Properties of Photochromic Diarylethenes by Introducing Electron-Withdrawing Substituents. *Asian J. Org. Chem.* **2013**, *2*, 250−256.
(51) Colby, K. A.; Burdett, J. J.; Frisbee, R. F.; Zhu, L.; Dillon, R. J.; Bardeen, C. J. Electronic Energy Migration on Different Time Scales: Concentration Dependence of the Time-Resolved Anisotropy and Fluorescence Quenching of Lumogen Red in Poly(methyl methacrylate). *J. Phys. Chem. A* **2010**, *114*, 3471−3482.
(52) Yeow, E. K. L.; Ghiggino, K. P.; Reek, J. N. H.; Crossley, M. J.; Bosman, A. W.; Schenning, A.; Meijer, E. W. The Dynamics of Electronic Energy Transfer in Novel Multiporphyrin Functionalized Dendrimers: A Time-Resolved Fluorescence Anisotropy. *J. Phys. Chem. B* **2000**, *104*, 2596−2606.
(53) Cametti, M.; Crousse, B.; Metrangolo, P.; Milani, R.; Resnati, G. The Fluorous Effect in Biomolecular Applications. *Chem. Soc. Rev.* **2012**, *41*, 31−42.
(54) Genovese, D.; Rampazzo, E.; Bonacchi, S.; Montalti, M.; Zaccheroni, N.; Prodi, L. Energy Transfer Processes in Dye-Doped Nanostructures Yield Cooperative and Versatile Fluorescent Probes. *Nanoscale* **2014**, *6*, 3022−3036.
(55) Davis, C. M.; Childress, E. S.; Harbron, E. J. Ensemble and Single-Particle Fluorescence Photomodulation in Diarylethene-Doped Conjugated Polymer Nanoparticles. *J. Phys. Chem. C* **2011**, *115*, 19065−19073.

DOI: 10.1021/acs.jpclett.5b00769
J. Phys. Chem. Lett. 2015, 6, 2259−2264

Supporting information

Exploiting Fast Exciton Diffusion in Dye-Doped Polymer Nanoparticles to Engineer Efficient Photoswitching

Kateryna Trofymchuk, Luca Prodi, Andreas Reisch, Yves Mély, Kai Altenhöner, Jochen Mattay, and Andrey S. Klymchenko

Experimental Methods

Poly(D,L-lactide-*co*-glycolide) (lactide 50 mole%, glycolide 50 mole%, Mn 24 000; PDI 1.7) and rhodamine B octadecyl ester (R18) perchlorate (≥98.0 %) were purchased from Sigma-Aldrich and used as received. Salts of R18 with hydrophobic counterions: R18/TPB, R18/F1-TPB and R18/F5-TPB were synthesized as described elsewhere.[1] The synthesis of photochromic dye PCD1 was described earlier.[2] Sodium phosphate monobasic (>99.0 %, Sigma-Aldrich) and sodium phosphate dibasic dihydrate (>99.0 %, Sigma-Aldrich) were used to prepare 20 mM phosphate buffer solutions at pH 7.4. MilliQ-water (Millipore) was used in all experiments.

Preparation of fluorescent NPs. PLGA (lactide:glycolide, 1:1, mole:mole) was dissolved at 2 mg/mL^{-1} in acetonitrile containing different amounts of dye (from 0 to 3 wt% relative to the PLGA). These solutions were added quickly and under stirring (shaking) using a micropipette to a 10-fold volume excess of 20 mM phosphate buffer at pH 7.4. The particle solution was then quickly diluted five-fold with the same buffer.

Characterization of NPs. Dynamic light scattering measurements were performed on a Zetasizer Nano series DTS 1060 (Malvern Instruments S.A.). It uses a laser source at 633 nm, which excludes any light excitation of our dye-doped NPs. Absorption and emission spectra were recorded on a Cary 400 Scan UV-visible spectrophotometer (Varian) and a FluoroMax-4 spectrofluorometer (Horiba Jobin Yvon) equipped with a thermostated cell compartment, respectively. For standard recording of fluorescence spectra, the excitation wavelength was set to 520 nm. The fluorescence spectra were corrected for detector response and lamp fluctuations. For fluorescence switching analysis, peak fluorescence intensity at the band maximum was used after correction from the background noise of the blank. To realize photoswitching in solution a small volume (200 μL) of the sample in 1 mL quartz cuvette was irradiated by a laser at 645 nm with a light flux of ~ 200 mW/cm^2 or a lamp of a fluorometer at 405 nm with a light flux of ~1 mW/cm^2. The time of illumination was varied dependent on the sample. For the solution of the photoswitch in dioxane it was 3 min at 405 nm and 20 min at 645 nm, while for the PLGA NPs it was 10 min at 405 nm and 40 min at 645 nm.

Calculation of FRET efficiency. In a model where one donor is surrounded with multiple acceptors the theoretical FRET efficiency E_n can be calculated using the following equation (1):[3]

$$E_n = \frac{nE_0}{1+(n-1)E_0} \quad (1)$$

where n is the number of acceptors and E_0 is the FRET efficiency in a classical one donor – one acceptor system:

$$E_0 = \frac{1}{1+\left(\frac{r}{R_0}\right)^6} \quad (2)$$

where r is a donor-acceptor distance and R_0 is the Förster radius.

Fluorescence microscopy. For single particle fluorescence measurements, the NPs were immobilized on glass surfaces covered by polyethyleneimine (PEI), as described earlier.[1] The solutions of NPs were diluted to a particle concentration of about 6 pM with buffer. 400 µL of these solutions per cm^2 were then brought in contact with the PEI covered glass for 15 min, followed by extensive rinsing with milliQ-water. The surfaces were left in milliQ-water during the microscopy measurements.
Single particle measurements were performed in the TIRF (Total Internal Reflection Fluorescence) mode on a home-made wide-field setup based on an Olympus IX-71 microscope with an oil immersion objective (NA = 1.49, 100x). A DPPS (Cobolt) continuous wave (CW) laser emitting at 532 nm was used for excitation of dye-doped NPs. The laser intensity for image recording was set to 0.2 W/cm^2 by using a polarizer and a half-wave plate (532 nm). The fluorescence signal was recorded with an EMCCD (ImagEM Hamamatsu) with an integration time of 50 ms. To switch the particles to the on state, the observation area was illuminated by 645 nm laser with 97 W/cm^2 power for 60 s. Then to switch them off 5 s illumination at 405nm with laser power 8.7 W/cm^2 was used. The image recording was realized after each illumination step. After background subtraction, the individual particle intensity was determined as a mean intensity in a circle with a fixed radius that included the signal from one NP. The average intensity was evaluated as an arithmetic mean of all NPs in one image. The average intensity variation was calculated as a ratio between average NPs intensity after each illumination and average fluorescence intensity at the off state in the first illumination cycle.

Table 1. Hydrodynamic diameter and polydispersity (PDI) of PLGA NPs encapsulating R18 with different counterions and PCD1 measured by DLS.[a]

NPs content	Fluorophore only		With 0.3% PCD1	
	Diameter (nm)	PDI	Diameter (nm)	PDI
1% ClO4	86	0.06	129	0.03
1% TPB	46	0.06	46	0.11
1% F1-TPB	44	0.13	44	0.1
1% F5-TPB	46	0.11	43	0.04
0.1% F5-TPB	47	0.13	42	0.07
3% F5-TPB	43	0.06	45	0.09

[a] Statistics by volume was used in the analysis.

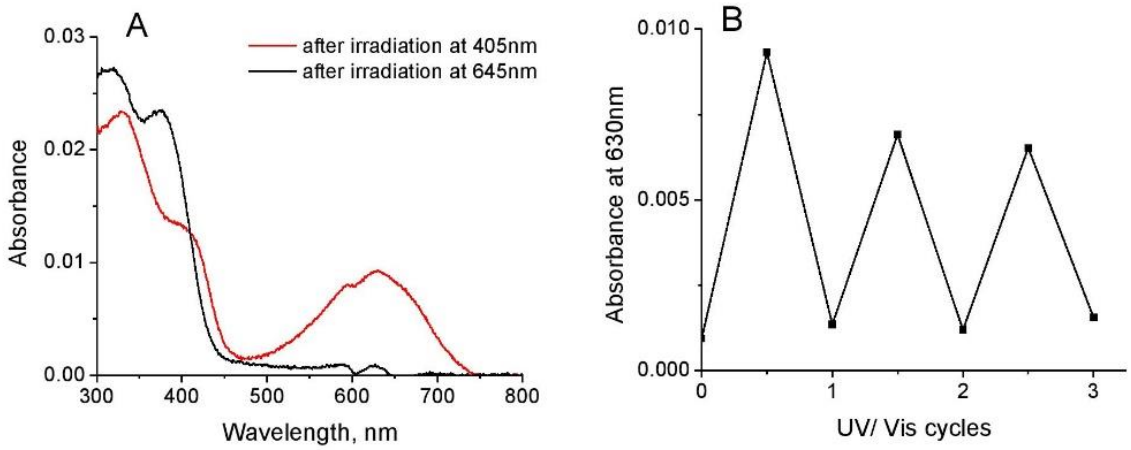

Fig. S1. (A) Absorption spectra of 1 wt% of photochromic dye PCD1 in PLGA matrix. (B) Absorbance at 630 nm of 1 wt% of PCD1 inside PLGA matrix under alternate illumination at 405 nm (higher values) and 645 nm (lower values).

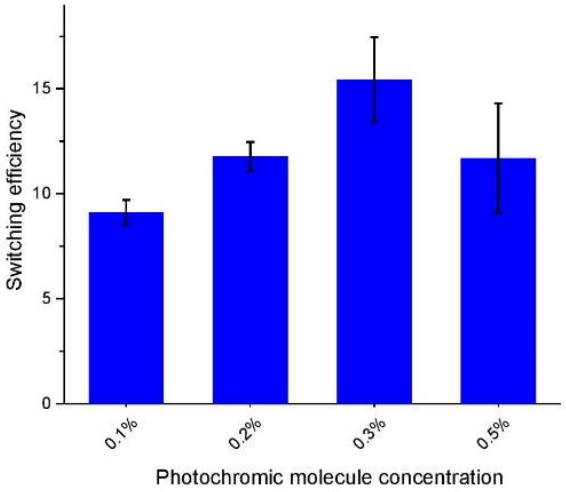

Fig. S2. Average switching efficiency (I_{on}/I_{off}) from four complete on/off cycles of NPs loaded with 1 wt% of R18/F5-TPB and different amounts (wt%) of photochromic molecule PCD1.

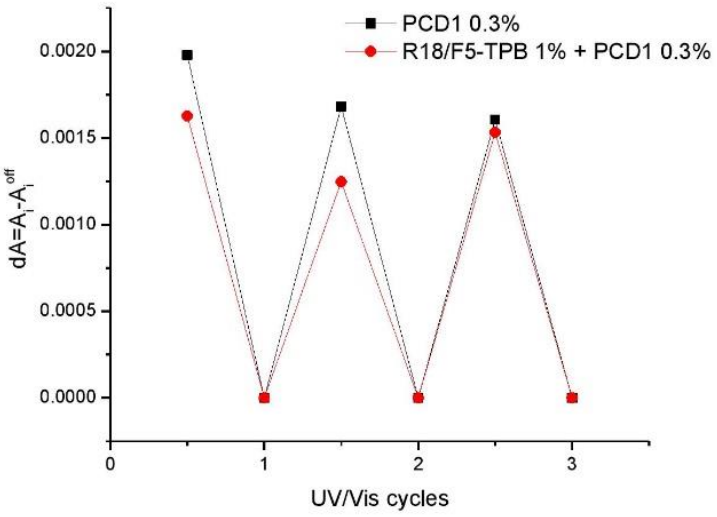

Fig. S3. Variation of absorbance at 630 nm under alternate irradiation presented as $dA=A_i- A_i^{off}$ of NPs loaded with PCD1 0.3% with and without 1 wt% of R18/F5-TPB.

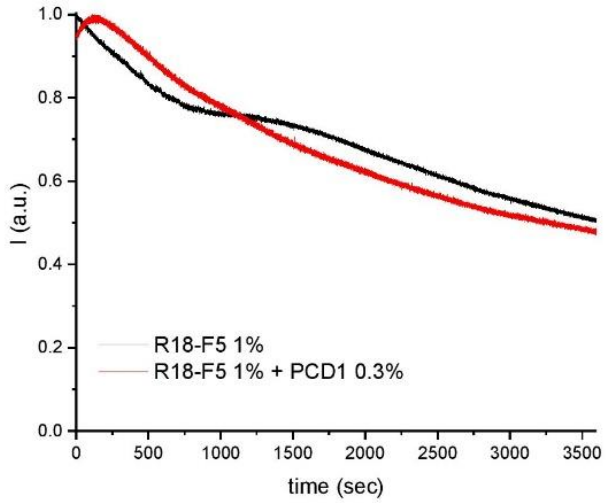

Fig. S4. Photostability of NPs loaded with 1 wt% of R18/F5-TPB in the presence or absence of PCD1 0.3%. Experiment was performed in low volume cuvette (50µl) under the illumination of the lamp of spectrofluorometer at excitation wavelength 560 nm. The illumination power was ~ 1mW/cm^2.

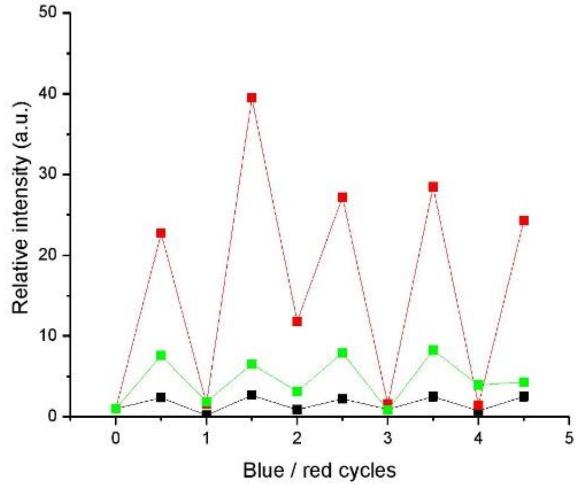

Fig. S5. Photoswitching of individual NPs under the microscope. Relative intensity of different NPs in the on- and off-state obtained from microscopy images after 405 and 645 nm illumination. The optimal conditions for photoswitching were 60 s illumination at 645 nm with laser power 97 W/cm^2, and 5 s illumination at 405nm with laser power 8.7 W/cm^2. To record fluorescence images the power of the laser at 532 was set to 0.2 W/cm^2.

References

(1) Reisch, A.; Didier, P.; Richert, L.; Oncul, S.; Arntz, Y.; Mely, Y.; Klymchenko, A. S. Collective Fluorescence Switching of Counterion-Assembled Dyes in Polymer Nanoparticles. *Nat. Commun.* **2014**, *5*, 4089.
(2) Altenhoener, K.; Lamm, J.-H.; Mattay, J. Novel Dithienylethenes with Extended Pi-Systems: Synthesis by Aldol Condensation and Photochromic Properties. *Eur. J. Org. Chem.* **2010**, 6033-6037.
(3) Fabian, A. I.; Rente, T.; Szoellosi, J.; Matyus, L.; Jenei, A. Strength in Numbers: Effects of Acceptor Abundance on Fret Efficiency. *ChemPhysChem* **2010**, *11*, 3713-3721.

2.2.2. Article 3: “Giant light harvesting nano-antenna for single-molecule detection at ambient light”

When multiple donors efficiently collect light energy and transfer it to a single acceptor through FRET mechanism, amplification of the emission of latter is observed. [180] A promising platform for fabrication of light-harvesting nano-antenna is dye-loaded polymer nanoparticles, where the dyes are encapsulated with minimal aggregation-caused quenching.[181] Our recent work showed that encapsulation of multiple dyes inside polymer NPs using bulky counterions minimized dye self-quenching and produced fluorescence switching (blinking) of up to 500 dyes per particle.[170] It was explained by unprecedented coupling of encapsulated dyes due to exciton migration, so that a single dark species could quench the whole dye ensemble.

We hypothesized that the use of much larger dye ensembles, coupled by EET inside NPs, could generate giant light-harvesting antenna for amplifying the fluorescence of a single dye. To this end, we created PMMAMA NPs of different size (from 30 to 107 nm according to TEM), loaded with high amount of R18/F5-TPB (30 wt%). PMMA was chosen, because according to our study described above, this matrix favors efficient fluorescence and EET at high dye loading. As expected, independently of the NPs size, the QY remained high (0.36-0.44).

Co-encapsulation of small amount of Cy5 (0.02 and 0.002 wt%, that corresponds to donor/acceptor ratio 1000 and 10000 respectively), which is known to be efficient energy acceptor for rhodamine dyes, resulted in the efficient FRET. We showed that NPs of ~60 nm size containing $>10^4$ donor dyes can efficiently transfer energy to 1-2 acceptors. For both D/A ratios, increase in the NPs size increased the FRET efficiency (Figure 2.16 a). The antenna effect (calculated as the ratio of the maximal excitation intensity of the donor to that of the acceptor [127]) also depended on the NPs size. For the lower donor/acceptor ratio, the antenna effect increased to a small extent from 160 to 330, whereas for donor/acceptor ratio of 10000, the strong increase in the antenna effect was observed for larger NPs (Figure 2.16 b). Remarkably, for NPs100 and NPs130 the enhancement of single acceptor emission (1.5 and 2.1 acceptors per NPs) reached 1000-fold, which, to our knowledge, is by far the highest FRET-based amplification of dye emission reported to date. (Figure 2.16).

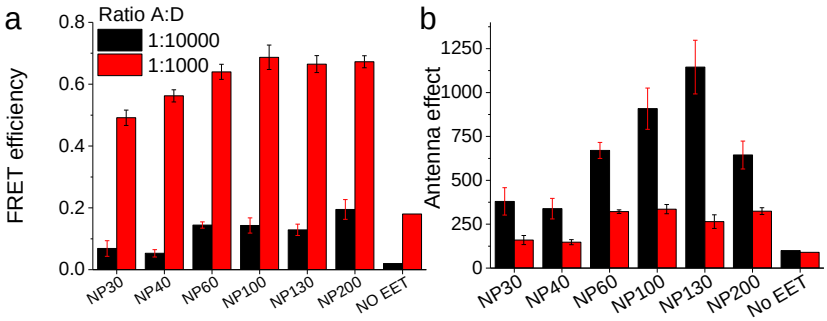

Figure 2.16. Effect of size of nano-antennas on their performance. **a)** FRET efficiency and **b)** antenna effect of PMMA-MA FRET NPs of different size loaded with 30 wt% of R18/F5-TPB and DiD. Donor/Acceptor ratios were 1:1000 or 1:10000. Error bars represent the standard error of the mean (n=3). Sample marked "No EET" represents theoretical calculations in case of absence of exciton diffusion within donor dyes.

Single particle measurements by TIRF microscopy confirmed high antenna effect. This amplification resulted in the brightness of 1-2 acceptors inside NP100 that were 25-times higher than that of the QD655, excited at the same power of 532-nm laser (Figure 2.17 a). Our NPs100 nano-antennas were used to observe single molecule events, such as one-step bleaching of the Cy5 (DiD) acceptor at extremely low laser powers of 1 mW/cm^2 which is 10^4 - 10^6 fold lower than typically used in single molecule measurements. (Figure 2.17 b).

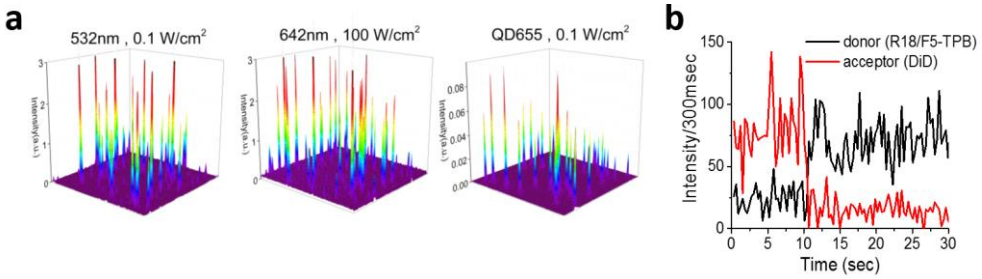

Figure 2.17. Single-particle evaluation of nano-antenna performance. **a)** 3D representation of wide-field images of acceptor emission from FRET NPs containing 30 wt% R18/F5-TPB and ~1.5 Cy5 (DiD) acceptors under the illumination at 532 nm with laser power 0.1 W/cm^2, under the direct excitation of acceptor at 642 nm with laser power 100 W/cm^2 and of QD 655 under the illumination at 532 nm with laser power 0.1 W/cm^2. In all cases integration time was set to 30.53 ms. **b)** Representative single particle trace excited at 532 nm with different power density of 1 mW/cm^2.

This means that we approach single molecule photography at ambient light without dedicated instrumentation.

The full description of the work can be found in the manuscript enclosed below.

Giant light harvesting nano-antenna for single-molecule detection at ambient light

*Kateryna Trofymchuk, Andreas Reisch, Pascal Didier, François Fras, Pierre Gilliot, Yves Mely, and Andrey S. Klymchenko**

Laboratoire de Biophotonique et Pharmacologie, UMR 7213 CNRS, Université de Strasbourg, Faculté de Pharmacie, 74, Route du Rhin, 67401 ILLKIRCH Cedex, France. E-mail: andrey.klymchenko@unistra.fr; Tel: +33 368 85 42 55

Abstract

In the present work, we explore the enhancement of single molecule emission by polymeric nano-antenna that can harvest energy from thousands of donor dyes to a single acceptor. In this nano-antenna, the cationic dyes are brought together in very close proximity using bulky counterions, thus enabling ultrafast diffusion of excitation energy (<60 fs) with minimal losses. Our 60-nm nanoparticles containing $>10^4$ donor dyes can efficiently transfer energy to 1-2 acceptors resulting in an antenna effect of ~1000. In this case, single acceptors (Cy5 derivative) are 25-fold brighter than QD655 at 532 nm excitation. This unprecedented amplification of the acceptor dye emission enables efficient observation of single molecules at illumination powers (1-10 mW/cm^2) that are $>10^4$-fold lower than required in single molecule measurements. Finally, using a basic setup, which includes 20x air objective and sCMOS camera, we could detect single Cy5 molecules by simply shining divergent light on the sample at powers equivalent to sunlight.

Introduction

Detection of single fluorescent molecules requires a dedicated microscopy setup with strong excitation power ranging between 100 and up to 5000 W/cm^2 because the brightness of fluorescent dyes is limited.[182, 183] The use of much lower excitation power would not only decrease photo-damage[184, 185] and the background related to auto-fluorescence, but would also enable fast and inexpensive high-throughput screening and diagnostics assays, which normally do not use microscopy setups and powerful light sources. For instance, fluorescent nanoparticles (NPs) that are many-fold brighter than single dyes can be detected even using a smartphone-based device.[186] The key question is can a low power excitation at levels similar to the ambient light intensity be used for single molecule detection? The typical light power of sunlight at the surface of the earth at a bandwidth of 10 nm in a visible range is ~1 mW/cm^2,[187] which is similar to the illumination power used in fluorimeters or plate readers. This power is 10^4-10^6 lower than those typically used in single molecule microscopy, which sounds like an impossible obstacle to single molecule detection under ambient light conditions. Recent works suggested metallic nanostructures, so-called plasmonic nano-antennas, which can amplify the excitation and emission of single molecules.[188-191] In this case, the amplification is achieved due to surface plasmon effects, which requires precise control of antenna geometry and the distance from the emitter to the metal surface.[192, 193] Thus, between two gold NPs, an amplification of up to 100-fold could be achieved.[194] Larger values of amplification were also reported, though it was achieved only when the fluorophore was initially poorly emissive or quenched.[195, 196] However, to detect single molecules under ambient light power, we need to achieve at least 1000-fold amplification of the signal coming from a high performance non-quenched fluorophore, such as cyanine 5 or Alexa567. A promising direction is to use a light-harvesting concept, where multiple donors due to high absorptivity can efficiently collect light energy and then deliver it to a single acceptor through a Förster Resonance Energy transfer (FRET) mechanism.[197] This is particularly efficient when the excitation energy can rapidly migrate within the donors up to the energy acceptor, as it is realized by Nature in photosynthetic centers.[198] Chemists developed highly efficient FRET systems that use conjugated polymers,[157, 199-202] dendrimers,[126, 203] multi-porphyrin arrays,[175] micellar NPs,[180, 204, 205] polymer NPs,[143] dye assemblies,[206, 207] metal-organic frameworks,[208] nucleic acids,[209, 210] etc. However, so far the obtained amplification of the acceptor has never reached 1000.[90] The common reasons that limit the efficient light harvesting is self-quenching of donors at high local concentration and/or

inefficient donor-donor coupling. A promising platform for fabrication of light-harvesting nano-antenna is dye-loaded polymer nanoparticles, where the dyes are encapsulated with minimal aggregation-caused quenching.[181] Our recent work showed that encapsulation of multiple dyes inside polymer NPs using bulky counterions minimized dye self-quenching and produced fluorescence switching (blinking) of up to 500 dyes per particle.[170] It was explained by unprecedented coupling of encapsulated dyes due to exciton migration, so that a single dark species could quench the whole dye ensemble. Later works using NPs composed of rhodamine salts and its bulky counterions confirmed the possibility of highly efficient FRET from ~300 dyes to a single acceptor[63] as well as efficient photo-switching of dye-loaded NPs.[211] Here, we hypothesized that the use of much larger dye ensembles coupled by efficient exciton migration (ultrafast excitation energy transfer (EET)) inside NPs could generate giant light-harvesting antenna for amplifying the fluorescence of a single dye. This hypothesis was successfully realized using cationic rhodamine dyes encapsulated in a poly(methyl methacrylate-*co*-methacrylic acid) (PMMA-MA) matrix using bulky fluorinated counterions (Figure 1). These NPs of ~60 nm diameter can generate unprecedented 1000-fold amplification (antenna effect) of a single cyanine 5 derivative (DiD) acceptor located inside the particles. This result enabled for the first time observation of single molecules using the power density of 1 mW/cm^2, which is 10^4 - 10^6 fold lower than typically used in single molecule measurements.

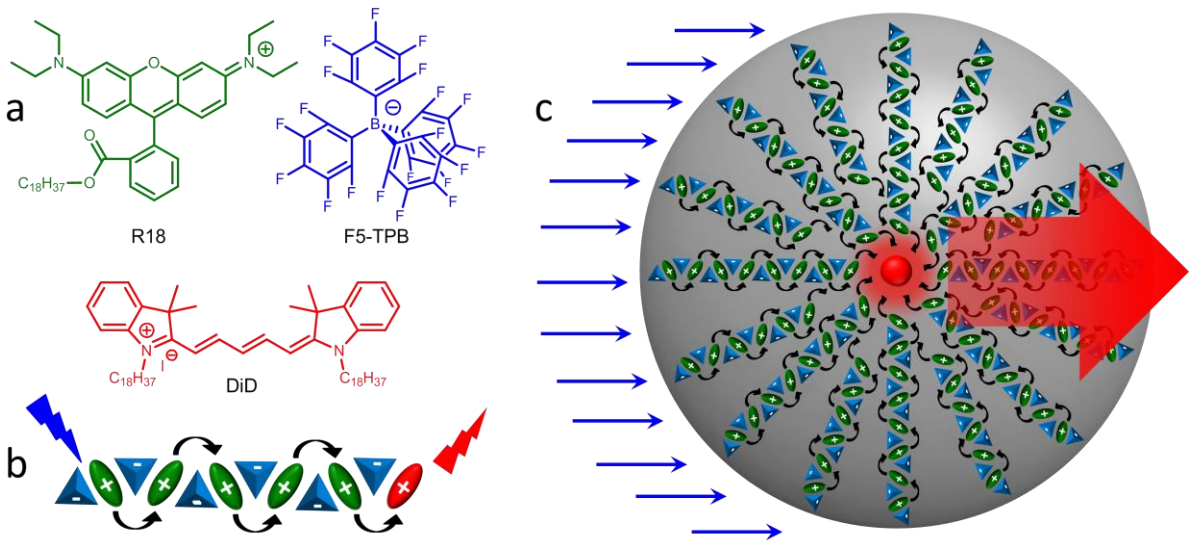

Figure 1. Concept of organic nano-antenna. (a) Chemical structures of the donor dye rhodamine B octadecyl ester (R18) and its counterion tetrakis(pentafluorophenyl)borate (F5-TPB) and of the acceptor dye cyanine 5 DiD. (b) Short-range ordering of R18 cations (green) by the F5-TPB counterion (blue) inside the PMMA-MA matrix prevents dye aggregation and

leads to short interfluorophore distance and ultrafast EET with subsequent FRET to a single acceptor molecule (red). (c) Schematic presentation of the giant light harvesting nano-antenna concept inside polymer NPs.

Results and discussion

The nano-antenna was designed based on PMMA-MA NPs, which were obtained using a previously proposed concept of nanoprecipitation based on hydrophobic polymers bearing few charged groups.[176] Nanoprecipitation of PMMA-MA from acetonitrile in phosphate buffer (pH 7.4) gave small NPs of ~40 nm (according to DLS) and narrow size distribution (PDI ~ 0.07), which is in good agreement with our previous studies.[170, 176] To encapsulate the energy donor dyes inside the NPs, they were mixed with the polymer in acetonitrile before the nanoprecipitation. A rhodamine B salt with the hydrophobic fluorinated counterion F5-TPB was used as it facilitates the dye encapsulation, minimizes self-quenching and ensures ultrafast exciton diffusion required for efficient energy transfer. To verify the role of EET on nano-antennas property we varied the interfluorophore distances by changing the level of dye loading. The increase in the dye content from 0.1 to 30 wt% (with respect to the mass of the polymer) produced some gradual increase in the NPs hydrodynamic diameter up to 65 nm, while keeping low values of the polydispersity index (PDI ~ 0.1). Nevertheless, according to TEM, the size of 30 wt% loaded NPs remained small (45 nm), which corresponded to 6300 dyes per NP (SI, Table S1).

The fluorescence quantum yields (QY) of the obtained NPs decreased with the dye loading but remained remarkably high (~36%) even at the highest loading (Figure 2a). This result corroborated with relatively small changes in the absorption spectra, where the short-wavelength shoulder, an indicator of dye aggregation,[212] showed minimal increase (Figure S1a). Moreover, the emission spectra of NPs displayed only small red shift without broadening (Figure S1b). According to our earlier report, the F5-TPB counterions function as a spacer between the charged dyes that prevent their self-quenching through pi-stacking.[170]

Nano-antenna with efficient FRET donor properties should present fast excitation energy transfer (EET) within the encapsulated donor dyes.[138, 211] When the energy migrates within encapsulated fluorophores that are randomly distributed inside a polymer matrix, the fluorescence anisotropy should decrease due to the energy hopping between dyes (Figure 2b).[213] As the dyes are confined within the rigid polymer matrix, the loss of fluorescence anisotropy in the system could be mainly attributed to the EET process. As expected, an increase in the dye loading produced a fast drop in the anisotropy values, indicating that shorter inter-fluorophore distances at higher loadings favored efficient exciton diffusion within these NPs (Figure 2a). At 30 wt% loading the average distance between encapsulated dyes should be ~1 nm, which is far below the Förster radius of homo-FRET transfer for R18/F5-TPB for this loading (4.6 nm) (SI, Table S2). Therefore, an efficient EET should take place, explaining this loss in the anisotropy, similarly to our previous studies.[170, 211] To understand better the EET process, we performed femtosecond anisotropy decay studies using a pump-probe technique. As expected, for low dye loading (1 wt% of R18/F5-TPB), the anisotropy remained stable during the first 10 ps, indicating that EET in this system should be very slow (Figure 2c). In sharp contrast, at high dye loading (30 wt%) the anisotropy decayed to zero already within 1 ps (Figure 2c). The bi-exponential fit revealed 30 fs (45%) and 600 fs (55%) components, the former being limited by the resolution of our setup (60 fs pulse width). This means that the EET process is exceptionally fast and thus can involve thousands of dyes within their emission lifetime (~4 ns[170]).

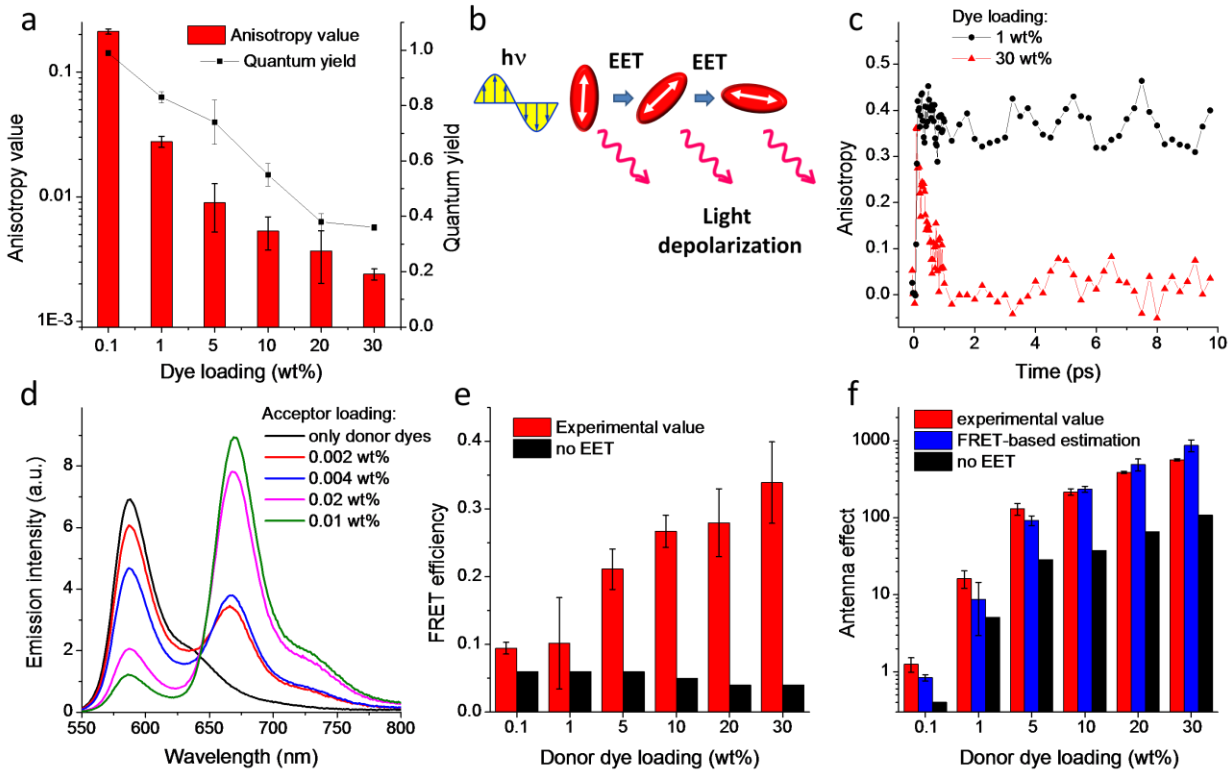

Figure 2. Spectroscopic characterization of organic nano-antennas. (a) Steady-state fluorescence anisotropy of the encapsulated donor dyes (R18/F5-TPB) as a function of their loading in PMMA-MA NPs of 65 nm hydrodynamic diameter (45 nm by TEM) and their quantum yield.[214] (b) Schematic presentation of fluorescence anisotropy loss due to EET within randomly oriented fluorophores (c) Anisotropy decay measured at 580 nm with a 50-fs probe beam for NPs loaded at 1 and 30 wt% of donor dyes. (d) Emission spectra of FRET NPs loaded with different amounts of the acceptor dyes while keeping the same amount of the donor (30 wt%). The emission intensity was normalized to the same absorbance of the donor. (e) Experimental FRET efficiency for FRET NPs with varied donor but constant acceptor (0.004 wt%) concentration and the calculated one for NPs without exciton diffusion (marked no EET). (f) Amplification factor of the acceptor emission (antenna effect) measured from the excitation spectra and its estimated values based on the observed FRET efficiency. Error bars in (a, e, f) represent the standard error of the mean (s.e.m., n=3). Samples marked "No EET" represent theoretical calculations in the absence of exciton diffusion within donor dyes.

Next we introduced a FRET acceptor dye into the NPs, by nano-precipitating an acetonitrile solution of polymer together with donor and accepter dyes in phosphate buffer. As the acceptor, we chose the lipophilic cyanine 5 derivative DiD. It is a perfect energy acceptor for rhodamine

B with very good spectral overlap, and its two hydrophobic octadecyl chains should ensure efficient encapsulation inside polymer matrix, as it was shown for PLGA NPs.[102] Being encapsulated at 0.02 wt%, DiD showed a high fluorescence quantum yield of 77±4%, so that our antenna was tested on a highly emissive acceptor. For NPs containing 30 wt% of donor dyes, an increase in the acceptor concentration resulted in a rapid growth of acceptor emission, accompanied by a drop of the donor emission, indicating a FRET process (Figure 2d). Remarkably, efficient FRET (34%) was already observed for 0.004 wt% of the acceptor (with respect to the mass of the polymer), which corresponds to 1.3 acceptors per 45 nm particle, and ensures that >70% of NPs will contain at least one acceptor according to Poisson distribution (Figure S2). Thus, in these NPs a single acceptor could produce FRET from ~6300 donors through distance of >20 nm (NPs radius) that is much larger than the Förster radius. To understand better the role of exciton diffusion in this efficient FRET process, we prepared NPs with a constant concentration of the acceptor (0.004 wt%) and varied the concentration of the donor (0.1-30 wt%). Theoretical prediction, assuming no donor-donor communication (no EET), suggested negligibly low FRET efficiency (4-6%) for 0.004 wt% acceptor independently from the donor loading (Figure 2c, Note S1, Table S3). However, according to our experiments, the increase in the donor loading produced a rapid growth of the acceptor relative intensity (Figure S3) due to increase in the FRET efficiency (Figure 2e). This efficient FRET is probably a result of fast EET within donors revealed by fluorescence anisotropy (Figure 2a-c).

Importantly, NPs characterized by efficient FRET from multiple donors to a single acceptor should behave like a giant light-harvesting nano-antenna. To quantify the antenna effect (AE), we recorded the excitation spectra of the donor and acceptor at the emission wavelength of the acceptor (700 nm, Figure S4). AE was measured as the ratio of the maximal excitation intensity of the donor to that of the acceptor with correction on the emission of the donor dyes in the acceptor channel, as described in Materials and Methods.[209] At low loading of the donor dye, no antenna effect was observed (AE<1), whereas at higher donor loadings, AE increased up to 560 for 30 wt% NPs of 45 nm (Figure 2f). These values correlated well with the antenna effect calculated based on the FRET efficiency, number and extinction coefficient of donor and acceptor dyes, that could be determined as AE = (nDεDE)/(nAεA), where nD and nA are the numbers of donors and acceptors, respectively, per particle, εD and εA are the extinction coefficients of donors and acceptors, respectively, and E is the FRET efficiency (Figure 2d).[63, 209] By contrast, theoretical estimations assuming no EET gave AE values much

below the experimental ones (3-6 fold lower), emphasizing the importance of the communication within donor dyes for obtaining an efficient antenna.

Exciton diffusion should propagate at relatively long distances and thus ensure efficient FRET even for nano-antennas that are much larger than the Förster radius of the FRET partners. Therefore, we investigated the influence of the size of nano-antenna on the FRET efficiency from multiple donors (30 wt% dye loading) to few acceptors inside NPs. As the charge of the polymer is the key factor for controlling the size of NPs prepared by nanoprecipitation,[176] we varied the pH of the phosphate buffer during the preparation of NPs, which should change the protonation state of the carboxylate of the PMMA-MA polymer. Based on DLS measurements, a decrease of pH from 9.0 and 5.8 produced an increase in NP size from 30 to 200 nm, while preserving a narrow polydispersity (Table 2). Transmission electron microscopy (TEM) confirmed the increase in NPs size with decrease in pH of buffer, but revealed that the sizes of NPs were smaller, in the range of 30-67 nm for pH range from 9.0 to 6.5. However, for pH 5.8 aggregates of >100 nm size were observed (Figure 3a).

Table 2. Hydrodynamic diameter and spectroscopic properties of PMMA-MA NPs encapsulating 30 wt% of R18/F5-TPB prepared at varied pH.

Sample	pH[a]	Size, DLS (nm)[b]	PDI	Size, TEM (nm)[c]	QY[d]	Anisotropy	Donors/NPs[e]	SPB[f] estim.	SPB[g] exp.
NPs30	9.0	36 ± 1	0.11	30±9	0.41±0.04	0.001	1900	1	1
NPs45	7.4	65 ± 4	0.11	45±8	0.39±0.03	0.0028	6300	3	5
NPs60	6.7	105 ± 5	0.11	60±22	0.38±0.02	0.0025	15000	8	12
NPs67	6.5	139 ± 8	0.13	67±27	0.36±0.03	0.0024	21000	11	20
NPs107	5.8	201± 11	0.17	107±43	0.35±0.03	0.0029	85000	45	31

[a] After preparation, NPs were diluted in pH 7.4 buffer. [b] Statistics by volume was used in DLS measurements (error is s.e.m., n ≥ 3). PDI is polydispersity index. [c] Error is the standard deviation based on analysis of 80 – 500 NPs. [d] Quantum yield of NPs without acceptor molecules (error is s.e.m., n ≥ 3). [e] Estimation is based on NPs size measured by TEM. [f] Estimated changes in single molecule brightness based on QY and size of NPs measured by

TEM. [g] Normalized single particle brightness of NPs under illumination of a 532 nm laser with power 0.1 W/cm^2.

Independently of the NPs size, the QY remained high (0.35-0.41, Table 2). Moreover, according to wide-field fluorescence microscopy of NPs immobilized on the surface, the single particle brightness increased with size (Figure 3b), so that the largest NPs (NPs107) were 31 times as bright as the smallest ones (NPs30) (Table 2). This was expected because larger NPs should encapsulate more dyes, proportionally to the particle volume. Moreover, the experimental brightness correlated well with our estimations based on QY and the size of NPs measured by TEM. Finally, the anisotropy values were close to zero for all particles sizes (Table 2), indicating that EET was efficient in all these systems.

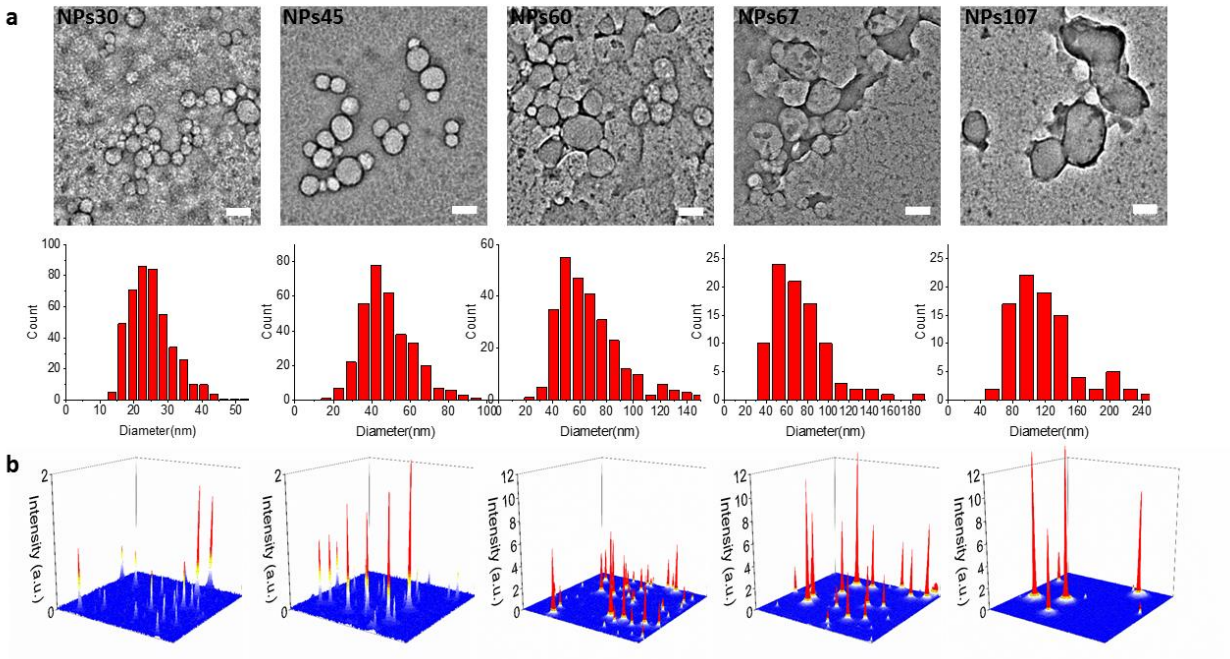

Figure 3. Structure and brightness of individual nano-antennas. (a) TEM images and size histograms of NPs prepared with different pH of buffer. Scale bar is 50 nm (b) 3-D representation of wide-field fluorescence microscopy images of NPs of different sizes containing 30 wt % R18/F5-TPB under illumination of a 532 nm laser with power 0.1 W/cm^2, integration time was set to 30.53 ms.

Using different pH of phosphate buffer, we prepared nano-antennas of different size containing 30 wt% of R18/F5-TPB donors with varied amount of acceptor corresponding to

donor/acceptor ratio 1000 and 10000 (0.02 and 0.002 wt%, respectively). For both ratios, an increase in the NP size increased the contribution of the acceptor emission (Figure 4a) and the FRET efficiency (Figure 4b). Thus, for the same donor/acceptor ratio, the larger antennas transfer the energy more efficiently to the acceptor (Figure S5). The antenna effect also increased with NP size, especially for NPs with donor/acceptor ratio of 10000 (Figure 4b). Remarkably, for NPs60 and NPs67 the enhancement of the acceptor emission (1.5 and 2.1 acceptors per NPs) reached 1000-fold (Figure 4b), which, to our knowledge, is by far the highest FRET-based amplification of dye emission reported to date.

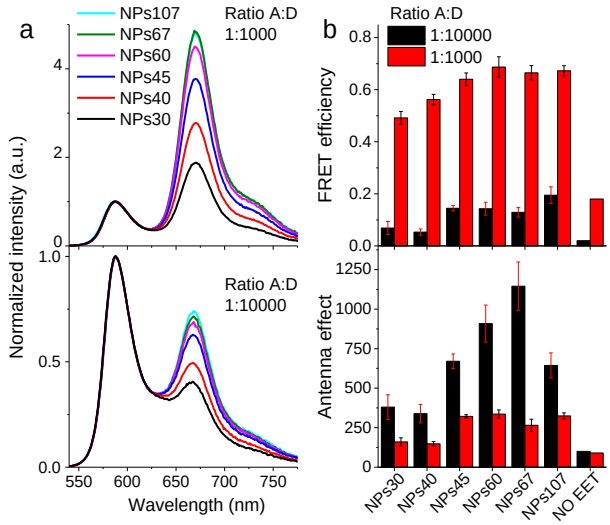

Figure 4. Effect of size of nano-antennas on their performance. Fluorescence spectra (a), FRET efficiency and antenna effect (b) of PMMA-MA FRET NPs of different size loaded with 30 wt% of R18/F5-TPB and DiD. Donor/Acceptor ratios were 1000:1 or 10000:1. Error bars represent the standard error of the mean (n=3). Sample marked "No EET" represents theoretical calculations in the absence of exciton diffusion within donor dyes.

Then, we immobilized our nano-antennas on the glass surface and imaged them by wide-field TIRF microscopy (Figure 5). The control NPs without acceptors appeared as bright spots at the donor channel and as dim spots at the acceptor channel. In the presence of ~1.5 acceptors particle the emission in the acceptor channel became comparable or brighter than that in the donor channel (Figure 5a). This result showed that inside the nano-antennas, the emission of 1-2 acceptors was comparable to the emission of thousands of donor dyes. However, the overlaid images revealed some heterogeneity in the relative donor/acceptor emission, because statistically some NPs did not contain any acceptor molecules, while others could contain more than one acceptor.

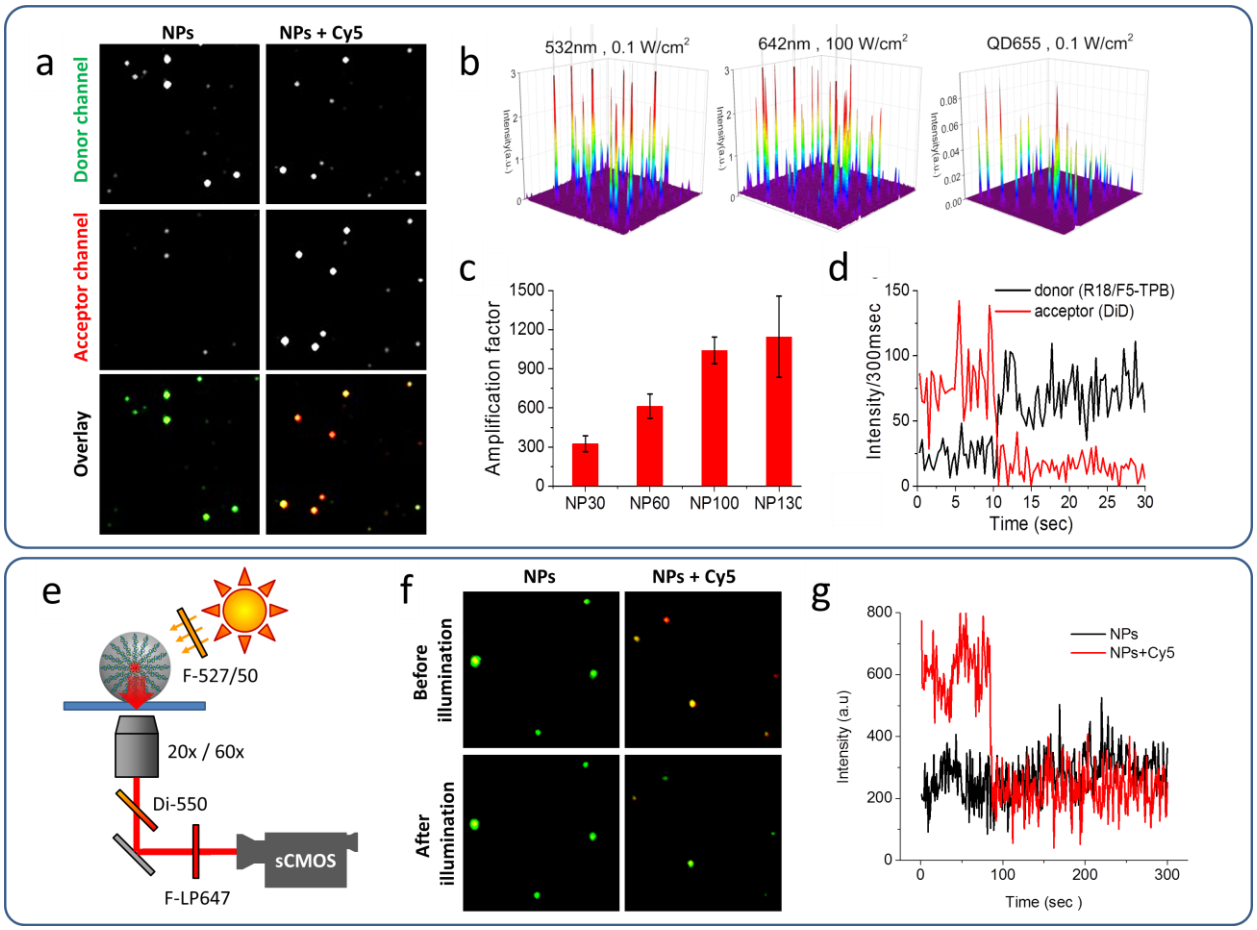

Figure 5. Single-particle evaluation of nano-antenna performance. (a) Wide-field fluorescence microscopy images of NPs. Right panel represents images of NPs (NPs60) without acceptor and left ones are the images of NPs containing 30 wt % R18/F5-TPB and ~1.5 Cy5 (DiD) acceptors per particle. The illumination at 532 nm was set to a laser power of 1 W/cm^2, integration time was set to 30.53 ms. Both channels are represented at the same intensity scale. Overlay images represent false color composite of two channels, where red color corresponds to the acceptor channel and green to donor channel. (b) 3D representation of wide-field TIRF images of acceptor emission from FRET NPs (60 nm size) containing 30 wt% R18/F5-TPB and ~1.5 Cy5 (DiD) acceptors under the illumination at 532 nm with laser power 0.1 W/cm^2, under the direct excitation of acceptor at 642 nm with laser power 100 W/cm^2 and of QD 655 under illumination at 532 nm with laser power 0.1 W/cm^2. In all cases integration time was 30.53 ms. (c) Amplification factor of acceptor emission calculated by eq. 1 for antennas of different size 1-2 acceptor per NP. (d) Representative single particle trace excited at 532 nm with a power density of 1 mW/cm^2. (e-g) Scheme of experimental setup and obtained results, using excitation by external light source that mimics direct sunlight. (f) Single particle

FRET microscopy with overlaid donor and acceptor channels under sunlight excitation mimics using NPs containing ~1.5 Cy5 before and after 5 min illumination. (g) Single particle traces at the acceptor channel for NPs without and with Cy5 acceptor.

To quantify the amplification of acceptor emission under the microscope, we compared the acceptor intensity under excitation through FRET at 532 nm to that obtained by direct excitation with a 642 nm laser. Remarkably, to obtain similar acceptor intensities, the excitation through nano-antennas NPs60 at 532 nm required ~1000-fold lower laser power than direct excitation of the acceptor at 642 nm (Figure 5b). The amplification factor of acceptor emission at the single particle level was determined as:

$$AF = \frac{I_A^{532nm}}{I_A^{642nm}} \times \frac{P^{642nm}}{P^{532nm}} \qquad (1)$$

where I_A^{532nm} , I_A^{642nm} are the mean intensities of acceptors under excitation at 532 and 642 nm, respectively, and P^{532nm} and P^{642nm} are laser powers at the corresponding wavelengths. Using equation (1), we found that the amplification factor increased with the particle size (Figure 5c). For NPs60, we obtained a ~1040±100-fold amplification factor, which is in good agreement with the antenna effect measured from the excitation spectra. Owing to this giant amplification factor, the brightness of 1-2 acceptors inside NPs60 was 25-times higher than that of a QD655 excited at 532 nm with the same power (Figure 5b). This is an exceptional performance of single Cy5 dyes, taking into account that the extinction coefficient of QD655 at 532 nm is 2.4×10^6 $M^{-1}cm^{-1}$ and QY is close to unity.

The values of antenna effect reported in the literature vary in the range of 3-100 dependent on the system. For instance, in DNA-origami containing intercalated donor and acceptor dyes the AE value reached 12.[209] In a recent report, nanocrystals of difluoroboron chromophores at high D/A ratio, which were claimed to be one of the most efficient light-harvesting systems, the AE value was 28-29.[215] Similar values of AE (31) was reported later on for dye-doped-polymer NPs loaded with coumarin 123 (donor) and Nile Red (acceptor) dyes.[216] Our recent report showed that this value can be increased to up to 200 in ionic NPs using R18 and bulky counterion,[63] though we did not provide direct proof for amplification using single molecule microscopy. Thus, the antenna effect achieved in the present work goes far beyond those reported for other light-harvesting systems. The unique efficiency of our system relies on two key factors. The first one is the high quantum yield of $>10^4$ donor dyes encapsulated within our polymeric nano-antenna at 30 wt%, which ensures that a large part of the excitation energy is

delivered to the acceptor with minimal energy losses. The second factor is the exceptional excitation energy migration within the encapsulated donor dyes on the time scale <60 fs (resolution of the setup). Though one could explain it by ultrafast Förster/Dexter homo-transfer mechanisms, recent works on light-harvesting systems propose coherent energy transfer[217, 218] for conjugated polymers,[219, 220] photosynthetic systems,[221, 222] and dye assemblies,[206] which could also take place in our nano-antenna. The coherent energy transfer in our nano-antennas could be favored by the very short inter-fluorophore distances (~1 nm) at 30 wt% dye loading.

Finally, using our NPs60 nano-antenna, we could observe single molecule events, such as one-step bleaching of the Cy5 (DiD) acceptor at extremely low laser powers of 1 mW/cm^2 (Figure 5d), which was accompanied by one step growth of the donor emission. This opposite behavior of donor and acceptor is typically observed in single molecule FRET measurements using one donor and acceptor dyes, but here FRET takes place between 15000 donors and 1-2 acceptors. Moreover, previous reports on single-molecule detection were systematically based on light power densities of 10-5000 W/cm^2. Presently, we obtained similar single molecule traces at 1-10 mW/cm^2, reaching the values of the ambient sunlight. Therefore, we tested whether our nano-antennas enable detection of single molecules using a simple microscopy setup where the excitation is provided by directly shining light on the sample at powers equivalent to sunlight. The measured power of direct sunlight (at midday, 19 October, 2016, Strasbourg) through the excitation filter 527/50 nm was 24 mW cm^{-2}. In our setup, we applied an artificial white light source providing 15 mW cm^{-2} through the same filter. The fluorescence of immobilized NPs60 nano-antennas with ~1.5 Cy5 dyes was collected using either 20x air or 60x oil immersion objective and detected using sCMOS camera (Figure 5e). According to overlaid images of donor (green) and acceptor (red) channels, these NPs displayed significant acceptor emission (appear in yellow-red), in contrast to control NPs without acceptor that appeared in green (Figure 5f). Moreover, after 5-min illumination with our artificial light source, the former NPs lost the acceptor emission, probably due to acceptor bleaching, and became similar to the control NPs. Strikingly, using 20x air objective, we were able to record in the acceptor channel one-step bleaching events, corresponding to single Cy5 dye molecules (Figure 5g). By contrast, the control NPs displayed much lower intensity at the acceptor channel without abrupt bleaching steps.

Thus, our nano-antennas enable detection of single molecules using a simple sCMOS-camera-based imaging setup under ambient sunlight-like conditions, which opens the way to single molecule photography.

Acknowledgements

This work was supported by the European Research Council ERC Consolidator grant BrightSens 648528. C. Ruhlmann for help with electron microscopy. K.T. was supported by a fellowship from the Ministre de la Recherche (France).

Author contributions

A.S.K. proposed the concept; A.S.K. and K.T. designed the experiments; K.T. performed most of the experiments and data analysis. A.R. helped with data analysis and electron microscopy. P.D. and F.F. performed time-resolved anisotropy measurements, Y.M. and P.G. participated in discussions and manuscript correction. A.S.K., K.T. and A.R. wrote the manuscript.

Competing financial interests

The authors declare no competing financial interests.

Additional information

Supplementary information is available in the online version of the paper. Reprints and permissions information is available online at www.nature.com/reprints. Correspondence and requests for materials should be addressed to A.S.K.

Methods

Materials. Poly (methyl methacrylate-co-methacrylic acid) (PMMA-MA, 1.3% methacrylic acid, Mn ~15000, Mw ~34000), acetonitrile (anhydrous, 99.8%), rhodamine B octadecyl ester perchlorate (>98.0%), lithium tetrakis (pentafluorophenyl)borate ethyl etherate were purchased from Sigma-Aldrich. DiD oil (1,1'-Dioctadecyl-3,3,3',3'-Tetramethylindodicarbocyanine Perchlorate) (Cy5) was purchased from Life-Technologies. Sodium phosphate monobasic (>99.0%, Sigma-Aldrich) and sodium phosphate dibasic dihydrate (>99.0%, Sigma-Aldrich) were used to prepare 20 mM phosphate buffers at pH 5.8-9.0. Milli-Q water (Millipore) was used in all experiments.

Synthesis. Rhodamine B Octadecyl Ester Tetrakis(penta-fluorophenyl)borate (R18/F5) was synthesized by ion exchange and purified by column chromatography as described previously.[1]

Nanoparticle Preparation. Stock solutions of the polymer in acetonitrile were prepared at a concentration 2 mg mL^{-1} containing different amount of R18/F5-TPB (0.1 to 30 wt % relative to the polymer). 50 µL of the polymer solutions were then added quickly using a micropipette and under shaking (Thermomixer comfort, Eppendorf, 1000 rpm) to 450 µL of 20 mM phosphate at 21°C. The particle solution was then quickly diluted 5-fold with the phosphate buffer 20 mM, pH7.4. For preparation of FRET nanoparticles, different concentrations of DiD (from 0.001 wt% to 0.04 wt % relative to the polymer) were added to the acetonitrile solution of polymer containing desired concentration of R18/F5-TPB, and the particles were prepared as described above. Preparation of NPs of different size was achieved by varying the pH of phosphate buffer at the first dilution.

Nanoparticle characterization. Measurements for the determination of the size of nanoparticles were performed on a Zetasizer Nano ZSP (Malvern Instruments S.A.). The mean value of the diameter of the size distribution per volume was used for analysis. Absorption spectra were recorded on a Cary 4000 scan UV-visible spectrophotometer (Varian), excitation and emission spectra were recorded on a FluoroMax-4 spectrofluorometer (Horiba Jobin Yvon) equipped with a thermostated cell compartment. For standard recording of fluorescence spectra, the excitation wavelength was set 530 nm. The fluorescence spectra were corrected for detector response and lamp fluctuations. To calculate FRET efficiency based on fluorescence spectra, a classical equation was used: $E_{FRET} = 1 - \frac{I_{D-A}}{I_D}$, where I_D is the integral donor intensity and $I_{D\text{-}A}$ integral intensity of donor in presence of acceptor. Measurement of fluorescence anisotropy was performed at 20°C with a Fluorolog spectrofluorometer (Horiba Jobin Yvon). Excitation wavelength was set at 530 nm and detection at 585 nm. Each

measurement of the anisotropy value corresponds to an average over 10 subsequent measurements of 0.1 s each. For standard recording of excitation spectra, the emission wavelength was set 700 nm. These spectra were corrected for the lamp intensity. The antenna effect was then expressed as the ratio of the maximal excitation intensity of the donor to that of the acceptor with correction on the emission of the donor dyes at 700 nm:

$$AF = \frac{I_{D-FRET}^{ex} - I_{D}^{ex} * f}{I_{A-FRET}^{ex} - I_{A}^{ex} * f}$$

Where I_{D-FRET}^{ex} and I_{A-FRET}^{ex} are the maximal excitation intensities of donor and acceptor in FRET NPs, respectively; I_{D}^{ex} and I_{A}^{ex} are the excitation intensities at the wavelengths of excitation maximum of donor and acceptor in NPs without acceptors, respectively; f is the correction factor calculated as the ratio of maximum emission intensity of donor for FRET NPs to that for NPs without acceptor dyes:

$$f = \frac{I_{D-FRET}^{em}}{I_{D}^{em}}$$

The value of the antenna effect was also estimated based on the FRET efficiency using the following equation: AE = ($n_D \times \varepsilon_D \times E$)/($n_A \times \varepsilon_A$), where nD and nA are the numbers of donors and acceptors, respectively, per particle, εD and εA are the extinction coefficients of donors and acceptors, respectively, and E is the FRET efficiency. QYs of NPs were calculated using Rhodamine 101(QY=1) in ethanol as a reference with an absorbance of 0.01 at 530 nm.[2] QY of an acceptor molecule DiD in PMMAMA matrix was calculated for the concentration 0.02 wt% using DiD in methanol (QY=0.33) as a reference.[3]

Time-resolved anisotropy. For the time-resolved anisotropy measurements, we used an amplified Ti:sapphire laser that produces ultrashort pulses (100 fs) at a repetition rate of 100 kHz. 60 fs linearly polarized pulses centered at 520 nm (Δλ = 12 nm) were obtained by means of an optical parametric amplifier (OPA). The pump's power density was around 120 W cm^{-2} for all the measurements. Ultrashort continuum probe pulses were generated in a sapphire crystal (500-800 nm). The normalized differential transmission of a 60 fs linearly polarized probe (parallel or perpendicular to the pump polarization) centered around 580 nm (Δλ=13 nm) was measured as a function of the pump-probe delay by using a monochromator coupled to a liquid nitrogen cooled CCD (Princeton Instrument). The anisotropy decay was calculated using

the following relation $\frac{\left(\frac{\Delta T_{//}}{T_{//}} - \frac{\Delta T_{\perp}}{T_{\perp}}\right)}{\left(\frac{\Delta T_{//}}{T_{//}} + 2\frac{\Delta T_{\perp}}{T_{\perp}}\right)}$ where // and ⊥ denotes for a probe beam with a linear polarization parallel and perpendicular with respect to the linear polarization of the pump beam. The decay curves were fitted with a bi-exponential function and the analysis took into account the laser pulse duration.

Transmission electron microscopy (TEM). Five microliters of the particle solution were deposited onto carbon-coated copper-rhodium electron microscopy grids that were used either as obtained or following an air or amylamine glow-discharge. The grids were then treated for 1 min with a 2%uranyl acetate solution for staining. They were then observed with a Philips CM120 transmission electron microscope equipped with a LaB6 filament and operating at 100 kV. Areas covered with nanoparticles of interest were recorded at different magnifications on a Peltier cooled CCD camera (Model 794, Gatan, Pleasanton, CA). Image analysis was performed using the Fiji software.

Fluorescence Microscopy. For single particle fluorescence microscopy measurements, the NPs were immobilized on glass surfaces on which a polyethylenimine (PEI) layer was initially adsorbed. The solutions of NPs were diluted 5000, 2000, 1000 and 500 times for NPs30, NPs45, NPs60, NPs67 and NPs107 correspondingly. 400 µL of these solutions per cm^2 were then brought in contact with the PEI covered glass for 15 min, followed by extensive rinsing with Milli-Q-water. The surfaces were left in Milli-Q water during microscopy.

Single particle measurements were performed in the TIRF (Total Internal Reflection Fluorescence) mode on a homemade wide-field setup based on an Olympus IX-71 inverted microscope with a high-numerical aperture (NA) TIRF objective (Apo TIRF 100 ×, oil, NA 1.49, Olympus). A 532 nm diode laser (Cobolt Samba 100) and a 642 nm diode laser (Spectra-Physics Excelsior 635) were used to excite the samples. The 532 nm laser intensity was set to 1mW/cm^2 – 100mW/cm^2 by using a polarizer and a half-wave plate (532 nm). For direct excitation of acceptor Cy5, the 642 nm laser was used with intensity 0.1kW/cm^2. The fluorescence signal was recorded with an EMCCD (ImagEM Hamamatsu) (0.106 μm pixel size) using an open source Micro-Manager software. The exposure time was set to 30.53 msec per image frame. To enable two channel images W-VIEW GEMINI image splitting optics were used with the following filter set: dichroic 640 nm (Semrock FF640-FDi01-25x36), bandpass

filters 593±20 nm(Semrock FF01-593/40-25) and 685±20 nm (Semrock FF02-685/40-25)) were used to image R18/F5-TPB and Cy5, respectively. Single particle analysis was performed using the Fiji software: particle locations were detected through a Fiji routine applied to a projection (maximum intensity) of 1000 frames. After the automatic background subtraction, the mean intensities of circular regions of interest with a diameter of 8 pixels around the found particle locations were then measured. At least three image sequences (245pixel × 245pixel) per condition were analyzed with, on average, 500-700 particles per sample.

Microscopy mimicking ambient sunlight excitation. The sunlight power density (24 mW cm^{-2}) was recorded at midday on 19 October, 2016, Strasbourg region, using Handheld Laser Power Meter, 1917-R and Semrock band-pass filter 527 nm (50 nm bandwidth). The artificial white light mimicking sunlight was provided by a Cold light source from Zeiss, type KL 1500 LCD. The sample was illuminated from the top ~2 cm from the divergent light source output through the same 527-nm filter, which corresponded to 15 mW cm^{-2} power density at the sample. Single-molecule imaging was done using Nikon Ti-E inverted microscope using CFI Plan Apo 20× air (NA = 0.75) and CFI Plan Apo 60× oil (NA = 1.4) objectives and Hamamatsu Orca Flash 4 camera. Donor channel was recorded through a 600-nm band-pass filter (50 nm bandwidth, Semrock), while the acceptor channel used 647-nm long-pass filter (Semrock). Data were recorded and analyzed using NIS Elements and Fiji software, respectively.

Supporting Information

Giant light harvesting nano-antenna for single-molecule detection at ambient light

Kateryna Trofymchuk, Andreas Reisch, Pascal Didier, François Fras, Pierre Gilliot, Yves Mely, and Andrey S. Klymchenko

Table S3. Hydrodynamic diameter and polydispersity of PMMA-MA NPs encapsulating different concentrations of R18/F5-TPB measured by DLS[a]

NPs loading (wt%)	Diameter (nm)	PDI[b]
0	41	0.067
0.1	49	0.105
1	53	0.103
5	55	0.096
10	58	0.091
20	60	0.103
30[c]	65	0.101

[a] Statistics by volume was used in the analysis. The standard error on the hydrodynamic diameter from 3 measurements was ±2 nm for all NPs, except NPs with 30 wt% of loading, where it was ±4 nm. [b] PDI is the polydispersity index. [c] According to TEM, the size of these NPs is 45 nm.

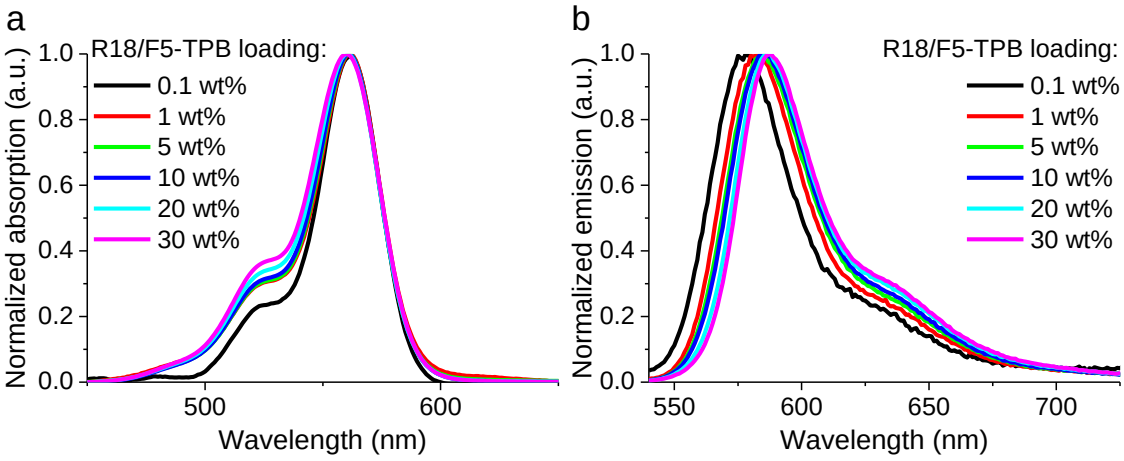

Figure S1. Spectroscopic properties of PMMA-MA loading with 0.1 wt%-30 wt% of R18/F5-TPB. (a) Normalized absorption spectra. (b) Normalized emission spectra. Excitation wavelength was set at 530 nm, slits were adjusted to obtain sufficient signal.

Table S2. Dependence of Förster distance for homo FRET on dye loading

NPs loading, wt%	Homo FRET distance R_0, nm	Average distance between encapsulated R18/F5-TPB dyes, nm [a]
0.1	6.6	7.3
1	6.2	3.4
5	5.6	2.0
10	5.3	1.6
20	4.8	1.2
30	4.6	1.0

[a] Distance was calculated for isotropic distribution of fluorophores by: $l_{iso}=0.504/\sqrt[3]{c}$, where c is the concentration of the dye.

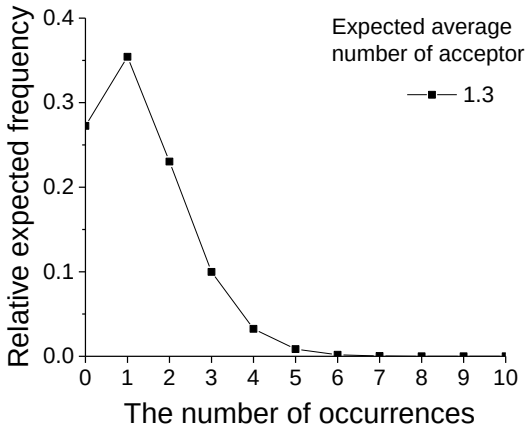

Figure S2. Poisson distribution of the number of acceptors (0.004 wt %) encapsulated per NP with 0.1-30 wt% of R18/F5-TPB. The horizontal axis corresponds to the number of acceptors per NP. The connecting lines are only guides for the eye.

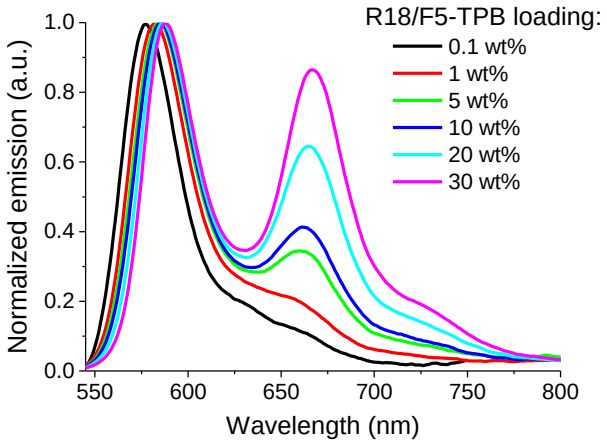

Figure S3. Normalized emission spectra of FRET NPs loaded with different amounts of the donor dyes while keeping the same level of the acceptor dyes (0.004 wt %).

Theoretical calculation of FRET efficiency

Note S1. Assuming an homogenous distribution of fluorophores, we can calculate the FRET efficiency inside NPs in case of absence of energy migration between donor dyes. To this end, we used the model of energy transfer to multiple acceptors in a homogeneous solution of donors and acceptors, without D–A diffusion. In the absence of homotransfer between donors, the steady state intensity of the donor is given by[223]

$$\frac{F_{DA}}{F_D} = 1 - \sqrt{\pi} * \gamma * \exp(\gamma^2)[1 - \mathrm{erf}(\gamma)].$$

In this expression $\gamma = \frac{A}{A_0}$, where A is the acceptor concentration. A_0 is the critical concentration representing the acceptor concentration that results in 76% energy transfer. It can be calculated by $A_0 = \frac{447}{R_0^3}$,where R_0 is in Å. The error function erf(γ) is given by:

$$\mathrm{erf}(\gamma) = \frac{2}{\sqrt{\pi}} \int_0^{\gamma} \exp(-x^2)\, dx$$

The FRET efficiency could be calculated as:

$$E_{FRET} = 1 - \frac{F_{DA}}{F_D} = \sqrt{\pi} * \gamma * \exp(\gamma^2)[1 - \mathrm{erf}(\gamma)]$$

The Förster distance was calculated by: $R_0 = 0.211 \left[\frac{k^2 Q_D J(\lambda)}{n^4}\right]^{1/6}$.

The overlap integral $J(\lambda)$ was calculated using the FluorTools software [224]. Though RhB emission has a tendency to red shift and thus to induce an increased spectral overlap with an increase in its loading, the drop of its donor quantum yield leads to a decrease of the Förster distance (Table S2).

Table S3. Comparison of the theoretical FRET efficiency inside NPs calculated in the absence of homo-FRET (EET) with the experimental FRET value.

NPs loading, wt%	$J(\lambda)$,$M^{-1}cm^{-1}nm^4$ [a]	Q_D [b]	Number of acceptors per NP	R_0 [c], Å	Theoretical calculation [d] E_{FRET}	Experimental value E_{FRET}
0.1	9.73×10^{15}	0.99	1.6	70	6%	9%
1	1.13×10^{16}	0.83	2.0	69	6%	10%
5	1.29×10^{16}	0.74	2.3	70	6%	21%
10	1.33×10^{16}	0.55	2.7	67	5%	27%
20	1.38×10^{16}	0.38	3	63	4%	28%
30	1.41×10^{16}	0.36	4.3	61	4%	34%

[a] Overlap integral. [b] Quantum yield of donor dyes. [c] R_0 is the Förster distance for FRET pair R18 and DiD, which depends on the donor loading. [d] Theoretical FRET efficiency calculated in the absence of exciton diffusion.

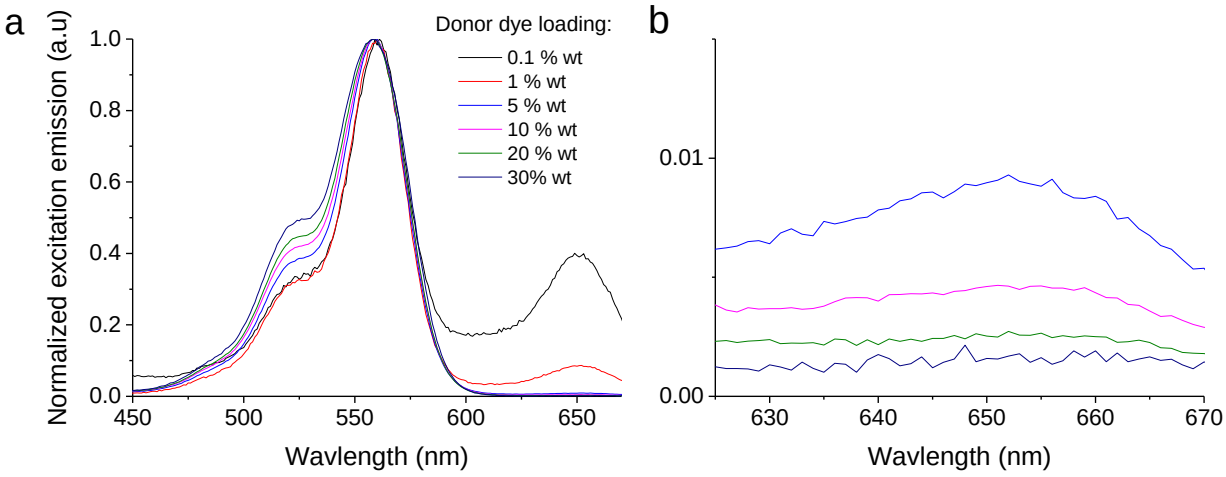

Figure S4. Excitation spectra describing the antenna effect. (a) Excitation spectra of NPs with 0.1-30 wt% R18/F5 containing 0.004 wt% of DiD acceptor dye. (b) Zoomed region of the excitation spectra focused on the excitation of the acceptor. Emission was detected at 700 nm.

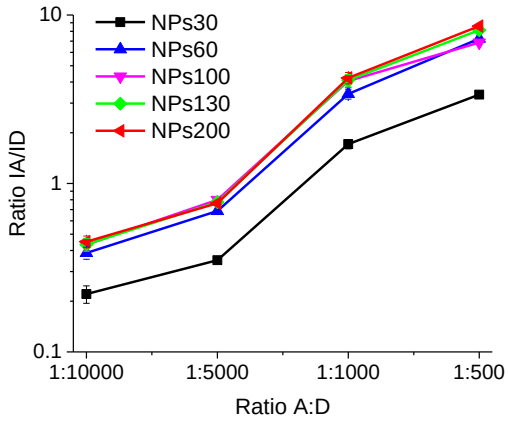

Figure S5. Ratio of acceptor and donor emission bands for NPs of different sizes as a function of the donor: acceptor ratio at the excitation wavelength of donor dyes (530 nm).

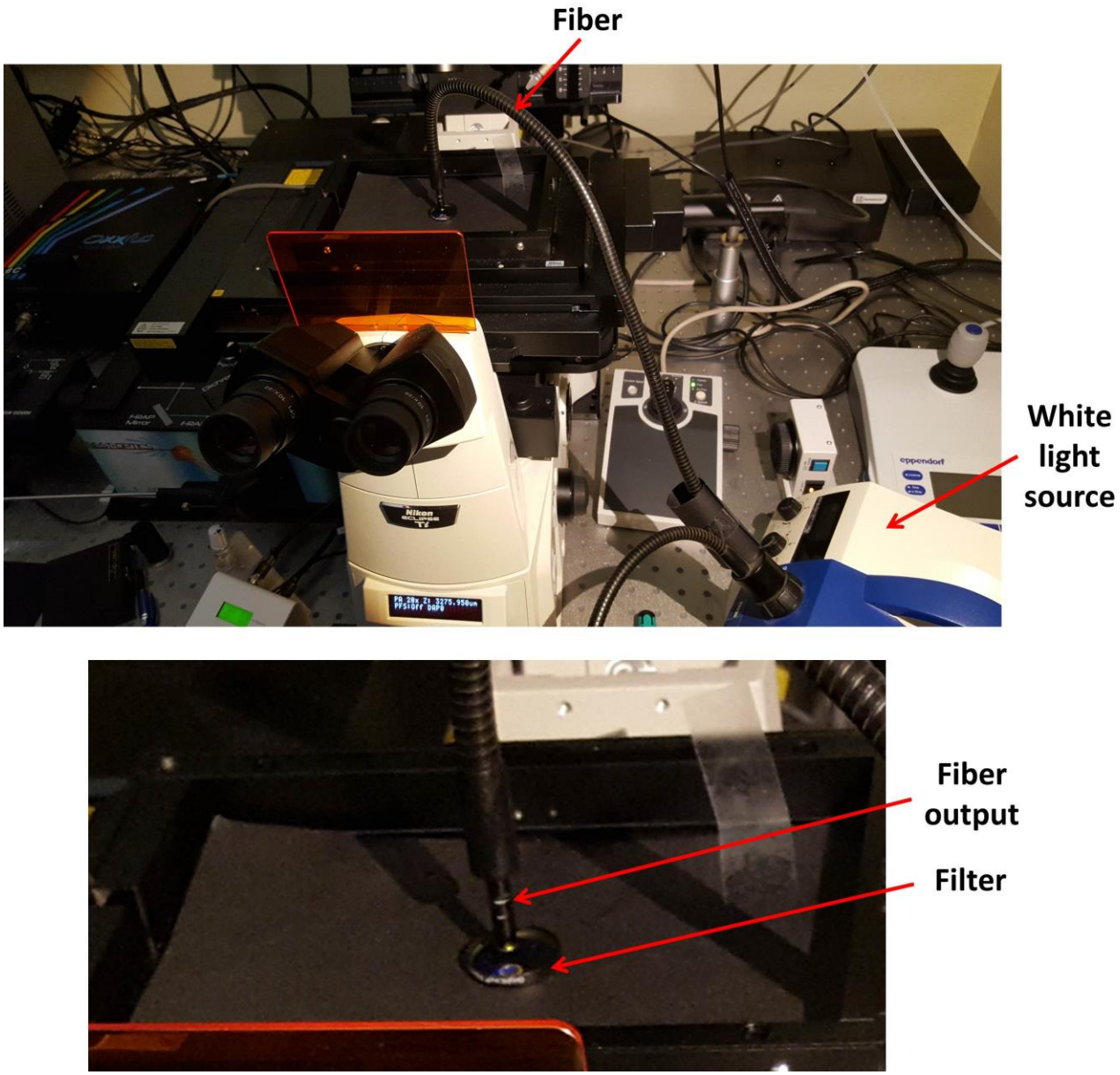

Figure S6. Photo of experimental setup that uses excitation by a divergent light, mimicking the sunlight. The divergent excitation light of the white light source was brought to the sample through a liquid optical fiber. The fiber output was pointed towards the sample (not visible in the figure) at ~2 cm distance. Filter (527 nm, 50 nm bandwidth) was placed between the fiber output and the sample. The light was collected from the bottom using 20x or 60x objective and recorded with a sCMOS camera.

2.3. **FRET to the surface of polymer NPs:** Organic nanoparticle antenna for amplified FRET-based biosensing

FRET is widely used for bioimaging applications due to its extremely high sensitivity to distance [2, 88] and the simplicity of building ratiometric sensors. [225] Conventional FRET biosensors based on molecular dyad of fluorophores connected covalently by a spacer, suffer from photobleaching and low signal-to-noise ratio. [226] FPs are also very useful for intracellular ratiometric sensing, but they have similar limitations, in addition to difficult preparation protocols and limited FRET efficiency due to larger size. [36] Application of NPs allows creation of ratiometric nanosensors that could overcome these problems. QDs, due to their high brightness and photostability, as well as size-control luminescence properties have been successfully applied for FRET-based biosensing. [144, 227] It was shown that 5 acceptor molecules attached to the proteins on the surface of 3 nm QDs can give ~ 58 % of FRET efficiency. [144] For QDs with diameter about 7.6 nm around 50 molecules were needed to obtain 50 % of FRET. [146] However, the larger amount of acceptors is needed for efficient FRET, the lower is the sensitivity of the FRET assay, so it is important to find fluorescent NPs with more efficient FRET to their surface. Therefore, application in this field of dye-loaded polymer NPs exhibiting collective behavior of dyes is a highly promising direction for the development of FRET-based nanoprobes.

Based on our previous studies, NPs, made of PLGA and loaded with R18/F5-TBP dye, displayed highly efficient EET. [81] We performed titration of PLGA NPs loaded with 5 wt% of R18/F5-TPB with Cy5-biotin conjugate. As our NPs have negative surface charge, and Cy5 is a cationic dye, the latter adsorbs on NPs surface and we observe the occurrence of FRET between encapsulated R18/F5 dyes and Cy5-biotin (Figure 2.18 a). However, the FRET efficiency appeared to be surprisingly low and reached only 30 % for 10 Cy5-biotin molecules per NP (Figure 2.18 b).

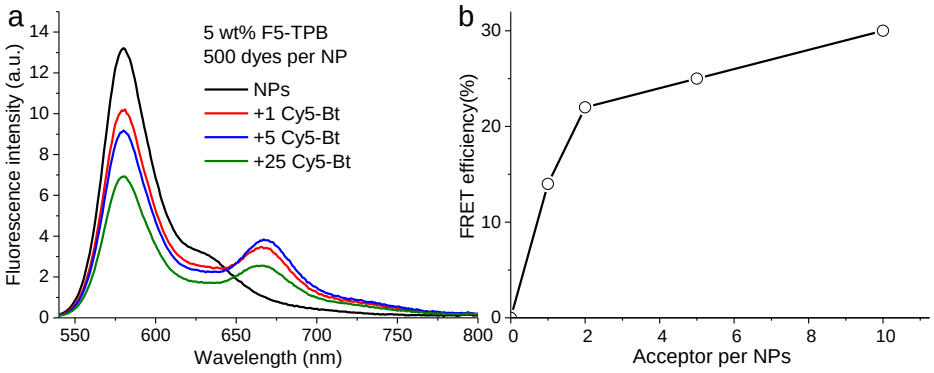

Figure 2.18.a) Fluorescence spectra of PLGA NPs loaded with 5 wt% of R18/F5 with addition of Cy5-biotin. The spectra were obtained at excitation wavelength λex= 530 nm. **b)** Calculated FRET efficiency.

We hypothesized that the origin of such low efficiency could be a core-shell like structure of our ~40 nm NPs, where the dyes form nuclei that surrounded by thick shell of polymer. This hypothesis is supported by the studies on the influence of polymer matrix on the collective behavior of encapsulated dyes, described above. To overcome this problem we decided to change polymer matrix to PMMA, where, according to our previous studies, dye distribute more homogeneously and have efficient EET at high level of dye loading (see chapter 2.1.2). To provide lower average distance between the encapsulated donor dyes and particle surface we decreased the size of NPs using a recently developed approach in our group. It was shown that a single charged group on the polymer PMMA results in a strong decrease in the size of obtained particles, reaching 15-20 nm diameter according to TEM.[176]

Nanoparticles preparation and characterization

NPs where prepared by nanoprecipitation from acetonitrile solution of polymer containing different amount of R18/F5-TPB (from 0.2 wt% to 20 wt%) to milliQ water. The increase in dye loading led to a small increase in relative contribution of the short wavelength shoulder in the absorption spectra. The emission maxima demonstrated a slight red shift with increase in the dye loading, together with a small reduction in the width of the spectra that evidenced of some assembly of dyes inside NPs (Figure 2.19). Nevertheless, the QY values remained very high ~ 0.5 even at the highest loading of 20 wt% (Table 2.2).

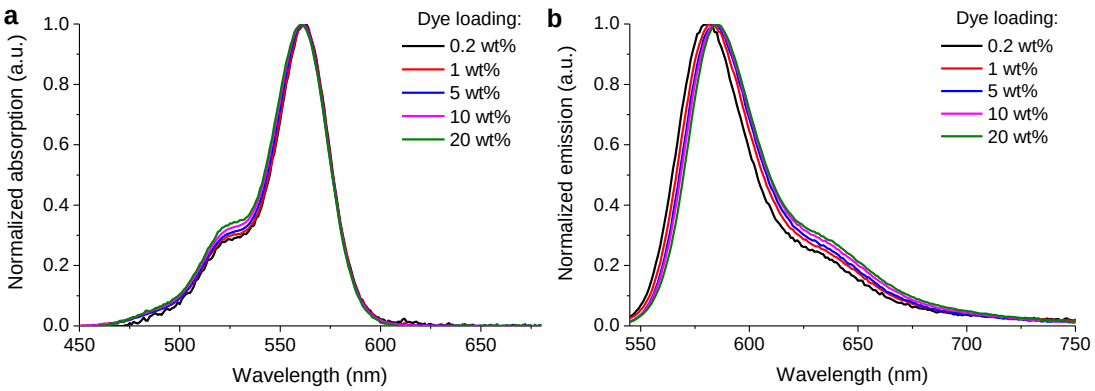

Figure 2.19. Normalized absorbance **(a)** and emission spectra **(b)** of PMMA-SO3 NPs loaded with different amounts of R18/F5-TPB. Emission spectra were recorded using excitation at 530 nm.

According to FCS with 2-photon excitation, size of NPs at the lowest loading was around 20 nm and increased with loading up to 25 nm. The slight increase in NPs concentration was also observed. Together with increase in loading we saw increase in two-photon brightness (expressed in the brightness of our reference 5(6)-carboxytetramethylrhodamine (TMR)) from 7 to 280. Although at low loading (from 0.2 wt% to 5 wt%) the increase of brightness was almost linear, then it slowed down due to the drop in QY. Based on the size of NPs and the loading the number of rhodamine dyes per NP was calculated and reached more than 700 for 20 wt% (Table 4).

Table 2.2. Size, concentration and two-photon brightness calculated from FCS measurements (830 nm, 2 mW) of NPs loaded with different concentrations of the R18/F5-TPB, their QY and calculated number of encapsulated fluorophores.

Sample	D, nm	C, nM	Brightness/TMR	QY [a]	#R18/F5-TPB
0.2 wt%	20	11.7	7	0.98±0.08	4
1 wt%	20	12.0	25	0.88±0.08	18
5 wt%	25	13.0	150	0.73±0.04	180
10 wt%	21	15.4	215	0.59±0.05	210
20 wt%	25	19.8	280	0.50±0.08	720

[a] Rhodamine 101 in ethanol was taken as a reference.

FRET to the NPs surface

To determine the efficiency of our NPs as energy donor to single acceptors located on their surface we performed the titration of NPs loaded with different amounts of R18/F5-TPB with Cy5-biotin conjugate. During the titration the later adsorbed on the NPs surface and we observed the occurrence of FRET between encapsulated dyes and Cy5-biotin. The addition of increasing concentration Cy5-biotin led to a drop of NPs fluorescence intensity and a rise of fluorescence at the acceptor emission wavelength. Remarkably, these processes were much more prominent at high loading of donor dyes, where already at 1 acceptor per particle, the acceptor emission became higher than the donor one. The acceptor emission reached saturation at about 10 acceptors per NP (100 nM concentration of acceptor), when the self-quenching of acceptors on NPs surface probably started to take place (Figure 2.20). The stability of the signal in time (over 25 min) confirmed that acceptor molecules remained on NPs surface. Control titration of NPs with DMSO, used in the titration, showed no significant change in the spectrum, confirming that observed effects were attributed to Cy5-biotin – NPs interactions.

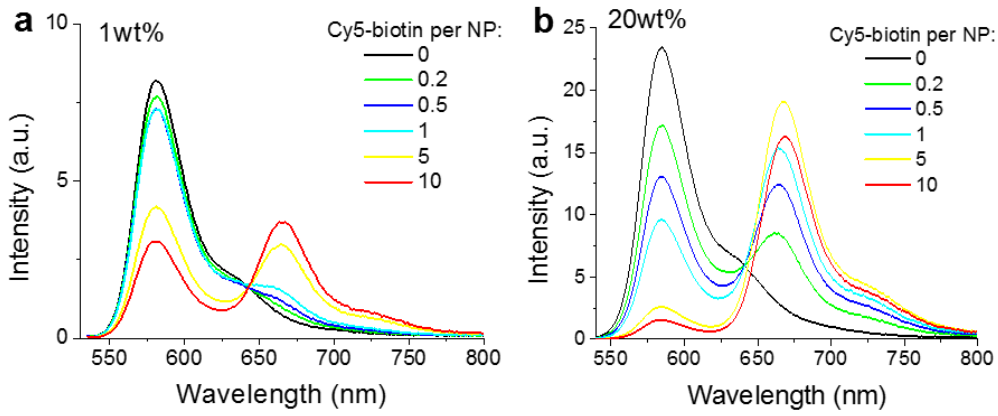

Figure 2.20. Fluorescence spectra changes of NPs loaded with 1 wt% **(a)** and 20 wt% **(b)** of R18/F5 dye

To estimate FRET efficiency we used the classical formula

$$E_{FRET} = 1 - \frac{I_D}{I_{D-A}}$$

were I_D- peak fluorescence intensity of the NPs, I_{D-A}- peak fluorescence intensity of the NPs with acceptor molecules adsorbed on their surface. This calculation showed that, for the same number of acceptors per particle, the increase

in donor dye loading increased the FRET efficiency. Remarkably, only 1 acceptor on the surface of the 25-nm NPs containing ~ 720 donor dyes produced FRET of >50% efficiency (Figure 2.21 a).

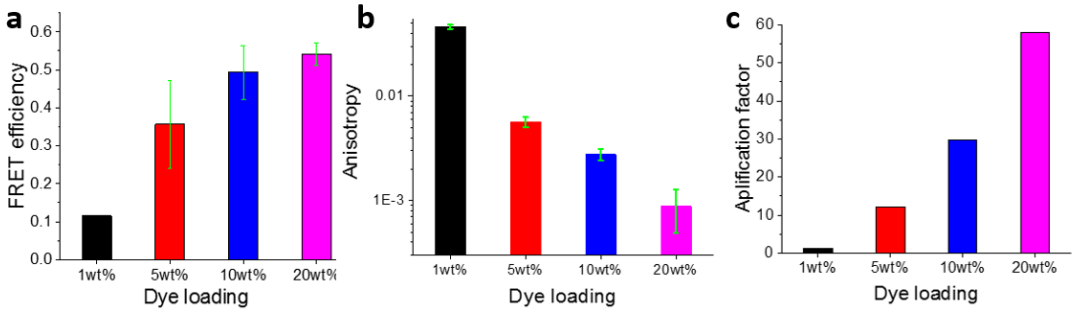

Figure 2.21. a) FRET efficiency calculated for NPs with different R18/F5 loading with one acceptor molecule adsorbed on its surface. **b)** Fluorescence anisotropy value for R18/F5 encapsulated into NPs. **c)** Amplification of acceptor emission intensity calculated for NPs with one acceptor molecule adsorbed on its surface.

To verify whether the FRET efficiency was related to the efficiency of EET between donors, we measured the steady-state anisotropy of NPs with different loading of R18/F5-TPB dye. Increase in the dye loading led to the dramatic drop in the anisotropy, indicating more efficient EET (Figure 2.21 b). [8]

As NPs contained a large number of fluorescent dyes that were strongly coupled by energy transfer, they could be very efficient energy donors, similar to light-harvesting complexes, and thus could amplify the fluorescence of acceptor dyes. To quantify the antenna effect (AE), we recorded the excitation spectra of the donor and the acceptor by detecting the emission of the acceptor and then measured the ratio of the maximal excitation intensity of the donor to that of the acceptor. [209] At the low loading of the donor dye, no antenna effect was observed (AE~1), whereas at higher donor loadings, AE increased up to 59 for 20 wt% dye loading in 25-nm NPs (Figure 2.21 c).

The high FRET efficiency together with ~60-fold amplification of acceptor emission suggested the possibility of using these NPs as efficient energy donor in FRET-based probes.

Application of efficient FRET and acceptor amplification for protein detection

To test whether the described above FRET system can sense proteins in solution, we adsorbed 1 equivalent of Cy5-biotin on the surface of NPs loaded with 20 wt% R18/F5-TPB. As a result, strong FRET signal was observed (Figure 2.22 a). Then

we titrated this complex with streptavidin. Due to high affinity to biotin, streptavidin bound Cy5-biotin conjugate and probably removed it from the NPs surface which resulted in the decrease of acceptor emission and change in I_A/I_D ratio (Figure 2.22 a, b). The change in this ratio was stabilized after 3 nM concentration of streptavidin. This stabilization could be relevant to that fact that streptavidin has four binding sites for biotin. Importantly, the addition of 1 µM of free biotin competitor inhibited the detection of streptavidin by NPs which confirmed specific recognition of the protein (Figure 2.22c).

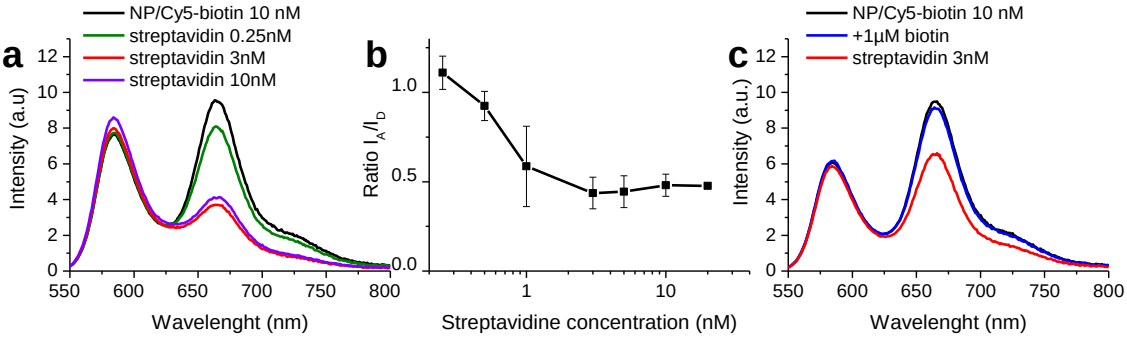

Figure 2.22. a) Fluorescence spectra changes of NPs loaded with 20 wt% R18/F5 with adsorbed single molecule of Cy5-biotin on its surface upon addition of streptavidin. **b)** Changes in IA/ID ratio due to addition of streptavidin. Error bars represent standard error between three experiments (n = 3). **c)** Fluorescence spectra changes of NPs loaded with 20 wt% R18/F5-TPB with adsorbed single molecule of Cy5-biotin on its surface upon addition of 3nM of streptavidin in the presence of 1µM of biotin. The spectra were obtained at excitation wavelength λ_{ex}= 530 nm.

Then we perform the same type of experiment to detect human Carbonic Anhydrase (hCA) to confirm versatility of proposed sensing strategy. To this end, we changed ligand from biotin to benzamidine (BA). The new conjugate Cy5-BA also showed highly efficient FRET signal when added to NPs. As the dissociation constant of hCA – BA complex ($K_D = 10^{-6}$) is much lower than that of biotin-streptavidin ($K_D = 10^{-15}$), to detect visible changes in the I_A/I_D ratio we had to use higher concentration of hCA (Figure 2.23 a, b). The addition of 10 µM hCA inhibitor EZA almost completely stopped the recognition of the enzyme by NPs, which confirmed specific recognition of hCA protein (Figure 2.23 a, c).

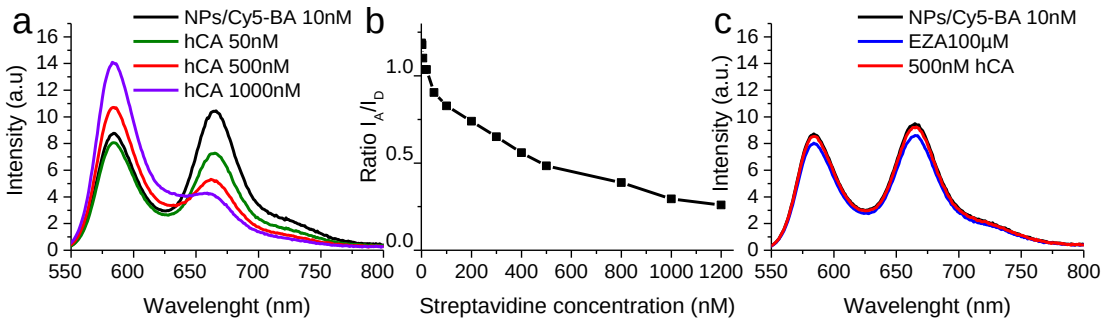

Figure 2.23. a) Fluorescence spectra changes of NPs loaded with 20 wt% R18/F5, with adsorbed single molecule of Cy5-BA on their surface upon addition of hCA. **b)** Changes in I_A/I_D ratio due to addition of hCA. **c)** Fluorescence spectra changes of NPs loaded with 20 wt% R18/F5-TPB, with adsorbed single molecule of Cy5-BA on their surface upon addition of 500 nM of hCA in the presence of 100 µM of EZA inhibitor. The spectra were obtained at excitation wavelength λex= 530 nm.

Detection of proteins at the single molecule level

Finally, we evaluated the performance of our NPs at the single-particle level using wide-field fluorescence microscopy. To this end, we immobilized fluorescent NPs containing 20 wt % R18/F5-TPB on the glass surface covered with positively charged polymer PEI. Then, using band pass filters 593/40 (donor channel) and 685/40 (acceptor channel), and a dichroic mirror at 640 nm to split the emission beam into two channels, we were able to record the emission of NPs on two channels under 532-nm excitation.

The NPs appeared as bright spots only on the donor channel and very dim spots on the acceptor channel. Merged image of both channels showed domination of the signal on the donor channel. Cy5-biotin was added to the well with NPs and spots on the donor channel became much dimmer, and we observed bright spots on the acceptor channel that suggested appearance of FRET. Merging channels demonstrated the presence of NPs with different ratio between the two channels, which suggests the presence of NPs with different levels of FRET. Three times washing of the well with MilliQ-water had no significant effects on the observed picture. Finally, the addition of 2.5 µM of streptavidin decreased the intensity of the acceptor channel back to the value observed for control NPs without acceptor. These results confirm that NPs could sense proteins at the level of individual particles (Figure 2.24 a). Remarkably, one step bleaching event of acceptor emission that was accompanied

by appearance of strong emission on the donor channel, confirmed that we really observe single molecule events on the NPs surface (Figure 2.24 b).

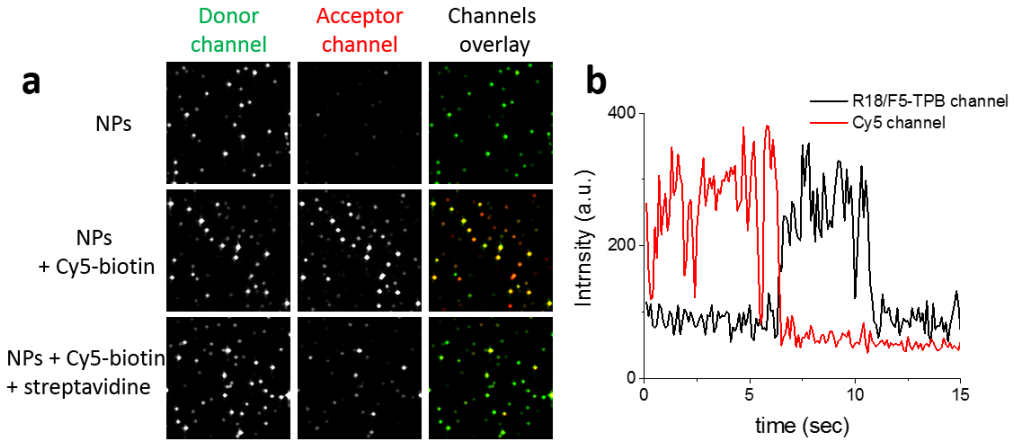

Figure 2.24. Single-particle observation of switching of NPs in two channels. **a)** Wide field image of NPs (upper panel), NPs with adsorbed Cy5-biotn on theirs surface (middle panel) and NPs with Cy5-biotn after the addition of streptavidin (lower panel).The images were obtained by illumination with laser 532nm with power 2 W/cm^2, integration time for each image was set at 0.1 sec. b) The representative trace of the NPs bearing Cy5-biotin in green and red channels in time under the illumination at 532 nm with laser power 0.2 W/cm^2.

Obtained results suggest that the created NPs could be used as a building block for creating nanoparticle probes with single molecule sensitivity.

2.4. Conclusions and perspectives

The aim of my PhD project was to develop non-toxic, biocompatible organic NPs with small size, high brightness and photostability, characterized by efficient switching due to FRET and then to apply them for biomolecular sensing.

In the first part of my work I investigated the influence of dye structure on encapsulation efficiency, brightness and photostability in case of perylene diimide dyes with bulky substitutes in the imide (PDI-1) and both imide and bay regions (Lumogen Red).The results demonstrated importance of introducing bulky side groups into structure of encapsulated dyes to prevent their aggregation (thus poor photostability). The excellent photostability and brightness of NPs loaded with LR make them biodegradable substitutes of quantum dots, that could find a variety of applications in biological imaging. Nevertheless, the size of NPs remains larger than size of QDs. For many cellular applications size should be decreased up to 5 – 15 nm, while preserving the high brightness, which can be achived by increasing the dye loading and developing efficient strategies against ACQ.

Then I studied the influence of polymer matrix (on the example of PLGA, PMMA and PCL) on the spatial organization of encapsulated dyes (R18/F5-TPB and PDI-1) as it had direct influence on QY, photostability of NPs and EET efficiency. PLGA NPs showed the evidences of much higher dye aggregation than the two other polymer matrices. Even more prominent differences were observed in the blinking behavior of these NPs. PLGA NPs displayed ON/OFF switching starting from 1 wt% of dye loading, whereas for PMMA and PCL NPs some partial blinking was observed only at very high (30 wt%) dye loading. The time-resolved fluorescence anisotropy studies suggested different rate of EET for NPs built from different polymers, suggesting that the interfluorophore distances are significantly shorter for PLGA, compared to the other two matrices. The difference in the dye organization could be linked to the solubility of the polymer in the solvent mixture, used for nanoprecipitation. In this case, PLGA with the highest solubility and thus slowest nanoprecipitation kinetics allows hydrophobic dyes to cluster inside the nanoparticle core, producing NPs with high dye cooperativity. By contrast, in PMMA and PCL the dyes are more dispersed with the polymer matrix, and thus giving NPs with higher quantum yield and photostability. The

choice between very high photostability and cooperative behavior depends on the experiment: NPs with constant emission could be applied for particle tracking, and those with complete on/off switching could be used in super-resolution imaging.

In the second part of my work, I exploited EET among donor dyes R18/F5-TPB in order to obtain efficient FRET to single acceptors inside NPs. The obtained results demonstrated importance of cooperative behavior of fluorophores inside NPs to ensure efficient FRET to the photochromic molecule and, thus, to produce efficient photoswitching. This system could be further improved by using photochromic molecules with higher extinction coefficient and better fatigue resistance, as well as by improving photostability of donor dyes with less pronounced blinking behavior (or its absence), but preserving their cooperativity. At the same time efficient homogeneous photoswitching at single particle level requires creation of more monodisperse NPs that would assure more uniform distribution of particle brightness.

Next, much larger dye ensembles coupled by EET inside NPs were used to generate giant light-harvesting antenna. It amplified the fluorescence of a single dye which enabled observation of single molecule events (one-step bleaching of the acceptor) at extremely low laser powers that approaches single molecule photography at ambient light without dedicated instrumentation. As energy from thousands of donors funnels to single acceptors, the excellent photostability of the latter one is of crucial importance for performance of the nano-antenna. Elimination of “energy traps” (such as dark state of R18/F5-TPB) that are competitors for energy with acceptor molecule would make possible obtaining even higher amplification of acceptor emission.

Finally, the possibility of FRET-based sensing of individual molecules on the surface of dye-loaded NPs was demonstrated. Due to ultra-fast EET between donor dyes, FRET with efficiency > 50% was achieved with a single acceptor. Using acceptor molecule conjugated with a specific ligand we prepared nanoparticle-based probes for proteins. In these nanoprobes, the acceptor-ligand conjugate is removed from NPs surface in the presence of the target protein, which stops FRET and thus changes the dual emission of NPs. So, created NPs could be used as building blocks for biosensors with single molecule sensitivity. However, robust biosensors would require covalent linking of acceptor dye to the surface of NPs. Encapsulation of higher amount of donor dyes with preserved high QY, as well as elimination of “energy traps” and using

acceptor with better photostability and QY would increase the antenna effect and improve performance of these biosensors.

Several remaining problems should be solved for further successful application of polymer NPs in bioimaging. First, monodispersity of particles should be improved, which is essential for quantitative detection of biomolecules. Solving the problem of leaching of the encapsulated dyes into biological media would minimize artefacts and maximize the signal to background ratio.

Achieved to-date properties and systematic work on the described problems promise the bright future to dye-loaded NPs in bioimaging applications.

PART 3. Materials and methods

3.1. Materials

All chemicals and solvents for synthesis were purchased from Alfa Aesar and Sigma Aldrich and used as received unless stated otherwise.

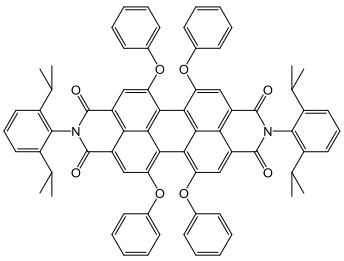

Lumogen Red (N,N′-Bis-(2,6-diisopropylphenyl)-1,6,7,12-tetraphenoxy-3,4,9,10-perylenebis(dicarboximide)) was purchased from ORGANICA® Feinchemie GmbH Wolfen.

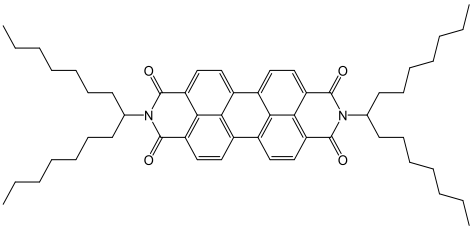

PDI-1 (N′-Bis(1-heptyloctyl)-3,4,9,10-perylenebis-(dicarboximide)) was synthesized by Ievgen Shulov from 1-heptyloctylamine (Sigma-Aldrich) and perylene-3,4,9,10-tetracarboxylic dianhydride (Sigma-Aldrich) as was described previously [228]

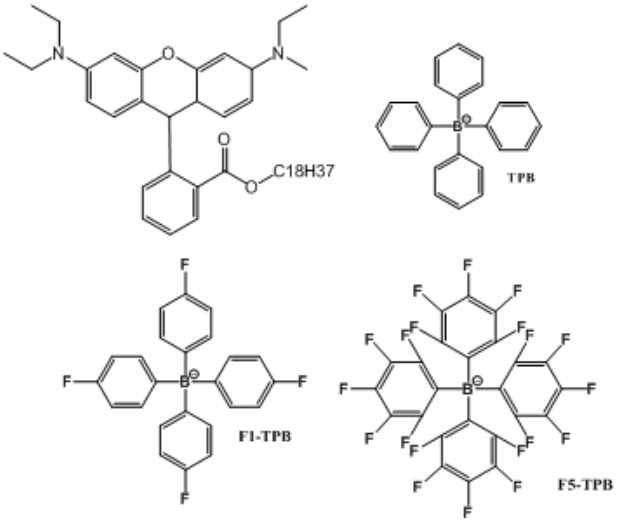

The salts of octadecyl rhodamine B with different counterions: **R18/TBP, R18/F1-TBP R18/F5-TBP** were obtained by Andreas Reisch by ion exchange followed by purification as described in ref. [81].

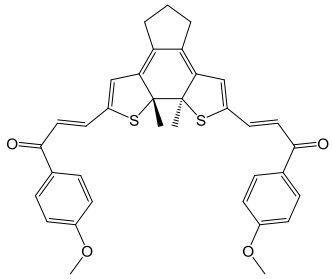

Photochromic molecule **PCDI** was obtained from collaborator Prf. Luca Prodi (University of Bologna, Italy). The synthesis was described earlier [229]

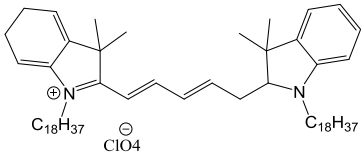

Cy5 derivative **DID** 1,1'-Dioctadecyl-3,3,3',3'-tetramethylindodicarbocyanine perchlorate was purchased from Thermo Fisher Scientific.

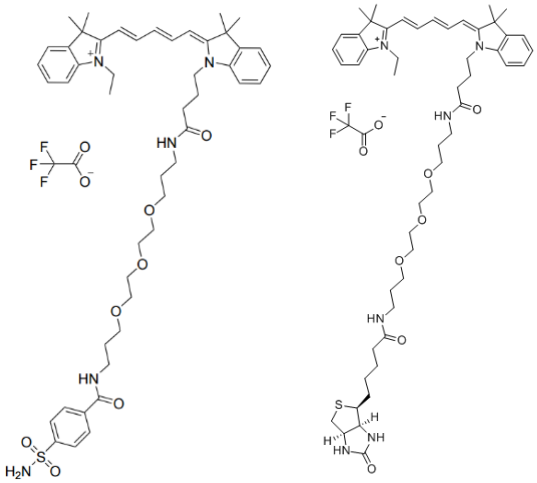

Cy5-Su and **Cy5-biotin** conjugates were synthesized by Ievgen Shulov.

Poly(D,L-lactide-co-glycolide) (PLGA, lactide 50 mol %, glycolide 50 mol %, acid terminated, Mn 24 000, PDI 1.7, and Mn 8800, PDI 1.7), poly-(methyl methacrylate-co-methacrylic acid) (PMMAMA, 1,3% methacrylic acid, Mn ~15 000, Mw~34 000) were purchased from Sigma-Aldrich. Synthesis of carboxylate bearing form of Polycaprolactone (PCL) (R,ω-dihydroxy functional, Mn ~10 000, Mw ~14 000) and sulfonate-bearing form of PMMAMA are described in ref. [176]

Sodium phosphate monobasic (>99.0%, Sigma-Aldrich) and sodium phosphate dibasic dihydrate (>99.0%, Sigma-Aldrich) were used to prepare 20 mM phosphate buffer solutions; tris(hydroxymethyl)amino methane (Tris base, >99.8%, SigmaAldrich) and HCl (1 M) were used to prepare 20 mM Tris buffer with a pH of 7.4. Milli-Q water (Millipore) was used in all experiments.

3.2. Preparation of polymer NPs

Stock solutions of polymers in acetonitrile were prepared at a concentration of 10 mg/ml. These solutions were then diluted with acetonitrile containing desired amount of dye, to the concentration of 1 or 2 mg/ml. 50 µL of the polymer solutions were then added quickly using a micropipette and under shaking (Thermomixer comfort, Eppendorf, 1000 rpm) to 450 µL of water or buffer. PLGA- and PMMA-based nanoparticles were prepared at 21°C, PCL nanoparticles were prepared at 27°C. $PMMASO_3$ NPs were prepared according to the same protocol, but with dilution in water at 21°C. The particles solution was then quickly diluted 5-fold with the same buffer. For varying the size of PMMAMA NPs the value of pH of buffer at the first dilution was varied between 5.8 and 9.

3.3. NPs characterization

Dynamic light scattering measurements were performed on a Zetasizer Nano series DTS 1060 (Malvern Instruments S.A.). It uses a laser source of 633 nm, so only NPs without excitation at this wavelength could be used. Absorption and emission spectra were recorded on a Cary 4000 scan UV-visible spectrophotometer (Varian) and a FluoroMax-4 spectrofluorometer (Horiba Jobin Yvon) equipped with a thermostated cell compartment, respectively. For standard recording of fluorescence spectra, the excitation wavelength was chosen to excite the sample optimally. The fluorescence spectra were corrected for detector response and lamp fluctuations. QY was calculated by comparative method, using appropriate reference sample. Steady-state anisotropy was measured on a SLM 8000 spectrofluorometer (Aminco) in a T-configuration.

3.4. Single particle measurements

3.4.1. Fluorescence correlation spectroscopy (FCS) and data analysis

FCS measurements of NPs loaded with R18/F5-TPB and LR were performed on a two-photon platform including an Olympus IX70 inverted microscope, as

described previously. [169] Two-photon excitation at 830 nm (from 1mW to 5mW laser output powers) was provided by a mode-locked Tsunami Ti:sapphire laser pumped by a Millenia V solid state laser (Spectra Physics). The measurements were carried out in a 96-well plate, using a 200-µL volume per well. The focal spot was set about 20 µm above the coverslip. The normalized autocorrelation function, *G(τ)* was calculated online by an ALV-5000E correlator (ALV, Germany) from the fluorescence fluctuations, σ*F(t)*, by $G(\tau)=\langle \sigma F(t)\sigma F(t+\tau)\rangle / \langle F(t)\rangle^2$ where $\langle F(t)\rangle$ is the mean fluorescence signal, and *τ* is the lag time. Assuming that NPs diffuse freely in a Gaussian excitation volume, the correlation function, *G(τ)*, calculated from the fluorescence fluctuations was fitted according to Thompson:[230]

$$G(\tau)=\frac{1}{N}\left(1+\frac{\tau}{\tau_d}\right)^{-1}\left(1+\frac{1}{S^2}\frac{\tau}{\tau_d}\right)^{-1/2}$$

where τ_d is the diffusion time, *N* is the mean number of fluorescent species within the two-photon excitation volume, and *S* is the ratio between the axial and lateral radii of the excitation volume. The excitation volume is about 0.34 fL and *S* is about 3 to 4. The measurements were done with respect to a reference 6-carboxytetramethylrhodamine (TMR from Sigma-Aldrich) in water. The hydrodynamic diameter, *d*, of NPs was calculated as: $d_{NPs} = \tau_{d(NPs)}/\tau_{d(TMR)} \times d_{TMR}$, where d_{TMR} is a hydrodynamic diameter of TMR (1.0 nm). Concentration of NPs was calculated from the number of species by: $C_{NPs} = N_{NPs}/N_{TMR} \times C_{TMR}$, using a TMR concentration of 50 nM.

3.4.2. Single particle imaging

For single particle fluorescence measurements, the NPs were immobilized on glass surfaces on which a polyethyleneimine (PEI) layer was initially adsorbed. The solutions of NPs were diluted to a particle concentration of about 6 pM with buffer. 400 µL of these solutions were then brought in contact with the PEI-covered glass for 15 min, followed by extensive rinsing with milliQ-water. The surfaces were left in milliQ water during the microscopy measurements. Quantum dots and FluoSpheres® red-orange at 6 pM concentration were immobilized and imaged in the same way as NPs. Single particle measurements were performed in the TIRF (Total Internal Reflection Fluorescence) mode on a homemade wide-field setup based on an Olympus IX-71 microscope with an oil immersion objective (NA = 1.49, 100×). The fluorescence signal

was recorded with an EMCCD (ImagEM Hamamatsu). A DPPS (Cobolt) continuous wave (CW) laser emitting at 532 nm was used for excitation NPs loaded R18/F5-TPB and LR. 642 nm diode laser (Spectra-Physics Excelsior 635) was used for excitation NPs containing Cy5 molecules. 488 nm diode laser Spectra-Physics Excelsior) was used for excitation of PDI-1 -encapsulated NPs. The fluorescence signal was recorded with an EMCCD (ImagEM Hamamatsu). Image analysis was performed using the Fiji software.

3.4.3. Detection of proteins at single molecule level

The fluorescent NPs containing 20 wt % R18/F5-TPB were immobilized on the glass surface covered with positively charged polymer PEI, as described in the protocol above. The fluorescence signal was recorded with an EMCCD (ImagEM Hamamatsu). A DPPS (Cobolt) continuous wave (CW) laser, emitting at 532 nm, and 642 nm diode laser (Spectra-Physics Excelsior 635) were used. W-VIEW GEMINI-image splitting optics with bandpass filters 593/40 (green channel) and 685/40 (red channel), and dichroic mirror at 640 nm were used to detect donor and acceptor emission. Cy5-biotin was added to the immobilized NPs from concentrated DMSO stock solution. Washing steps were performed with milliQ-water. Finally, streptavidin was added to the immobilized NPs from concentrated aqueous solution.

3.4.4. TEM imaging

Five microliters of the particles solution were deposited onto carbon-coated copper-rhodium electron microscopy grids that were used either as obtained or following an air or amylamine glow-discharge. The grids were then treated for 1 min with a 2%uranyl acetate solution for staining. They were then observed with a Philips CM120 transmission electron microscope equipped with a LaB6 filament and operating at 100 kV. Areas covered with nanoparticles of interest were recorded at different magnifications on a Peltier cooled CCD camera (Model 794, Gatan, Pleasanton, CA). Image analysis was performed using the Fiji software.

3.4.5. Time-resolved fluorescence

The measurements were performed with the time-correlated, single-photon counting technique using the excitation pulses at 480 nm provided by a pulse-picked frequency doubled Ti-sapphire laser (Tsunami, Spectra Physics) pumped by a Millenia X laser (Spectra Physics). The emission was collected through a polarizer set at the magic angle and an 8 nm band-pass monochromator (Jobin-Yvon H10) at 582 nm. The instrumental response function was recorded with a polished aluminium reflector, and its full-width at half-maximum was 40 ps. For time-resolved anisotropy measurements, the fluorescence decay curves were recorded at the vertical and horizontal positions of the excitation polarizer and with the emission polarizer set to the vertical position, and analysed by the following equation:

$$r(t) = \frac{I_v(t) - G \cdot I_h(t)}{I_v(t) + 2 \cdot G \cdot I_h(t)} \quad (1)$$

where Iv and Ih are the intensities collected at vertical and horizontal excitation polarizations, respectively, and G is the geometry factor at the emission wavelength, determined in independent experiments.

3.5. Cellular studies

HeLa cells (ATCC® CCL-2) were grown in Dulbecco's modified Eagle's medium (DMEM, Gibco-Invitrogen), supplemented with 10% fetal bovine serum (FBS, Lonza) and 1% antibiotic solution (penicillin–streptomycin, Gibco-Invitrogen) at 37 °C in a humidified atmosphere containing 5%CO2. Cells were seeded onto a chambered cover glass (IBiDi) at a density of 5 × 10^4 cells per well 24 h before the microscopy measurement. For imaging, the culture medium was removed and the attached cells were washed with Opti-MEM (Gibco-Invitrogen). Then, a freshly-prepared solution of NPs loaded with 1 wt% LR (at 20-fold dilution of the original formulation corresponding to ~0.15 nM of NPs) in Opti-MEM was added to the cells and incubated for different time periods. Cell membrane staining with wheat germ agglutinin-Alexa488 (Life Technologies) was done for 10 min at rt before the measurements. Confocal fluorescence images of the cells were taken on a Leica TSC SPE confocal microscope. For cytotoxicity studies, HeLa cells were seeded in 96-well plates at a concentration of 104 cells per well in 100 µL of the DMEM growth medium and then

incubated overnight at 37 °C in a humidified atmosphere containing 5% CO2. Next, the PLGA NPs loaded with 1 wt% of PDI-1 or LR were added, by substituting the culture medium with the fresh one containing variable concentrations of NPs. After incubation for 24 h, the medium was removed and the adherent cell monolayers were washed with PBS. Then, the wells were filled with cell culture medium containing MTT, incubated for 4 h at 37 °C, and the formed formazan crystals were dissolved by adding 100 µL of a 10% sodium dodecylsulfate (SDS), 0.01 M hydrochloric acid solution. The absorbance was then measured at 570 nm with a microplate reader. Experiments were carried out in triplicate and expressed as the percentage of viable cells compared to the control group.

Résume de la thèse en français

Contrôle de la fluorescence dans des nanoparticules organiques par transfert d'énergie en vue d'applications en bioimagerie

L'organisme humain est composé d'une grande variété de cellules, chacune contenant une quantité importante de biomolécules différentes. Leurs concentrations, leurs modifications et interactions sont généralement contrôlées avec une précision tant spatiale que temporelle élevée. Tout changement dans ces processus complexes peut conduire à des maladies létales. Il est donc essentiel de développer une voie de diagnostic précoce pour toute modification en biochimie humaine afin d'augmenter le taux de survie des patients. Etant donné sa haute sensibilité, sa détection rapide et non-invasive la fluorescence est une technique très prometteuse pour détecter des biomolécules même à faible concentration. [231] En outre, le signal de fluorescence peut être modulé, par transfert d'énergie résonant (FRET), [232] en réponse à la présence de biomolécules cibles.

La vitesse, la résolution et la sensibilité de la bioimagerie peuvent être significativement améliorées à l'aide des nanoparticules fluorescentes (NPs) présentant une luminosité supérieures aux sondes organiques et protéines fluorescentes. A l'heure actuelle, les NPs les plus couramment utilisées sont inorganiques comme par exemple les *quantum dots* (QDs). [41] Si les nanoparticules organiques fluorescentes sont des alternatives intéressantes aux QDs, au vu de leur biodégradabilité potentielle, leur préparation est difficile étant donné le problème d'auto-inhibition des fluorophores encapsulés et, en outre, une photostabilité des fluorophores nettement plus faible que celle des QDs. De plus, leur taille (~10-60 nm) est beaucoup plus grande que le rayon de FRET ce qui présente un obstacle pour une application réussie dans ce domaine.

L'objectif de mon projet de doctorat a été de développer des nanoparticules fluorescentes organiques non toxiques et biocompatibles, présentant une petite taille, une luminosité et une photostabilité élevées, capables de changer d'un état éteint à

un état allumé (allumage) grâce au FRET et de les appliquer à la détection de biomolécules. Dans ce but, nous nous sommes intéressés aux nanoparticules polymériques dopées en fluorophores préparées par nano-précipitation à partir de polymères biodégradables et biocompatibles approuvés par la FDA (Food and Drug Administration). Les fluorophores pour l'encapsulation doivent satisfaire à un certain nombre de critères: avoir un bon coefficient d'extinction moléculaire, un rendement quantique élevés, être photostables, procurer un bon contraste pour une faible puissance d'excitation (afin d'éviter une phototoxicité pour des expériences prolongées) et être suffisamment hydrophobes pour co-précipiter avec le polymère et ne pas fuir dans le milieu biologique (comme une tumeur ou le cytosol) afin d'assurer un faible bruit de fond de fluorescence.

Pour surmonter les problèmes de biodégradabilité, de photostabilité et d'auto-inhibition des colorants incorporés, nous avons étudié l'encapsulation de dérivés de pérylène diimide (PDI), qui sont à ce jour les fluorophores les plus photostables connus, [171] dans des nanoparticules polymériques à base d'acide poly(lactique-co-glycolique) PLGA. L'un de ces dérivés porte des groupements hydrophobes volumineux dans la région imide (PDI-1), alors que l'autre a été substitué dans les deux régions imide et basse (Lumogen Red) (Figure 1).

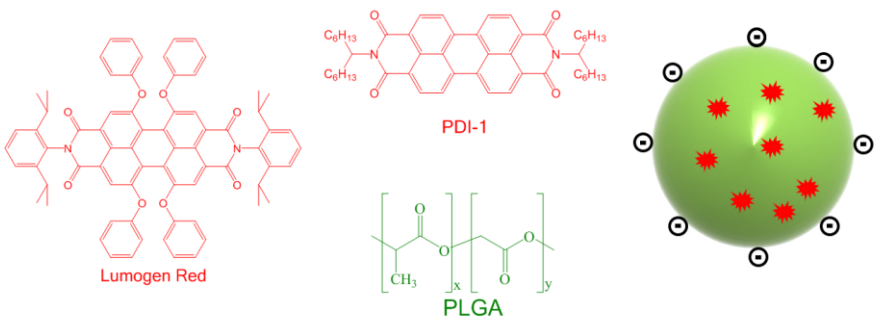

Figure 1. Structure chimique de PDI-1, des fluorophores LR et du polymère PLGA + schéma d'une nanoparticule de PLGA dopée en colorant.

L'encapsulation de PDI-1 a résulté en une forte agrégation des fluorophores même pour un dopage faible (>0.02 pourcentage massique (wt%)), accompagnée par une modulation de sa couleur d'émission du vert au rouge ainsi qu'une chute de son rendement quantique de fluorescence et de sa photostabilité, ce qui n'a jamais été observé pour des PDIs. Au contraire, le Lumogen Red n'a montré pratiquement

aucune agrégation à l'intérieur des nanoparticules et a conservé un rendement quantique élevé. Selon des mesures de microscopie de fluorescence à champ large en excitation laser à 352 nm, nos nanoparticules ayant une taille de 40 nm et dopée avec 1%wt de Lumogen Red sont 10 fois plus lumineux que des quantum dots (QD 585) (Figure 2 a) et sont plus photostables que des FluoroSphères (Invitrogen, 0.04 µm, 565/580 nm). La stabilité des nanoparticules en présence de 10% en sérum a été confirmée par spectroscopie à corrélation de fluorescence (fluorescence correlation spectroscopy, FCS). Ces nanoparticules ont été incubées avec des cellules HeLa pour être ensuite imagées par microscopie confocale à fluorescence (Figure 2 b). Nous avons attesté par test MTT que les nanoparticules entrent spontanément dans les cellules par endocytose et ceux sans aucun signe de cytotoxicité.

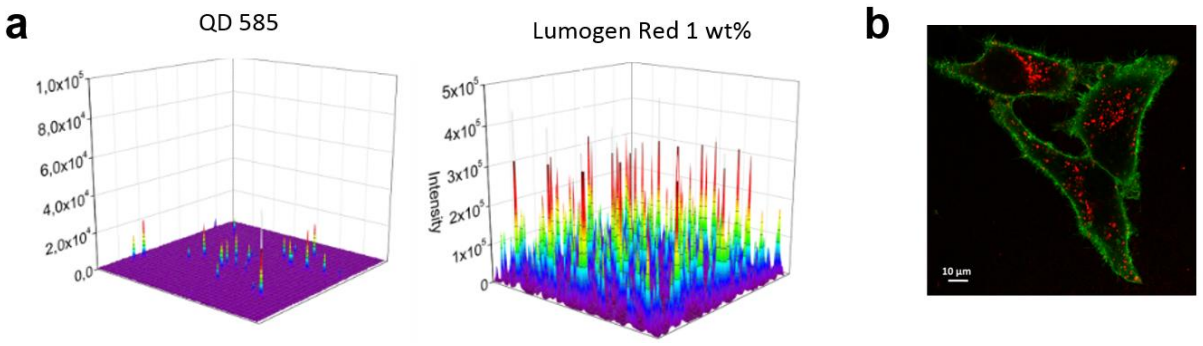

Figure 2. a) Représentation 3D de l'intensité de fluorescence de nanoparticules individuelles chargées avec 1 % en poids de Lumogen Red et de quantum dots QD585, mesurée par microscopie TIRF, avec excitation de laser de 532 nm. **b)** Imagerie, après 2h d'incubation, de nanoparticules chargées avec 1 wt% de Lumogen Red dans des cellules HeLa (l'agglutinine-Alexa488 a été utilisée pour marquer la membrane cellulaire).

En tenant compte de leur excellente photostabilité, ces nanoparticules peuvent être considérées comme des substituts biodégradables aux quantum dots pouvant donner lieu à toute une gamme d'applications en bioimagerie.

Une autre possibilité pour prévenir l'auto-inhibition des fluorophores à l'intérieur des nanoparticules consiste en l'utilisation de contre-ions volumineux qui serviront comme espaceur. Il a été montré, par co-encapsulation d'un contre-ion perfluoré volumineux en présence de Rhodamine B (R18/F5-TPB), que l'auto-inhibition du fluorophores est minimisée et qu'il se produit une alternance collective photo-induite entre un état fluorescent et un état noir (*blinking*) de plus de 500 fluorophores par

particule. [81] La raison pour un tel comportement coopératif réside dans la migration excitonique (transfert d'énergie d'excitation ultra-rapide (excitation energy transfer, EET)) qui fait qu'une seule espèce noire peut inhiber l'ensemble de la population.

Nous avons émis l'hypothèse que l'utilisation de larges populations de fluorophores couplées par EET à l'intérieur de nanoparticules peut générer des antennes collectrices géantes en amplifiant la fluorescence d'un fluorophore unique. Cette hypothèse a été prouvée avec succès en utilisant R18/F5-TPB dans une matrice de poly(méthacrylate de méthyle-co-acide méthacrylique) (PMMA-MA) (Figure 3).

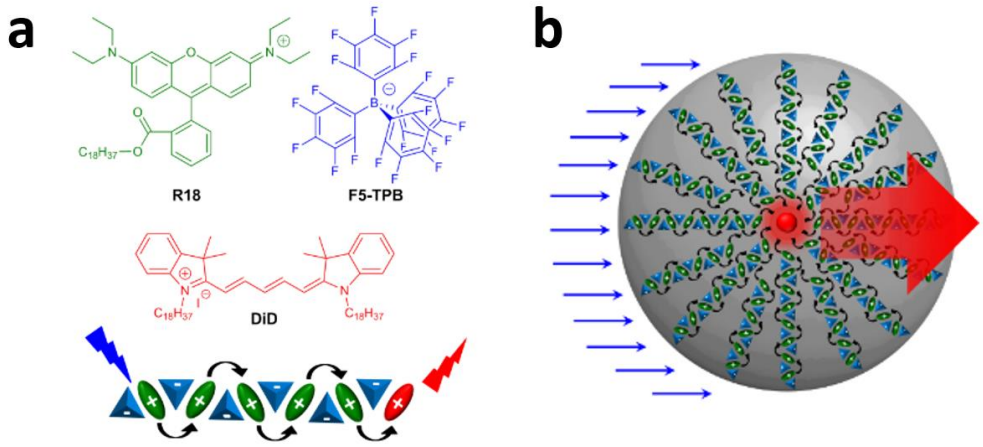

Figure 3. a) Structures chimiques du donneur octadecyl ester rhodamine B (R18) et de son contre-ion tétrakis(pentafluorophényl)borate (F5-TPB) et de l'accepteur cyanine 5 DiD + ordre à courte échelle de cations R18 (vert) et de leurs contre-ions F5-TPB (bleu) dans la matrice PMMA-MA, qui empêche l'agrégation du colorant et conduit à une courte distance inter-fluorophore et un EET ultra-rapide et un FRET résultant sur une molécule d'accepteur unique (rouge). **b)** Schéma conceptuel d'une nano-antenne collectrice géante à l'intérieur d'une nanoparticule polymérique.

Nous avons montré que les nanoparticules avec une taille comprise entre 60 et100 nm et contenant environ 104 fluorophores donneurs peuvent transférer efficacement l'énergie à un minimum d'accepteurs (rapport accepteur/donneur de 10-4) résultant en un effet d'antenne proche de 1000. Ces résultats, à savoir une amplification inégalée de l'accepteur, permettent d'observer efficacement des molécules acceptrice uniques avec une puissance d'illumination proche du visible (1 mW/cm^2) (Figure 4). Une telle puissance est de loin la plus basse utilisée à ce jour pour des mesures en molécule unique, pour lesquelles les puissances généralement utilisées sont 104-106 fois plus élevées. Ceci signifie que nous approchons d'une

photographie de la molécule unique pour laquelle la détection de molécules deviendrait possible dans le visible et sans l'utilité d'une instrumentation dédiée.

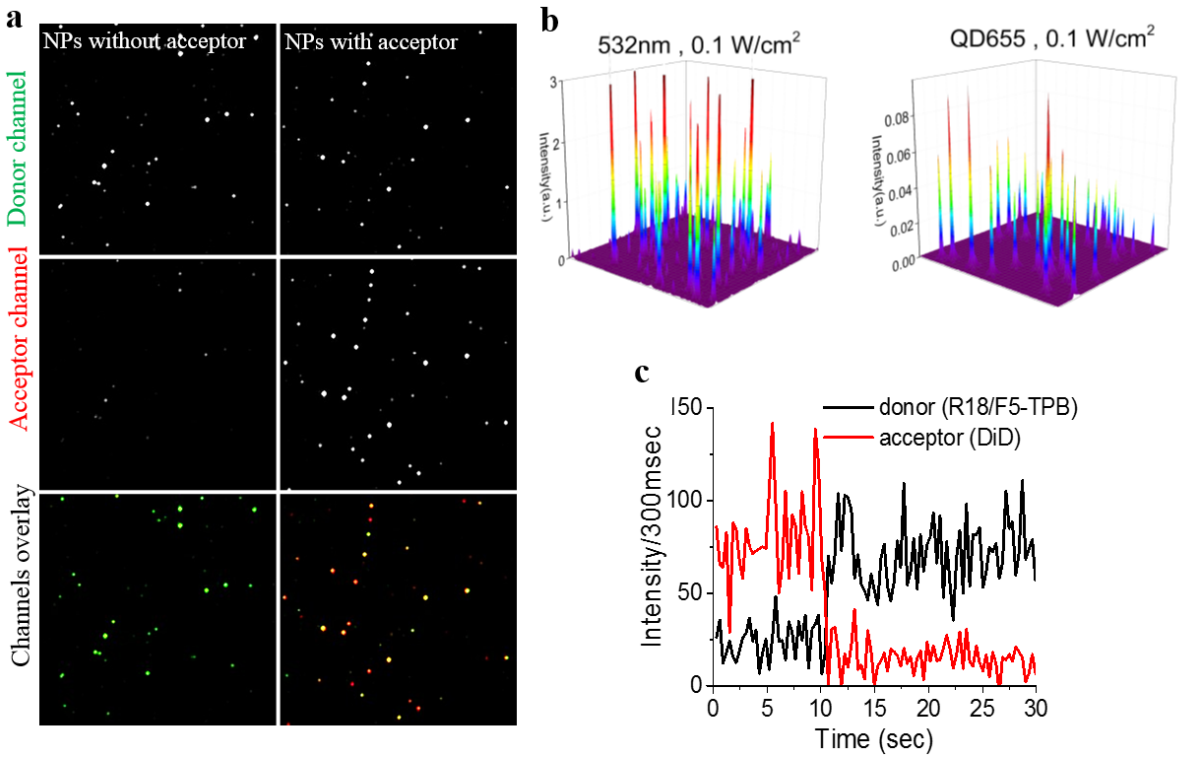

Figure 4. a) Observation en particule unique de sondes sur deux canaux spectraux (vert pour l'émission du donneur, rouge pour celle de l'accepteur. **b)** Représentation 3D de l'intensité de fluorescence de nanoparticules individuelles chargées avec 30 % en poids de R18/F5-TPB et de ~1.5 Cy5 per nanoparticule de quantum dots QD655, mesurée par microscopie TIRF avec excitation de laser de 532 nm c)Traces représentatives d'une particule unique excitée à 532 nm à une puissance de 1mW/cm^2.

Nous avons ensuite exploité l'EET entre les colorants donneurs pour amplifier l'efficacité de l'alternance photo-induite (photocommutation) dans des nanoparticules de polymères dopées en fluorophores, et obtenir ainsi des matériaux ayant de nombreuses applications potentielles, particulièrement en imagerie de fluorescence à haute résolution. [233] Dans ce but, nous avons utilisé R18/F5-TPB ayant le rôle de donneur à l'intérieur d'une matrice de PLGA et un accepteur photochrome de la famille des diaryléthènes (PCD1) (Figure 5).

Pour comprendre le rôle de l'EET, nous avons préparé des nanoparticules avec différents contre-ions, qui ne favorisent pas la diffusion excitonique de la rhodamine. Parmi les contre-ions testés, seul le tétraphénylborate perfluoré, qui favorise la

coopérativité du flurophore, permet une bonne efficacité de la photocommutation (rapport on/off ~ 20) (Figure 6). Ces nanoparticules ont été testées en solution et au niveau de la particule unique. Ce nouveau concept ouvre la voie pour de nouveaux photocommutateurs nanoscopiques efficaces.

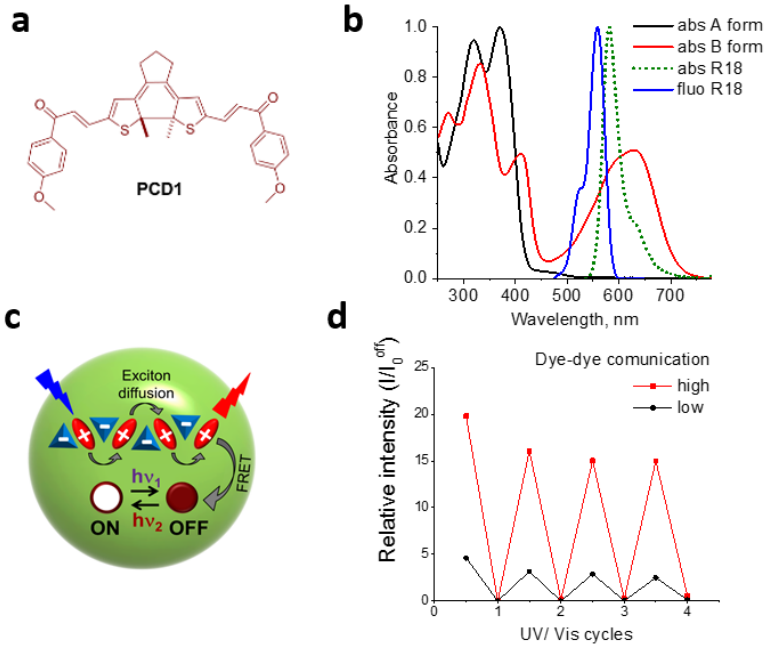

Figure 5. a) Structure chimique de l'accepteur photochrome de la famille des diaryléthènes en forme fermée. **b)** Spectre d'absorption dans le dioxane comparé aux spectres d'absorption et d'émission de R18/F5-TPB dans des NPs de PLGA (chargées à 1 wt%). **c)** Schéma du concept photocommutation à l'intérieur d'une nanoparticule. **d)** Variation d'intensité relative, sous irradiation alternée, de nanoparticules de PLGA dopées en flurophore Rhodamine R18 avec différents contre-ions (1 wt%) et en fluorophore photochrome PCD1 (0.3 wt%).

Pour des applications de détection, les nanoparticules doivent être capables de transférer efficacement l'énergie à une molécule localisée à leur surface. Ceci signifie que la distance moyenne des molécules de donneurs dans une NP et l'unique molécule d'accepteur devrait être approximativement égale au rayon des NPs ce, qui est supérieur au rayon de Förster. Ceci apparaît comme une barrière insurpassable pour l'application des nanoparticules comme donneurs en FRET. Par exemple, il a été montré que pour obtenir 50% d'efficacité de FRET pour des quantum dot, cela nécessiterait au moins 10 accepteurs en surface.[146]

Nous avons utilisé le comportement coopératif unique des nanoparticules dopées en R18/F5-TPB pour obtenir un FRET efficace à la surface des nanoparticules. Pour cela, nous avons synthétisé des nanoparticules de 25 nm à partir de poly (méthacrylate de méthyle) sulfonate (PMMA-SO_3H).[176] Des mesures spectroscopiques ont mis en évidence qu'une seule molécule d'accepteur (Cy5) absorbée à la surface des nanoparticules est suffisante pour obtenir une efficacité de FRET de 50%, accompagnée d'une amplification X 100 du signal d'émission de l'accepteur. Grâce à ce phénomène de FRET inégalé à la surface des nanoparticules, nous avons réalisé un biosenseur basé sur la désorption. Pour cela, une molécule unique de Cy5-biotine a été absorbée à la surface de la nanoparticule, ce qui résulte en deux bandes d'émission de fluorescence. En réponse à la détection de la streptavidine, la bande d'émission de l'accepteur décroit, car les conjugués de Cy-5 sont désadsorbé la surface des nanoparticules (Figure 6). Ce senseur ratiométrique permet de détecter la streptavidine avec une limite de détection de 0.7 nM. La versatilité de ce senseur a été confirmée en utilisant la Cy5-benzene sulfonamide comme accepteur pour la détection de l'anhydrase carbonique humaine (hCA).

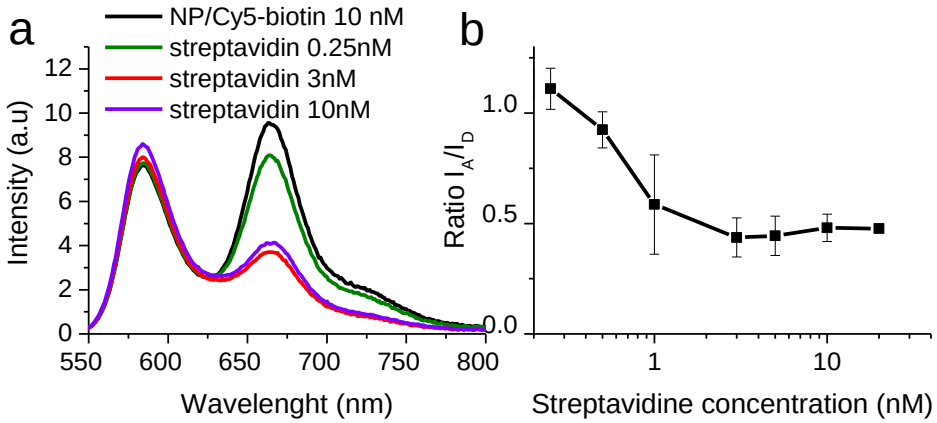

Figure 6. a) Modification du spectre d'émission des NPs dopées avec 20 wt% de R18/F5 et avec une molécule de Cy5-biotine absorbée à la surface lors de la détection de la streptavidine. **b)** Le changement du I_A/I_D lors de la détection de la streptavidine.

Le système a été validé au niveau de la particule unique en utilisant la microscopie de fluorescence à champ large où la détection de la streptavidine s'observe par la disparition d'un signal dans le canal de détection rouge (Figure 7 a). Un blanchiment de l'accepteur, résultant en une baisse de son émission, accompagné par une forte augmentation simultanée de l'émission du donneur, confirme que nous

observons réellement des processus au niveau de la molécule unique à la surface des nanoparticules (Figure 7 b).

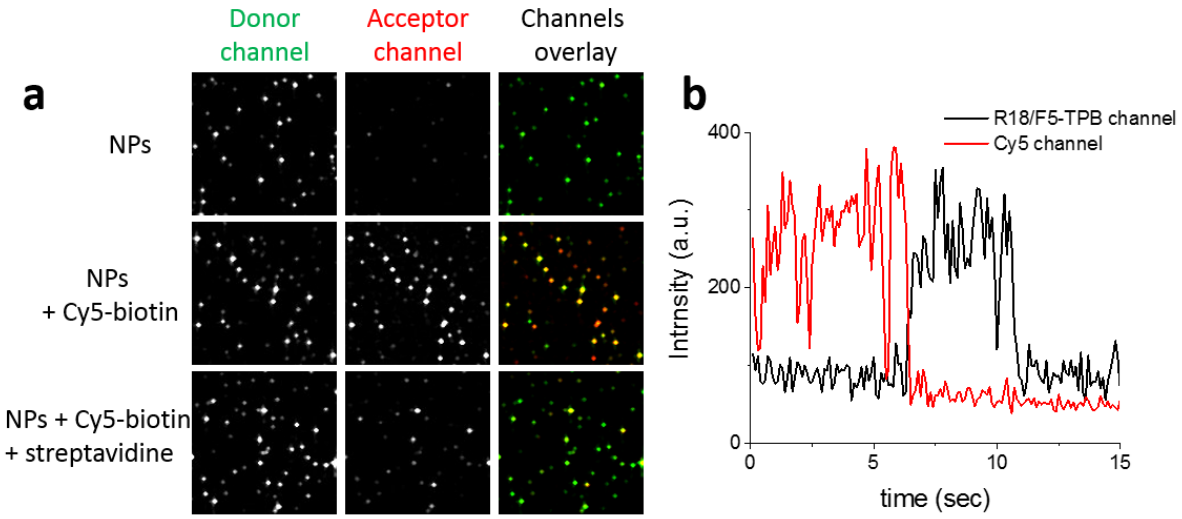

Figure 7. a) Observation en particule unique de sondes sur deux canaux spectraux (vert pour l'émission du donneur, rouge pour celle de l'accepteur) avant et après l'addition de streptavidine. **b)** Traces représentatives en particule unique en excitation 532 nm pour des nanoparticules avec l'accepteur adsorbé.

L'obtention de sondes fluorescentes présentant une luminosité, une photostabilité et une sensibilité supérieures est d'une importance cruciale pour tracer et suivre en temps réel les événements biologiques tant au niveau cellulaire que biomoléculaire. Les applications potentielles des nanoparticules doivent améliorer significativement ces approches. Il reste néanmoins plusieurs défis à relever dans le domaine des sondes nanoparticules fluorescentes pour des applications en bioimagerie *in vivo*.

Durant les trois années de mon projet de doctorat, je me suis focalisée sur la compréhension des relations existant entre la structure des fluorophores encapsulés, leurs propriétés photophysiques et les propriétés des nanoparticules de polymériques que nous avons conçus afin de développer de petites nanoparticules avec une luminosité et une photostabilité suffisamment importantes pour permettre de détecter des biomolécules à des concentrations extrêmement faibles. A l'exemple des dérivés de colorant PDI, la nécessité d'introduire des groupements hydrophobes volumineux dans la structure du fluorophores pour obtenir des nanoparticules lumineuses et photostables a été mise en évidence.

Pour obtenir des nanoparticules efficaces pour le FRET, la possibilité d'exploiter l'EET entre des molécules de donneurs a été étudiée. Ainsi, nous sommes parvenus à une excellente efficacité de FRET entre 10^4 de molécules donneur et des molécules d'accepteur uniques localisées à l'intérieur des nanoparticules, accompagné par une amplification jamais obtenue jusqu'à présent d'un facteur 1000 de l'émission de l'accepteur. Cela ouvre la voie à la détection de molécules uniques sans instrumentation dédiée. Le FRET efficace à l'intérieur des nanoparticules a été exploité pour créer des nanoparticules avec une photocommutation amplifiée. Finalement, la possibilité de détecter des biomolécules individuelles avec une amplification d'un facteur 100 de leur intensité de fluorescence a été démontrée tant en solution qu'au niveau de la particule unique.

L'excellente luminosité et l'efficacité inégalée dans le domaine du FRET font des nanoparticules conçues une classe de candidats parfaits pour la détection et le traçage de biomolécules dans les cellules vivantes au niveau de la molécule unique.

References

1. N.Prasad, P., *Introduction to biophotonics*. 2003, Hoboken, New Jersey.: John Wiley & Sons, Inc.
2. Lakowicz, J.R., *Principles of Fluorescence Spectroscopy*. Vol. Third Edition. 2006, Singapore: Springer.
3. Helmchen, F. and W. Denk, *Deep tissue two-photon microscopy.* Nat Meth, 2005. **2**(12): p. 932-940.
4. Horton, N.G., et al., *In vivo three-photon microscopy of subcortical structures within an intact mouse brain.* Nat Photon, 2013. **7**(3): p. 205-209.
5. Norris, G., et al., *A promising new wavelength region for three-photon fluorescence microscopy of live cells.* Journal of Microscopy, 2012. **246**(3): p. 266-273.
6. Becker, W., *Fluorescence lifetime imaging – techniques and applications.* Journal of Microscopy, 2012. **247**(2): p. 119-136.
7. Berberan-Santos, B.V.a.M.N., *Molecular Fluorescence*. Second Edition ed. 2012, Weinheim, Germany: Wiley-VCH.
8. Colby, K.A., et al., *Electronic energy migration on different time scales: concentration dependence of the time-resolved anisotropy and fluorescence quenching of lumogen red in poly (methyl methacrylate).* The Journal of Physical Chemistry A, 2010. **114**(10): p. 3471-3482.
9. Demchenko, A.P., *Introduction to Fluorescence Sensing, Second Edition*. 2015, Switzerland: Springer International Publishing.
10. Kobayashi, H., et al., *New Strategies for Fluorescent Probe Design in Medical Diagnostic Imaging.* Chemical Reviews, 2010. **110**(5): p. 2620-2640.
11. Irvine, D.J., et al., *Direct observation of ligand recognition by T cells.* Nature, 2002. **419**(6909): p. 845-849.
12. Pansare, V., et al., *Review of Long-Wavelength Optical and NIR Imaging Materials: Contrast Agents, Fluorophores and Multifunctional Nano Carriers.* Chemistry of materials : a publication of the American Chemical Society, 2012. **24**(5): p. 812-827.
13. Geiger, M.W. and N.J. Turro, *PYRENE FLUORESCENCE LIFETIME AS A PROBE FOR OXYGEN PENETRATION OF MICELLES.* Photochemistry and Photobiology, 1975. **22**(6): p. 273-276.
14. Adan, A., et al., *Flow cytometry: basic principles and applications.* Critical Reviews in Biotechnology, 2016: p. 1-14.
15. Aitken, C.E., R.A. Marshall, and J.D. Puglisi, *An Oxygen Scavenging System for Improvement of Dye Stability in Single-Molecule Fluorescence Experiments.* Biophysical Journal, 2008. **94**(5): p. 1826-1835.
16. Altman, R.B., et al., *Enhanced photostability of cyanine fluorophores across the visible spectrum.* Nat Meth, 2012. **9**(5): p. 428-429.
17. Qi, J., et al., *Fluorescent pH Sensors for Broad-Range pH Measurement Based on a Single Fluorophore.* Analytical Chemistry, 2015. **87**(12): p. 5897-5904.
18. Sabnis, R.W., *Handbook of Fluorescent Dyes and Probes*. 2015: John Wiley & Sons, Inc.

19. Lavis, L.D. and R.T. Raines, *Bright Ideas for Chemical Biology.* ACS Chemical Biology, 2008. **3**(3): p. 142-155.
20. Wilhelmsson, L.M., *Fluorescent nucleic acid base analogues.* Quarterly reviews of biophysics, 2010. **43**(02): p. 159-183.
21. Shynkar, V.V., et al., *Fluorescent Biomembrane Probe for Ratiometric Detection of Apoptosis.* Journal of the American Chemical Society, 2007. **129**(7): p. 2187-2193.
22. Klymchenko, Andrey S. and R. Kreder, *Fluorescent Probes for Lipid Rafts: From Model Membranes to Living Cells.* Chemistry & Biology, 2014. **21**(1): p. 97-113.
23. Levitus, M. and S. Ranjit, *Cyanine dyes in biophysical research: the photophysics of polymethine fluorescent dyes in biomolecular environments.* Quarterly reviews of biophysics, 2010. **44**(1): p. 123-151.
24. Kucherak, O.A., et al., *Switchable Nile Red-Based Probe for Cholesterol and Lipid Order at the Outer Leaflet of Biomembranes.* Journal of the American Chemical Society, 2010. **132**(13): p. 4907-4916.
25. Klymchenko, A.S., et al., *Visualization of lipid domains in giant unilamellar vesicles using an environment-sensitive membrane probe based on 3-hydroxyflavone.* Biochimica et Biophysica Acta (BBA) - Biomembranes, 2009. **1788**(2): p. 495-499.
26. M'Baye, G., et al., *Liquid Ordered and Gel Phases of Lipid Bilayers: Fluorescent Probes Reveal Close Fluidity but Different Hydration.* Biophysical Journal, 2008. **95**(3): p. 1217-1225.
27. Sivaraman, G., T. Anand, and D. Chellappa, *Pyrene based selective-ratiometric fluorescent sensing of zinc and pyrophosphate ions.* Analytical Methods, 2014. **6**(7): p. 2343-2348.
28. Zhao, M., et al., *2-(1-Pyrenyl) benzimidazole as a ratiometric and "turn-on" fluorescent probe for iron(iii) ions in aqueous solution.* Analyst, 2016. **141**(7): p. 2308-2312.
29. Tian, M., et al., *A fluorescent sensor for pH based on rhodamine fluorophore.* Dyes and Pigments, 2012. **95**(1): p. 112-115.
30. Ni, Y. and J. Wu, *Far-red and near infrared BODIPY dyes: synthesis and applications for fluorescent pH probes and bio-imaging.* Organic & Biomolecular Chemistry, 2014. **12**(23): p. 3774-3791.
31. Hirano, T., et al., *Development of an 'OFF-ON-OFF' fluorescent pH sensor suitable for the study of intracellular pH.* Tetrahedron, 2016. **72**(32): p. 4925-4930.
32. Chandrasekharan, N. and L.A. Kelly, *A Dual Fluorescence Temperature Sensor Based on Perylene/Exciplex Interconversion.* Journal of the American Chemical Society, 2001. **123**(40): p. 9898-9899.
33. Papkovsky, D.B. and R.I. Dmitriev, *Biological detection by optical oxygen sensing.* Chemical Society Reviews, 2013. **42**(22): p. 8700-8732.
34. Carter, K.P., A.M. Young, and A.E. Palmer, *Fluorescent Sensors for Measuring Metal Ions in Living Systems.* Chemical Reviews, 2014. **114**(8): p. 4564-4601.
35. Heim, R., A.B. Cubitt, and R.Y. Tsien, *Improved green fluorescence.* Nature, 1995. **373**(6516): p. 663-664.
36. Chudakov, D.M., et al., *Fluorescent Proteins and Their Applications in Imaging Living Cells and Tissues.* Physiological Reviews, 2010. **90**(3): p. 1103-1163.

37. McRae, S.R., C.L. Brown, and G.R. Bushell, *Rapid purification of EGFP, EYFP, and ECFP with high yield and purity.* Protein Expression and Purification, 2005. **41**(1): p. 121-127.
38. Lukyanov, K.A., et al., *Photoactivatable fluorescent proteins.* Nat Rev Mol Cell Biol, 2005. **6**(11): p. 885-890.
39. Shcherbakova, D.M., et al., *Photocontrollable Fluorescent Proteins for Superresolution Imaging.* Annual review of biophysics, 2014. **43**: p. 303-329.
40. Alivisatos, A.P., *Semiconductor Clusters, Nanocrystals, and Quantum Dots.* Science, 1996. **271**(5251): p. 933.
41. Michalet, X., et al., *Quantum Dots for Live Cells, in Vivo Imaging, and Diagnostics.* Science, 2005. **307**(5709): p. 538-544.
42. Dahan, M., et al., *Time-gated biological imaging by use of colloidal quantum dots.* Optics Letters, 2001. **26**(11): p. 825-827.
43. Kuno, M., et al., *Nonexponential "blinking" kinetics of single CdSe quantum dots: A universal power law behavior.* The Journal of Chemical Physics, 2000. **112**(7): p. 3117-3120.
44. Hardman, R., *A Toxicologic Review of Quantum Dots: Toxicity Depends on Physicochemical and Environmental Factors.* Environmental Health Perspectives, 2006. **114**(2): p. 165-172.
45. Chen, G., et al., *Upconversion Nanoparticles: Design, Nanochemistry, and Applications in Theranostics.* Chemical Reviews, 2014. **114**(10): p. 5161-5214.
46. Zhou, B., et al., *Controlling upconversion nanocrystals for emerging applications.* Nat Nano, 2015. **10**(11): p. 924-936.
47. Liu, H., T. Ye, and C. Mao, *Fluorescent Carbon Nanoparticles Derived from Candle Soot.* Angewandte Chemie International Edition, 2007. **46**(34): p. 6473-6475.
48. Zhai, X., et al., *Highly luminescent carbon nanodots by microwave-assisted pyrolysis.* Chemical Communications, 2012. **48**(64): p. 7955-7957.
49. Dong, Y., et al., *Polyamine-functionalized carbon quantum dots for chemical sensing.* Carbon, 2012. **50**(8): p. 2810-2815.
50. Sun, Y.-P., et al., *Quantum-Sized Carbon Dots for Bright and Colorful Photoluminescence.* Journal of the American Chemical Society, 2006. **128**(24): p. 7756-7757.
51. Lim, S.Y., W. Shen, and Z. Gao, *Carbon quantum dots and their applications.* Chemical Society Reviews, 2015. **44**(1): p. 362-381.
52. Tuncel, D. and H.V. Demir, *Conjugated polymer nanoparticles.* Nanoscale, 2010. **2**(4): p. 484-494.
53. Wu, C. and D.T. Chiu, *Highly Fluorescent Semiconducting Polymer Dots for Biology and Medicine.* Angewandte Chemie International Edition, 2013. **52**(11): p. 3086-3109.
54. Singh, U., M.M. Dar, and A.A. Hashmi, *Dendrimers: synthetic strategies, properties and applications.* Oriental Journal of Chemistry, 2014. **30**(3): p. 911-922.
55. Abbasi, E., et al., *Dendrimers: synthesis, applications, and properties.* Nanoscale Research Letters, 2014. **9**(1): p. 1-10.
56. Lee, C.C., et al., *Designing dendrimers for biological applications.* Nat Biotech, 2005. **23**(12): p. 1517-1526.

57. Klymchenko, A.S., *Emerging field of self-assembled fluorescent organic dye nanoparticles.* J.Nanosci.Lett., 2013. **3**(21).
58. An, B.-K., et al., *Enhanced Emission and Its Switching in Fluorescent Organic Nanoparticles.* Journal of the American Chemical Society, 2002. **124**(48): p. 14410-14415.
59. Zhang, J., et al., *Highly Stable Near-Infrared Fluorescent Organic Nanoparticles with a Large Stokes Shift for Noninvasive Long-Term Cellular Imaging.* ACS Applied Materials & Interfaces, 2015. **7**(47): p. 26266-26274.
60. Su, J., et al., *Giant Amplification of Photoswitching by a Few Photons in Fluorescent Photochromic Organic Nanoparticles.* Angewandte Chemie International Edition, 2016. **55**(11): p. 3662-3666.
61. Yao, H., Z. Ou, and K. Kimura, *Ion-based organic nanoparticles: Synthesis, characterization, and optical properties of pseudoisocyanine dye nanoparticles.* Chemistry Letters, 2005. **34**(8): p. 1108-1109.
62. Ou, Z.-m., H. Yao, and K. Kimura, *Organic nanoparticles of cyanine dye in aqueous solution.* Bulletin of the Chemical Society of Japan, 2007. **80**(2): p. 295-302.
63. Shulov, I., et al., *Fluorinated counterion-enhanced emission of rhodamine aggregates: Ultrabright nanoparticles for bioimaging and light-harvesting.* Nanoscale, 2015. **7**(43): p. 18198-18210.
64. Zhang, X., Z. Chen, and F. Würthner, *Morphology Control of Fluorescent Nanoaggregates by Co-Self-Assembly of Wedge- and Dumbbell-Shaped Amphiphilic Perylene Bisimides.* Journal of the American Chemical Society, 2007. **129**(16): p. 4886-4887.
65. Shulov, I., et al., *Non-coordinating anions assemble cyanine amphiphiles into ultra-small fluorescent nanoparticles.* Chemical Communications, 2016. **52**(51): p. 7962-7965.
66. Yuan, W.Z., et al., *Changing the Behavior of Chromophores from Aggregation-Caused Quenching to Aggregation-Induced Emission: Development of Highly Efficient Light Emitters in the Solid State.* Advanced Materials, 2010. **22**(19): p. 2159-2163.
67. Bonacchi, S., et al., *Luminescent Silica Nanoparticles: Extending the Frontiers of Brightness.* Angewandte Chemie International Edition, 2011. **50**(18): p. 4056-4066.
68. Montalti, M., et al., *Dye-doped silica nanoparticles as luminescent organized systems for nanomedicine.* Chemical Society Reviews, 2014. **43**(12): p. 4243-4268.
69. Burns, A., et al., *Core/Shell Fluorescent Silica Nanoparticles for Chemical Sensing: Towards Single-Particle Laboratories.* Small, 2006. **2**(6): p. 723-726.
70. Ow, H., et al., *Bright and Stable Core−Shell Fluorescent Silica Nanoparticles.* Nano Letters, 2005. **5**(1): p. 113-117.
71. Reisch, A. and A.S. Klymchenko, *Fluorescent Polymer Nanoparticles Based on Dyes: Seeking Brighter Tools for Bioimaging.* Small, 2016. **12**(15): p. 1968-1992.
72. Rao, J.P. and K.E. Geckeler, *Polymer nanoparticles: Preparation techniques and size-control parameters.* Progress in Polymer Science, 2011. **36**(7): p. 887-913.
73. Tian, Z., A.D. Shaller, and A.D.Q. Li, *Twisted perylene dyes enable highly fluorescent and photostable nanoparticles.* Chemical Communications, 2009(2): p. 180-182.
74. Chen, J., et al., *Synthesis and Characterization of Novel Reversible Photoswitchable Fluorescent Polymeric Nanoparticles via One-Step Miniemulsion Polymerization.* The Journal of Physical Chemistry B, 2011. **115**(13): p. 3354-3362.

75. Candau, F., M. Pabon, and J.-Y. Anquetil, *Polymerizable microemulsions: some criteria to achieve an optimal formulation.* Colloids and Surfaces A: Physicochemical and Engineering Aspects, 1999. **153**(1–3): p. 47-59.
76. Geng, J., et al., *Eccentric Loading of Fluorogen with Aggregation-Induced Emission in PLGA Matrix Increases Nanoparticle Fluorescence Quantum Yield for Targeted Cellular Imaging.* Small, 2013. **9**(11): p. 2012-2019.
77. Kwon, G.S. and K. Kataoka, *Block copolymer micelles as long-circulating drug vehicles.* Advanced Drug Delivery Reviews, 2012. **64, Supplement**: p. 237-245.
78. Mora-Huertas, C.E., H. Fessi, and A. Elaissari, *Influence of process and formulation parameters on the formation of submicron particles by solvent displacement and emulsification–diffusion methods: Critical comparison.* Advances in Colloid and Interface Science, 2011. **163**(2): p. 90-122.
79. Li, K. and B. Liu, *Polymer-encapsulated organic nanoparticles for fluorescence and photoacoustic imaging.* Chemical Society Reviews, 2014. **43**(18): p. 6570-6597.
80. Meallet-Renault, R., et al., *Fluorescent nanoparticles as selective Cu(ii) sensors.* Photochemical & Photobiological Sciences, 2006. **5**(3): p. 300-310.
81. Reisch, A., et al., *Collective fluorescence switching of counterion-assembled dyes in polymer nanoparticles.* Nat Commun, 2014. **5**.
82. Valeur, B., *Molecular Fluorescence Principles and Applications*, ed. W.-V.V. GmbH. 2001.
83. Ishikawa-Ankerhold, H.C., R. Ankerhold, and G.P. Drummen, *Advanced fluorescence microscopy techniques—Frap, Flip, Flap, Fret and flim.* Molecules, 2012. **17**(4): p. 4047-4132.
84. Jares-Erijman, E.A. and T.M. Jovin, *FRET imaging.* Nat Biotech, 2003. **21**(11): p. 1387-1395.
85. http://www.fluortools.com/software/ae/documentation/tools/FRET.
86. Bates, M., T.R. Blosser, and X. Zhuang, *Short-range spectroscopic ruler based on a single-molecule optical switch.* Physical review letters, 2005. **94**(10): p. 108101.
87. Stein, I.H., et al., *Single-Molecule FRET Ruler Based on Rigid DNA Origami Blocks.* Chemphyschem, 2011. **12**(3): p. 689-695.
88. Sapsford, K.E., L. Berti, and I.L. Medintz, *Materials for fluorescence resonance energy transfer analysis: Beyond traditional donor-acceptor combinations.* Angewandte Chemie-International Edition, 2006. **45**(28): p. 4562-4588.
89. Marras, S.A.E., F.R. Kramer, and S. Tyagi, *Efficiencies of fluorescence resonance energy transfer and contact-mediated quenching in oligonucleotide probes.* Nucleic Acids Research, 2002. **30**(21): p. e122.
90. Peng, H.-Q., et al., *Biological Applications of Supramolecular Assemblies Designed for Excitation Energy Transfer.* Chemical Reviews, 2015. **115**(15): p. 7502-7542.
91. Tan, W., K. Wang, and T.J. Drake, *Molecular beacons.* Current Opinion in Chemical Biology, 2004. **8**(5): p. 547-553.
92. Giordano, L., et al., *Diheteroarylethenes as Thermally Stable Photoswitchable Acceptors in Photochromic Fluorescence Resonance Energy Transfer (pcFRET).* Journal of the American Chemical Society, 2002. **124**(25): p. 7481-7489.
93. Klajn, R., *Spiropyran-based dynamic materials.* Chemical Society Reviews, 2014. **43**(1): p. 148-184.

94. Dempsey, G.T., et al., *Photoswitching Mechanism of Cyanine Dyes.* Journal of the American Chemical Society, 2009. **131**(51): p. 18192-18193.
95. Irie, M., *Diarylethenes for Memories and Switches.* Chemical Reviews, 2000. **100**(5): p. 1685-1716.
96. Mahajan, N.P., et al., *Novel mutant green fluorescent protein protease substrates reveal the activation of specific caspases during apoptosis.* Chemistry & Biology, 1999. **6**(6): p. 401-409.
97. Teo, Y.N. and E.T. Kool, *DNA-Multichromophore Systems.* Chemical Reviews, 2012. **112**(7): p. 4221-4245.
98. Hoeben, F.J.M., et al., *About Supramolecular Assemblies of π-Conjugated Systems.* Chemical Reviews, 2005. **105**(4): p. 1491-1546.
99. Hong, Y., J.W.Y. Lam, and B.Z. Tang, *Aggregation-induced emission.* Chemical Society Reviews, 2011. **40**(11): p. 5361-5388.
100. Fábián, Á.I., et al., *Strength in Numbers: Effects of Acceptor Abundance on FRET Efficiency.* Chemphyschem, 2010. **11**(17): p. 3713-3721.
101. Wagh, A., S.Y. Qian, and B. Law, *Development of Biocompatible Polymeric Nanoparticles for in Vivo NIR and FRET Imaging.* Bioconjugate Chemistry, 2012. **23**(5): p. 981-992.
102. Wagh, A., et al., *Polymeric nanoparticles with sequential and multiple FRET cascade mechanisms for multicolor and multiplexed imaging.* Small, 2013. **9**(12): p. 2129-2139.
103. Zhu, L., et al., *Reversibly Photoswitchable Dual-Color Fluorescent Nanoparticles as New Tools for Live-Cell Imaging.* Journal of the American Chemical Society, 2007. **129**(12): p. 3524-3526.
104. Chen, J., et al., *Fabrication of Novel Polymer Nanoparticle-Based Fluorescence Resonance Energy Transfer Systems and their Tunable Fluorescence Properties.* Journal of Macromolecular Science, Part A, 2011. **48**(3): p. 219-226.
105. Chen, J., et al., *Fabrication of Novel Reversible Photoswitchable Fluorescent Nanoparticles.* Journal of Macromolecular Science, Part A, 2011. **48**(8): p. 637-643.
106. Chen, J., et al., *One-pot synthesis of amphiphilic reversible photoswitchable fluorescent nanoparticles and their fluorescence modulation properties.* Polymer Chemistry, 2012. **3**(3): p. 685-693.
107. Chen, J., et al., *Design and Synthesis of FRET-Mediated Multicolor and Photoswitchable Fluorescent Polymer Nanoparticles with Tunable Emission Properties.* The Journal of Physical Chemistry B, 2012. **116**(14): p. 4354-4362.
108. Frigoli, M., K. Ouadahi, and C. Larpent, *A Cascade FRET-Mediated Ratiometric Sensor for Cu2+Ions Based on Dual Fluorescent Ligand-Coated Polymer Nanoparticles.* Chemistry – A European Journal, 2009. **15**(33): p. 8319-8330.
109. Ouadahi, K., et al., *FRET-mediated pH-responsive dual fluorescent nanoparticles prepared via click chemistry.* Nanoscale, 2012. **4**(3): p. 727-732.
110. Valanne, A., et al., *A dual-step fluorescence resonance energy transfer-based quenching assay for screening of caspase-3 inhibitors.* Analytical Biochemistry, 2008. **375**(1): p. 71-81.
111. E.C.C. Gomes, I.M.M.d.C., I.C.N. Diógenes, E.H.S. de Sousa, E. Longhinotti *On the incorporation of Rhodamine B and 20,70-dichlorofluorescein dyes in silica: Synthesis*

of fluorescent nanoparticles. Optical Materials, 2014. http://dx.doi.org/10.1016/j.optmat.2014.02.028.
112. Wang, L. and W.H. Tan, *Multicolor FRET silica nanoparticles by single wavelength excitation.* Nano Letters, 2006. **6**(1): p. 84-88.
113. Wang, L., et al., *Fluorescent nanoparticles for multiplexed bacteria monitoring.* Bioconjugate Chemistry, 2007. **18**(2): p. 297-301.
114. Melucci, M., et al., *Facile tuning from blue to white emission in silica nanoparticles doped with oligothiophene fluorophores.* Journal of Materials Chemistry, 2010. **20**(44): p. 9903-9909.
115. Biffi, S., et al., *Multiple dye-doped NIR-emitting silica nanoparticles for both flow cytometry and in vivo imaging.* RSC Advances, 2014. **4**(35): p. 18278-18285.
116. Fölling, J., et al., *Synthesis and characterization of photoswitchable fluorescent silica nanoparticles.* Small, 2008. **4**(1): p. 134-142.
117. May, F., et al., *Synthesis and characterization of photoswitchable fluorescent SiO2 nanoparticles.* Chemistry–A European Journal, 2012. **18**(3): p. 814-821.
118. He, X.X., et al., *Fluorescence Resonance Energy Transfer Mediated Large Stokes Shifting Near-Infrared Fluorescent Silica Nanoparticles for in Vivo Small-Animal Imaging.* Analytical Chemistry, 2012. **84**(21): p. 9056-9064.
119. Liu, B.Y., et al., *A FRET-based ratiometric sensor for mercury ions in water with multi-layered silica nanoparticles as the scaffold.* Chemical Communications, 2011. **47**(31): p. 8913-8915.
120. Liu, B.Y., et al., *Ratiometric sensing of mercury(II) based on a FRET process on silica core-shell nanoparticles acting as vehicles.* Microchimica Acta, 2013. **180**(9-10): p. 845-853.
121. Saleh, S.M., et al., *Novel multicolor fluorescently labeled silica nanoparticles for interface fluorescence resonance energy transfer to and from labeled avidin.* Analytical and Bioanalytical Chemistry, 2010. **398**(4): p. 1615-1623.
122. Babu, E., P.M. Mareeswaran, and S. Rajagopal, *Highly Sensitive Optical Biosensor for Thrombin Based on Structure Switching Aptamer-Luminescent Silica Nanoparticles.* Journal of Fluorescence, 2013. **23**(1): p. 137-146.
123. Hu, X., et al., *Architecture and mechanism of the light-harvesting apparatus of purple bacteria.* Proceedings of the National Academy of Sciences, 1998. **95**(11): p. 5935-5941.
124. Liu, Z., et al., *Crystal structure of spinach major light-harvesting complex at 2.72[thinsp]A resolution.* Nature, 2004. **428**(6980): p. 287-292.
125. Scholes, G.D., et al., *Lessons from nature about solar light harvesting.* Nat Chem, 2011. **3**(10): p. 763-774.
126. Adronov, A. and J.M.J. Frechet, *Light-harvesting dendrimers.* Chemical Communications, 2000(18): p. 1701-1710.
127. Woller, J.G., J.K. Hannestad, and B. Albinsson, *Self-Assembled Nanoscale DNA–Porphyrin Complex for Artificial Light Harvesting.* Journal of the American Chemical Society, 2013. **135**(7): p. 2759-2768.
128. Xu, Z. and J.S. Moore, *Design and synthesis of a convergent and directional molecular antenna.* Acta Polymerica, 1994. **45**(2): p. 83-87.

129. Balzani, V., et al., *Designing Dendrimers Based on Transition-Metal Complexes. Light-Harvesting Properties and Predetermined Redox Patterns.* Accounts of Chemical Research, 1998. **31**(1): p. 26-34.
130. Schenning, A.P.H.J., E. Peeters, and E.W. Meijer, *Energy Transfer in Supramolecular Assemblies of Oligo(p-phenylene vinylene)s Terminated Poly(propylene imine) Dendrimers.* Journal of the American Chemical Society, 2000. **122**(18): p. 4489-4495.
131. Yang, J., et al., *Excitation energy transfer in multiporphyrin arrays with cyclic architectures: towards artificial light-harvesting antenna complexes.* Chemical Society Reviews, 2012. **41**(14): p. 4808-4826.
132. Kim, D. and A. Osuka, *Directly Linked Porphyrin Arrays with Tunable Excitonic Interactions.* Accounts of Chemical Research, 2004. **37**(10): p. 735-745.
133. Parkinson, P., et al., *Ultrafast Energy Transfer in Biomimetic Multistrand Nanorings.* Journal of the American Chemical Society, 2014. **136**(23): p. 8217-8220.
134. Spillmann, C.M. and I.L. Medintz, *Use of biomolecular scaffolds for assembling multistep light harvesting and energy transfer devices.* Journal of Photochemistry and Photobiology C: Photochemistry Reviews, 2015. **23**: p. 1-24.
135. Díaz, S.A., et al., *FRET: Extending DNA-Based Molecular Photonic Wires with Homogeneous Förster Resonance Energy Transfer (Advanced Optical Materials 3/2016).* Advanced Optical Materials, 2016. **4**(3): p. 339-339.
136. Spillmann, C.M., et al., *Extending FRET cascades on linear DNA photonic wires.* Chemical Communications, 2014. **50**(55): p. 7246-7249.
137. Miller, R.A., A.D. Presley, and M.B. Francis, *Self-Assembling Light-Harvesting Systems from Synthetically Modified Tobacco Mosaic Virus Coat Proteins.* Journal of the American Chemical Society, 2007. **129**(11): p. 3104-3109.
138. Genovese, D., et al., *Energy transfer processes in dye-doped nanostructures yield cooperative and versatile fluorescent probes.* Nanoscale, 2014. **6**(6): p. 3022-3036.
139. Rampazzo, E., et al., *Energy Transfer from Silica Core–Surfactant Shell Nanoparticles to Hosted Molecular Fluorophores.* The Journal of Physical Chemistry B, 2010. **114**(45): p. 14605-14613.
140. Rampazzo, E., et al., *A Versatile Strategy for Signal Amplification Based on Core/Shell Silica Nanoparticles.* Chemistry – A European Journal, 2011. **17**(48): p. 13429-13432.
141. Genovese, D., et al., *Prevention of Self-Quenching in Fluorescent Silica Nanoparticles by Efficient Energy Transfer.* Angewandte Chemie International Edition, 2013. **52**(23): p. 5965-5968.
142. Yao, H. and K. Ashiba, *Efficient Excitation-Energy Transfer in Ion-Based Organic Nanoparticles with Versatile Tunability of the Fluorescence Colours.* Chemphyschem, 2012. **13**(11): p. 2703-2710.
143. Bhattacharyya, S., B. Jana, and A. Patra, *Multichromophoric Organic Molecules Encapsulated in Polymer Nanoparticles for Artificial Light Harvesting.* Chemphyschem, 2015. **16**(4): p. 796-804.
144. Clapp, A.R., et al., *Fluorescence Resonance Energy Transfer Between Quantum Dot Donors and Dye-Labeled Protein Acceptors.* Journal of the American Chemical Society, 2004. **126**(1): p. 301-310.
145. Medintz, I.L., et al., *Quantum dot bioconjugates for imaging, labelling and sensing.* Nat Mater, 2005. **4**(6): p. 435-446.

146. Halivni, S., et al., *Effect of nanoparticle dimensionality on fluorescence resonance energy transfer in nanoparticle–dye conjugated systems.* ACS Nano, 2012. **6**(3): p. 2758-2765.
147. Díaz, S.A., et al., *Photoswitchable Water-Soluble Quantum Dots: pcFRET Based on Amphiphilic Photochromic Polymer Coating.* ACS Nano, 2011. **5**(4): p. 2795-2805.
148. Zhang, C.-Y., et al., *Single-quantum-dot-based DNA nanosensor.* Nat Mater, 2005. **4**(11): p. 826-831.
149. Petryayeva, E. and W.R. Algar, *Multiplexed Homogeneous Assays of Proteolytic Activity Using a Smartphone and Quantum Dots.* Analytical Chemistry, 2014. **86**(6): p. 3195-3202.
150. Shi, J., et al., *Nanoparticle based fluorescence resonance energy transfer (FRET) for biosensing applications.* Journal of Materials Chemistry B, 2015. **3**(35): p. 6989-7005.
151. Zhang, P., et al., *Design of a Highly Sensitive and Specific Nucleotide Sensor Based on Photon Upconverting Particles.* Journal of the American Chemical Society, 2006. **128**(38): p. 12410-12411.
152. Cheng, L., et al., *Multicolor In Vivo Imaging of Upconversion Nanoparticles with Emissions Tuned by Luminescence Resonance Energy Transfer.* The Journal of Physical Chemistry C, 2011. **115**(6): p. 2686-2692.
153. Tian, Z., et al., *Amplified energy transfer in conjugated polymer nanoparticle tags and sensors.* Nanoscale, 2010. **2**(10): p. 1999-2011.
154. Lee, J.-I., et al., *Energy Transfer in a Blend of Electroluminescent Conjugated Polymers.* Chemistry of Materials, 1996. **8**(8): p. 1925-1929.
155. Wu, C., et al., *Energy Transfer Mediated Fluorescence from Blended Conjugated Polymer Nanoparticles.* The Journal of Physical Chemistry B, 2006. **110**(29): p. 14148-14154.
156. Grigalevicius, S., et al., *Excitation Energy Transfer from Semi-Conducting Polymer Nanoparticles to Surface-Bound Fluorescent Dyes.* Macromolecular Rapid Communications, 2006. **27**(3): p. 200-202.
157. Wu, C.F., et al., *Energy transfer in a nanoscale multichromophoric system: Fluorescent dye-doped conjugated polymer nanoparticles.* Journal of Physical Chemistry C, 2008. **112**(6): p. 1772-1781.
158. Wu, C., et al., *Energy Transfer in a Nanoscale Multichromophoric System: Fluorescent Dye-Doped Conjugated Polymer Nanoparticles.* The Journal of Physical Chemistry C, 2008. **112**(6): p. 1772-1781.
159. Grimes, A.F., et al., *Toward Efficient Photomodulation of Conjugated Polymer Emission: Optimizing Differential Energy Transfer in Azobenzene-Substituted PPV Derivatives.* The Journal of Physical Chemistry B, 2006. **110**(39): p. 19183-19190.
160. Wu, C., et al., *Ratiometric Single-Nanoparticle Oxygen Sensors for Biological Imaging.* Angewandte Chemie International Edition, 2009. **48**(15): p. 2741-2745.
161. *Dynamic Light Scattering: Common Terms Defined . Malvern Instruments. v*http://www.biophysics.bioc.cam.ac.uk/wp-content/uploads/2011/02/DLS_Terms_defined_Malvern.pdf.
162. *Dynamic Light Scattering: An introduction in 30 minutes. Malvern Instruments.*http://www.nanobiotec.iqm.unicamp.br/download/particles-Artigo%20Malvern.pdf.

163. Sasaki, A. and M. Kinjo, *Monitoring intracellular degradation of exogenous DNA using diffusion properties.* Journal of Controlled Release, 2010. **143**(1): p. 104-111.
164. Schwille, P., *Fluorescence correlation spectroscopy*, in *Encyclopedic Reference of Genomics and Proteomics in Molecular Medicine*. 2005, Springer. p. 576-578.
165. http://www.microscopemaster.com.
166. Shan, Y. and H. Wang, *The structure and function of cell membranes examined by atomic force microscopy and single-molecule force spectroscopy.* Chemical Society Reviews, 2015. **44**(11): p. 3617-3638.
167. Wolfbeis, O.S., *An overview of nanoparticles commonly used in fluorescent bioimaging.* Chemical Society Reviews, 2015. **44**(14): p. 4743-4768.
168. Demchenko, A.P., *Nanoparticles and nanocomposites for fluorescence sensing and imaging.* Methods and Applications in Fluorescence, 2013. **1**(2).
169. Klymchenko, A.S., et al., *Highly lipophilic fluorescent dyes in nano-emulsions: Towards bright non-leaking nano-droplets.* RSC Adv., 2012. **2**(31): p. 11876-11886.
170. Reisch, A., et al., *Collective fluorescence switching of counterion-assembled dyes in polymer nanoparticles.* Nature Communications, 2014. **5**.
171. Würthner, F., *Perylene bisimide dyes as versatile building blocks for functional supramolecular architectures.* Chemical Communications, 2004(14): p. 1564-1579.
172. Langhals, H., R. Ismael, and O. Yürük, *Persistent Fluorescence of Perylene Dyes by Steric Inhibition of Aggregation.* Tetrahedron, 2000. **56**(30): p. 5435-5441.
173. Samadi, N., et al., *The effect of lauryl capping group on protein release and degradation of poly(d,l-lactic-co-glycolic acid) particles.* Journal of Controlled Release, 2013. **172**(2): p. 436-443.
174. Zeng, Y., et al., *Dendrimers: A Mimic Natural Light-Harvesting System.* Chemistry – An Asian Journal, 2010. **5**(5): p. 992-1005.
175. Yang, J., et al., *Excitation energy transfer in multiporphyrin arrays with cyclic architectures: towards artificial light-harvesting antenna complexes.* Chemical Society Reviews, 2012. **41**(14): p. 4808-4826.
176. Reisch, A., et al., *Charge-Controlled Nanoprecipitation as a Modular Approach to Ultrasmall Polymer Nanocarriers: Making Bright and Stable Nanoparticles.* ACS Nano, 2015. **9**(5): p. 5104-5116.
177. Trofymchuk, K., et al., *Tuning the color and photostability of perylene diimides inside polymer nanoparticles: towards biodegradable substitutes of quantum dots.* Nanoscale, 2014. **6**(21): p. 12934-12942.
178. Hell, S.W., *Microscopy and its focal switch.* Nat Meth, 2009. **6**(1): p. 24-32.
179. Colby, K.A., et al., *Electronic energy migration on different time scales: concentration dependence of the time-resolved anisotropy and fluorescence quenching of Lumogen Red in poly(methyl methacrylate).* J Phys Chem A, 2010. **114**(10): p. 3471-82.
180. Peng, H.-Q., et al., *Artificial Light-Harvesting System Based on Multifunctional Surface-Cross-Linked Micelles.* Angew. Chem. Int. Ed., 2012. **51**(9): p. 2088-2092.
181. Reisch, A. and A.S. Klymchenko, *Fluorescent Polymer Nanoparticles Based on Dyes: Seeking Brighter Tools for Bioimaging.* Small, 2016. **DOI: 10.1002/smll.201503396**.
182. Holzmeister, P., et al., *Breaking the concentration limit of optical single-molecule detection.* Chemical Society Reviews, 2014. **43**(4): p. 1014-1028.
183. Sauer, M., J. Hofkens, and J. Enderlein, *Handbook of Fluorescence Spectroscopy and Imaging: From Ensemble to Single Molecules*. 2011: Wiley-VCH.

184. Magidson, V. and A. Khodjakov, *Chapter 23 - Circumventing Photodamage in Live-Cell Microscopy*, in *Methods in Cell Biology*, S. Greenfield and E.W. David, Editors. 2013, Academic Press. p. 545-560.
185. Dixit, R. and R. Cyr, *Cell damage and reactive oxygen species production induced by fluorescence microscopy: effect on mitosis and guidelines for non-invasive fluorescence microscopy.* The Plant Journal, 2003. **36**(2): p. 280-290.
186. Wei, Q.S., et al., *Fluorescent Imaging of Single Nanoparticles and Viruses on a Smart Phone.* Acs Nano, 2013. **7**(10): p. 9147-9155.
187. Prakash, H.P.G.J., *Solar energy : fundamentals and applications*, ed. N.D.T. McGraw-Hill. 2000: New Delhi : Tata McGraw-Hill.
188. Novotny, L. and N. van Hulst, *Antennas for light.* Nature Photonics, 2011. **5**(2): p. 83-90.
189. Su, L., et al., *Super-resolution Localization and Defocused Fluorescence Microscopy on Resonantly Coupled Single-Molecule, Single-Nanorod Hybrids.* Acs Nano, 2016. **10**(2): p. 2455-2466.
190. Kinkhabwala, A., et al., *Large single-molecule fluorescence enhancements produced by a bowtie nanoantenna.* Nat Photon, 2009. **3**(11): p. 654-657.
191. Garcia-Parajo, M.F., *Optical antennas focus in on biology.* Nat Photon, 2008. **2**(4): p. 201-203.
192. Sun, D.Z., et al., *Light-Harvesting Nanoparticle Core-Shell Clusters with Controllable Optical Output.* Acs Nano, 2015. **9**(6): p. 5657-5665.
193. Tinnefeld, P., *Single-molecule detection: Breaking the concentration barrier.* Nat Nano, 2013. **8**(7): p. 480-482.
194. Acuna, G.P., et al., *Fluorescence Enhancement at Docking Sites of DNA-Directed Self-Assembled Nanoantennas.* Science, 2012. **338**(6106): p. 506-510.
195. Puchkova, A., et al., *DNA Origami Nanoantennas with over 5000-fold Fluorescence Enhancement and Single-Molecule Detection at 25 mu M.* Nano Letters, 2015. **15**(12): p. 8354-8359.
196. Yuan, H.F., et al., *Thousand-fold Enhancement of Single-Molecule Fluorescence Near a Single Gold Nanorod.* Angewandte Chemie-International Edition, 2013. **52**(4): p. 1217-1221.
197. Gartzia-Rivero, L., J. Bañuelos, and I. López-Arbeloa, *Excitation energy transfer in artificial antennas: from photoactive materials to molecular assemblies.* International Reviews in Physical Chemistry, 2015. **34**(4): p. 515-556.
198. Scholes, G.D., et al., *Lessons from nature about solar light harvesting.* Nature Chemistry, 2011. **3**(10): p. 763-774.
199. Groff, L.C., X.L. Wang, and J.D. McNeill, *Measurement of Exciton Transport in Conjugated Polymer Nanoparticles.* Journal of Physical Chemistry C, 2013. **117**(48): p. 25748-25755.
200. Tian, Z.Y., et al., *Amplified energy transfer in conjugated polymer nanoparticle tags and sensors.* Nanoscale, 2010. **2**(10): p. 1999-2011.
201. Yeo, H., K. Tanaka, and Y. Chujo, *Effective Light-Harvesting Antennae Based on BODIPY-Tethered Cardo Polyfluorenes via Rapid Energy Transferring and Low Concentration Quenching.* Macromolecules, 2013. **46**(7): p. 2599-2605.
202. Thomas Iii, S.W., G.D. Joly, and T.M. Swager, *Chemical sensors based on amplifying fluorescent conjugated polymers.* Chemical Reviews, 2007. **107**(4): p. 1339-1386.

203. Galindo, J.F., et al., *Dynamics of Energy Transfer in a Conjugated Dendrimer Driven by Ultrafast Localization of Excitations.* Journal of the American Chemical Society, 2015. **137**(36): p. 11637-11644.
204. Chadha, G., Q.Z. Yang, and Y. Zhao, *Self-assembled light-harvesting supercomplexes from fluorescent surface-cross-linked micelles.* Chemical Communications, 2015. **51**(65): p. 12939-12942.
205. Sun, H.C., et al., *Micelle-Induced Self-Assembling Protein Nanowires: Versatile Supramolecular Scaffolds for Designing the Light-Harvesting System.* Acs Nano, 2016. **10**(1): p. 421-428.
206. Winiger, C.B., et al., *Long-Distance Electronic Energy Transfer in Light-Harvesting Supramolecular Polymers.* Angewandte Chemie-International Edition, 2014. **53**(49): p. 13609-13613.
207. Lin, H.Z., et al., *Collective Fluorescence Blinking in Linear J-Aggregates Assisted by Long-Distance Exciton Migration.* Nano Lett., 2010. **10**(2): p. 620-626.
208. Son, H.J., et al., *Light-harvesting and ultrafast energy migration in porphyrin-based metal-organic frameworks.* Journal of the American Chemical Society, 2013. **135**(2): p. 862-869.
209. Woller, J.G., J.K. Hannestad, and B. Albinsson, *Self-Assembled Nanoscale DNA-Porphyrin Complex for Artificial Light Harvesting.* Journal of the American Chemical Society, 2013. **135**(7): p. 2759-2768.
210. Stadler, A.L., et al., *Fluorescent DNA Nanotags Featuring Covalently Attached Intercalating Dyes: Synthesis, Antibody Conjugation, and Intracellular Imaging.* Bioconjugate Chemistry, 2011. **22**(8): p. 1491-1502.
211. Trofymchuk, K., et al., *Exploiting Fast Exciton Diffusion in Dye-Doped Polymer Nanoparticles to Engineer Efficient Photoswitching.* Journal of Physical Chemistry Letters, 2015. **6**(12): p. 2259-2264.
212. Wurthner, F., T.E. Kaiser, and C.R. Saha-Moller, *J-Aggregates: From Serendipitous Discovery to Supramolecular Engineering of Functional Dye Materials.* Angewandte Chemie-International Edition, 2011. **50**(15): p. 3376-3410.
213. Colby, K.A., et al., *Electronic Energy Migration on Different Time Scales: Concentration Dependence of the Time-Resolved Anisotropy and Fluorescence Quenching of Lumogen Red in Poly(methyl methacrylate).* Journal of Physical Chemistry A, 2010. **114**(10): p. 3471-3482.
214. Magde, D., G.E. Rojas, and P.G. Seybold, *Solvent dependence of the fluorescence lifetimes of xanthene dyes.* Photochemistry and Photobiology, 1999. **70**(5): p. 737-744.
215. Chen, P.Z., et al., *Light-Harvesting Systems Based on Organic Nanocrystals To Mimic Chlorosomes.* Angew. Chem. Int. Ed. Engl. , 2016. **55**: p. 2759-2763.
216. Patra, A., B. Jana, and S. Bhattacharyya, *Functionalized Dye Encapsulated Polymer Nanoparticle Attached with BSA Scaffold as Efficient Antenna Materials for Artificial Light Harvesting.* Nanoscale, 2016. **10.1039/C6NR05201K**.
217. Beljonne, D., et al., *Beyond Förster Resonance Energy Transfer in Biological and Nanoscale Systems.* J. Phys. Chem. B, 2009. **113**(19): p. 6583-6599.
218. Collini, E., *Spectroscopic signatures of quantum-coherent energy transfer.* Chemical Society Reviews, 2013. **42**(12): p. 4932-4947.

219. Collini, E. and G.D. Scholes, *Coherent Intrachain Energy Migration in a Conjugated Polymer at Room Temperature.* Science, 2009. **323**(5912): p. 369-373.
220. Hwang, I. and G.D. Scholes, *Electronic Energy Transfer and Quantum-Coherence in π-Conjugated Polymers.* Chem. Mater., 2011. **23**(3): p. 610-620.
221. Engel, G.S., et al., *Evidence for wavelike energy transfer through quantum coherence in photosynthetic systems.* Nature, 2007. **446**(7137): p. 782-786.
222. Strümpfer, J., M. Şener, and K. Schulten, *How Quantum Coherence Assists Photosynthetic Light-Harvesting.* J. Phys. Chem. Lett., 2012. **3**(4): p. 536-542.
223. Lakowicz, J.R., *Principles of Fluorescence Spectroscopy*. 2006, Singapore: Springer.
224. www.fluortools.com, *UV-Vis-IR Spectral Software 1.2*, FluorTools, Editor.
225. Chen, G., et al., *Fluorescent Nanosensors Based on Fluorescence Resonance Energy Transfer (FRET).* Industrial & Engineering Chemistry Research, 2013. **52**(33): p. 11228-11245.
226. Doussineau, T., et al., *On the Design of Fluorescent Ratiometric Nanosensors.* Chemistry – A European Journal, 2010. **16**(34): p. 10290-10299.
227. Boeneman, K., et al., *Quantum Dots and Fluorescent Protein FRET-Based Biosensors*, in *Nano-Biotechnology for Biomedical and Diagnostic Research*, E. Zahavy, et al., Editors. 2012, Springer: Dordrecht. p. 63-74.
228. Demmig, S. and H. Langhals, *Highly soluble, Lightfast Perylene Fluorescent Dyes.* Chemische Berichte, 1988. **121**: p. 225-230.
229. Altenhöner, K., J.H. Lamm, and J. Mattay, *Novel Dithienylethenes with Extended π-Systems: Synthesis by Aldol Condensation and Photochromic Properties.* European Journal of Organic Chemistry, 2010. **2010**(31): p. 6033-6037.
230. Thompson, N.L., in *Topics in Fluorescence Spectroscopy Techniques*, J.R. Lakowicz, Editor. 1991, Plenum Press: New York. p. 337.
231. Udenfriend, S., *Fluorescence assay in biology and medicine*. Vol. 2. 2014: Academic Press.
232. Jares-Erijman, E.A. and T.M. Jovin, *FRET imaging.* Nature Biotechnology, 2003. **21**(11): p. 1387-1395.
233. Fernandez-Suarez, M. and A.Y. Ting, *Fluorescent probes for super-resolution imaging in living cells.* Nat Rev Mol Cell Biol, 2008. **9**(12): p. 929-43.

List of publications

1. Trofymchuk, K.; Reisch, A.; Shulov, I.; Mely, Y.; Klymchenko, A. S., Tuning the color and photostability of perylene diimides inside polymer nanoparticles: towards biodegradable substitutes of quantum dots. *Nanoscale* **2014**, 6 (21), 12934-12942.
2. Jain, N., Arntz, Y., Ercelen, S., Trofymchuk, K., Mély, Y., Klymchenko, A. S. Synthesis and self-assembly of new unsymmetrical bolaamphiphiles: spontaneous monolayer formation on mica surface. *Journal of Nanoscience Letters* **2014**, 4, pp.38.
3. Trofymchuk, K.; Prodi, L.; Reisch, A.; Mely, Y.; Altenhoener, K.; Mattay, J.; Klymchenko, A. S., Exploiting Fast Exciton Diffusion in Dye-Doped Polymer Nanoparticles to Engineer Efficient Photoswitching. *Journal of Physical Chemistry Letters* **2015**, 6 (12), 2259-2264.
4. Trofymchuk, K.; Reisch, A.; Didier, P.; Fras, F.; Gilliot, P.; Mely, Y.; Klymchenko, A. S., Giant light harvesting nano-antenna for single-molecule detection at ambient light (submitted).
5. Trofymchuk, K.; Shulov, I.; Reisch, A.; Mély, T.; Klymchenko, A. S., Organic nanoparticle antenna for amplified FRET-based biosensing (in preparation).
6. Reisch, A.; Trofymchuk, K.; Runser, A.; Fleith, G.; Rawiso, M.; Klymchenko, A.S., Polymer controlled organization of molecules in nanoparticles and its application to tailoring fluorescence and blinking in dye loaded nanoparticles(in preparation).

List of conferences

1. Kateryna Trofymchuk, Andreas Reisch, Yves Mely, Andrey S. Klymchenko, Ultrabright switchable organic nanoparticles, *Journée des Doctorants ED414*, **2014** (poster presentation).
2. Kateryna Trofymchuk, Andreas Reisch, Yves Mely, Andrey S. Klymchenko, Ultrabright switchable organic nanoparticles, *Journée Campus Illkirch*, **2014**, (poster presentation).
3. Kateryna Trofymchuk, Andreas Reisch, Ievgen Shulov, Yves Mely, Andrey S. Klymchenko, Controlled switching of fluorescent organic nanoparticles, *Journée Campus Illkirch*, **2015** (poster presentation).
4. Kateryna Trofymchuk, Andreas Reisch, Luca Prodi, Jochen Mattay, Yves Mely, Andrey S. Klymchenko, Controlled switching of fluorescent organic nanoparticles, *14th conference on methods and applications in fluorescence, Germany*, **2015** (poster presentation).
5. Kateryna Trofymchuk, Andreas Reisch, Luca Prodi, Jochen Mattay, Yves Mely, Andrey S. Klymchenko, Exploiting fast exciton diffusion in dye-doped polymer nanoparticles to engineer efficient photoswitching through FRET, *Second International Discussion Meeting on Förster Resonance Energy Transfer in the Life Sciences, Germany*, **2016** (oral presentation).

Kateryna TROFYMCHUK

Controlled switching of fluorescent organic nanoparticles through energy transfer for bioimaging applications

Résumé

Les performances des techniques de bioimagerie et de biodétection peuvent être améliorées grâce aux nanoparticules fluorescentes (NPs) permettant un transfert d'énergie résonante de type Förster (FRET) efficace. Le but de mon projet de thèse est le développement de NPs polymériques brillantes et ultrastables encapsulant des fluorophores, capables de produire un FRET au-delà du rayon de Förster. Il a été montré que les groupements encombrés sont essentiels pour minimiser l'auto-extinction et le blanchiment des fluorophores encapsulés. Par ailleurs, la matrice polymérique joue un rôle crucial dans le contrôle de l'effet collaboratif entre fluorophores du au transfert d'énergie d'excitation. Puis, en utilisant cet effet collaboratif entre fluorophores, nous avons conçu des NPs présentant une photocommutation efficace, ainsi qu'un phénomène de "light harvesting" très important. Enfin, de très petites NPs avec un FRET efficace à leur surface ont été élaborées et appliquées pour la détection ultra-sensible de protéines. Les résultats obtenus fournissent de nouvelles perspectives dans le développement des nanoparticules brillantes avec un transfert d'énergie efficace, ainsi que des nano-sondes pour la détection de molécules uniques.

Mots-clés : nanoparticules fluorescentes organiques, le transfert d'énergie d'excitation, bioimagerie

Résumé en anglais

Performance of biosensing and bioimaging techniques can be improved by fluorescent nanoparticles (NPs) capable of efficient Förster resonance energy transfer (FRET). The aim of my PhD project is to develop bright and photostable dye-loaded polymer NPs capable to undergo efficient FRET beyond the Förster radius. We showed that bulky groups are essential for minimizing self-quenching and bleaching of encapsulated dyes. Moreover, polymer matrix plays a crucial role in controlling the inter-fluorophore communication by excitation energy transfer. Then, by exploiting communication of dyes, we designed NPs exhibiting efficient photoswitching as well as giant light-harvesting. Finally, very small NPs with efficient FRET to their surface were developed and applied for ultra-sensitive molecule detection of proteins. The obtained results provide new insights in the development of bright nanoparticles with efficient energy transfer as well as nano-probes for single-molecule detection.

Keywords: fluorescent organic nanoparticles, excitation energy transfer, bioimaging